Additive Manufacturing of Ni-based Superalloys: Effects of Composition



UNIVERSITY OF OXFORD

Joseph N. Ghoussoub

Supervisor: Prof. Roger C. Reed

Department of Materials

University of Oxford

Submitted for the degree of

Doctor of Philosophy

St. Peter's College June 2022

This thesis is dedicated to

Nassif Ghoussoub

Abstract

Additive manufacturing (AM) is now reaching maturity as a method for processing metal alloys. It promises to bring about multifunctional component design integrating fully digital manufacturing. However, preventing cracking during processing remains a key challenge to overcome. This is of particular importance for the Ni-based superalloys used in high temperature applications such as aeronautics and power generation. In this work the effects of alloy composition on the cracking tendencies and performance of Ni-based superalloys are investigated. This study is motivated by the need to develop a better understanding of how to design new alloys specifically tailored for AM. A set of fifteen different compositions – some heritage and some novel – are studied in order to elucidate composition-microstructure-property relationships in 3D-printed Ni-based superalloys.

Quantitative characterisation procedures are here developed to distinguish the two dominant cracking types that occur during AM: solidification and solid-state cracks. Experiments are carried out to explore the effects of alloy composition on the thermophyiscal, thermo-mechanical, and microstructural properties of the alloys and how these relate to the cracking phenomena observed. The magnitude of the ductility-dip (exacerbated by increasing amounts of solid solution strengthening elements) and the solidification path (widened by greater interstitial content) are unambiguously proven to be the critical factors giving rise to solid-state and solidification type cracks respectively. A model for solid-state cracking is proposed, based on an incapacity to relax the thermal stress and withstand the thermal strain arising from differential thermal contraction. This is supported by the development of novel methods for measuring the stress development during constrained cooling using electro-thermal mechanical testing. Stress relaxation by creep was found to be inconsequential during constrained bar cooling given the rapid cooling conditions of AM. This suggests that the development of highly creep resistant yet readily processable alloys is possible. The influence of the (Nb+Ta)/Al ratio is studied to tailor the properties of the novel alloys. This ratio is determined to dictate the trade-off of strength in the athermal regime, creep resistance, oxidation assisted cracking resistance, and oxidation resistance at high temperatures via alumina scale formation. The novel alloys print to γ phase and following sub-solvus heat treatment (with no solutionizing step) generate desirable γ/γ' microstructures tied to good properties. Further assessment of the high temperature oxidation behaviour of all fifteen alloys provides alloy design guidelines for developing oxidation-resistant alloys for AM. In summary, this work highlights the potential to develop new alloys specifically for AM with properties matching those of the heritage ones designed for investment casting.

Preface

The research in this thesis is in preparation for publication or been published as follows:

- Joseph N. Ghoussoub, Yuanbo T. Tang, Chinnapat Panwisawas, André A.N. Németh, and Roger C Reed. On the influence of alloy chemistry and processing conditions on additive manufacturability of Ni-based superalloys. *Superalloys 2020*, pages 153–162, 2020.

- Joseph N. Ghoussoub, Yuanbo T. Tang, William J B. Dick-Cleland, André A.N. Németh, Yilun Gong, D. Graham McCartney, Alan C.F. Cocks, Roger C. Reed. On the influence of alloy composition on the additive manufacturability of Ni-based superalloys. *Metallurgical and Materials Transactions A*, 53, 962-983 (2022).

- Joseph N. Ghoussoub, William J B. Dick-Cleland, Przemysław Klupś, Kathryn E. Rankin, Satoshi Utada, Paul A.J. Bagot, David J. Crudden, D. Graham McCartney, Yuanbo T. Tang, Roger C. Reed. A New Class of Alumina-Forming Superalloy for 3D Printing. *Additive Manufacturing*, Volume 52, April 2022, 102608.

- Joseph N. Ghoussoub, Satoshi Utada, Yuanbo T. Tang, Yilun Gong, Roger C. Reed. Alloy design for additive manufacturing: Early-stage oxidation of Ni-based superalloys (Submitted for publication in *Eurosuperalloys 2022*).

Declaration

I hereby declare that except where specific reference is made to the work of others, the contents of this dissertation are original and have not been submitted in whole or in part for consideration for any other degree or qualification in this, or any other university. This dissertation is my own work and contains nothing which is the outcome of work done in collaboration with others, except as specified in the text and Acknowledgements. This dissertation contains fewer than 40,000 words.

Joseph N. Ghoussoub

June 2022

Acknowledgements

First and foremost I would like to thank Professor Roger Reed for giving me the opportunity of a lifetime at the University of Oxford. Roger always pushed, supported and believed in me through everything and I owe him a debt that can never be repaid. Second, I need to thank Dr. Yuanbo Tang who supported and advised all of this work day and night these past 3 years. I am eternally grateful for the entire reseach group – Mrs. Karen Bamford, Dr. Yilun Gong, Hirokazu Usuki, Dr. Satoshi Utada, Jieming Zhang, Celal Polatoğlu, Prof. D. Graham McCartney, Prof. Chinnapat Panwisawas, Prof. Daniel Barba, Dr. Sabin Sulzer and Alan C.F. Cocks – for their friendship and support. Special thanks goes to my industrial supervisor Dr. André Németh whose infectious optimism and excitement lifted me during many hard times. I am very grateful for my industrial colleague William Dick-Cleland, without which much of this would not have been possible. I want to acknowledge the immensely talented research staff who supported this work including Greg Cook, Jennifer Holter, Jeff Fullerton, Stuart Carter, Chris Salter, and Dr. Katy Rankin.

My experience at the University of Oxford was defined by the incredible fellowship forged with my colleagues in other fields who I had the fortune of meeting at St. Peters College. Words cannot express my gratitude to Dominic McGann, Robert Klapper, and Mark Collett for the amazing impact they have had on my life. Special thanks to the brilliant Mark Collett for his efforts in editing this thesis. Thank you to Matthew Fawkes, Will Cross-Bermingham, and Przemysław Klupś for their camaraderie

living together during a global pandemic, and to PK in particular for his atom probe tomography work which supported this research. A further thank you to Kimberly Glassman and Alex Solovyev for their enduring friendship throughout my DPhil.

I want to express how thankful I am for the friendship of Will Andrews whose strength through adversity was an inspiration to me these past years. To Will and the entire Oxford University Ice Hockey Club thank you so much for an incredible experience playing with the Blues. I will always remember the times in Prague, Budapest, and St. Moritz. It was a honour to be a part of this historic team. Special thanks to Matthew Downer, Christian Norton, Aneel Brar, Joey Seney, Nestor Maslej, Eric Budgell, and Rob Smith who have such character and made Blues hockey unforgettable.

My time in the University of British Columbia Materials Department was key in putting me on the path and giving me the skills I needed for this DPhil. Thank you to my friends Nevin Taylor, Ryan Grutze, and Paula Andruschak for helping me get through it all and the amazing time we had. Thank you to Prof. Warren Poole, Prof. Chadwick Sinclair, and Prof. Steve Cockcroft for their mentorship and guidance in helping me get here.

Thank you to all the amazing friends and engineers I met in California. Especially Mojan Sohi and Alexander Stadnyk for their incredible mentorship and helping me become the engineer I am today. Of course thank you to Siddhant Malik, Omar James, Taylor Simpson, Chloe Redmond, Nate Martin, Fiona Pierce Martin, Eric Heichert, Steven Rintoul, Eden Murray, Cyrus Neary, and Ben Coull whose friendship I will always cherish. Thank you to the Murray family, Paul, Kim, Madi, Logan, and Kelly for hosting me and supporting my research during much of the pandemic.

I am so grateful for the lifelong support from my friends Melvin Chan, Jaryd Te, Nicholas von Hahn, Matthew Ebert, Brenton Wong, and Tim Lau who have always been there for me through thick and thin. Thank you to the Te, Chan, and von Hahn

families, especially Larry, Linda, and Carola for being my home away from home and taking care of me all these years. A special thank you to my incredible sisters Mireille and Michelle who paved the way for everything I ever did and my parents Louise and Nassif for always pushing me to be my best.

Lastly, I would like the thank the Natural Sciences and Engineering Research Council of Canada (NSERC) and Alloyed Ltd. (formerly OxMet Technologies) for their financial support of this research.

Table of contents

List of figures **xix**

List of tables **xxxiii**

Nomenclature **xxxv**

1 Introduction **1**

1.1 Nickel-based superalloys 1

1.2 Additive manufacturing 2

1.3 The challenge: 3D printing superalloys 6

1.4 Thesis structure 7

2 Literature Review **13**

2.1 Physical metallurgy of Ni-based superalloys 13

2.2 Additive manufacturing: key process variables and physical mechanisms 17

2.2.1 Powder feedstock 17

2.2.2 Processing parameters 18

2.2.3 Heat and mass transport 20

2.2.4 Thermal-mechanical considerations 21

2.2.5 Additively manufactured microstructure 22

2.3 Processing induced defects 24

2.3.1 Cracking mechanisms 24
2.3.2 Lack of fusion and porosity 30
2.4 Solutions 32
2.4.1 Process optimization 32
2.4.2 Alloy design 35

3 On the influence of processing conditions on additive manufacturability 39

3.1 Introduction 39
3.2 Alloy design approach 40
3.3 Experimental methods 42
3.3.1 Feedstock material 42
3.3.2 Additive manufacturing trials 43
3.3.3 Quantification of cracking severity and morphology 44
3.3.4 Microstructure and phase characterization 46
3.4 Results 47
3.4.1 On the propensity for alloys to crack at a single processing condition 47
3.4.2 Influence of processing conditions on cracking 48
3.4.3 On the presence of multiple crack mechanisms 50
3.5 Discussion and analysis 51
3.5.1 Considerations of the role of solidification range and path 51
3.5.2 On the influence of processing conditions on microstructure . . . 54
3.6 Rationalization by simple thermal model 57
3.7 Summary and conclusions 59

4 On the influence of alloy composition on the additive manufacturability of Ni-based superalloys 61

4.1 Introduction 61
4.2 Experimental methods 63
4.2.1 Choice of alloy compositions 63
4.2.2 Additive manufacturing 64
4.2.3 Assessment of additive manufacturability 66
4.2.4 Assessment of mechanical and stress relaxation behaviour 67
4.2.5 Assessment of solidification range and phase transformation temperatures 72
4.3 Results 73
4.3.1 On the assessment of cracking severity, morphology, and mechanism 73
4.3.2 On the influence of mechanical properties on additive manufacturability 79
4.3.3 Characterisation of as-printed microstructure and influence of freezing range 87
4.4 Analysis and discussion 95
4.4.1 Modelling of stress development during cooling leading to solid-state cracking 95
4.4.2 Analysis of solidification cracking susceptibility 101
4.5 Final considerations 106
4.6 Summary and conclusions 111

5 On the influence of composition on the performance of additively manufactured Ni-based superalloys 115

5.1 Introduction 115
5.2 Experimental methods 116
5.2.1 Alloy compositions and feedstock materials 116
5.2.2 Processing by additive manufacturing 117

5.2.3 Materials characterization 118
5.2.4 Differential scanning calorimetry and heat treatment 121
5.2.5 Oxidation study 123
5.2.6 Thermo-mechanical testing 123
5.3 Results 125
5.3.1 Resistance to processing induced defects 125
5.3.2 On the influence of heat treatment and microstructure 129
5.3.3 On the alloy properties developed 134
5.3.4 Oxidation behaviour 138
5.4 Discussion 141
5.4.1 On the mechanism of super-solvus ductility loss 141
5.4.2 On the resistance to oxidation-assisted cracking 142
5.4.3 Composition-processing-performance trade-offs 144
5.5 Summary and conclusions 147

6 On the influence of alloy composition on oxidation behaviour 149
6.1 Introduction 149
6.2 Experimental methods 150
6.2.1 Alloy compositions and feedstock material 150
6.2.2 Thermo-gravimetric analysis 152
6.2.3 Microstructural characterisation 153
6.3 Results and analysis 155
6.3.1 Mass gain 155
6.3.2 Growth kinetics and parabolic rate coefficient 157
6.3.3 γ' depletion zones 159
6.3.4 Oxide layers 159
6.3.5 Analysis of quantitative microscopy 167

6.3.6 Design for oxidation resistance 167
6.4 Summary and conclusions 168

7 Conclusions and future work **173**
7.1 Conclusions 173
7.2 Recommendations for future work 176
7.2.1 Factors influencing the ductility limit 177
7.2.2 Assessment of liquation and strain-age cracking susceptibility . . 179
7.2.3 Thermo-mechanical fatigue 179

References **181**

Appendix A Supplemental Data **205**

List of figures

1.1 Evolution of the take off turbine entry temperature (TET) of jet engines over the years. Adapted from ref. [1]. Cutaway renders of (b) the General Electric GE9X high-bypass turbofan. Adapted from ref. [2] and (c) the Siemens Hyflexpower gas turbine. Adapted from ref. [3]. 3

1.2 (a) General Electric additively manufactured fuel nozzle. Adapted from ref.[4]. Additively manufactured Ni-based superalloy rocket engine combustion chamber – adapted from ref. [5] – showing (b) the as-built and (c) post-machined geometry (d) being fired. 4

1.3 Summary of the steps for producing a part through L-PBF/SLM and EBM. Adapted from ref. [6]. 6

1.4 Comparison of the thermal history and heat treatment strategy for conventional investment cast material in red and the proposed strategy for AM material in black. 7

1.5 Spider plot representing alloy characteristics where red exemplifies the sub-optimal condition, green shows the improved characteristics, and grey the optimal. 8

1.6 Summary of the thesis structure and progression. 9

List of figures

2.1 (a) Elements in the periodic table highlighted categorically by their alloying function in Ni-based superalloys (b) secondary electron (SE) micrograph exemplifying γ' precipitates (c) backscattered electron (BSE) micrograph exemplifying a carbide phase at a grain boundary. The arrangements of Ni and Al atoms in (d) the disordered FCC γ phase and (e) the ordered Ni_3Al γ' phase (f) the simple cubic structure of an MC type carbide. 15

2.2 Map of the deformation mechanisms in polycrystalline γ' strengthened Ni-based superalloys. Adapted from Ref. [7]. 16

2.3 Schematic diagram illustrating the multi-physics involved in L-PBF. Adapted from Ref. [8]. 21

2.4 (a) EBSD inverse pole figure (IPF) z-axis (performed by Dr. Yuanbo Tang) of the planes perpendicular and parallel to the build direction for the ABD900AM Ni-based superalloy produced by AM (b) BSE micrographs of showing the XY, XZ, and YZ planes (c) SE micrograph of the 3 planes showing the dendrite directionality. 23

2.5 (a) Schematic diagram showing the L-PBF build process (b) the material state and length scale at which solidification and solid-state cracking occur with corresponding SEM image examples of a (c) solidification crack and (d) a solid-state crack in IN939 as well as (e) SEM micrographs of etched CM247LC in the as-printed condition showing the γ matrix and MC carbide and CM247LC in the heat treated condition (reproduced from ref. [9]) with γ' precipitates. 27

2.6 A modified weldability diagram showing predictions of increased strain-age cracking susceptibility with increased amounts of γ' forming elements, where W denotes weight percent. Adapted from Ref. [9]. 29

2.7 Scanning electron micrographs of (a) porosity (b) lack of fusion and (c) cracking defects. Adapted from Ref. [10]. 31
2.8 Methodology for alloy designed outlined by (a) Tang et al. [9] and (b) Xu et al. [11, 12]. 37

3.1 Computational alloy design spaces used for new grades of superalloy; locations of heritage alloys are also plotted for comparison. (a) strain-age cracking merit index and its relationship to creep merit index and (b) γ' fraction (c) the magnitude of freezing range in relation to the creep merit index and (d) γ' fraction. The final design space used to isolate new grades of alloy is shown in Figure 2.8. Adapted from Ref. [9]. . . . 41
3.2 Scanning electron microscopy images of powder employed to produce specimens. 43
3.3 (a) Sample geometry, build plate, (b) laser path, and (c) process variables - adapted from [13] - shown across multiple length scales. 43
3.4 Optical micrograph of CM247LC material at the sample corner, as observed in the XY plane with a black and white threshold applied. . . 46
3.5 Optical micrographs taken of the XZ plane at the 5 mm height of the as-fabricated material for all four alloys under investigation. Micrographs have had a black and white threshold applied. The regions investigated display cracks and minor porosity in CM247LC and IN939, and some µm length scale porosity in ABD850AM. 47
3.6 The experimentally determined cracking severity as a function of hatch distance and laser velocity fitted with interpolating contours for (a) CM247LC (b) IN939, the solid points represent the samples as shown in Table 3.2. 49

3.7 Superimposed surfaces representing the crack severity for IN939, CM247LC, and the ABD alloys as a function of processing conditions. 51
3.8 Scanning electron micrographs showing examples of (a) solid-state cracks observed in CM247LC and IN939 samples A and C and (b) solidification cracks observed in CM247LC and IN939 samples A and C. 52
3.9 Contour plot of (a) average grain size (diameter) (b) texture component vs processing conditions for CM247LC (c) texture of CM247LC at conditions A, B, and C as shown through pole figures, and the in plane inverse pole figure (IPF-Z). The EBSD analysis was performed by Dr. Yuanbo T. Tang of the University of Oxford high temperature materials research group. 56
3.10 Contour plot representing the 2-dimensional energy density deposited as a function of hatch distance and velocity. Points A and C correspond to the thermal histories modelled in Figure 3.11 below. 58
3.11 Temperature histories resulting from a fixed node given processing conditions of (a) large hatch distance and small velocity (b) large hatch distance and large velocity (c) small hatch distance and small velocity (d) small hatch distance and large velocity. 59
3.12 Snapshots in time at (a) 500µs (b) 1700µs (c) 2900µs and (d) 4900µs of temperature contours from simulation of a heat source passing back and forth across a 10 mm×10 mm 2D substrate with point distance 60µm and hatch distance 120µm – implemented in MATLAB. 59

4.1 The sample geometry used for ETMT tensile, stress relaxation, and constrained bar testing. 68
4.2 (a) Thermal-mechanical approximation of melt pool cooling and (b) schematic diagram of the ETMT setup. 69

4.3 A schematic illustration of temperature, strain and stress profile as a function of time during the stress relaxation and constrained bar cooling test. 70

4.4 (a) The average coefficient of thermal expansion α measured during pre-test heating under free expansion conditions on the ETMT vs the Al content (wt.%) and (b) the average elastic modulus determined at 800 °C vs the equilibrium γ' volume fraction at 800 °C fraction acquired by Thermo-Calc (TTNi8 database). Error bars represent the minimum and maximum values measured. 71

4.5 Bar chart showing crack length density and crack count density for the six unprocessable alloys. 74

4.6 Optical images of the XY plane for each alloy with a binary threshold applied exemplifying cracking or lack thereof in each alloy. It is evident the ExpAM, CM247LC, IN939, IN713, IN738LC and ABD850+CB demonstrated extensive cracking and hence are not readily processable. 76

4.7 Optical micrographs taken of the XZ plane exemplifying cracks observed at the edge and within the bulk of CM247LC, IN939, ExpAM, and IN713, as well as SEM micrographs of solidification and solid-state cracks observed in respective alloys on the XZ plane. 77

4.8 Scatter plots quantifying the morphology of the cracks observed in IN939, CM247LC, IN713, and ExpAM in terms of perimeter/area values, aspect ratio's, and caliper diameters. The probability distribution of the perimeter to area ratio of cracks shown in (i)-(l) is most effective in identifying a composition dependence of crack morphology. 78

4.9 Violin plots showing the median, interquartile range, lower/upper adjacent values, and probability distribution of the perimeter/area ratio. As well as examples of solidification and solid-state cracks and their corresponding perimeter/area values. 79
4.10 The isothermal tensile response of (a) IN625, (b) AM-Dev, and (c) CM247LC at 25, 600, 800, 1000, and 1100 °C in the as-printed state. Summary of the temperature dependence of (d) the elastic modulus, (e) the flow stress, and (f) the strain to failure. 80
4.11 The tensile response of (a) the processable heritage alloys (b) unprocessable heritage alloys (c) processable novel alloys (d) unprocessable novel alloys at 800 °C. 82
4.12 (a) The mean flow stress vs the mean engineering strain to failure at 800 °C after 3 tests, error bars show the minimum and maximum values of the 3 repeats. (b) The flow stress vs the engineering strain to failure at 25 °C. 83
4.13 The stress relaxation behaviour of the (a) processable heritage alloys (b) unprocessable heritage alloys (c) processable novel alloys (d) unprocessable novel alloys at 1000 °C. 84
4.14 The stress relaxation behavior of (a) ABD850AM+CB (b) AM-Dev (c) Waspaloy and (d) IN939 at various temperatures. 85
4.15 Comparison of the stress developed during constrained bar cooling of the CM247LC, IN939, Waspaloy, and IN625 alloys at a cooling rate of 50 °C/s. 86
4.16 SEM and EDX analysis at the crack tip for a typical solid-state crack in (a) IN713 and solidification cracks observed in (b) IN738LC and (c) CM247LC. 88

4.17 Backscattered electron (BSE) micrographs of the as-printed microstructure after tensile testing at 800 °C showing the γ matrix and the intercellular carbides as well as EDX linescans across the carbides showing the carbide enrichment in each alloy. 89
4.18 DSC signal from ExpAM and the respective phase transformations determined by interpretation of (a) the heating cycle and (b) the cooling cycle. 92
4.19 Results of differential scanning calorimetry performed on the 12 compositions. 93
4.20 Summary of the magnitude of the freezing range determined (a) experimentally by DSC and by scheil model using (b) the TCNI8 and (c) the TTNi8 thermodynamic databases. 94
4.21 The stress evolution during cooling at different rates in (a) ABD850AM+CB, (b) Waspaloy, and (c) IN939. 96
4.22 The stress evolution during cooling at 50 °C/s superimposed with the temperature dependent flow stress and linear thermal-elastic stress development for (a) IN625 and (b) CM247LC. 96
4.23 Comparison of the experimentally measured stress during cooling and the fitted thermal-elastic-plastic-viscoplastic model for stress (left axis) and strain (right axis) development of (a) Waspaloy and (b) CM247LC. 101
4.24 Strain developed during constrained cooling for CM247LC, IN939, Waspaloy, and IN625 compared to the ductility limit of the 12 alloys at 800 °C and the ductility limit of CM247LC and IN625 across the full temperature range. 102

4.25 Solidification cracking susceptibility as predicted by the Clyne-Davies criterion, the Rappaz-Drezet-Gremaud criterion, the Kou criterion, and a modified Clyne-Davies criterion, each determined as a function of the solidification path determined experimentally and via scheil with the TCNI8 and TTNi8 databases. 104

4.26 (a) Comparison of the experimentally determined flow stress and the solid solution strengthening model at 800 °C and (b) strengthening coefficients as a function of atomic number for solutes in the 3d, 4d, and 5d groups. 109

4.27 Fracture surfaces of CM247C, AM-Dev, and IN625 after tensile tests at 800 °C illustrating the transition from intra/transgranular to intergranular fracture. 110

4.28 Processing map demonstrating four classes of alloys based upon measurements of their cracking severity (left axis) and flow stress at 800 °C (right axis) as a function of their the ductility at 800 °C. 111

5.1 Results of differential scanning calorimetry upon heating of (a) Alloy 1 (b) Alloy 2 (c) Alloy 3 (d) CM247LC with superimposed equilibrium γ' volume fraction ($\phi_{\gamma'}$) predicted by Thermo-Calc. 122

5.2 (a-d) Optical micrographs with black and white threshold applied showing the cracking in CM247LC vs lack thereof in Alloys 1-3. SEM micrographs showing examples of (e) solid-state cracking (f) solidification and (g) liquation cracking observed in CM247LC. 126

5.3 Slices of the CM247LC blade sample XY and XZ planes as observed by XCT and 3D reconstruction of cracks as observed on each plane. Quantification of porosity and 3D reconstruction showing where porosity occurred in CM247LC and Alloy 2. XCT was performed by Dr. Kathryn E. Rankin at the μ-VIS X-ray Imaging Centre of the University of Southampton. 128

5.4 Tensile response of Alloy 2 at various temperatures following (a) HT 1 (super-solvus) and (b) HT 2 (sub-solvus), as well as their summarized (c) flow stress and (d) ductility across the temperature range. SE micrographs of the Alloy 2 microstructure following (e) HT 1 (f) HT 2 (g) HT 3 showing the γ' inside the grain on the XZ plane. 131

5.5 SE micrographs showing the bi-modal distributions of γ' produced after HT 3 in (a) Alloy 1 (b) Alloy 2 (c) Alloy 3 (d) CM247LC. Concentration profiles across the γ-γ' interface for (e) primary (f) secondary and (g) tertiary γ' observed in Alloy 3 by APT. (h) 3D reconstruction of the atom probe tip of the Alloy 3 microstructure showing the γ' precipitates and cuboid regions of interest used to extract the concentration profiles. Atom probe tomography was carried out by Przemysław Klupś at the University of Oxford APT research group. 133

5.6 Tensile response of (a) Alloy 1 (b) Alloy 2 (c) Alloy 3 (d) CM247LC when strained at $10^{-2}\,s^{-1}$ and summary of their (e) flow stress vs temperature and (f) engineering strain to failure vs temperature. 135

5.7 Plot of the stress level vs Larson-Miller parameter for the compositions creep tested with the build directon as the tensile axis with data from the literature superimposed on the results of this study [14, 9, 15]. . . . 137

5.8 (a) mass change vs time during isothermal thermo-gravimetric testing. (b) BSE micrographs of the oxide developed on each composition following testing. (c) EDX maps showing the distributions of elements in the oxide layers formed on Alloy 2 and CM247LC. 140

5.9 Microstructural analysis of the super-solvus embrittlement showing for super and sub-solvus respectively (a-b) EBSD inverse pole figure along the z-axis on the XY plane (c-d) BSE micrographs on the XZ plane (e-f) SE micrographs of the grain boundary microstructures on the XZ plane (where γ matrix has been etched away). EBSD was carried out by Dr. Yuanbo T. Tang of the University of Oxford high temperature materials research group. 143

5.10 Strain rate dependence of the tensile response of (a) Alloy 1 (b) Alloy 2 (c) Alloy 3 and (d) CM247LC illustrating the their susceptibility to oxidation-assisted cracking. Summary of the strain rate sensitivity of (e) the flow stress and (f) the ductility. 145

5.11 Spider plots summarizing the alloy design trade-offs with varying (Nb+Ta)/Al ratio. 147

6.1 SEM micrographs showing the precipitation of γ' in the bulk of each alloy after 24 h at 1000 °C. 154

6.2 Results thermo-gravimetric analysis at 1000 °C for 24 h for (a) the novel alloys and (b) the heritage alloys. 156

6.3 Summary of the mass gain in 24 h for each alloy. 157

6.4 The evolution of the parabolic rate coefficient measured by the standard method for (a) the novel alloys and (b) the heritage alloys and the method outlined by Monceau et al [16] for (c) the novel alloys and (d) the heritage alloys. 158

6.5 BSE micrographs showing the oxide layers formed at the surface of each alloy after 24 h at 1000 °C. 162
6.6 Phases in each alloy identified by high resolution SEM-EDX after 24 h at 1000 °C. 163
6.7 Schematic representation of the mechanism of internal nitridation caused by cracks and pores in the oxide scale from Ref. [17]. 165
6.8 Summary of the measured γ' depletion zone size for each alloy. Error bars represent 1 standard deviation. 166
6.9 Summary of the measured oxide layer thickness for each alloy. Error bars represent 1 standard deviation. 166
6.10 Summary of the measured mass gain, oxide layer thickness, and γ' depletion zone size as a function of Al content (at%.). 170
6.11 Plot of Al vs Cr content (at%.) for the 15 alloy compositions with regions of different oxide phases highlighted in groups. 171

7.1 The as-printed flow stress vs ductility for the 12 alloys discussed in Chapter 4. The ductility threshold below which alloys crack during processing is highlighted as well as a flow stress – arbitrarily chosen – representing a performance threshold. These thresholds superimposed on the empirically determined strength/ductility trade-off are used to identify the optimal property space that needs to be targeted when designing superalloys for AM. 178

A.1 (a) Temperature histories predicted numerically for L-PBF processing conditions from the literature [18–22] (b) the tracer diffusivity of carbon and boron in γ as a function of temperature as determined through the MOBNI3 thermodynamic database, reproduced from [23]. Contour plots showing the magnitude of the backdiffusion coefficient α as a function of the cooling rate and the temperature of (c) carbon and (d) boron in γ. With the cooling rate extracted from the temperature histories in (a) overlaid. As the cooling rates do not intersect $\alpha = 1$ backdiffusion is deemed negligible in this analysis and simulation of AM solidification is performed under scheil assumptions. 206

A.2 Room temperature tensile response of the 12 alloys discussed in Chapter 4, tests performed with strain rate of $10^{-2}\,s^{-1}$. 207

A.3 Fracture surfaces of ExpAM, CM247LC, AM-Dev, ABD850AM, Waspaloy, and IN625 after tensile tests at 800 °C illustrating the transition from intra/transgranular to intergranular fracture as the amount of solid solution strengtheners is increased. 208

A.4 Optical micrographs of the side profile from the 800 °C tensile specimens after testing. The side profiles show pre-existing defects pointing along the tensile axis as well as cavitation incurred during tensile testing oriented perpendicular to the tensile axis. 209

A.5 (a-i) Analysis of the influence of different elements (at.%) on the 800 °C ductility (j) best fit expression for ductility as a function of the composition solved by multiple linear regressions with Eureqa [24]. 210

A.6 (a-d) SEM micrographs of the Alloy 1-3 feedstock powders (e) the equilibrium γ' volume fraction at 900 °C vs the magnitude of the freezing range predicted by Thermo-Calc under scheil assumptions, (f) predicted alloy density vs predicted temperature at which the creep life is 1000 hrs given 137 MPa applied stress, (g) the estimated alloy cost vs predicted maximum theoretical strength. 211

A.7 SEM micrographs showing the γ' and Al depletion zones each alloy following thermo-gravimetric analysis. 212

List of tables

2.1 Summary of various AM processes and the parameters that distinguish them. Reproduced from Ref. [25]. 19

2.2 Summary of terminology, phase transformations, and mechanical driving force for the different crack mechanisms discussed in welding and AM. . 30

2.3 Alloy compositions of superalloys designed specifically for AM (wt.%). . 38

3.1 Measured alloy powder compositions (wt.%). 42

3.2 Sample processing conditions in the bulk. 45

3.3 DSC results and measures of solidification cracking susceptibility. . . . 53

4.1 Measured alloy powder compositions (wt.%). 65

4.2 Experimentally determined phase transformation temperatures and carbide enrichment. 92

4.3 Strengthening coefficients for solution strengthening in Ni for AM at 800 °C in comparison to [26] (MPa at. Fraction$^{1/2}$). 108

5.1 Compositions of the alloy powders (at.%). 117

5.2 Summary of phase transformation temperatures determined experimentally. 121

5.3 Heat treatment process's applied to Alloy 2. 121

5.4 Spider plot performance values. 146

List of tables

6.1 Measured alloy powder compositions (at.%). 151

6.2 Measured alloy powder compositions (wt.%). 152

6.3 Summary of oxide scales formed after 24 h at 1000 °C. 164

Nomenclature

Other Symbols

α Coefficient of Thermal Expansion

β Shrinkage Factor

Δm Mass Change

$\Delta T_{\text{freezing}}$ Magnitude of the Freezing Range

$\Delta t_{\text{stress relief}}$ Time during which material can relieve stress

$\Delta t_{\text{vulnerable}}$ Time during solidification which the alloy is vulnerable to cracking

$\dot{\varepsilon}$ Strain Rate

$\dot{T}$ Cooling Rate

$\dot{\varepsilon}_{\text{max}}$ Maximum strain rate before formation of a void for a given cavitation pressure.

γ Gamma Phase

γ' Gamma Prime Phase

γ'' Gamma Double Prime Phase

κ Thermal Conductivity

λ_{cell} Cell Spacing

$\mathrm{d}T/\mathrm{d}t$ Cooling Rate

μ Viscosity

$\phi_{\gamma'}$ Gamma Prime Volume Fraction

Φ_{CD} Clyne-Davies Criterion

Φ_{Kou} Kou Criterion

Φ_{RDG} Rappaz-Drezet-Gremaud Criterion

ρ Density

σ Stress

σ_{Thermal} Thermal Strain

σ_{Yield} Yield Stress

ε Strain

A Pre-Exponential Constant in Norton's Law

C_{p} Specific Heat Capacity

D_{C} Chemical diffusion coefficient of carbon in γ

d_{point} Point Distance

E Modulus

f_{s} Fraction solid

G Thermal Gradient

h Heat Transfer Coefficient

h_{distance} Hatch Distance

k_n Solid Solution Strengthening Coefficient

k_{p} Parabolic Rate Coefficient

m Material Dependent Constant in the Ramberg-Osgood relationship

n Creep Exponent in Norton's Law

Q Activation Energy for Creep

R Ideal Gas Constant

T Temperature

t Time

T_{ce} Creep-Elastic Transition Temperature

T_{cg} Grain Coalescence Temperature

t_{distance} Time between laser pulses

t_{exposure} Exposure Time

$T_{\text{L}'}$ Onset of Solidification

T_{L} Liquidus

$T_{\text{S}'}$ Onset of Incipient Melting

T_{S} Solidus

$T_{x\%}$ temperature associated with a remaining solid fraction of $x\%$

v_{T} Isotherm velocity

x_i Concentration of Solute i

Acronyms / Abbreviations

ABD Alloys By Design

AC Air Cool

AM Additive Manufacturing

APB Anti-Phase Boundary

APT Atom Probe Tomography

BSE Backscattered Electron

CAD Computer Aided Design

CD Clyne-Davies

CET Columnar Equiaxed Transition

CFD Computational Fluid Dynamics

CSC Cracking Susceptibility Coefficient

DDC Ductility-Dip Cracking

DED Directed Energy Deposition

DSC Differential Scanning Calorimetry

EB Electron Beam

EBM Electron Beam Melting

EBSD Electron Backscatter Diffraction

EDM Electrical Discharge Machining

EDX Energy-Dispersive X-ray Spectroscopy

EOS Electro Optical Systems

ETMT Electro-Thermal Mechanical Testing

FCC Face Centered Cubic

FEA Finite Element Analysis

FEG Field Emission Gun

FEM Finite Element Method

FVM Finite Volume Method

GA Gas Atomization

GB Grain Boundary

GE General Electric

GMA Gas Metal Arc

HAGB High Angle Grain Boundaries

HIP Hot Isostatic Pressing

HT Heat Treatment

ICF Image Compression Factor

ICP-OES Inductively Coupled Plasma-Optical Emission Spectroscopy

Nomenclature

IPF Inverse Pole Figure

IVAS Integrated Visualization and Analysis Software

KPV Key Process Variables

LGP Low Gamma Prime

LMP Larson Miller Parameter

LOF Lack of Fusion

L-PBF Laser-Powder Bed Fusion

NT Neutron Tomography

OAC Oxidation Assisted Cracking

PA Plasma Arc

PBF Powder Bed Fusion

PREP Plasma Rotating Electrode Process

PWHT Post Weld Heat Treatment

RA Rotary Atomization

RDG Rappaz Drezet Gremaud

SAC Strain-Age Cracking

SE Secondary Electron

SLM Selective Laser Melting

STEM Scanning Transmission Electron Microscopy

TCP Topologically Close Packed

TET Turbine Entry Temperature

TGA Thermo-Gravimetric Analysis

XCT X-ray Computed Tomography

XRD X-Ray Diffraction

Chapter 1

Introduction

1.1 Nickel-based superalloys

The development of the jet engine forever changed the nature of transport. This innovation was made possible due to the invention of the first nickel-based superalloys in the 1940's. These so-called superalloys were unique in their ability to maintain their structural integrity and withstand elevated stresses at high temperatures. Increasing the operating temperature of engineering materials presents substantial economic and environmental advantages, since increasing the temperature an engine cycle improves efficiency, thus reducing fuel consumption. The first generation of superalloys enabled the design of jet engines with hot sections capable of handling turbine entry temperature (TET) of $\sim$800° C. Over the past 80 years, the TET of jet engines has increased to $\sim$1500° C as a result of superalloy development, turbine cooling, and thermal barrier coatings. Figure 1.1 shows the evolution of the TET from 1940 to the late 2000's. Applications of Ni-based superalloys extend beyond the jet engine. Engineering systems including (but not limited to) gas turbines, rocket propulsion, and automotive turbochargers also require the ability to maintain structural integrity at elevated temperatures. Notable examples of how these superalloys have been recently integrated

into complex engineering systems include the General Electric GE9X high-bypass turbofan and the Siemens Hyflexpower gas turbine.

The development of Ni-based superalloys is integrally interlinked with the emergence of new methods by which they are processed; the history of the field demonstrates that a new process usually ushers in new grades of superalloy, such as IN718 for vacuum melting, CMSX-4 for single crystal processing, and Rene 95 for powder-based routes [27]. The novel processing technology of additive manufacturing (AM) is now rapidly maturing, and may be poised to help usher in a new step in the performance of high temperature engineering design.

1.2 Additive manufacturing

Additive manufacturing (AM), also known as 3D printing, is a process by which a part is produced through the consecutive addition of material. Conventionally, engineering components are cast, forged, wrought, rolled, or extruded and then machined to achieve the desired geometry. Production of parts by AM offers many advantages for manufacturers, such as rapid prototyping and design adjustments, and reduced weight through new design techniques like topology optimization, reduction of part count, and material waste. This process is especially well suited for high value low volume production, and dovetails well with the use of Ni-based superalloys, which are high value materials on account of their reliance on expensive elements such as Ta, Nb, Co, Mo, W, and Hf. Disadvantages of the AM process include size restrictions on the parts produced and the propensity for processing induced defects, as well as the stochastic nature of the powder-bed and any heterogeneity that may ensue. A contemporary example of the practical application of AM's advantages is the GE-produced Co-based fuel injection nozzle, shown in Figure 1.2, which had been manufactured and shipped over 100,000 times as of August 2021 [28].

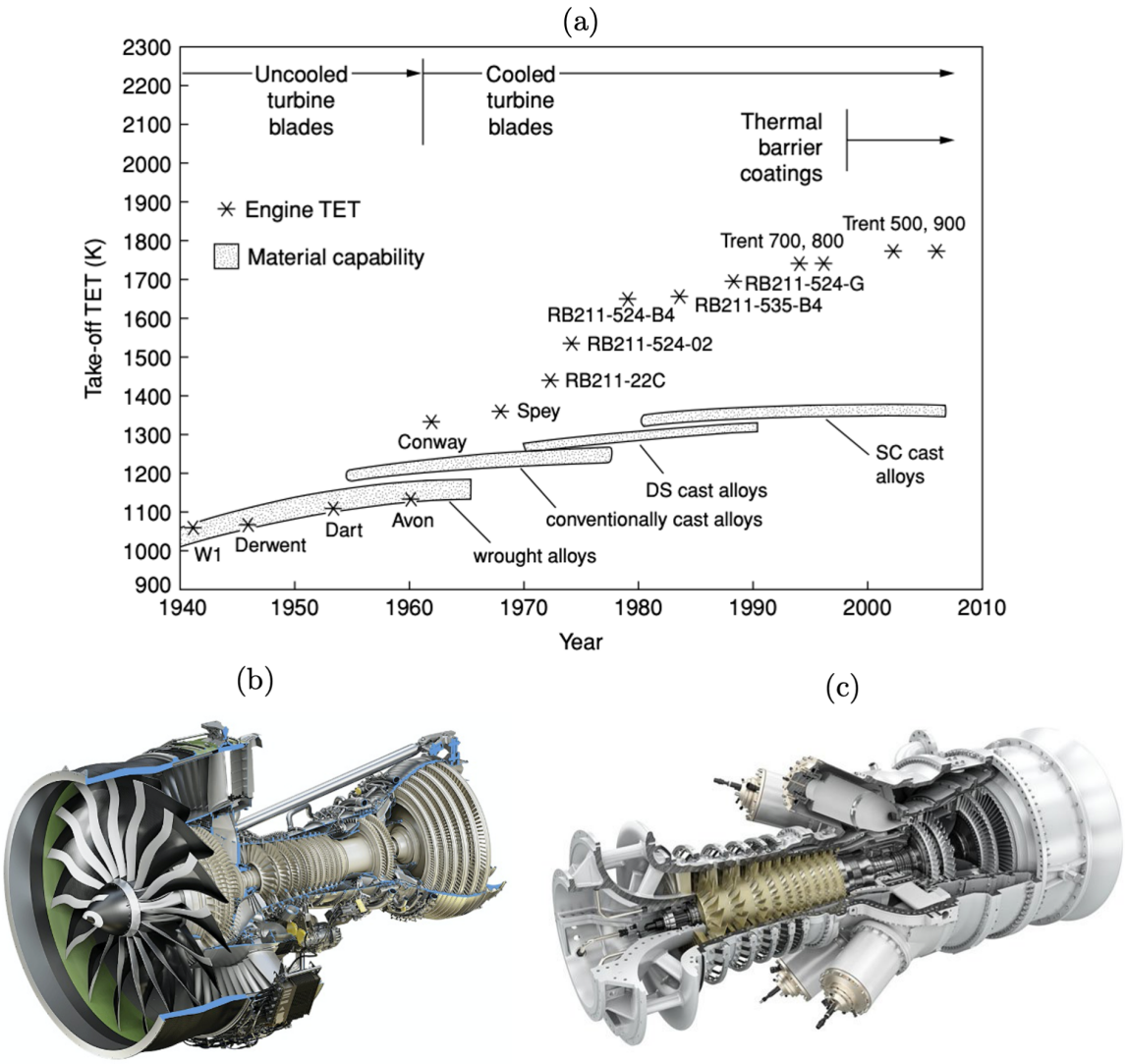

Fig. 1.1 Evolution of the take off turbine entry temperature (TET) of jet engines over the years. Adapted from ref. [1]. Cutaway renders of (b) the General Electric GE9X high-bypass turbofan. Adapted from ref. [2] and (c) the Siemens Hyflexpower gas turbine. Adapted from ref. [3].

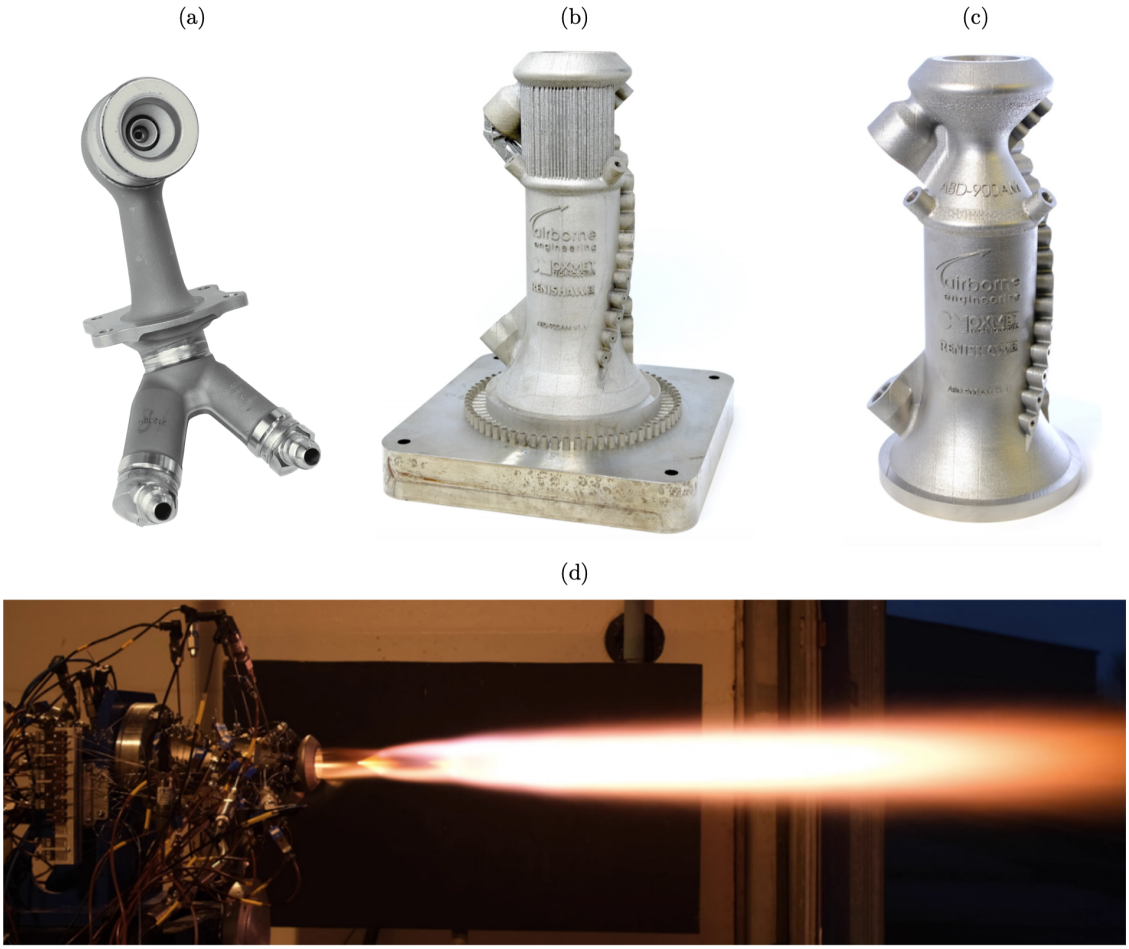

Fig. 1.2 (a) General Electric additively manufactured fuel nozzle. Adapted from ref.[4]. Additively manufactured Ni-based superalloy rocket engine combustion chamber – adapted from ref. [5] – showing (b) the as-built and (c) post-machined geometry (d) being fired.

The geometry of this part involves complex cooling channels, cavities, and a mounting bracket, all of which would have otherwise required a 20 piece assembly, uneconomical casting of a single part, or impossible machining [29]. Another example looking specifically at Ni-alloys is the production of a rocket engine combustion chamber [5] which is shown attached to the base-plate, after removal, and being tested. The use of AM facilitated the rapid production of the component with substantially reduced part count and with computer aided design (CAD) integration.

The initial development of modern AM took place during the 1980's, when a process named stereolithography was developed. This technique involved solidifying consecutive layers of light-sensitive liquid polymer using an ultraviolet light to build up a final part [30]. In the mid 1990's, Electro Optical Systems (EOS) developed the first metal 3D printer, which produced parts by direct metal laser sintering (DMLS). Since then, laser-powder bed fusion (L-PBF) – also refered to as selective laser melting (SLM) – and electron beam melting (EBM) have all been developed. These processes involve initial digital design through CAD the distribution of a fine powder over a flat layer, followed by the passing of a heat source (laser or electron beam) over the correct region to melt and solidify a single layer. The stage is then lowered, and the process repeated until a solid part is buried in powder, the stages of the process are shown in Figure 1.3.

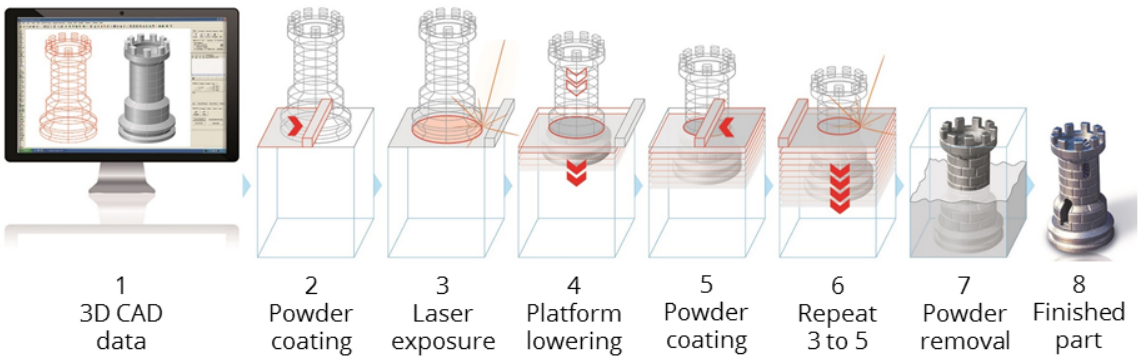

Fig. 1.3 Summary of the steps for producing a part through L-PBF/SLM and EBM. Adapted from ref. [6].

.

EBM offers many advantages, such as consistent high temperature operation which results in reduced residual stress accumulation, as well as the ability to precisely tailor microstructure [31]. Despite these, focus is placed here on L-PBF, the advantages of which include improved surface finish, greater build accuracy, and thinner wall thickness, as well as a broader range of industrial suppliers.

1.3 The challenge: 3D printing superalloys

Combining high performance Ni-superalloys and additive manufacturing presents substantial engineering challenges. First, their compositional complexity requires as many as 15 different alloying elements to be present. This broadens the freezing range, and thus exacerbates the risk of solidification-related cracking whereby the remaining liquid fails to fill the partially solidified microstructure, which is then pulled apart by shrinkage effects [32]. Second, the superalloys are prone to solid-state cracking due to a lack of ductility, particularly in the so-called ductility dip regime of 700 to 900 °C. These factors, in conjunction with the rapid cooling rates characteristic of L-PBF process and resulting high thermal stresses, make the alloys highly susceptible

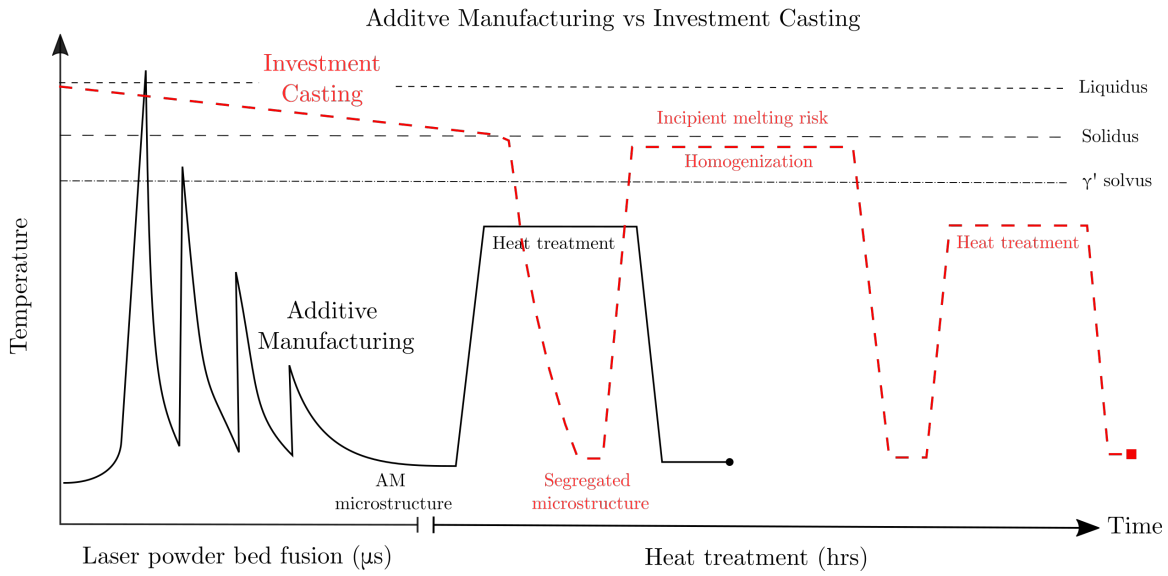

Fig. 1.4 Comparison of the thermal history and heat treatment strategy for conventional investment cast material in red and the proposed strategy for AM material in black.

to cracking as the laser melts the powder layer by layer. The thermal history of a part being processed by AM is summarized in Figure 1.4; this is contrasted with the typical thermal cycle for investment casting.

The cracking susceptibility of the Ni-based superalloys is further increased by the qualities of high strength and creep resistance for which they are so desirable in the first place. Maximizing all material properties such as strength, creep resistance, processability, and oxidation resistance simultaneously (exemplified in Figure 1.5) is challenging. In light of these difficulties, the engineer must wonder if there are processing conditions or specific alloy compositions which would enable the successful printing of high performance superalloys despite the challenges presented by the process.

1.4 Thesis structure

The structure and progression of the thesis is summarized in Figure 1.6. Chapter 2 begins by reviewing the physical metallurgy of the Ni-based superalloys followed by a

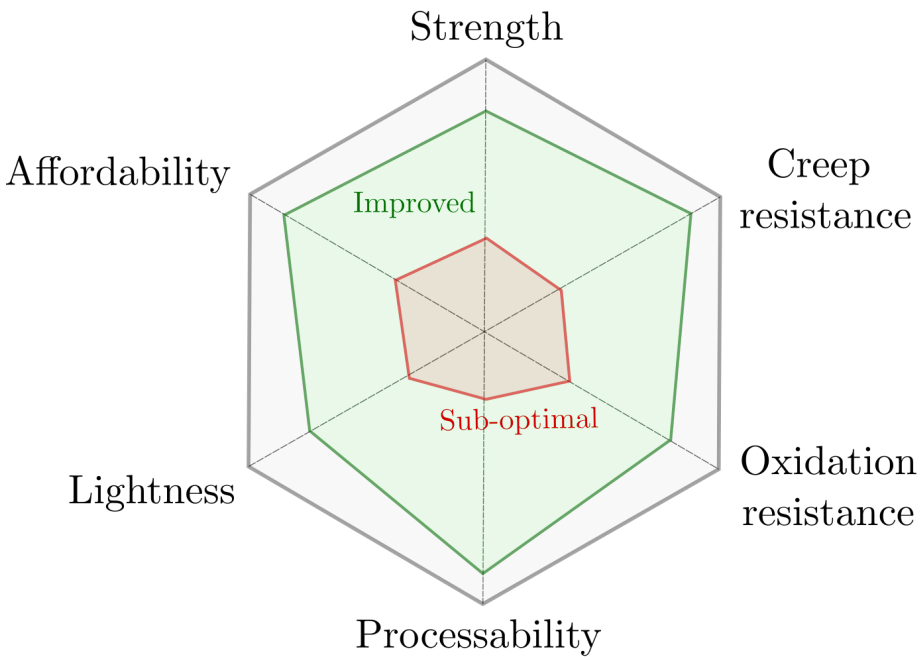

Fig. 1.5 Spider plot representing alloy characteristics where red exemplifies the sub-optimal condition, green shows the improved characteristics, and grey the optimal.

survey of the relevant literature on the topic of their processing by AM. An overview of the various processing induced defects such as cracking, lack of fusion, and porosity defects incurred during AM is presented. This is followed by a more specific dive into the metallurgical and thermal-mechanical phenomena responsible for the occurrence of different cracking mechanisms such as solidification, liquation, and solid-state. Lastly, a review is made of the various attempts to address the issue of cracking during AM such as process modelling and alloy design.

Chapter 3 focuses on understanding the influence of processing conditions on the additive manufacturability of Ni-based superalloys. This study is carried out to compare two solutions to cracking during AM, the first being optimizing processing condition for a fixed alloy composition and the second the processing of alloys developed specifically for 3D printing. The processability of the alloys – with emphasis on their capability to resist cracking – is assessed by comparing the two legacy alloys IN939

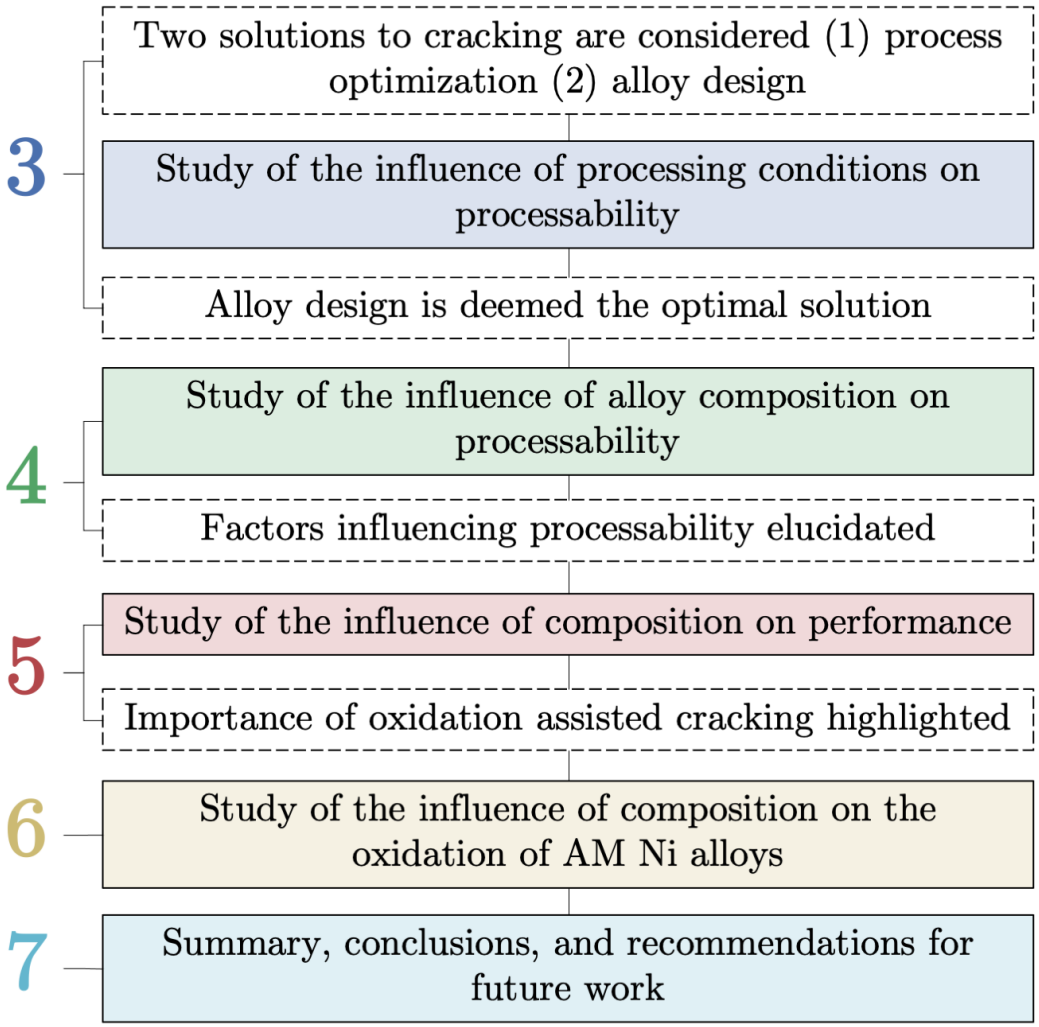

Fig. 1.6 Summary of the thesis structure and progression.

and CM247LC to two novel alloys, ABD850AM and ABD900AM. Thermo-physical testing and quantitative characterization, particularly via stereology, are used to help rationalize the physical basis of the improved manufacturability displayed.

An investigation of the influence of alloy composition on additive manufacturability is performed in Chapter 4. This based on the findings of Chapter 3, which point to alloy design being the more efficient solution to AM processing, as opposed to extensive process parameter optimization. Twelve different alloys – some of existing (heritage) type but also other newly-designed examples – are considered. Stereological procedures

are developed to enable the two dominant defect types found – solidification cracks and solid-state ductility-dip cracks – to be distinguished and quantified. Differential scanning calorimetry, creep stress relaxation tests and measurements of tensile ductility are used to interpret the effects of alloy composition. A model for solid-state cracking is proposed, based on an incapacity to relax the thermal stress arising from constrained differential thermal contraction; its development is supported by experimental measurements using a constrained bar cooling test. A modified solidification cracking criterion is proposed based upon freezing range but including also a contribution from the stress relaxation effect.

Chapter 5 investigates the influence of composition on the performance of the Ni-based superalloys designed for AM. After all, what good is achieving processability if the properties of the end product are insufficient? The effect of varying the (Nb+Ta)/Al ratio is emphasised, in an effort to confer adequate low-temperature strength whilst maintaining oxidation resistance via alumina scale formation. Three distinct attributes are considered: processability, heat treatment response and finally mechanical behaviour. In this way, a holistic picture of the processing/property relationship is built up. CM247LC, which is a widely available heritage alloy usually processed using conventional investment casting is used as a benchmark. Consistent with the intended applications of these materials, the high temperature properties are emphasised particularly with regards to creep and oxidation; the low temperature strength in the athermal regime is also considered.

Chapter 6 discusses the oxidation resistance of the Ni-based superalloys processed by AM. A wide range of alloys is investigated, some heritage and some designed for AM. A combination of isothermal oxidation testing and post-mortem characterization is used to develop key oxidation related alloy design parameters.

Chapter 7 outlines the key outcomes of this research, as well as suggestions for future work required for the development of high performance Ni-based superalloys engineering components processable by additive manufacturing.

Chapter 2

Literature Review

2.1 Physical metallurgy of Ni-based superalloys

The microstructure of Ni-based superalloys is typically comprised of a combination of a γ matrix and, γ' precipitates. Carbides, borides, topologically close packed phases (TCP) [33], and γ'' may also make up the microstructure depending on the specific alloy composition [34]. The γ phase has disordered face centered cubic (FCC) structure, whereas γ' is a precipitate of ordered FCC $L1_2$ structure which is typically coherent with the matrix, this phase provides precipitation strengthening in the low to moderate temperature regime [35]. At high temperatures greater than 850 °C deformation in such alloys is diffusion driven, as dislocation can move through γ channels between precipitates [36] . Carbides are often included in order to reduce grain boundary (GB) sliding [1]. As many as 15 different elements are used to achieve the desired microstructure and properties. Figure 2.1 summarizes the rationale for their additions. Ni, Co, and in older grades of alloy Fe make up the base matrix of the material. Al is the principal addition which promotes γ' formation, though Nb, Ti, and Ta can also be substituted in smaller amounts [37]. Cr is generally added for moderate temperature oxidation resistance where it promotes the formation of

protective Cr_2O_3 oxide layers [38]. W, Mo, Hf, and Re can be added to provide solid solution strengthening. Furthermore, these elements have low diffusivity in Ni [39]. This improves the creep resistance of the alloys by inhibiting transport through the γ channels. C, B, and Zr promote the formation of grain boundary phases such as carbides with MC, $M_{23}C_6$, M_6C structures and borides with structures such as M_5B_3 and M_3B_2 [40, 41].

Superalloys must resist deformation across a broad temperature range. The impeding of dislocations by γ' precipitates ensures resistance to deformation up to ~850 °C. Under these conditions dislocations must shear through the precipitate in order to bypass. The ability to resist the entering of the dislocation into the precipitate and then ultimately shear through it derives from the anti-phase boundary (APB) energy [42]. Hence in this regime the size, volume fraction, and composition of γ' are critical to performance. At temperatures exceeding ~850 °C dislocations can transport through γ between precipitates as well as climb to bypass the precipitates due to the elevated temperature [43]. At moderate temperatures given slow strain rates continuous faults and microtwinning are consequential deformation processes [44–46]. However, the rapid rate of deformation taking place during AM diminishes their import in this body of work. Barba et al summarize the deformation mechanisms in superalloys from 25 °C to 1100 °C in [7] which is shown in Figure 2.2. The grades of Ni-based superalloys initially developed contained low or no γ'. These grades derive their strength primarily from the contribution of solid solution strengthening and come at lower cost and reduced flow stress due to their lack of ability to impede dislocation movement with precipitates.

Grain boundary sliding (GBS) at elevated temperatures necessitates the inclusion of the aforementioned grain boundary phases. The influence of the nature of grain boundaries on mechanical properties such as strength and ductility has been considered in terms of shape and the extent of serrations [47, 48]. Experiments involving in-situ

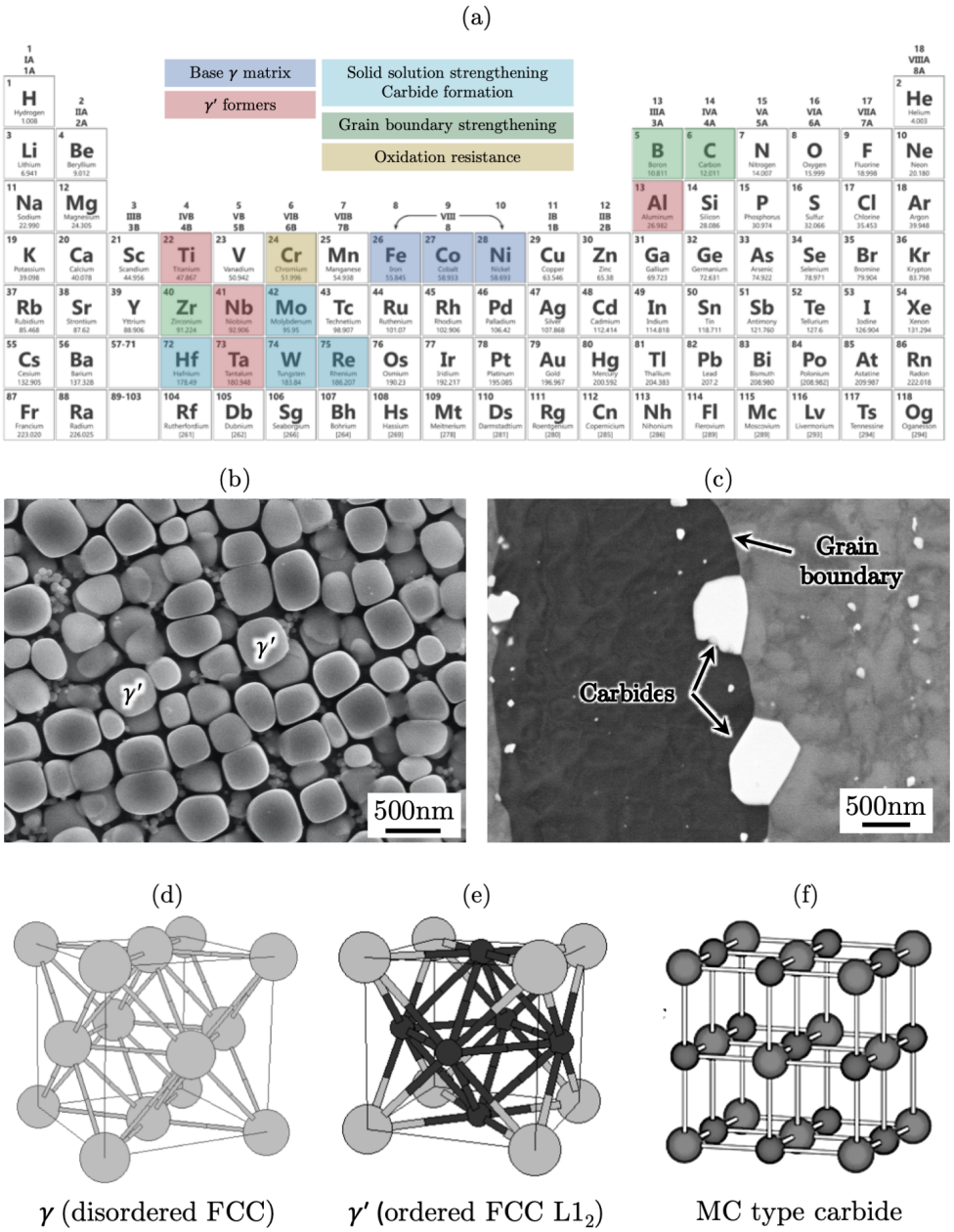

Fig. 2.1 (a) Elements in the periodic table highlighted categorically by their alloying function in Ni-based superalloys (b) secondary electron (SE) micrograph exemplifying γ' precipitates (c) backscattered electron (BSE) micrograph exemplifying a carbide phase at a grain boundary. The arrangements of Ni and Al atoms in (d) the disordered FCC γ phase and (e) the ordered Ni_3Al γ' phase (f) the simple cubic structure of an MC type carbide.

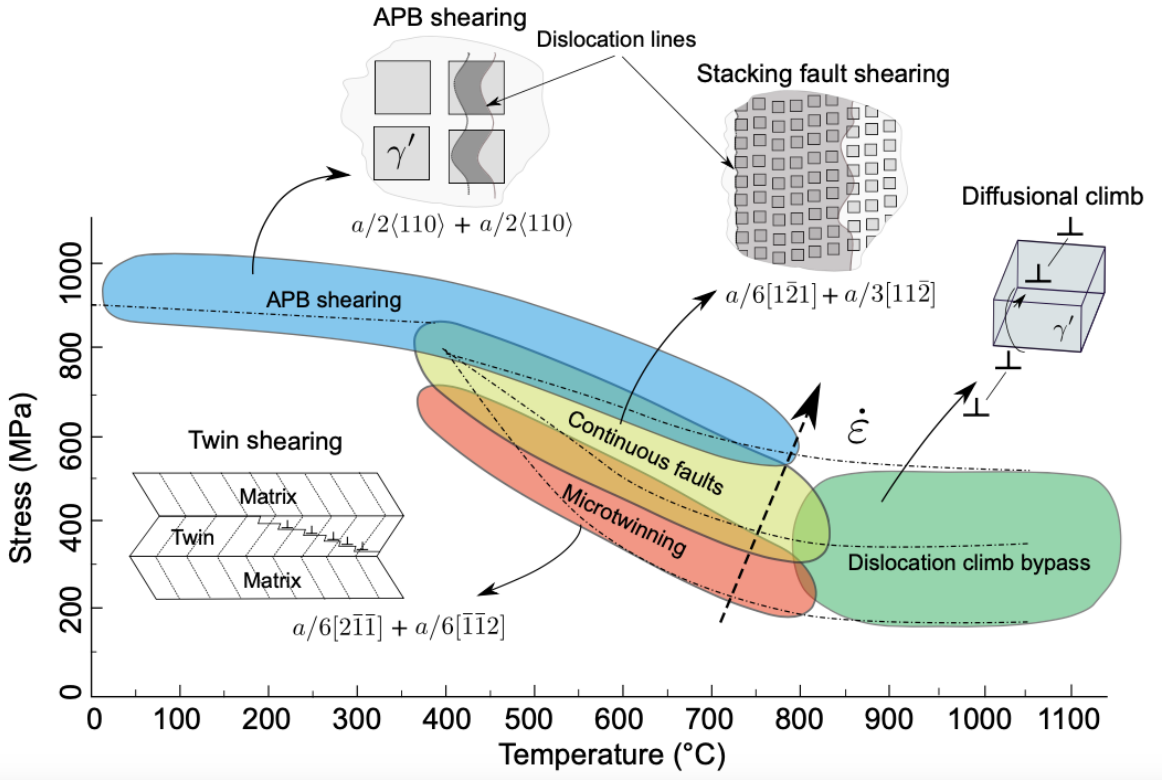

Fig. 2.2 Map of the deformation mechanisms in polycrystalline γ' strengthened Ni-based superalloys. Adapted from Ref. [7].

observation and modelling by crystal plasticity have confirmed that grain boundary tortuosity retards damage evolution by heterogeneously distributing strain [49]. The effect of grain boundary phases on the ductility and deformation of polycrystalline superalloys has been shown to be critical, as the presence of small volume fractions of carbides and borides can unlock improved ductility [50–52]. Single crystal processing removes the grain boundaries, but is a challenge to achieve by AM. To date, the most promising methodology developed employed EBM to control the average layer heat flow such that it followed a classic pigtail pattern [31], a single crystal was achieved in the bulk with small grains at the sample edge [53].

2.2 Additive manufacturing: key process variables and physical mechanisms

Here the influence of various process variables such as feedstock material and processing conditions on the thermo-fluid and thermo-mechanical conditions during processing are reviewed. These in turn dictate the quality, microstructure, defects, and performance of the produced alloy.

2.2.1 Powder feedstock

As with conventional metallurgical processing, the quality of feedstock material is of utmost importance in ensuring the quality of final components. Debroy et al have demonstrated that to achieve optimal flow through feeder nozzles and a well-controlled melt pool small particles of uniform size distribution and smooth surface are desirable [25]. Hence, quality can be characterized in terms of powder morphology, density, size distribution, and flowability [54–56]. Different powder production processes yield different powder quality. Some of the most common include: plasma rotating electrode

process (PREP), rotary atomization (RA), and gas atomization (GA) [25]. PREP involves the melting of metal though plasma or electric arc, rotating to expel resulting solidifying powder. This produces higher quality powder of spherical nature and good surface finish but at a higher cost [57]. RA occurs by the pouring of liquid metal on a rotating platform, hence similarly ejecting now solidified powder. This produces powder of good surface finish but irregular shape [58]. Lastly, GA offers a compromise, yielding spherical powder of lower surface quality. This is achieved by applying high pressure nitrogen or argon gas flow to liquid metal [59, 60]. GA produced with Ar is the method of manufacture of primary concern in this research. Should the spatial interaction of the beam be of the same order of magnitude as the particles with which it interacts, the placement and size of each particle can be the undoing of a part's integrity should the process not be optimized. In light of this, the stochastic nature of powder spreading marks one of AM's unique challenges.

2.2.2 Processing parameters

Two major classes of process encapsulate part production via AM: Directed Energy Deposition (DED) and Powder Bed Fusion (PBF). DED consists of deposition of the feedstock material via wire or powder as the heat source is applied to melt it. The heat sources can include laser (L), electron beam (EB), plasma arc (PA), and gas metal arc (GMA) [25]. For PBF processing, the powder is distributed over the entirety of a layer before the heat source is passed over selectively in the specific regions. Heat sources for PBF are laser and electron beam. A summary of the conditions for these AM processes is shown in Table 2.2.2.

Table 2.1 Summary of various AM processes and the parameters that distinguish them. Reproduced from Ref. [25].

Process	DED			PBF	
Feedstock	Powder	Wire		Powder	
Heat source	Laser	E-beam	Electric arc	Laser	E-beam
Nomenclature	DED-L	DED-EB	DED-PA/DED-GMA	L-PBF	EBM
Powder (W)	100-3000	500-2000	1000-3000	50-1000	
Speed (mm/s)	5-20	1-10	5-15	10-1000	
Max. feed rate (g/s)	0.1-1.0	0.1-2.0	0.2-2.8	-	
Max. build size (mm×mm×mm)	2000×1500×750	2000×1500×750	5000×3000×1000	500×500×250	
Production time	High	medium	low	high	
Dimensional accuracy (mm)	0.5-1.0	1.0-1.5	No fine features	0.04-0.2	
Surface roughness (um)	4-10	8-15	Machining needed	7-20	
Post processing	HIP (sometimes)	Surface finish machining		HIP (sometimes)	

Figure 1.3 shows the use of L-PBF – the process considered in this body of work – for productuon of a chess piece. The piece is produced by melting a fine layer of powder in the shape of a 3D parts planar cross section, shifting the now solid region downwards, spreading new powder over the surface, and repeating. Due to the high temperature nature of the process, it is carried out under Ar atmosphere to prevent oxidation of reactive powders [61]. The specifics of how the laser passes over the powder has a large influence on the resulting material. Details such as the laser scan path can be tailored to achieve different microstructures [62]. Other parameters of note include laser path, velocity, or power to introduce a few. The complete array of parameters changes depending on the make of the metal 3D printer. Within the subset of L-PBF, both pulsed laser and continuous laser systems have been developed. Key process variables characteristic of the Renishaw AM 400 pulsed fiber laser system used in this body of work include powder layer thickness, laser power, laser spot size, laser pulse exposure time, laser path hatch spacing, and laser path point spacing. In order to achieve homogeneity it is typical for the scanning pattern coordinate reference frame to be rotated by 67° after each layer [63]. The influence of specific processing conditions is discussed further in what follows.

2.2.3 Heat and mass transport

Figure 2.3 summarizes the physical mechanisms taking place during L-PBF [8]. Despite the many similarities between metal AM and multi-pass welding [64, 65], its small time and length scales exacerbate typical welding challenges [66]. Energy from the heat source is either absorbed or reflected. Energy absorbed incites melting of the powder particles, under certain conditions causing the liquid metal to evaporate [67] or spatter due to gas flow [68, 69]. This heat is also conducted through powder in contact and the solid material. Further heat sinks includes the transport of heat away from the

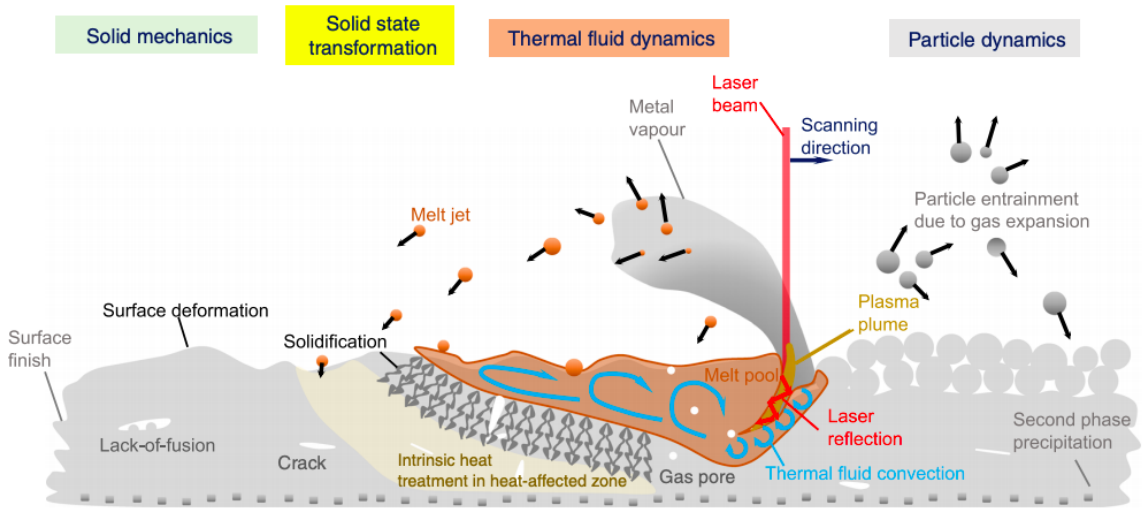

Fig. 2.3 Schematic diagram illustrating the multi-physics involved in L-PBF. Adapted from Ref. [8].

part by radiation and convection. Lastly, at small length scales the Marangoni effect must be considered: temperature gradient induced differential surface tensions drive convective transport within the melt pool [68, 70].

With such a complex combination of transport phenomena occurring at such small length scales, the thermal histories of parts become complex and highly variable across the build height [71]. Furthermore, layers that have already been melted will experience reheating and in some cases remelting [72] depending on the laser powder and layer thickness employed [67]. When this degree of intricacy is compounded with further complexities such as scan strategy or geometry, the result is a highly heterogeneous thermal history, which has repercussions, namely the accumulation of residual stress.

2.2.4 Thermal-mechanical considerations

Engineering components must conform to quality standards. This includes not only the mechanical and thermo-physical properties, but geometric fidelity. Parts manufactured through AM often incur significant warping [73]. This is particularly true of Ni-based superalloys which maintain their strength at high temperatures [74]. The concepts of

thermal strain and residual stress are well studied in the casting and welding literature [75–79]. Thermal strain develops as a result of temperature gradients. A bar subjected to a temperature change will expand or contract in accordance to its thermal expansion coefficient α following

$$\varepsilon_{\text{Thermal}} = \alpha \Delta T \tag{2.1}$$

where $\varepsilon_{\text{Thermal}}$ is the thermal strain. For a given modulus E this strain will result in a stress σ_{Thermal} consistent with hookes law as shown below.

$$\sigma_{\text{Thermal}} = E\varepsilon_{\text{Thermal}} \tag{2.2}$$

If the σ_{Thermal} exceeds the yield stress of the material σ_{Yield}, the deformation is plastic and permanent. Parts that incur significant thermal stress during processing may relieve this to an extent by deforming when detached from the baseplate. This deformation, or warping, can lead to parts that are off-specification. Academic and industrial efforts are ongoing to develop predictive capabilities such that parts can be designed in anticipation of warping and part yield can be improved [80–84]. Industrial software include ANSYS Additive Print, Flow Science's FLOW-3D, COMSOL Multiphysics, and AlphaSTAR Corporation's GENOA 3DP to name a few. Notable benchmarking of these was done by Peter et al of EOS in a comprehensive manner [85].

2.2.5 Additively manufactured microstructure

Extreme cooling rates of of 10^5-10^7 K/s [86–89] and small characteristic length scales unique to AM make for a novel area of metallurgical study. This in conjunction with the unique thermal history of AM highlighted previously bring into the question the presence of second phase precipitation, the degree of layer remelting and the possibility of recrystallization. The microstructures produced by AM are orthotropic. Figure

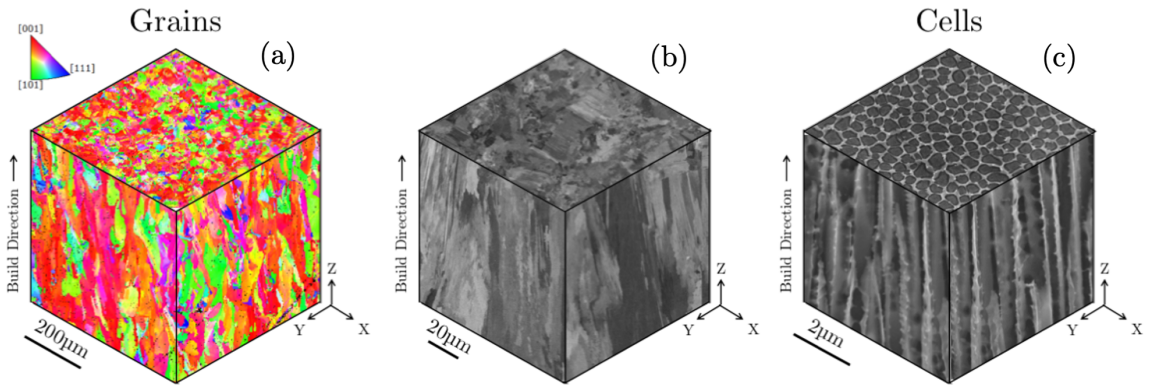

Fig. 2.4 (a) EBSD inverse pole figure (IPF) z-axis (performed by Dr. Yuanbo Tang) of the planes perpendicular and parallel to the build direction for the ABD900AM Ni-based superalloy produced by AM (b) BSE micrographs of showing the XY, XZ, and YZ planes (c) SE micrograph of the 3 planes showing the dendrite directionality.

2.4 shows grain structure and dendritic structure on various planes. When the plane perpendicular to the build direction – designated the XY plane – is observed, small equiaxed grains are apparent, when either plane running parallel to the build direction – XZ and YZ – grains appear long and columnar. A similar phenomena is observed at the dendrite length scale: the rapid cooling rates of AM result in cellular dendrites with no secondary dendrite arms, these grow radially with the melt pool, as a result they appear to largely point in the build direction. This microstructures is widely reported for alloys produced by AM [87, 10, 90, 91], and confirmed unambiguously by 3D electron backscatter diffraction (EBSD) – or TriBeam – by Polonsky et Al [92].

High resolution characterization by scanning transmission electron microscopy (STEM) energy-dispersive x-ray spectroscopy (EDX) shows Hf, Ti, and Ta rich carbides at the cell boundaries in as-printed CM247LC [87]. These fine dendrites and small carbides are observed in many superalloys processed by L-PBF including IN713, IN625, IN718, IN738LC, and IN939 though their influence on cracking and the accumulation of residual stress is not well understood [93]. The degree to which γ' precipitates are present in the as-printed state of Ni-based superalloys produced by L-PBF is disputed,

some studies have found evidence of γ' at sample edges [94], whereas others have found none following synchrotron methods [95]. Likely the specific processing conditions of each study and the propensity of the composition employed to precipitate γ' mean the answer is highly study specific. Regardless it is clear that the equilibrium volume fraction of γ' does not fully precipitate. Furthermore it has been shown that the γ' formers are expelled to the interdendritic regions when the γ dendrites growing with the solidification front [96]. Characterization of this nature allows for the development of a basic understanding of the local microstructural heterogeneity which in turn serves to elucidate the mechanisms of defect formation discussed in what follows.

2.3 Processing induced defects

2.3.1 Cracking mechanisms

The incremental improvement of powder feedstock quality, AM apparatus, and knowledge of processing is facilitating ever better printing of alloys. However, success with specific alloy compositions remains elusive as they are prone to cracking. Over the years much effort has been made to understand why these alloys – deemed un-weldable – crack during conventional welding. These efforts serve as a strong basis for the study of cracking during AM [97–100]. Parallels have been drawn between welding and AM [64, 101] citing similar thermo-mechanical phenomena with altered boundary conditions [65]. Carter et al were among the first to specifically investigate cracking during L-PBF of Ni-based superalloys. They found that cracks developed when processing the CM247LC alloy occurred to variable extent and had different morphologies based on the energy density of the build [102, 15, 103, 104]. The crack mechanisms proposed by the authors were solidification cracking, liquation cracking, ductility-dip cracking, and strain age cracking. These mechanisms are discussed further in what follows. For

each mechanism, the phase transformation, mechanical driving force, and method for identifying the crack post-mortem are discussed as well as the influence of processing conditions and alloy composition on the propensity for the mechanism to occur.

Nomenclature and classification The naming conventions for the different crack mechanisms are now distinguished for clarity. A full summary of the classification of the various mechanisms is given in Table 2.2. Crack mechanisms are broadly split under two umbrellas: hot cracking and cold cracking. Hot cracking comprises the two crack mechanisms that occur during a transition between liquid and solid. These are (1) solidification cracking or hot/interdendritic tearing and (2) liquation/liquidation cracking. Cold cracking comprises both crack mechanisms taking place when the material is fully solid; ductility-dip/solid-state cracking and strain-age cracking.

Solidification cracking

Solidfication cracking, hot tearing, and interdendritic tearing are all terms used in literature to characterize the formation of a crack during solidification due to tensile strain and a lack of feeder liquid. The occurrence of solidification cracking has been confirmed unambiguously as a crack mechanism plaguing AM processing [102, 105, 106]. The presence of intact dendrite arms – see Figure 2.5 – definitively distinguishes solidification cracks from the other mechanisms. These remain intact on either side of a crack as the material is pulled apart due to shrinkage strain and no liquid fills the gap. The two edges of a solidification cracks do not align as they were never fully connected. Chauvet et al have recently demonstrated that hot cracking of a Ni-based superalloy produced by electron beam melting (EBM) occurs only on high angle (>15°) grain boundaries (HAGB) [105], concluding that the final liquid film to solidify remains stable at lower temperatures given this configuration, which increases the susceptibility to cracking as per Rappaz et al. [107]. In particular, the influence of segregated boron

in the final liquid to solidify was emphasized. The segregation of alloying elements such as C, B, Zr, Si, and Hf to the final solidification products has now been widely reported to be responsible for triggering solidification cracking during AM [10, 105, 108–114]. The magnitude of an alloy's freezing range has traditionally thought to be a critical indicator of its susceptibility to solidification cracking, as the final material to solidify must bear increasing thermal strain with increasing under cooling [115–118]. While extensive alloying certainly leads to a depression of the solidus which exacerbates solidification cracking, it is possible that recent works overemphasize the simulation of this phenomena and underappreciate the contribution of composition on the local mechanical shrinkage pulling the solidification fronts apart.

Liquation cracking

Lippold's works on the topic of cracking during welding in the late 1980s were among the first to deeply investigate liquation cracking [97]. Since then, many influential articles by the likes of Kou [119], Dye et al [66], and Ojo et al [120] have shed light on this phenomenon, through studies of asutenitic stainless steels, Ni alloys, and defect prediction respectively. Liquation cracking, like the aforementioned solidification cracking, occurs at grain boundaries. However, it does not show the characteristic dendrites post-mortem, instead exhibiting a smooth topographical surface due to the presence of a solidified liquid film [119]. The mechanism of liquation cracking established in the welding literature relates to the melting of non-equilibrium-phases at grain boundaries. This occurs uring subsequent passes of the heat source which remelt phases and interfaces with low melting points in the heat affected zone (HAZ) [97, 121, 122]. If liquation occurs and the local material is in a state of tension, the liquid – incapable of carrying load – will open as a crack [119]. Identifying the presence of small liquid films characteristic of liquation cracks is challenging due to

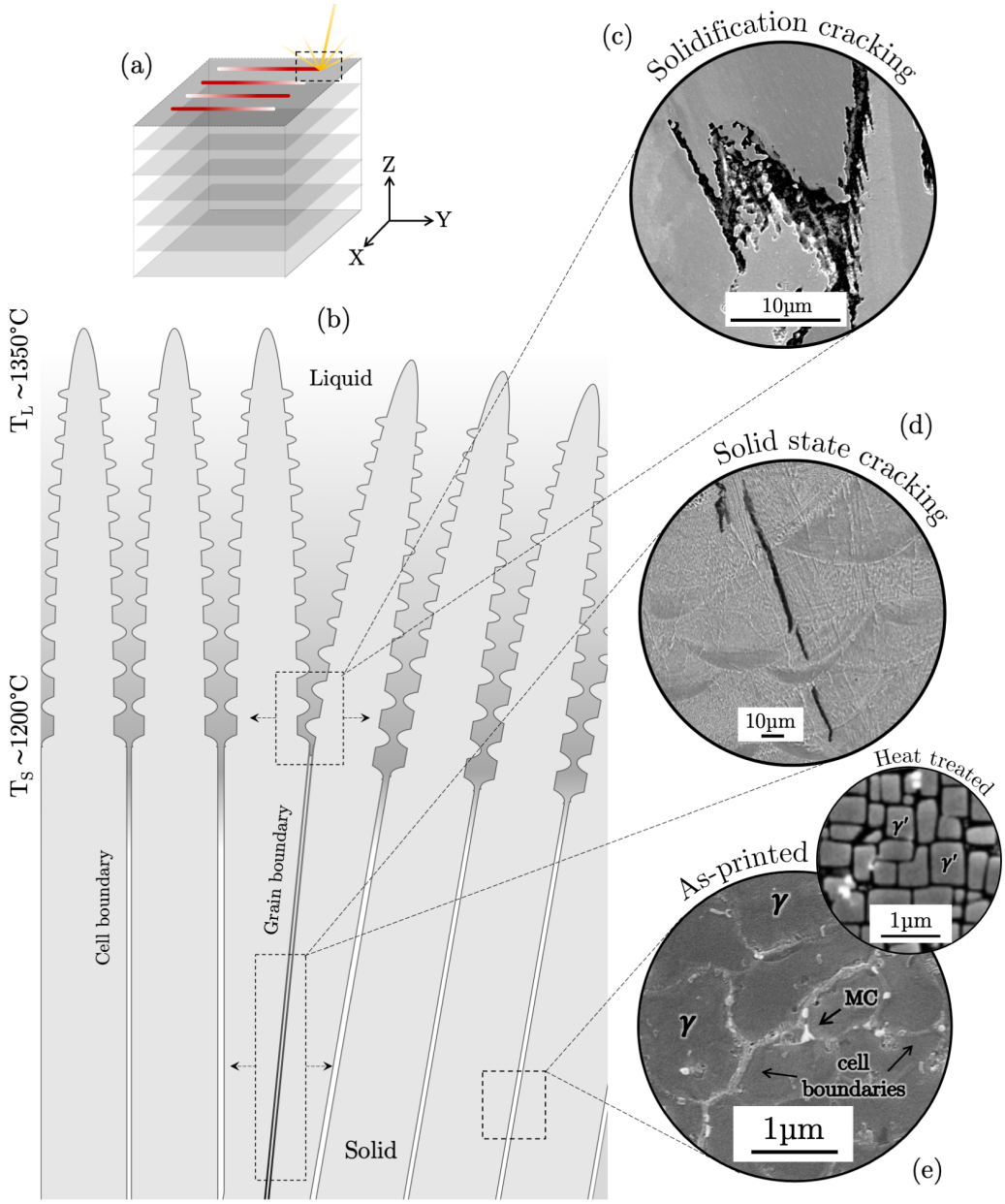

Fig. 2.5 (a) Schematic diagram showing the L-PBF build process (b) the material state and length scale at which solidification and solid-state cracking occur with corresponding SEM image examples of a (c) solidification crack and (d) a solid-state crack in IN939 as well as (e) SEM micrographs of etched CM247LC in the as-printed condition showing the γ matrix and MC carbide and CM247LC in the heat treated condition (reproduced from ref. [9]) with γ' precipitates.

their re-solidification after the cracking event. One solution to determining if a crack occurred due to liquation is to investigate solely the final solidification event, as the HAZ will not be confused with other regions [123, 124]. Li et al's investigation of HAZ cracking in the Ni-based superalloy DZ125L highlights that γ/γ' eutectics are highly susceptible to liquation [125, 126]. Notable simulations of liquation cracking include the works of Radhakrishnan et al [127] and Dye et al [66].

Ductility-dip cracking

Ductility-dip cracking (DDC) has been established in the welding literature as resulting from the intersection of (1) processing induced thermal strain and (2) high temperature alloy embrittlement [98, 99, 128]. Under specific welding conditions the presence of substantial tensile stresses and strains can occur in material at an embrittled temperature [66]. Thus ductility exhaustion and cracking occurs depending on the magnitude of the induced mechanics and the materials capability. For Ni-based superalloys, the temperature range of embrittlement is approximately 650 °C to 1000 °C [129]. Several studies have demonstrated that DDC susceptibility is increased by localized stress along grain boundaries, exacerbated by the presence of $M_{23}C_6$ type carbides that form in the same temperature regime as the ductility dip [130–132]. These cracks can be readily identified on account of having two crack edges that align due to them having been previously been connected. In theory a material with no ductility-dip could experience ductility-dip cracking if the processing induced strain was great enough. Because of this these previously named ductility-dip cracks are referred to as solid-state cracks in this body of work.

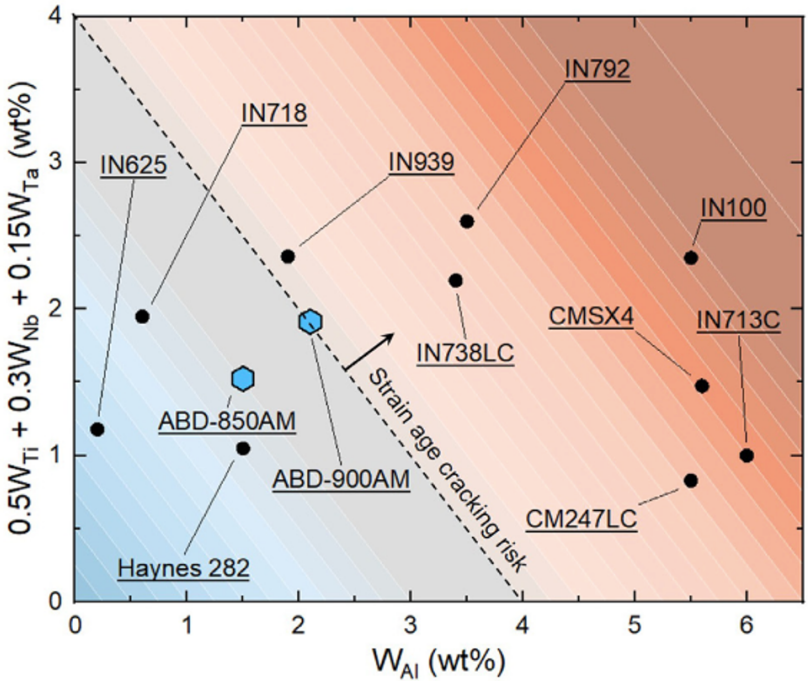

Fig. 2.6 A modified weldability diagram showing predictions of increased strain-age cracking susceptibility with increased amounts of γ' forming elements, where W denotes weight percent. Adapted from Ref. [9].

Strain-age cracking

Strain-age cracking (SAC) occurs due to tensile strain caused by the volume change resulting from the $\gamma \rightarrow \gamma + \gamma'$ solid-state reaction [133, 134].

$$\varepsilon_{\text{ageing}} \propto \Delta V_{\gamma \rightarrow \gamma'} \tag{2.3}$$

This is generally a challenge that influences processing taking place over longer time-scales such as its namesake – ageing – also referred to as post weld heat treatment (PWHT) where the precipitation of γ' can occur [135, 136] and in alloys with high amounts of γ' formers such as Al, Ti, Ta, and Nb [137, 138]. The propensity for strain-age cracking to occur has often been used interchangeably with weldability [98, 99] and is often described by the traditional weldability diagram shown in Figure 2.6.

The occurrence of SAC during AM hinges on the previous discussion of the presence of γ' immediately after L-PBF. If the precipitation γ' is indeed fully suppressed during initial processing, macroscopic cracks occurring in the solid state cannot be due to SAC. However, if γ' is observed the contribution of SAC to cracking cannot be ruled out.

Table 2.2 Summary of terminology, phase transformations, and mechanical driving force for the different crack mechanisms discussed in welding and AM.

Umbrella term	Hot cracking		Cold cracking	
Specific nomenclature	Hot tearing or solidification cracking	Liquation or liquidation cracking	Ductility-dip or solid-state cracking	Strain-age cracking
State change	Liquid→solid	Solid→liquid	None	None
Phase transformation	Liquid→γ	GB phase→liquid	None	γ→γ'
Mechanical driving force	Differential thermal strain			$\gamma \rightarrow \gamma'$ volume change
Defining features	Intact dendrite arms	Solidified Liquid film	Longer than one melt event	Presence of γ'

2.3.2 Lack of fusion and porosity

Volumetric defects manifest during AM in the form of lack of fusion (LOF) and porosity. While the primary focus of this work is cracking in AM, these volumetric defects must

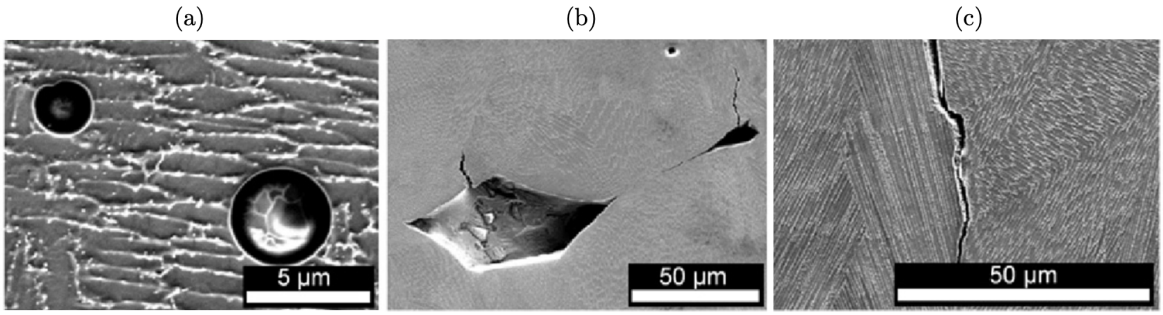

Fig. 2.7 Scanning electron micrographs of (a) porosity (b) lack of fusion and (c) cracking defects. Adapted from Ref. [10].

be understood as their presence may promote cracking by means of stress concentration. Cloots et al summarize these defects as shown in Figure 2.7.

Early work on AM was focused largely on successfully printing adequately dense material by optimization of processing conditions [139]. Over the past 10 years the elimination of LOF has been mostly achieved by a combination of thermal modelling and empirical trials [140–144]. Through either of these methods processing maps can be generated which specify regions of excessive energy input where vaporization occurs, regions of insufficient energy where material does not get fully bonded, and the optimal in between. Modelling of particle melting and thermal-fluid flow in order to eliminate lack of fusion has continually improved as computational power and thermo-physical property databases are incrementally improved [68, 145, 146].

The root causes for the presence of porosity are generally attributed to unfavourable thermal fluid flow and keyholing. Meso-scale modelling suggest gas entrainment in a turbulent melt pool can result in porosity [147, 148], though melt-pool dynamics can be tailored through processing conditions to reduce the phenomenon [149]. Further modelling of fluid flow points to depression collapse during keyholing as a critical mechanism for porosity [67]. This occurs when excessive power is applied to a volume of material, rapidly removing mass from the sample and transporting gas to the bottom of the melt pool [68, 150].

2.4 Solutions

Two principle solutions to cracking during AM are widely attempted: optimizing processing to prevent cracking [151–153] and optimizing alloy chemistry [9, 154, 155] to prevent cracking. Here the major studies employing each solution are reviewed.

2.4.1 Process optimization

Optimization by tailoring of the laser path, melt pool size, microstructure, and resulting stress state are primary ways in which crack mitigation is being attempted.

Laser control Novel studies have taken place to determine if cracking can be reduced through optimized scanning. Of note is the investigation performed by Catchpole et al on the reduction of cracking through fractal scanning strategies [62]. Two novel scan patterns entitled Hilbert and Gosper were employed in an attempt to reduce thermal strain and resulting cracking. While these scan strategies significantly reduced the extent to which cracking occurred in a traditionally non-weldable Ni-based superalloy, the fact that only reduction in cracking as opposed to complete elimination of cracking was achieved following this fine tuning of the process suggests the limits of process optimization are being approached. Other notable methods used to mitigate cracking and facilitate processing include the pre-heating of the powder bed and/or baseplate [156] as well as the use of pulsed and continuous wave emission modes to stabilize melt pool geometry [157].

Melt pool characteristics The characteristics of solidification are of utmost importance to the nucleation of cracks during AM. Naturally the melt pool dynamics, shape, size, and temperature will dictate much with respect to solidification front velocity, stability and the thermal gradient. Different analytical and numerical solutions

have been applied over the years to determine the distributions of temperature and heat around the heat source. Traditional solutions such as Rosenthal moving beam, Pavelic, or Gaussian distribution serve as good starting points [158, 159], though more recently, finite volume method (FVM), element method (FEM), computational fluid dynamics (CFD) or other varied multi-physics based approaches have been employed [160–162]. Notably, Basoalto et al used a multi-physics framework to predict melt pool characteristics as a function of alloy composition, concluding that the thermo-physical properties of alloys strongly dictate the melt pool size, thermal gradients, and residual stresses [70]. Mukherjee et al reinforce this work, constructing numerical models that predict different melt pool shape and temperature distribution for SS 316, Ti-6Al-4V, IN718, and AlSi10Mg [163].

Microstructure prediction An extensive literature on the nature of solidification under AM conditions has developed in the past decade. More specifically the capability to model the influence of processing conditions on the transition between columnar to equiaxed microstructure has been advanced. Haines et al concluded that compositional changes were unable to drastically alter the nature of the columnar equiaxed transition (CET) and that a combination of both chemistry and processing is required for specific tailoring [164]. Lee et al showed that by manipulation of two heat sources the thermal gradient and velocity of the solidification front could be tailored to achieve a desired microstructure [165, 166]. Opportunities for site specific microstructure have been explored by Babu et al, who predict and experimentally validate the spatial variation in microstructure [65]. Similarly, Dehoff et al successfully tailored grain structure by rapidly moving the electron beam to promote specific thermal gradients giving rise to nucleation as desired [167]. Other approaches include phase field modelling to predict the solidification and local microstructure as a function of processing variables [168], as well as parameter selection in an effort to generate isotropic microstructure [90].

Residual stress prediction The development of thermal-mechanical models for AM remains a key area of development. The extent to which analytical and numerical solutions developed for welding are applicable to AM is briefly discussed by Wei et al, they emphasize the increased cooling rates as a major obstacle in direct applicability of these heritage methods to AM [101]. Mukherjee et al. developed a model for prediction of residual stresses and distortion which took a simulated thermal profile from a heat transfer and fluid flow model and imported it to commercial finite element analysis (FEA) software Abaqus in order to determine the stress field [83]. Their simulations highlights the changing of stress state from tensile to compression at the layer interfaces [83]. EBM is modelled in the process, hence the temperature distribution is more uniform and the stresses are less severe they would be in the case of L-PBF. The modelling approach required by Mukherjee et al. highlights complexity of modelling cracking in AM, since crack initiation at the meso-scale may propagate macroscopically, which then requires a separate macroscopic structural thermal-mechanical analysis by FEA. In their review of the published work regarding simulating residual stress in powder bed AM processes, Schoinochoritis et al. conclude that Abaqus and ANSYS are the most commonly applied commercial FEM software's for addressing the problem [161].

In-situ process monitoring In-situ detection of defects offers an opportunity to correct builds on the go and understand the formation of discontinuities. Everton et al. highlight the need for development of improved optical and infrared imaging capabilities, citing major limitations as poor spatial resolution, limited field of view, high temporal loads, and excessive data storage requirements [169]. A specific example of progress in the field of in-situ infrared thermography is the works of Rodriguez et al. who developed a procedure for determining powder emissivity required for thermography calibrating pre and post melting [170]. Neutron tomography (NT) methods can be applied to

the AM progress to achieve the spatial resolution of which eludes optical and infrared imaging. Turner et Al applied such methods to the AM build of Ni-based superalloy in order to detect porosity and compositional discontinuity [171]. Two phenomena were uncovered as a result; heterogeneity with respect to the spatial distribution of porosity, and the segregation of elements to grain boundaries [171]. Among the more exciting possibilities for in-situ work in the field of AM includes the potential to intentionally create heterogeneous parts, potentially allowing for variable material properties on an as needed basis. Ma et al conducted in-situ alloying of titanium aluminides in order to achieve a fully dense build [172]. Investigations of on the fly alteration of material properties via alloying addition and processing conditions like this are now becoming more widespread [173, 174]

2.4.2 Alloy design

One school of thought is that for a new revolutionary process a new branch of alloys is required. Historical examples of this include the inception of the infamous CMSX-4, which was developed as an alloy for single crystal casting [175]. Up to 2018 some studies on modifying conventional alloys had been undertaken but the design of new novel grades of alloy for AM was limited. Harrison et al. modified the Si, Mn, W, and C content of Hastelloy-X to reduce cracking by 65% [176], Tomus et al. performed similar studies but was still unable to inhibit cracking entirely [113]. In the realm of aluminum alloy systems Montero et al. have demonstrated that increasing the Si content improves printability, attributing this to the grain refining effect and cracking dependence on grain size [177], and thus revealing the limitations of conclusions drawn from alternate alloy systems. However, in the past 3 years much investment has gone into designing new grades of alloy. Currently eight new superalloys designed specifically for AM are published in the literature. Of those two – ABD850AM, ABD900AM –

are discussed heavily in this work [9, 178, 179]. The developers, compositions, and published works on these alloy are summarized in Table 2.3.

The design strategies for the MAD and the Alloy-By-Design (ABD) alloys both involve a mitigation of cracking modes by controlling material properties. Tang et al. mitigate solidification cracking in ABD by selecting composition with a solidification interval under ∼280°C (as predicted under scheil assumptions), and inhibits what they refer to as "strain-age cracking" by limiting the equilibrium γ' volume fraction [9]. Xu et al. builds their processability criterion for MAD on the basis of an understanding that the microstructure of superalloys processed by AM is essentially a 2 phase composite comprised of γ cells and a intercellular region enriched with rejected solute and γ' formers. In order to predict the processability, the composition of the initial and final material to solidify is predicted thermodynamically and their theoretical strength and melting points are simulated. The differential between bulk and segregated material melting point is used as a metric for solidification cracking susceptibility and the differential between bulk and segregated material strength is used as the metric for solid-state cracking susceptibility [12]. Figure 2.8 summarizes the ideal alloy design space predicted by each of these methods and superimposes where the compositions of several heritage superalloys. The design of SB-CoNi-10 was done in similar fashion, printability was conferred by minimizing the freezing range and performance was tailored by increasing the γ' volume fraction [180].

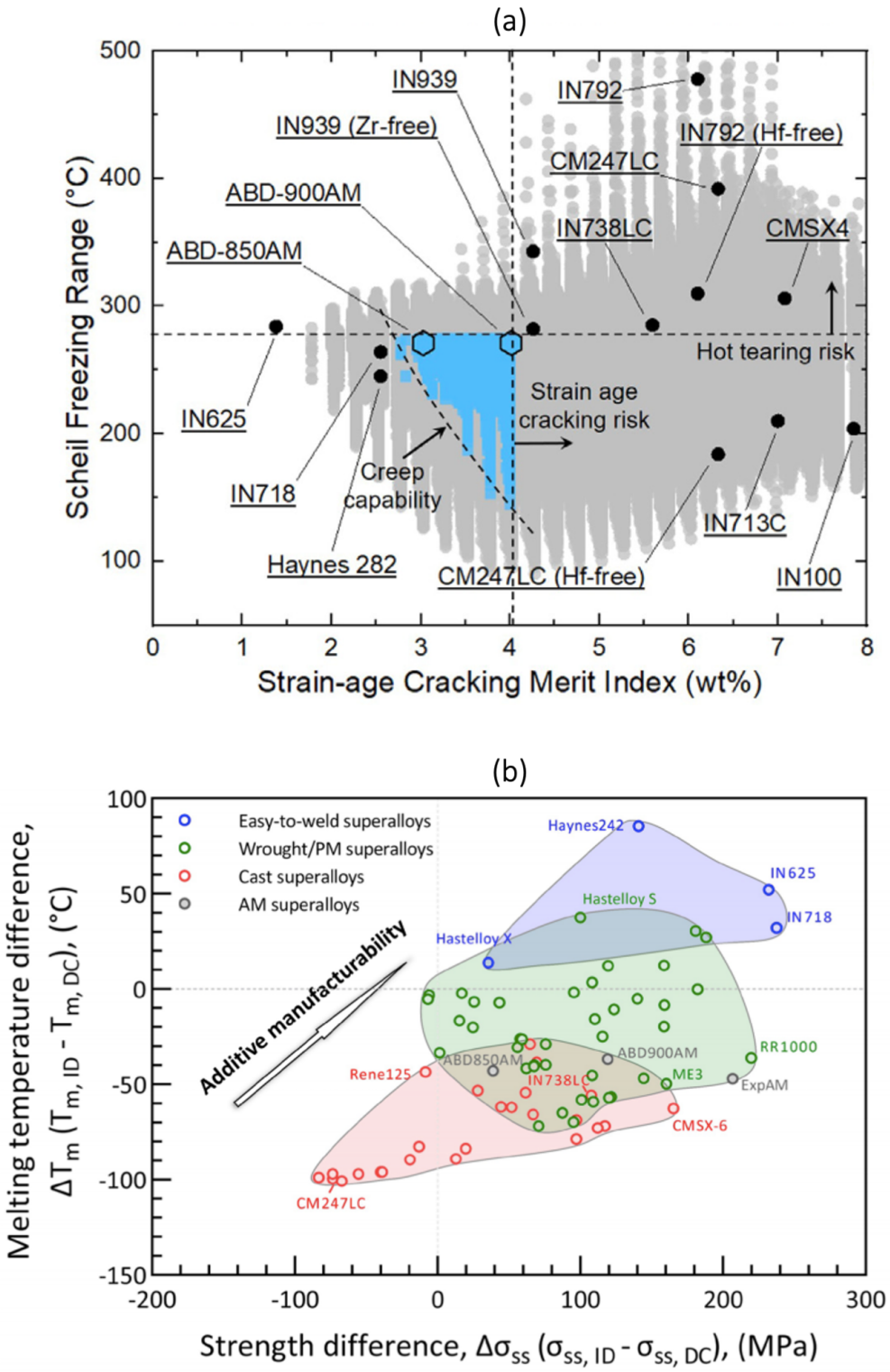

Fig. 2.8 Methodology for alloy designed outlined by (a) Tang et al. [9] and (b) Xu et al. [11, 12].

Table 2.3 Alloy compositions of superalloys designed specifically for AM (wt.%).

Developer	Alloy	Ni	Al	Co	Cr	Mo	Nb	Ta	Ti	W	C	B	Zr	Hf	Fe	Published in
Liburdi Turbine Services Inc.	LW 4275	55.6	5.1	20.4	9.6	1.2	-	2.2	-	5.5	0.120	-	-	0.30	0.03	[181]
Wayne State University	WSU 150	59.6	2.4	9.3	17.8	5.3	0.5	0.9	2.8	1.3	0.090	-	-	0.00	-	[182]
Linköping University	MAD542	63.9	5.0	8.0	8.0	5.0	2.0	3.0	1.0	4.0	0.100	<0.001	<0.002	0.00	-	[11, 154, 12]
Dalian University of Technology	NiCrlike-2	68.7	0.9	-	19.2	3.1	6.9	-	1.2	-	-	-	-	0.00	-	[183]
University of California Santa Barbara	SB-CoNi-10	45.1	7.5	23.5	6.6	-	0.0	13.4	-	3.9	0.020	0.018	-	0.07	-	[180]
Carpenter Technology Corporation	ExpAM-mod	64.7	4.0	5.2	9.9	3.0	4.0	7.9	-	1.2	0.077	0.015	0.01	0.00	-	[14]
Alloyed Ltd. University of Oxford	ABD850AM	50.5	1.3	18.0	19.9	2.0	0.6	0.5	2.3	4.9	0.010	0.003	<0.005	0.00	-	[9, 178, 179]
Alloyed Ltd. University of Oxford	ABD850AM+CB	49.6	1.5	18.6	19.7	2.0	0.4	0.6	2.4	5.1	0.133	0.007	<0.005	0.00	-	[9, 178, 179]
Alloyed Ltd. University of Oxford	ABD900AM	49.9	2.1	20.3	17.1	2.1	1.9	1.2	2.4	3.1	0.047	0.003	<0.005	0.00	-	[9, 178, 179]
Alloyed Ltd. University of Oxford	Alloy 1	52.9	5.2	19.1	9.0	1.2	2.2	3.3	0.1	6.9	0.037	0.005	<0.005	0.00	-	[X]
Alloyed Ltd. University of Oxford	Alloy 2	51.9	4.7	18.9	8.9	1.2	2.8	4.5	0.1	6.9	0.037	0.005	<0.005	0.00	-	[X]
Alloyed Ltd. University of Oxford	Alloy 3 / AM-Dev	50.6	4.2	19.1	8.7	1.2	3.6	5.5	0.1	7.1	0.031	0.005	<0.005	0.00	-	[X]

Chapter 3

On the influence of processing conditions on additive manufacturability

3.1 Introduction

In this chapter, the suitability of the nickel-based superalloys for the AM process is studied. As highlighted in Chapter 2, the unique multi-physics of the AM process results in defects such as cracks and pores. While the precise mechanisms by which these defects arise are not entirely agreed upon at present, many studies have shed light on their nature [65, 105, 184]. Characterization at high spatial and chemical resolution is needed to better elucidate the factors influencing defect formation. Specifically, systematic processing trials are needed to compare the behaviour of different alloys: both the heritage ones but also the new grades being designed specifically for this process. The work reported here was motivated with these factors in mind.

3.2 Alloy design approach

The specific mechanisms by which cracking may occur referred to in welding and additive manufacturing literature are generally accepted to be the hot cracking mechanisms – solidification and liquation cracking – and those occurring in the solid-state such as strain-age and ductility-dip cracking.

An alloy's susceptibility to each crack mechanism is dependent on the alloy composition. For example, the freezing range as well as the terminal solidification products determine the susceptibility of a given alloy to the formation of solidification cracks [115, 116]. In addition, low melting point solidification products such as carbides, borides, and γ'-phase eutectic increase the vulnerability to liquation cracking in the heat affected zone [121]. Strain-age cracking can occur during cooling to the base-plate temperature and/or during the subsequent heat treatment. The key challenge is the hardening caused by γ' precipitation in conjunction with the presence of process induced stresses [185]. The link to composition (Al+Ti) is often captured in the so-called weldability diagram [186].

In this chapter, two novel Ni-based superalloys designed for crack free additive manufacture are investigated; ABD850AM and ABD900AM, whose compositions are given in Table 3.1 [187]. These alloys have been designed using the compositional space outlined in Figure 3.1. The equilibrium γ' volume fraction $\phi_{\gamma'}$ of each alloy at 500 °C as determined using the Thermocalc TCNI8 database is shown in Table 3.1. For more on the heat treatment and mechanical behaviour of ABD900AM see [179]. Both alloys have been isolated via a large-scale modelling-based approach termed 'Alloys-by-Design' [188, 189]. The method combines high throughput computational thermodynamics with physical leading-edge scientific models to quantify the effect of alloy chemistry on the risk to one of the outlined crack mechanisms during additive manufacture. In addition, engineering properties such as yield strength, creep resistance, and thermo-physical

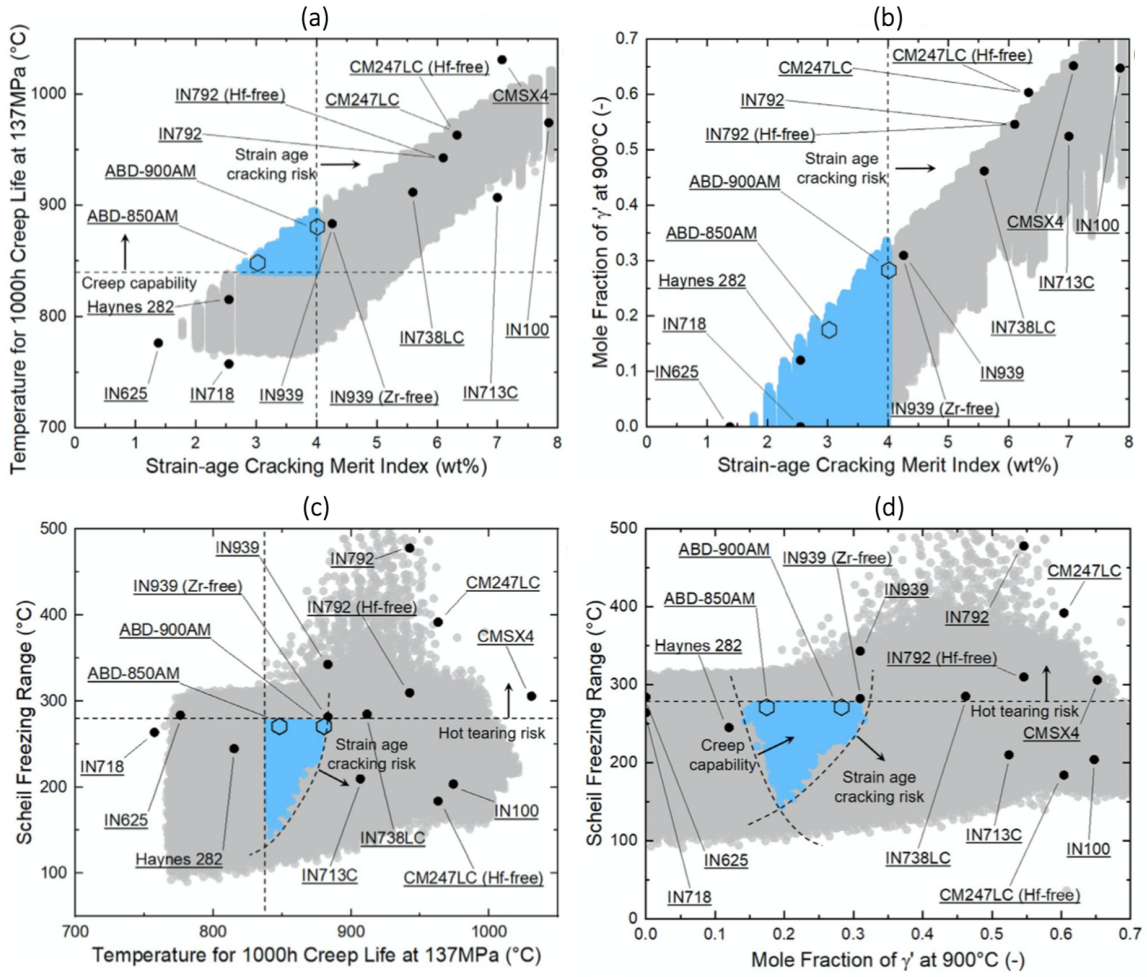

Fig. 3.1 Computational alloy design spaces used for new grades of superalloy; locations of heritage alloys are also plotted for comparison. (a) strain-age cracking merit index and its relationship to creep merit index and (b) γ' fraction (c) the magnitude of freezing range in relation to the creep merit index and (d) γ' fraction. The final design space used to isolate new grades of alloy is shown in Figure 2.8. Adapted from Ref. [9].

Table 3.1 Measured alloy powder compositions (wt.%).

Alloy	Ni	Al	Co	Cr	Mo	Nb	Ta	Ti	W	C	B	Hf	$\phi_{\gamma'}$
ABD850AM	bal.	1.5	18.3	19.3	2.00	0.50	0.37	2.64	4.95	0.040	0.010	-	0.27
ABD900AM	bal.	2.1	20.3	17.1	2.09	1.85	1.21	2.39	3.06	0.047	0.003	-	0.34
CM247LC	bal.	5.5	9.3	8.3	0.55	0.00	3.20	0.73	9.66	0.070	0.020	1.35	0.75
IN939	bal.	1.8	18.8	22.5	0.00	1.00	1.30	3.60	1.60	0.160	0.011	-	0.33

properties such as oxidation resistance and thermal expansion/contraction are included. For a more detailed description of the ABD approach see [190].

The use of a computational tool for alloy design is motivated by the large number of alloying elements in Ni-base superalloys which results in a considerable composition space. Empirical design is not feasible for a multi-objective alloy design optimizing the processability and high temperature properties trade-off. Moreover, the Alloys-by-Design approach takes into consideration the advantages of powder metallurgy and the rapid cooling rates of this process. Segregation of alloying elements during additive manufacture is significantly reduced compared to casting processes for which conventional alloys have been developed. As a result, a new class of Ni-based superalloy for additive manufacture can be isolated.

3.3 Experimental methods

3.3.1 Feedstock material

Four different feedstock materials have been studied: the legacy alloys IN939 and CM247LC and the above mentioned new superalloys ABD900AM and ABD850AM. While the alloys investigated vary in γ' volume fraction, IN939 and CM247LC serve as benchmarks with highly desirable corrosion resistance and mechanical properties respectively. The feed stock powders were produced via argon gas atomisation. Their particle size distributions were measured with a MasterSizer 2000 particle size analyser

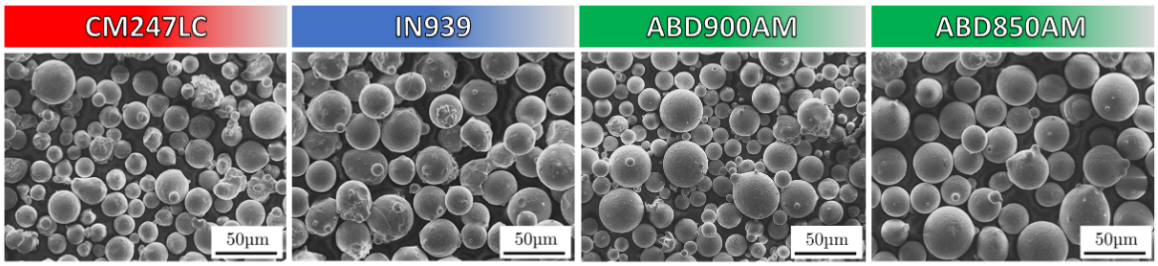

Fig. 3.2 Scanning electron microscopy images of powder employed to produce specimens.

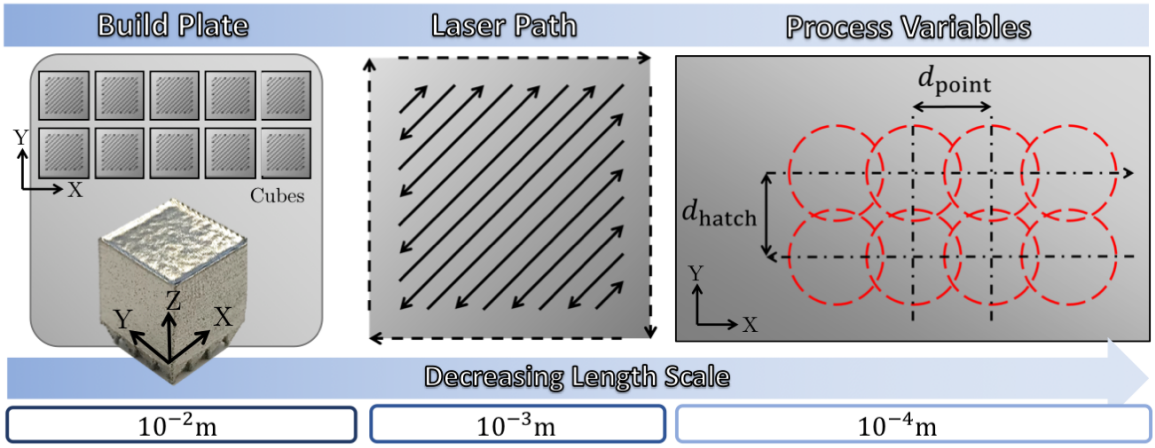

Fig. 3.3 (a) Sample geometry, build plate, (b) laser path, and (c) process variables - adapted from [13] - shown across multiple length scales.

in accordance to ASTM B822. Not strictly identical, the D50's were found to be similar at 32.3, 33.5, 33.1, and 36.5 µm respectively; they flow adequately and have particle size distributions such as to result in samples largely free of lack of fusion defects [25]. Scanning electron microscopy images of the powders are shown in Figure 3.2.

3.3.2 Additive manufacturing trials

In order to assess the printability of various alloys the same geometry was used for all alloys processed. This consisted of building cubes of dimensions $10\times10\times10\,\mathrm{mm}^3$, see Figure 3.3. These were manufactured with 16 inverted pyramid legs in order to allow for easy sample removal from the baseplate. Samples were produced via laser-powder bed fusion (L-PBF) with a Renishaw AM 400 pulsed fibre laser system of wavelength

1075 nm, laser spot size of diameter 70 µm, and build plate size of 250×250 mm^2. Additive manufacturing was carried out under an argon atmosphere using powder layer thickness of 30 µm and laser power of 200 W. The laser scan path was kept constant for all samples printed; a 'meander' hatching pattern was performed on each layer followed by a border finish consistent with Renishaw's recommended practice as shown in Figure 3.3. On the borders, a laser velocity of 50.0 cm/s was employed for all samples manufactured. As is consistent with industrial practice, the laser velocity v is defined as follows for the pulse laser system:

$$v = \frac{d_{\text{point}}}{t_{\text{exposure}} + t_{\text{distance}}} \tag{3.1}$$

where d_{point} is the distance between the laser pulses, t_{exposure} is the time spent depositing the laser pulse, and t_{distance} is the time spent travelling between laser pulses. An experimental window has been selected based on empirical evidence in order to investigate the influence of changing printing parameters within a small window where legacy alloys are printed free of excessive porosity and lack of fusion defects, allowing for an isolated investigation of cracking. The printing parameters in the bulk of the samples were varied with respect to velocity and hatch distance, h_{distance}, the two process variables which define the spatial distribution of energy input as illustrated in Figure 3.3. The processing parameters used for the experimental trials are listed in Table 3.2. After each 30 µm thick layer is processed, the hatching pattern frame of reference is rotated by 67 ° relative to the scanning that was previously performed [63]. Operation of the additive manufacturing apparatus was done by William Dick-Cleland.

3.3.3 Quantification of cracking severity and morphology

Quantitative stereology was performed on the as-printed material, in order to assess printability on the basis of cracking propensity. This was accomplished using a Zeiss

Table 3.2 Sample processing conditions in the bulk.

Sample	d_{hatch} (µm)	d_{point} (µm)	v (cm/s)
A	50	60	75.0
B	70	70	87.5
C	90	80	100
D	50	80	100
E	60	70	87.5
F	60	80	100
G	70	60	75.0
H	70	80	100
I	80	60	75.0
J	80	70	87.5
K	90	60	75.0

Axio A1 optical microscope and MIPAR software package. For each sample, 10 optical images of the XZ plane were analysed at 100× magnification. Cracking severity is expressed here in terms of the number of cracks per unit area. Individual crack length is defined by the maximum caliper diameter; the largest line length fitting across a crack. Features of maximum caliper diameter smaller than 10 µm are rejected from the analysis due to unreliable resolution at such magnification. Many studies have investigated the variance in microstructure with increasing build height, showing that the initial hundreds of layers incur significant microstructure heterogeneity [191]. In light of these findings, the samples are analysed in the XY plane at the sample height midpoint of 5 mm, and the XZ plane from the sample height midpoint to the top surface. Images used for crack quantification were taken from regions of greater than 500 µm inwards of the sample edge, as shown in Figure 3.4. Additively manufactured materials are highly prone to spatial variance in cracking, with surface connected cracks posing a unique problem due to their inability to be removed via hot isostatic pressing (HIP).

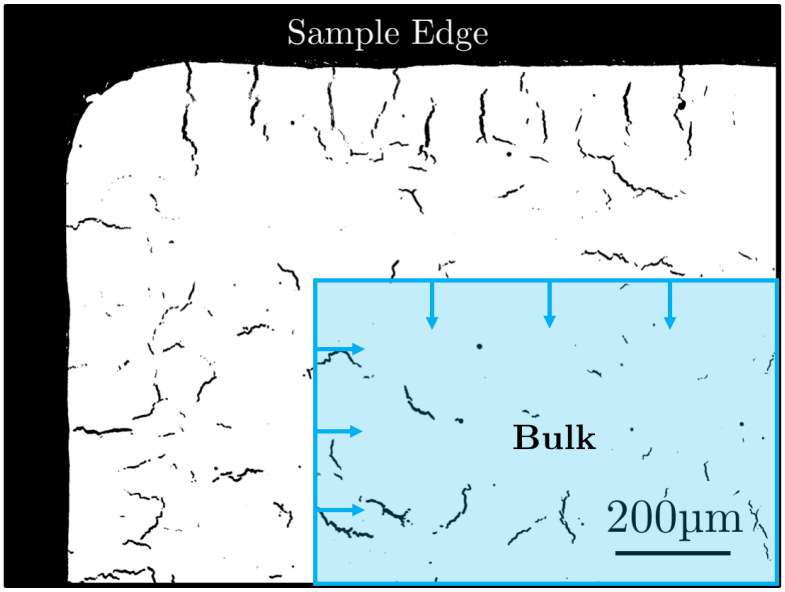

Fig. 3.4 Optical micrograph of CM247LC material at the sample corner, as observed in the XY plane with a black and white threshold applied.

3.3.4 Microstructure and phase characterization

Microstructures were analysed by SEM and electron backscatter diffraction (EBSD) analysis performed with a Zeiss Merlin Gemini 2 field emission gun scanning electron microscope (FEG-SEM) equipped with a Bruker EBSD detector. Differential scanning calorimetry (DSC) was performed with a NETZSCH 404 F1 Pegasus DSC. Heating was carried out from 700 °C to 1450 °C at 10 °K/min followed by cooling back down to 700 °C at the same rate. The specific heat capacity C_p was determined in accordance to ASTM E1269, the solidus and liquidus temperatures were determined following Chapman and Quested [192, 193].

3.4 Results

3.4.1 On the propensity for alloys to crack at a single processing condition

Images of the XZ plane of four alloys printed given conditions E are shown in Figure 3.5. At this condition, many cracks are apparent in legacy alloys CM247LC and IN939. However, with the resolution employed, no cracks were resolved in the ABD alloys. Such findings were confirmed through observation of both the XZ and XY planes.

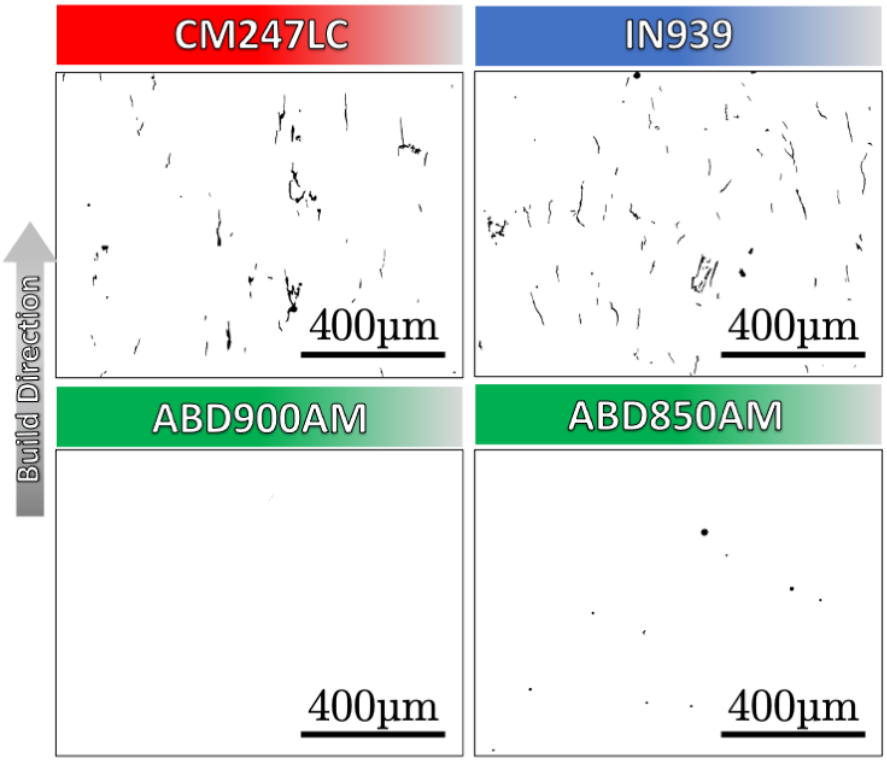

Fig. 3.5 Optical micrographs taken of the XZ plane at the 5 mm height of the as-fabricated material for all four alloys under investigation. Micrographs have had a black and white threshold applied. The regions investigated display cracks and minor porosity in CM247LC and IN939, and some µm length scale porosity in ABD850AM.

3.4.2 Influence of processing conditions on cracking

The analysis of the four alloys processed at a single condition is now expanded to a range of conditions. The number of cracks per unit area, the index of cracking severity, is plotted in Figure 3.7 against hatch distance and laser velocity, and fitted with an interpolating function. Figure 3.7 shows two ways by which cracking can be reduced: through varying processing conditions, and changing alloy. In this case, the latter appears to have been more successful. In order to better understand the influence of processing conditions, surfaces in Figure 3.7 are displayed as contour plots in Figure 3.6. These illustrate that for both legacy alloys the cracking is most severe when processed with conditions A and C, where the hatch distance and velocity are either both smallest and both largest respectively. In summary, this quantitative comparison of alloy printability reveals two significant findings: the degree to which cracking occurs is highly dependent on both alloy composition and processing conditions.

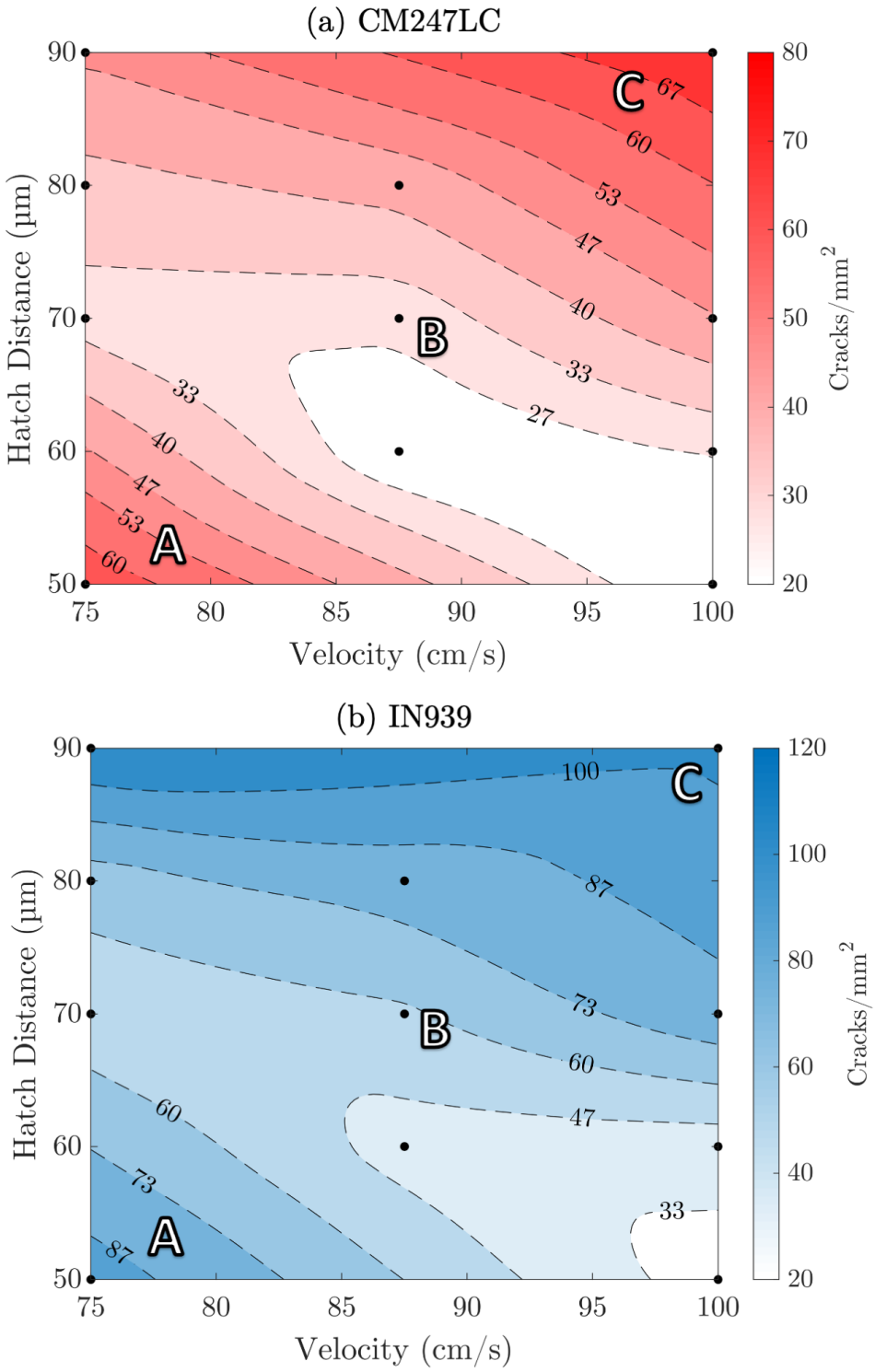

Fig. 3.6 The experimentally determined cracking severity as a function of hatch distance and laser velocity fitted with interpolating contours for (a) CM247LC (b) IN939, the solid points represent the samples as shown in Table 3.2.

3.4.3 On the presence of multiple crack mechanisms

Imaging of individual cracks by means of SEM allows for an assessment of the mechanism by which they occurred. Solidification cracks, recognizable by the presence of intact dendrite arms [194] are found in the sub optimal regions of the processing diagram. Samples A and C, having cracked to the largest extent, both exhibit solidification type cracks, an example is shown in Figure 3.8. Such is the case for both CM247LC and IN939 alloys. No γ' precipitates could be resolved through SEM of samples prepared by 3 V, 10 s, 10 % phosphoric acid electropolish or polished to 0.04 µm colloidal silica finish, this is due to the ultra fast cooling rates present during the L-PBF process. However, the presence of γ' precipitates of size too small to resolve through SEM is possible. As the γ' precipitates are either suppressed or very small, it is concluded that the contribution of the strain-age cracking mechanism is minimal. Solid-state cracking may occur regardless due to insufficient material ductility in the presence of excessive thermal gradient induced stresses [100]. Consequently, all non-solidification type cracking is classified here as solid-state cracking. Examples of solid-state cracks and solidification cracks found in IN939 and CM247LC when processed using conditions A and C are shown in Figure 3.8. For IN939 and CM247LC, cracks of both mechanisms are found in samples in the regimes of most pronounced cracking.

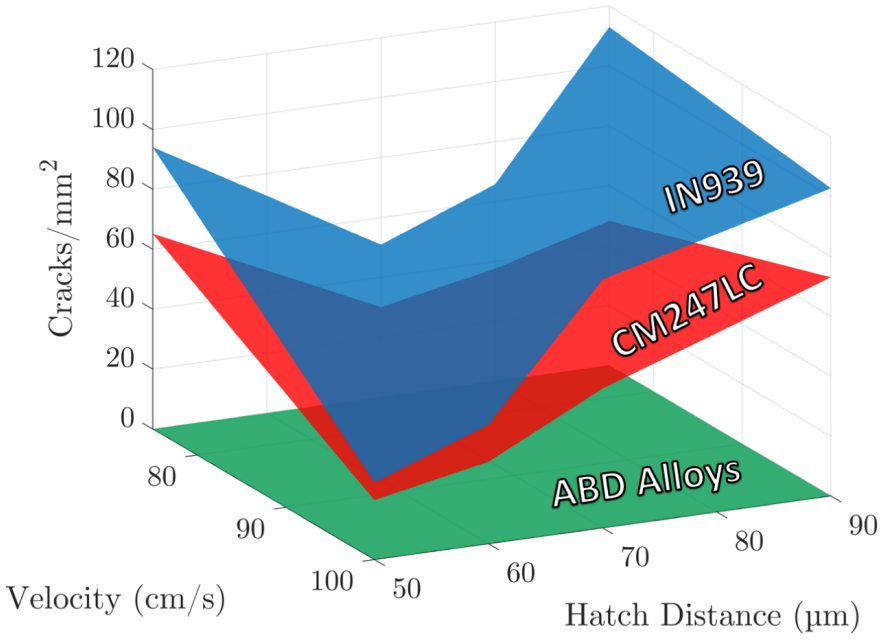

Fig. 3.7 Superimposed surfaces representing the crack severity for IN939, CM247LC, and the ABD alloys as a function of processing conditions.

3.5 Discussion and analysis

While the above results shed light on the influence of processing and alloy composition on the extent to which cracking occurs, several pertinent questions arise that demand further rationalization. Why do the ABD alloys demonstrate improved additive manufacturability and Is there a link between reduction in cracking severity and the material microstructure? These questions are addressed in what follows.

3.5.1 Considerations of the role of solidification range and path

The reduction in solidification cracking achieved through alloy design demonstrated in Figures 3.5 and 3.7 may be rationalised through the effect of chemistry on solidification characteristics. During the final stage of the solidification process, liquid remains in

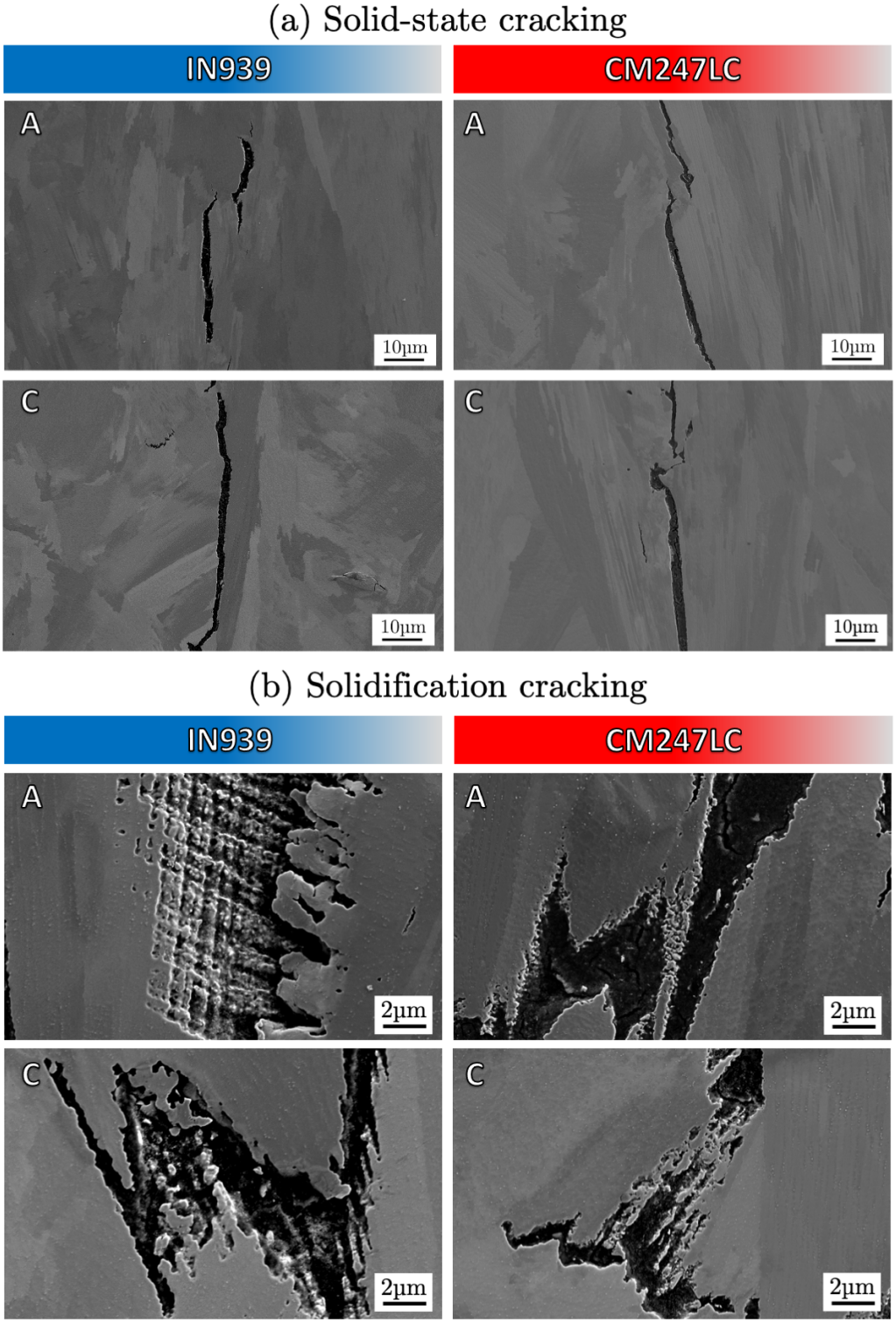

Fig. 3.8 Scanning electron micrographs showing examples of (a) solid-state cracks observed in CM247LC and IN939 samples A and C and (b) solidification cracks observed in CM247LC and IN939 samples A and C.

Table 3.3 DSC results and measures of solidification cracking susceptibility.

Alloy	γ' dissolution (°C)	T_{Liquidus} (°C)	T_{Solidus} (°C)	T_{L} - T_{S} (°C)	Cracks/mm^2	CSC
IN939	1086	1328	1203	125	> 25.6	0.25
CM247LC	1251	1376	1260	116	> 19.8	0.36
ABD900AM	1084	1362	1264	98	< 0.1	0.55
ABD850AM	1061	1352	1275	77	< 0.1	0.35

isolated interdendritic regions. If this liquid is retained over too wide a temperature range, or is otherwise unable to fill any gaps between dendrites that open up due to the contraction associated with solidification and cooling, then solidification cracking may occur [115, 117]. Clyne proposed a solidification cracking susceptibility coefficient (CSC) as the ratio of the time at which the material is vulnerable to local solidification cracking to the time where stress relief is feasible [118]. Values of CSC are determined from experimental DSC results, shown in Figure 4.19, given the assumptions that (a) only one phase transformation is occurring, (b) the fraction solidified is proportional to the enthalpy divided by the total enthalpy of the phase transformation as determined by integration of $C_{\text{p}} - T$ and (c) the ratio of the vulnerable period to stress relief period is proportional to the corresponding temperature ranges [66] as follows

$$\text{CSC} = \frac{T_{99\%} - T_{90\%}}{T_{90\%} - T_{40\%}} \tag{3.2}$$

where the $T_{x\%}$ are the temperatures associated with a remaining solid fraction of $x\%$. The experimentally determined liquidus, solidus, freezing range, and CSC values are shown in Table 3.3. In addition, the onset of γ' dissolution is determined by the inflexion in the DSC signal, where the presence of γ' is detected due to the slow heating rate of 10 °K/min.

Table 3.3 summarizes each alloys respective CSC and cracks/mm^2, these do not correlate. Clyne notes that dynamic processes with more complex mechanics may have their cracking susceptibility better estimated by magnitude of their susceptible period

[118]. It is indeed found that the magnitude of the solidification range correlates with the extent to which cracking occurs in respective alloys, but findings suggest the need for a more involved cracking susceptibility criteria. Several studies have investigated the influence of alloy chemistry on cracking during additive manufacturing. While the effects of major alloying elements are generally understood due to extensive welding research in the past [100, 99], the influence of minor additions such as carbon and boron remains a topic of discussion [176, 113], as it remains to some extent in welding [195–197].

3.5.2 On the influence of processing conditions on microstructure

It is apparent that there exists optimal processing conditions at which cracking in CM247LC and IN939 is minimized. An attempt to rationalize this phenomenon for CM247LC is made by means of EBSD performed on the XY plane, revealing the nature of the microstructure in terms of grain size distribution and texture. The average grain diameter and the strength of the texture correlate inversely with cracking severity across the processing diagram; in essence, samples with largest grain size and strongest texture are found to have cracked the least.

Previous studies on the topic of weldability of Ni-based superalloys provide some rational for the observation of such a correlation: it has been shown that greater density of grain boundaries increased the probability of intergranular cracking during welding of IN718 [198], conversely, Lippold et al. reported that larger grain size can increase liquation cracking susceptibility by means of increased segregation of minor alloying elements [99]. Recent works showed cracking during electron beam melting occurred exclusively on high angle grain boundaries (HAGB) of intergranular misorientation greater than 15 ° [105]. In this work, it is found that the proportion of

grain boundary length occurring on a HAGB for samples A, B, and C is 75, 60, and 88 % respectively, a trend following that of the determined cracking severity. On the basis of this, it is proposed that there may indeed be scope to reduce cracking during AM of traditionally non-weldable legacy alloys through grain boundary engineering and microstructure control, albeit while sacrificing material isotropy. While some processing, microstructure, properties relationships have been discussed, a greater appreciation of the influence of processing conditions on the thermal-mechanical response and stress state is required in order to fully rationalize the extent to which various cracking mechanisms occur for variable alloy compositions and across the processing regime investigated.

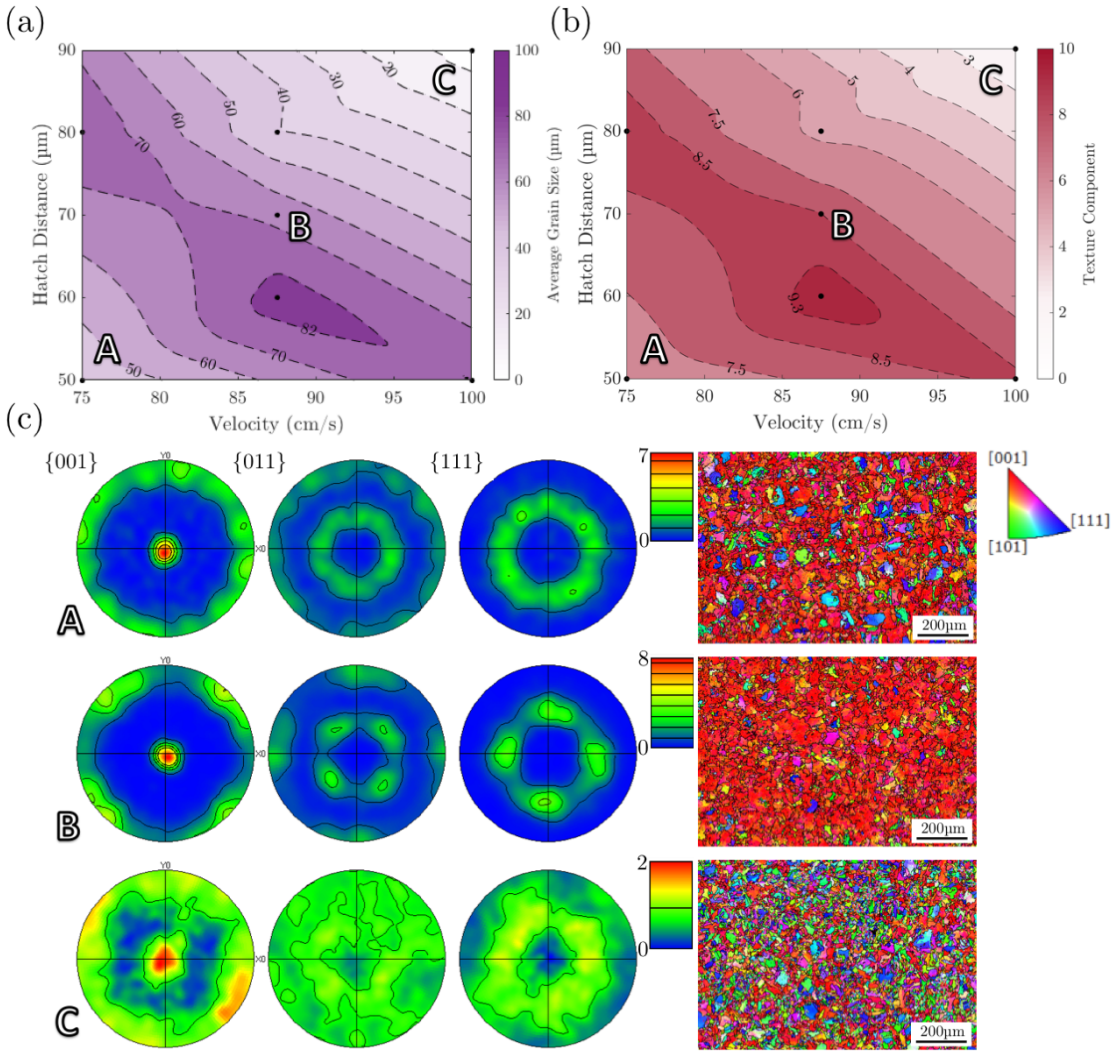

Fig. 3.9 Contour plot of (a) average grain size (diameter) (b) texture component vs processing conditions for CM247LC (c) texture of CM247LC at conditions A, B, and C as shown through pole figures, and the in plane inverse pole figure (IPF-Z). The EBSD analysis was performed by Dr. Yuanbo T. Tang of the University of Oxford high temperature materials research group.

3.6 Rationalization by simple thermal model

A simple 2D finite difference thermal model is constructed to assess how the variable processing conditions may resulted in the microstructures observed. The model was implemented in MATLAB to predict the temperature at a point as a function of time and position with a beam passing back and forth over the substrate. A square nodal grid comprised of 2500 nodes of total size $10\times10\,\mathrm{mm}^2$ with $\Delta x = \Delta y = 20\,\mu\mathrm{m}$ having initial temperature of 298 K is modelled, The time step used was 10^{-6} s resulting in in discretized beam velocity of $20\,\mu\mathrm{m} \times n \;/\; 10^{-6}\,\mathrm{s}$ where n is the nodal interval between laser pulses. Estimates for the thermal-physical properties for solid CM247LC at room temperature are employed; $C_\mathrm{p} = 790\,\mathrm{J/KgK}$, $\kappa = 29\,\mathrm{W/mK}$, and $\rho = 8250\,\mathrm{kg/m^3}$. Heat is input explicitly to a node at a time, where the heat input is defined by a snaking path, the heat equation is solved for time steps $\mathrm{d}t = 1\,\mu\mathrm{s}$. The heat equation was explicitly as follows;

$$\frac{{T^{n+1}}_{i,j} - {T^{n}}_{i,j}}{\Delta t} = \kappa\Big(\frac{{T^{n}}_{i,j+1} - 2{T^{n}}_{i,j} + {T^{n}}_{i,j-1}}{\Delta x^2} + \frac{{T^{n}}_{i+1,j} - 2{T^{n}}_{i,j} + {T^{n}}_{i-1,j}}{\Delta x^2}\Big) + \frac{{Q^{n}}_{i,j}}{\rho C_p} \tag{3.3}$$

subject to the stability condition;

$$\frac{2\kappa\Delta t}{\Delta x^2} \leq 1 \tag{3.4}$$

The nodes at the edge are set to cool by convective heat transfer with ambient temperature 298K and heat transfer coefficient $h = 50\,\mathrm{W/m^2}$. The model was constructed to be computationally inexpensive while having some basic predictive capabilities regarding the dependence of the temperature history on the point and hatch spacing. The output of the model at several time steps is shown in Figure 3.12. Probing the temperature at

a single node in the bulk of the material for different values of hatch and point distance shows clearly illustrates how changing the density of the laser pulses influences the thermal history, Figure 3.10 shows the energy density across the processing map and Figure 3.11 shows how the thermal history varies for 4 different pulse configurations. When the pulses are closer together the energy density is greater and the heating and cooling rate experienced by the material is reduced as the beam more gradually approaches the probed node. When the pulses are more spread the heating and cooling rates are increased since the beam suddenly approaches and departs the vicinity of the node. It is hypothesized on the basis of this that the grain size is reduced at conditions A and C but maximized at condition B because; (1) low energy density results in little grain growth under processing condition C, conversely, grain growth occurs at condition A but some recrystallization of small grains reduces the average grain size. At condition B the energy density is substantial enough to promote grain growth with no recrystallization.

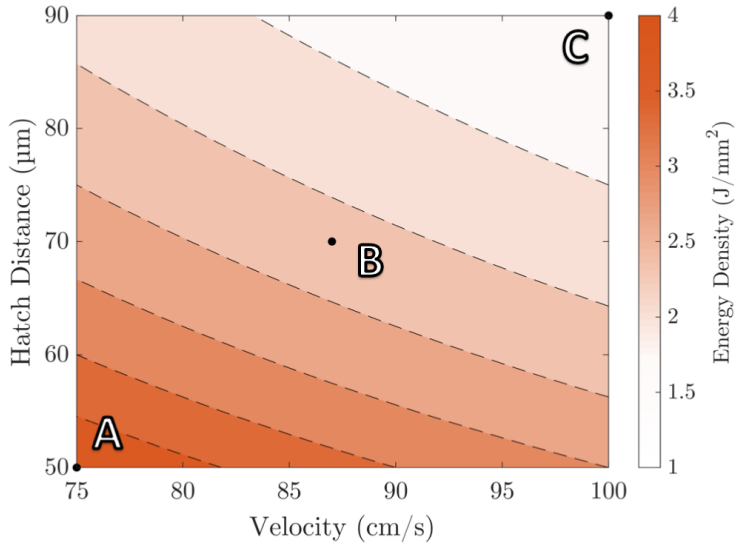

Fig. 3.10 Contour plot representing the 2-dimensional energy density deposited as a function of hatch distance and velocity. Points A and C correspond to the thermal histories modelled in Figure 3.11 below.

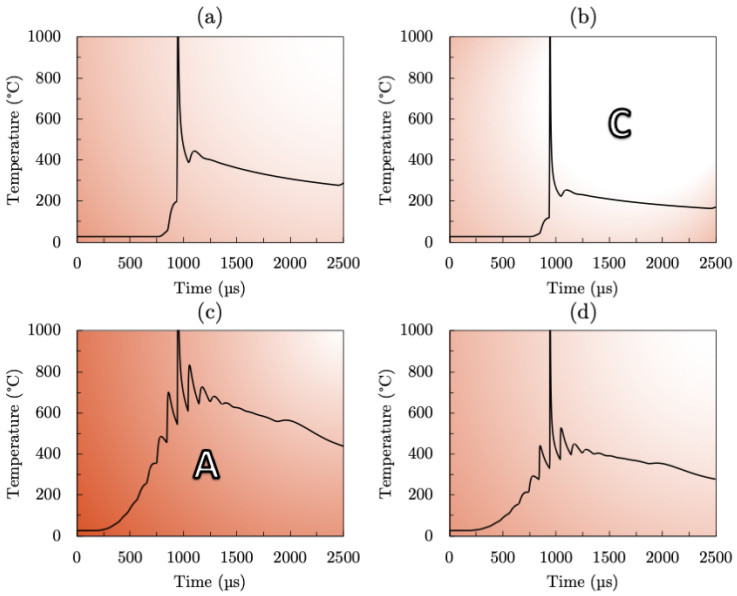

Fig. 3.11 Temperature histories resulting from a fixed node given processing conditions of (a) large hatch distance and small velocity (b) large hatch distance and large velocity (c) small hatch distance and small velocity (d) small hatch distance and large velocity.

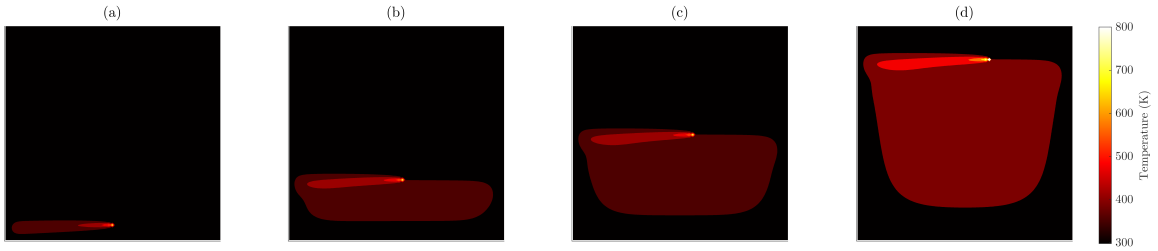

Fig. 3.12 Snapshots in time at (a) 500µs (b) 1700µs (c) 2900µs and (d) 4900µs of temperature contours from simulation of a heat source passing back and forth across a 10 mm×10 mm 2D substrate with point distance 60µm and hatch distance 120µm – implemented in MATLAB.

3.7 Summary and conclusions

Four different Ni-based superalloys have been processed using laser-based additive manufacturing: the alloys CM247LC, IN939, and two new grades of superalloy – ABD900AM and ABD850AM, which have been designed specifically for their suitability for additive manufacture. Assessment of additive manufacturability with a Renishaw

AM 400 has been made on the basis of observed cracking severity; alloys have been ranked on this basis for a range of processing conditions, namely, the laser velocity and hatch distance.

1. The IN939 and CM247LC Ni-based superalloys are found to be susceptible to solidification cracking and solid-state cracking mechanisms.

2. New novel alloys ABD850AM and ABD900AM exhibit increased additive manufacturability with respect to their reduced susceptibility to solidification cracks. This appears to have been achieved by the reduction of the magnitude of their freezing ranges.

3. The propensity for alloy CM247LC to crack as a function of hatch distance and velocity within the processing regime investigated correlates strongly with the nature of the resulting microstructure; namely, the grain size, texture, and proportion of high angle grain boundaries.

4. Both solid-state cracking and solidification cracking in CM247LC can be reduced through the careful control of processing conditions and resulting microstructure, though at the cost of incurring significant material anisotropy. As such, new novel grades of alloys are required in order to achieve crack free material with microstructure tailored for mechanical properties, and not crack reduction.

5. This work confirms that some Ni-based superalloys are indeed more processable than others, and that there is scope for designing new grades of Ni-based superalloy which are more amenable to AM than the heritage alloys which were designed for conventional processing routes.

Chapter 4

On the influence of alloy composition on the additive manufacturability of Ni-based superalloys

4.1 Introduction

As introduced in Chapter 1, AM is a promising technology for processing of metal alloys [86] and more specifically the nickel-based superalloys best known for their applications in aeronautics, hypersonics, rocketry and high temperature technologies [34]. AM has potential for these materials in particular because it opens up the possibility of producing complex engineering components using multifunctional component design with significant geometrical precision. However, like any process, AM relies on the quality of the material feedstock for its success, and therein lies a dilemma. Can existing superalloys be made to process well under the extreme cooling rates and

stress-states induced [199, 200]? The findings of Chapter 3 and Tang et al. [9] suggest that new grades of alloy will be necessary instead.

The Ni-based superalloys are an excellent test-case for the additive manufacturing process for several reasons. First, their compositional complexity requires as many as 15 different alloying elements to be present; this broadens the freezing range and thus exacerbates solidification-related cracking whereby the remaining liquid fails to fill the partially solidified microstructure which is then pulled apart by shrinkage effects [32], see Figure 2.5. Recent work on solidification cracking in AM has revealed that grain boundary misorientation is critical to susceptibility; hot cracks form only on high angle grain boundaries (HAGB) [105] and that grain boundary segregation and ensuing liquid film stability influence crack formation [106, 184]. Second, the superalloys are prone to solid-state cracking due to a lack of ductility particularly in the so-called ductility-dip regime of 700 to 900 °C. In the literature, the terminology used for this phenomenon is confusing, being referred to variously as ductility-dip cracking, strain-age cracking and post weld heat treatment cracking. The all-encompassing term solid-state cracking is chosen to reflect the fact that – in the AM process – such cracks propagate when the material is in the solid-state [201]. Solid-state cracks are characterized by their morphologies which are long and sharp, in contrast to the more meandering nature of solidification cracks. Work in recent years has successfully mitigated such crack formation by increased solid solution strengthening [176], or by control of γ' content to limit the strength induced and improve ductility [180]. And third, the multifunctional nature of their applications necessitates thin-walled and porous structures, to promote for example light-weighting and heat transfer.

The work reported in this paper was motivated with the above in mind. The temptation to fix on one alloy system, and then conduct processing trials exhaustively in an effort to work out the best combination of key process variables (KPVs) to

optimise manufacturing has been avoided here. Instead, consistent with the ushering in of new processing methods for the superalloys — vacuum melting, powder metallurgy, Bridgeman single crystal processing for example — which have always led to new compositional grades, the alternative approach has been taken: work out which alloys perform best for the process, and why. This has necessitated experimentation on a range of different alloys, including some designed specifically for additive manufacturing.

4.2 Experimental methods

4.2.1 Choice of alloy compositions

Twelve different superalloy compositions have been studied in this chapter – five novel compositions and seven better-known so-called heritage grades, including the cast/wrought alloys IN625, IN718, and Waspaloy of moderate γ' content but then also IN713, IN738LC, IN939 and CM247LC which are widely employed for investment casting applications – these display excellent creep properties on account of their high γ' fraction. The new alloys termed ABD850AM, ABD900AM, and AM-Dev are new alloys designed specifically for the AM process, with the objective of maintaining both performance and processability. Lastly, ExpAM and ABD850AM+CB are experimental compositions, with low and high carbon and boron contents respectively, aimed at assessing the influence of C and B, as well as a very high γ' volume fraction in the case of ExpAM. Feedstock powders were produced via argon gas atomization; their particle size distributions each had D10 and D90 values ranging from 19.2 to 56.1 µm respectively and D50 between 32.3 and 36.5 µm. The measured alloy compositions as determined by inductively coupled plasma-optical emission spectroscopy (ICP-OES) and ICP-combustion analysis are given in Table 4.1.

4.2.2 Additive manufacturing

Processing was carried out by the laser powder bed fusion (L-PBF) method in an argon atmosphere using a Renishaw AM 400 pulsed fiber laser system of wavelength 1075 nm and build plate size of $250 \times 250\,\mathrm{mm}^2$. The processing parameters employed were: laser power 200 W, laser spot size diameter 70 µm, powder layer thickness 30 µm, and pulse exposure time 60 µs. A 'meander' laser scan path pattern was used with hatch spacing of 70 µm and laser speed of 0.875 m/s, the path frame of reference was rotated by 67 ° with each layer [63]. Consistent with Renishaw's recommended practice for producing a good surface finish, the speed on the borders was reduced to 0.5 m/s. To assess the composition-dependence of the severity of cracking, cubes of dimensions $10 \times 10 \times 10\,\mathrm{mm}^3$ were printed. Vertical bars of dimensions $10 \times 10 \times 52\,\mathrm{mm}^3$ were also printed to assess the mechanical properties of the alloy variants. These were manufactured with 16 inverted pyramid legs to allow for easy removal from the baseplate. Cylinders of diameter 3 mm and height 1 mm were produced for differential scanning calorimetry (DSC). Each alloy and geometry was processed with identical parameters, as determined to be optimal for minimizing cracking in this manufacturing system [178].

Table 4.1 Measured alloy powder compositions (wt.%).

Alloy	Ni	Al	Co	Cr	Fe	Mo	Nb	Ta	Ti	W	C	B	Si	Hf
ABD850AM	Bal	1.3	18.0	19.9	-	2.02	0.64	0.48	2.25	4.85	0.010	0.003	-	-
ABD850AM+CB	Bal	1.5	18.6	19.7	-	2.03	0.37	0.57	2.42	5.05	0.133	0.007	-	-
ABD900AM	Bal	2.1	20.3	17.1	-	2.09	1.85	1.21	2.39	3.06	0.047	0.003	-	-
AM-Dev	Bal	4.2	19.1	8.7	-	1.20	3.60	5.50	0.12	7.10	0.030	0.005	-	-
CM247LC	Bal	5.5	9.3	8.3	-	0.55	-	3.20	0.73	9.66	0.070	0.020	-	1.4
ExpAM	Bal	5.6	7.6	11.7	-	2.00	1.10	-	2.00	3.70	0.004	<0.001	-	-
IN625	Bal	0.1	-	19.9	3.80	8.81	3.65	-	0.17	-	0.049	<0.001	-	-
IN713	Bal	6.0	-	12.0	0.20	4.30	2.10	-	0.70	-	0.060	0.010	-	-
IN718	Bal	0.6	1.1	19.2	17.2	3.20	4.90	-	0.80	-	0.080	0.001	0.35	-
IN738LC	Bal	3.3	8.5	15.7	0.02	1.73	0.87	1.69	3.29	2.71	0.110	0.011	0.03	-
IN939	Bal	1.8	18.8	22.5	-	0.00	1.00	1.30	3.60	1.60	0.160	0.011	-	-
Waspaloy	Bal	1.3	12.0	20.0	0.04	4.37	-	-	3.00	-	0.050	0.008	0.07	-

4.2.3 Assessment of additive manufacturability

The printability was assessed by measurement of cracking severity and morphology. First, extensive quantitative stereological assessment was made with optical micrographs taken using a Zeiss Axio A1 optical microscope at 100× magnification. For this purpose, the cube samples were sectioned on (i) planes with normal corresponding to the build direction (termed XY plane) at mid-height and (ii) planes with normal perpendicular to the build direction (termed XZ). The severity of cracking was determined by imaging the XY plane at the sample height midpoint and on the XZ plane through the centre; 5 images were considered per alloy. In this analysis the bulk of the sample – 400 µm from the sample edge – was considered. The ImageJ software was used to compare the alloys by determining the crack count density (cracks/mm^2) and crack length density (mm/mm^2) – note that the crack length was defined as the caliper diameter corresponding to the largest line length across each crack. 8-bit images were processed in ImageJ with an automated black and white threshold and as discussed in Chapter 3 the particle analysis macro was run excluding features of maximum caliper diameter smaller than 10 µm.

In the case of a pulsed laser, solidification occurs in discrete melting events; it follows that a solidification crack must be of length equal to or smaller than a single melt pool radius. Conversely, any crack of length greater than one melt pool radius must have propagated as a solid-state crack, although of course one cannot eliminate the possibility that the solid-state crack propagated from a solidification crack. In order to provide quantitative information, the perimeter to area ratio (units µm^{-1}) of cracks was assessed. Images were taken at a magnification of 100×, giving a resolution high enough to identify the jagged features of solidification cracks. A further 70 images were taken of each alloy to compare the contributions of each mechanism on a representative scale; where cracking occurred, many thousands of cracks were analysed.

To garner further information concerning cracking mechanisms at higher spatial resolution, a Zeiss Merlin Gemini 2 field emission gun scanning electron microscope (FEG-SEM) was used equipped with an Oxford Instruments XMax 150 mm/mm^2 energy-dispersive X-ray spectroscopy (EDX) detector. Line scans were performed to determine qualitatively the composition of carbides observed in the microstructure. Scans comprised 500 points at an accelerating voltage of 5 kV and probe current 500 pA resulting in an estimated interaction width and depth of 100 nm. The microstructure of the alloys after manufacturing always comprised γ and MC carbide with γ' absent; an example of the CM247LC as-printed microstructure compared to the heat-treated microstructure following electrolytic etching with 10% phosphoric acid at 3 V direct current is given in Figure 2.5. In what follows, it is emphasized that only material in the as-printed condition is considered.

4.2.4 Assessment of mechanical and stress relaxation behaviour

Uniaxial tensile, isothermal stress relaxation and constrained cooling tests were performed with an Instron electro-thermal mechanical testing (ETMT) machine. Specimens were machined with axis along the build direction using electrical discharge machining (EDM) with dimensions as given in Figure 4.3. To negate the influence of any machining-induced surface roughness, all surfaces were polished to a 4000 grit finish by hand. For each of the three types of test, joule heating under free expansion conditions ($\sigma = 0$ MPa) was employed to reach the test temperature using a heating rate of 200 K/s, thus avoiding any second phase precipitation. Since it was needed for the interpretation of the results, an estimate of the average linear coefficient of thermal expansion between 300 and 800 °C was made during this pre-test sample heating as shown in Figure 4.4. The coefficient of thermal expansion is found to have a dependence on the Al content, as previously reported in [202].

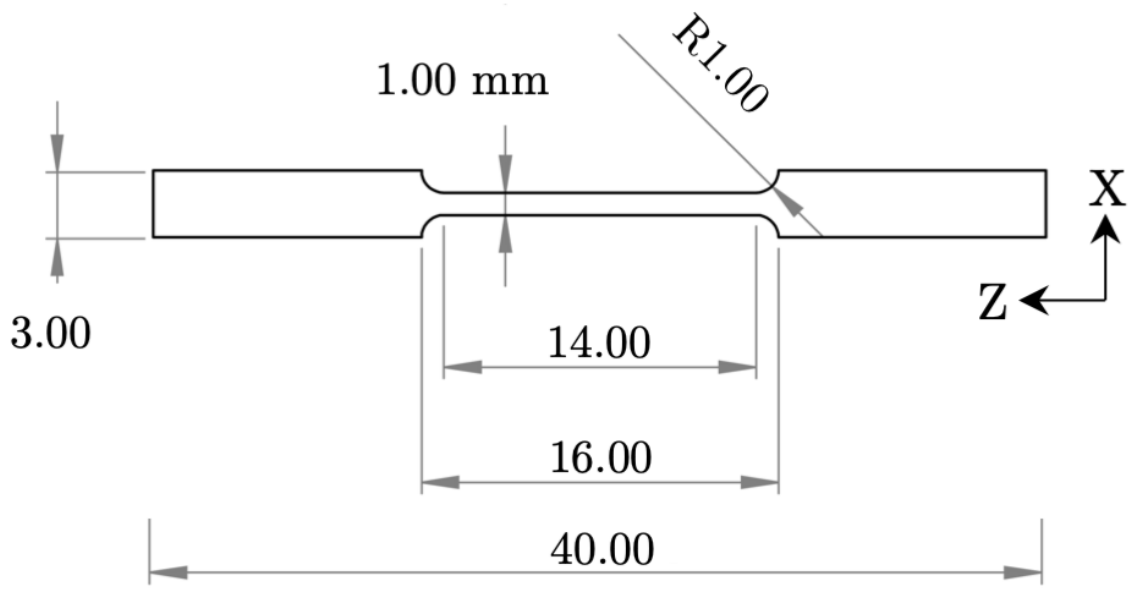

Fig. 4.1 The sample geometry used for ETMT tensile, stress relaxation, and constrained bar testing.

Isothermal uniaxial tensile tests were performed for all the alloys at room temperature and at 800 °C – this temperature being taken to be representative of where the ductility dip is likely to be severe [9]. Specimens were strained rapidly at a rate of $10^{-2}\,s^{-1}$ to reduce the influence of any dynamic precipitation during testing. An iMetrum non-contact digital image correlation system was employed for measuring the strain; 3 repeats were performed for each alloy. The elastic modulus of each alloy was determined between 150-300 MPa. The modulus determined at 800 °C correlated with increasing equilibrium γ' volume fraction, see Figure 4.4, though was likely due to the contributions of γ' formers in solid solution of γ.

Stress relaxation tests were performed to quantify the capacity of the alloys to relieve the stress accumulated by processing. Tensile specimens were heated to 1000 °C allowing for free expansion to occur as shown in Figure 4.3, followed by a loading to 100 MPa at 25 MPa/s after which the sample grips were instantaneously locked into position, in order to observe the relaxation of the stress during cooling [203]. The

ability to stress relax was benchmarked by comparing the stress remaining after 60 s. Further stress relaxation tests at various super-solvus temperatures (1100-1200 °C) were performed on the ABD850AM+CB, Waspaloy, and IN939 alloys by the same procedure.

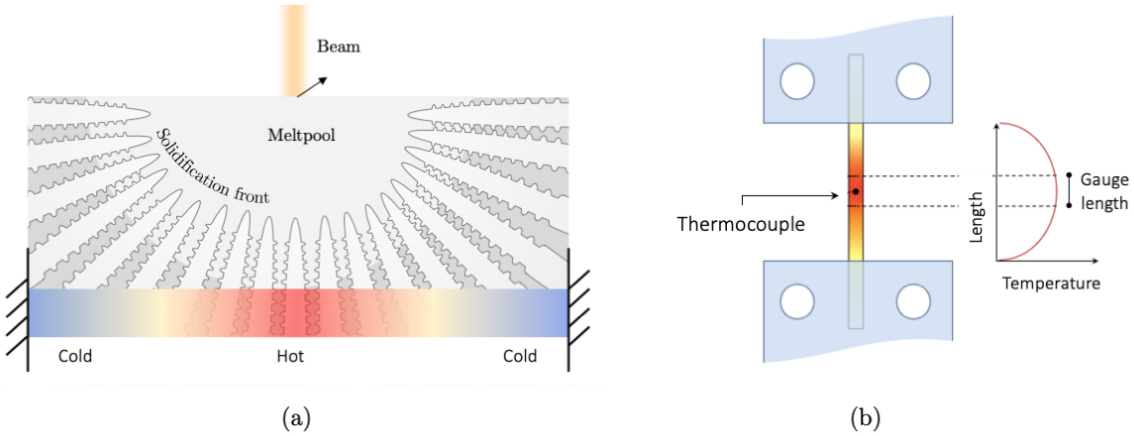

Fig. 4.2 (a) Thermal-mechanical approximation of melt pool cooling and (b) schematic diagram of the ETMT setup.

A constrained bar cooling test was performed to simulate the stress build up expected of additive manufacturing (illustrated in Figure 4.2). Tensile specimens were heated under free expansion conditions to 1100 °C then left for 20 s to ensure thermal-mechanical equilibrium. The displacement of the ETMT grips was then fixed, and the sample was cooled to 300 °C. The accumulated stress during cooling was measured for the various alloys at cooling rates of 100 K/s, 80 K/s, 50 K/s, and 25 K/s.

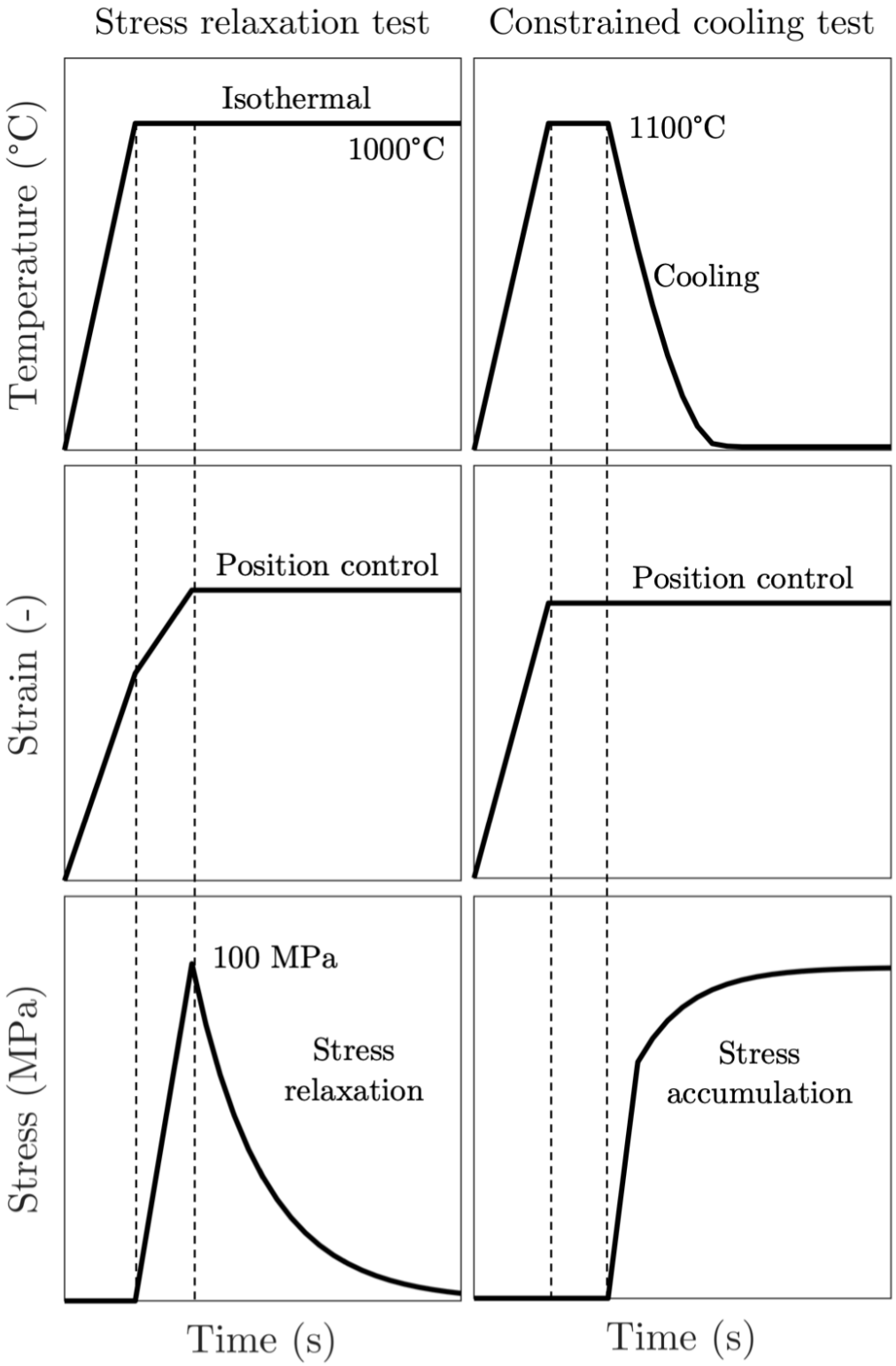

Fig. 4.3 A schematic illustration of temperature, strain and stress profile as a function of time during the stress relaxation and constrained bar cooling test.

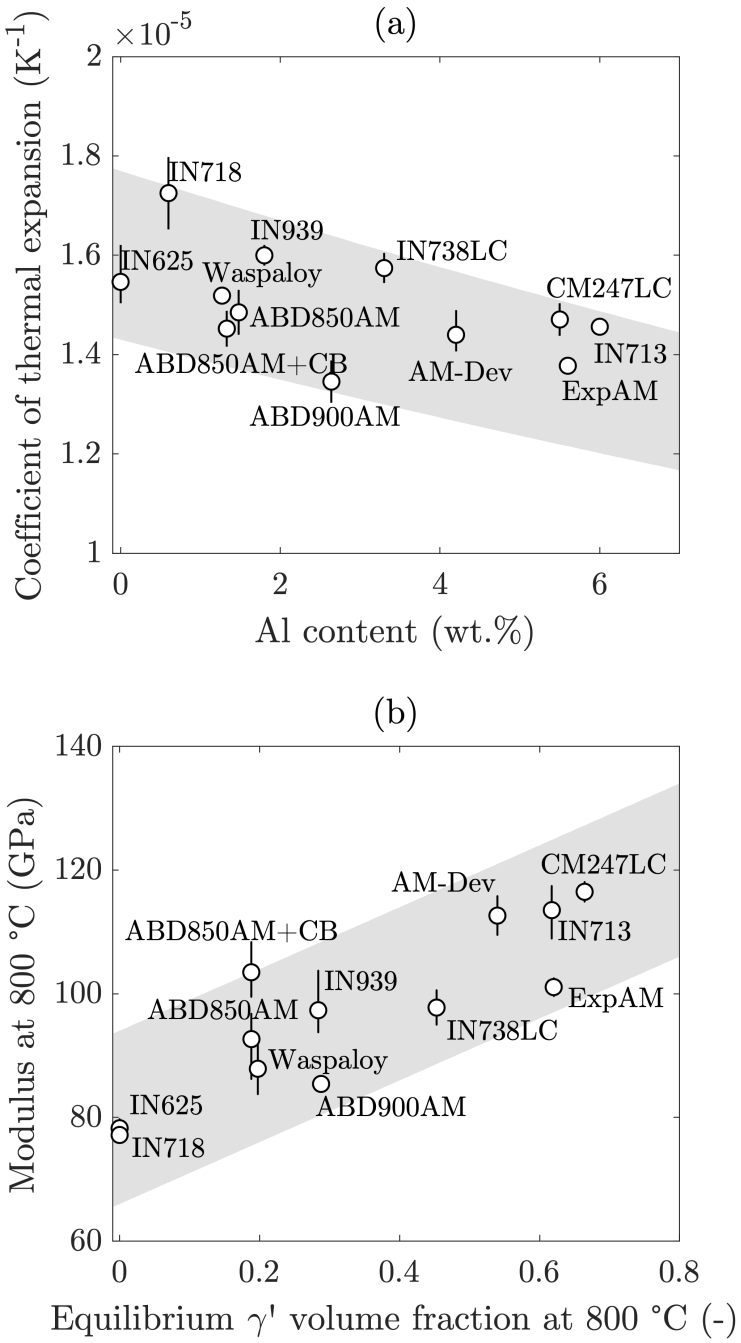

Fig. 4.4 (a) The average coefficient of thermal expansion α measured during pre-test heating under free expansion conditions on the ETMT vs the Al content (wt.%) and (b) the average elastic modulus determined at 800 °C vs the equilibrium γ' volume fraction at 800 °C fraction acquired by Thermo-Calc (TTNi8 database). Error bars represent the minimum and maximum values measured.

4.2.5 Assessment of solidification range and phase transformation temperatures

A NETZSCH 404 F1 Pegasus DSC was used to compare solidification behaviour of the as-processed microstructure, albeit at cooling rates far lower than those experienced during AM processing. The alloys were subjected to a thermal history consisting of (i) heating to 700 °C at 20 °C/min, (ii) heating from 700 °C to 1450 °C at 10 °C/min (iii) cooling to 700 °C at the same rate, and (iv) cooling to room temperature at 20 °C/min. The DSC signal from the first heat causes the transformation from a non-equilibrium additively manufactured microstructure to a homogeneous liquid. The first cool was indicative not of AM conditions, but of the solidification path from homogeneous liquid to solid at 10 °C/min. The thermophysical properties of interest derived from the DSC signal upon heating were the onset of incipient melting $T_{S'}$, and the liquidus T_L, as illustrated in Figure 4.18a. From cooling the onset of solidification $T_{L'}$ and the solidus temperature T_S were extracted as shown in Figure 4.18b. The solidus and onset of incipient melting as well as liquidus and onset of solid nucleation temperatures were estimated following the procedures of Boettinger, Chapman, and Quested [204, 192, 193]. In order to evaluate legacy crack criteria on the basis of an experimentally determined solidification path, the solid fraction as a function of temperature was estimated by considering it proportional to the ratio of the enthalpy of the transformation at T to the total enthalpy of the phase transformation. This estimate is subject to possible error because other phase transformations may have occurred throughout the freezing range.

Modeling of solidification under equilibrium and Scheil-Gulliver assumptions was implemented using Thermo-Calc employing the TCNI8 and TTNi8 databases to simulate the alloy solidification path [205]. In the case of the Scheil models, solidification was considered to have ended at a liquid fraction remaining of 0.01. The propensity for

backdiffusion of C to occur was deemed negligible in accordance with the dimensionless back diffusion parameter α [206].

$$\alpha = \frac{4D_{\mathrm{C}}}{\lambda_{\mathrm{cell}}^2} \frac{\Delta T_{\mathrm{freezing}}}{\mathrm{d}T/\mathrm{d}t} \tag{4.1}$$

where D is the chemical diffusion coefficient of carbon in γ at temperature [23], λ_{cell} is the cell spacing, and $\Delta T_{\mathrm{freezing}}$ is the magnitude of the freezing range. Given an experimentally determined λ_{cell} of 1 µm [9], and typical cooling rates reported in the literature [18–21] the value of α is substantially less than unity. Hence, backdiffusion of C was deemed negligible and modelling of solidification under Scheil assumptions was considered a reasonable first approximation. This is demonstrated for C and B in Figure A.1 in Appendix A.

4.3 Results

4.3.1 On the assessment of cracking severity, morphology, and mechanism

This experimentation involving extensive characterization of cracking provides proof of the significant effect of composition on processability. This is apparent in the optical micrographs of the XY transverse section – normal corresponding to build direction – in Figure 4.6. Cracking is prevalent in the legacy alloys IN713, IN738LC, IN939, and CM247LC as well as the two experimental compositions – ExpAM and ABD850AM+CB. The other alloys examined here process largely crack-free. The distribution of cracks across the XY plane is uniform in IN713 and ExpAM, whereas the others cracked to a greater extent at the edges, where the effective laser scan speed was reduced. If one puts aside the prevalence for surface cracking for one moment

and considers the cracking information for the bulk, the data for different measures of crack severity developed here – count density and length density – are consistent with each other, see Figure 4.5. When examined on the longitudinal XZ plane, there is a clear disposition for the cracks to be aligned along the build direction, see Figure 4.7, with SEM images indicating that cracks of both solid-state type and solidification type are present in all cracked alloys. Solid-state cracks tend to exhibit a long and straight morphology, whereas solidification cracks appear more jagged.

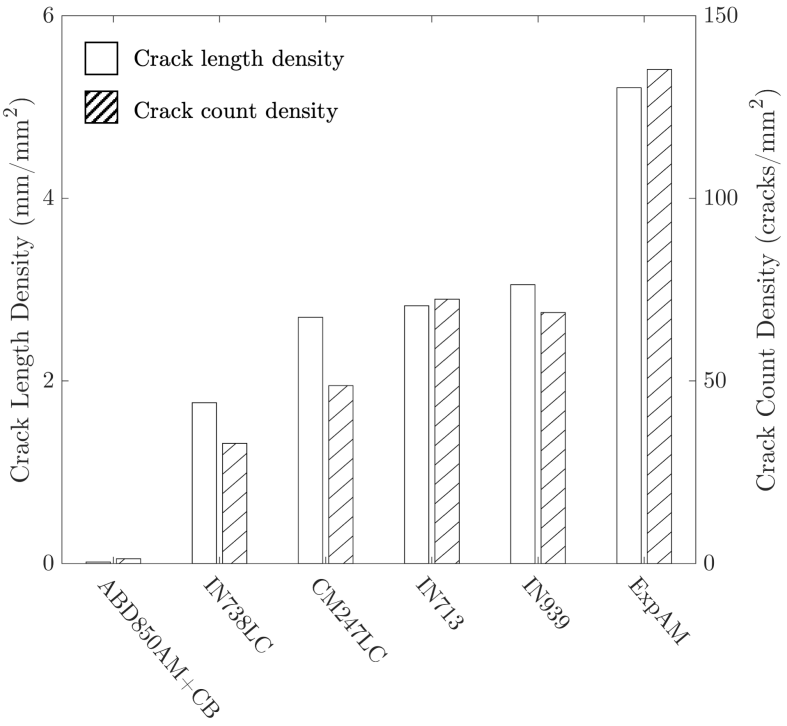

Fig. 4.5 Bar chart showing crack length density and crack count density for the six unprocessable alloys.

In order to strengthen these findings further, detailed quantitative stereological analysis has been employed to quantify the extent to which solidification and solid-state cracks occur in each alloy, and to allow for distinguishing between them. The quantification of cracks at depth in the bulk is emphasized first, since these are the greatest in number and since it may be possible to improve the surface cracking

susceptibility by tailoring the processing conditions at the surface still further. The morphology of cracks was initially quantified in terms of perimeter/area ratio, aspect ratio, and caliper diameter, this analysis carried out on 4 of the cracked alloys (shown in Figure 4.8) showed the perimeter to area ratio was best suited to differentiating crack mechanisms in different alloys. Following from this conclusion the morphology of cracks in different alloys was summarized by the kernel density estimate of the probability distribution of the perimeter to area ratio μm^{-1} of cracks in each of the 6 cracked alloys, see Figure 4.9. Solidification cracks, distinguished by their characteristic jagged morphology and lower perimeter to area ratio, arise to greater extent in the IN738LC, IN939, CM247LC and ABD850AM+CB. This is proven by the deviation of their perimeter to area ratio distributions, which possess a smaller median, interquartile range, and lower/upper adjacent values relative to IN713 and ExpAM. Solid-state cracking is the dominant mechanism in IN713 and ExpAM; in these alloys, cracks are longer and straighter, exemplified by the shift of their perimeter to area distributions towards greater values. Nevertheless, overlap between the distributions for some alloys is apparent for approximately $0.5 <$ perimeter/area < 0.7, suggesting that the two mechanisms are both operating simultaneously and competing against each other. Cracks in this range are of mixed mode, indicating they began as solidification cracks and then propagated further in the solid-state. The probability distribution of ABD850AM+CB is cut off at 0.19 and 0.67 as the distribution is comprised of only 24 cracks observed.

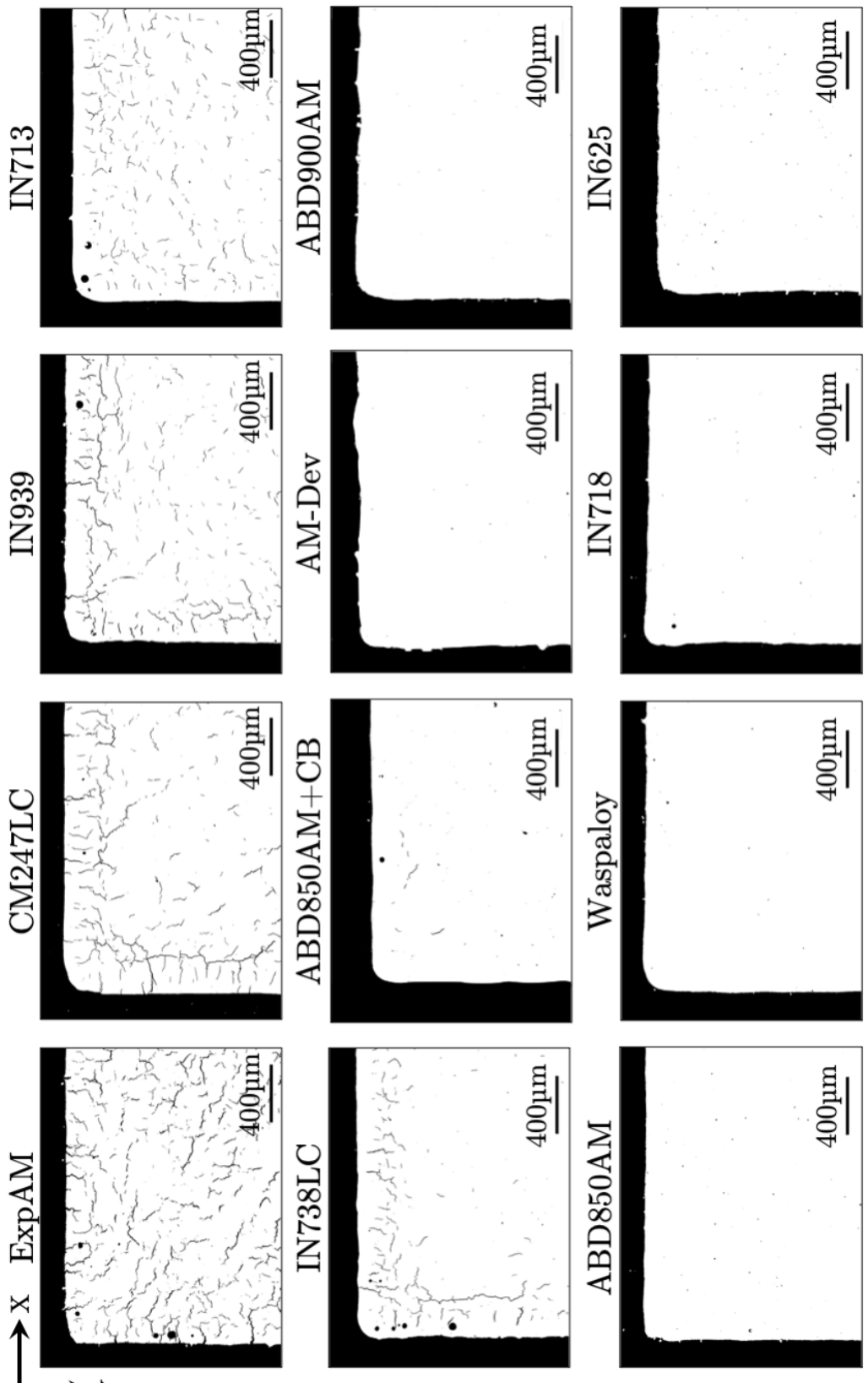

Fig. 4.6 Optical images of the XY plane for each alloy with a binary threshold applied exemplifying cracking or lack thereof in each alloy. It is evident the ExpAM, CM247LC, IN939, IN713, IN738LC and ABD850+CB demonstrated extensive cracking and hence are not readily processable.

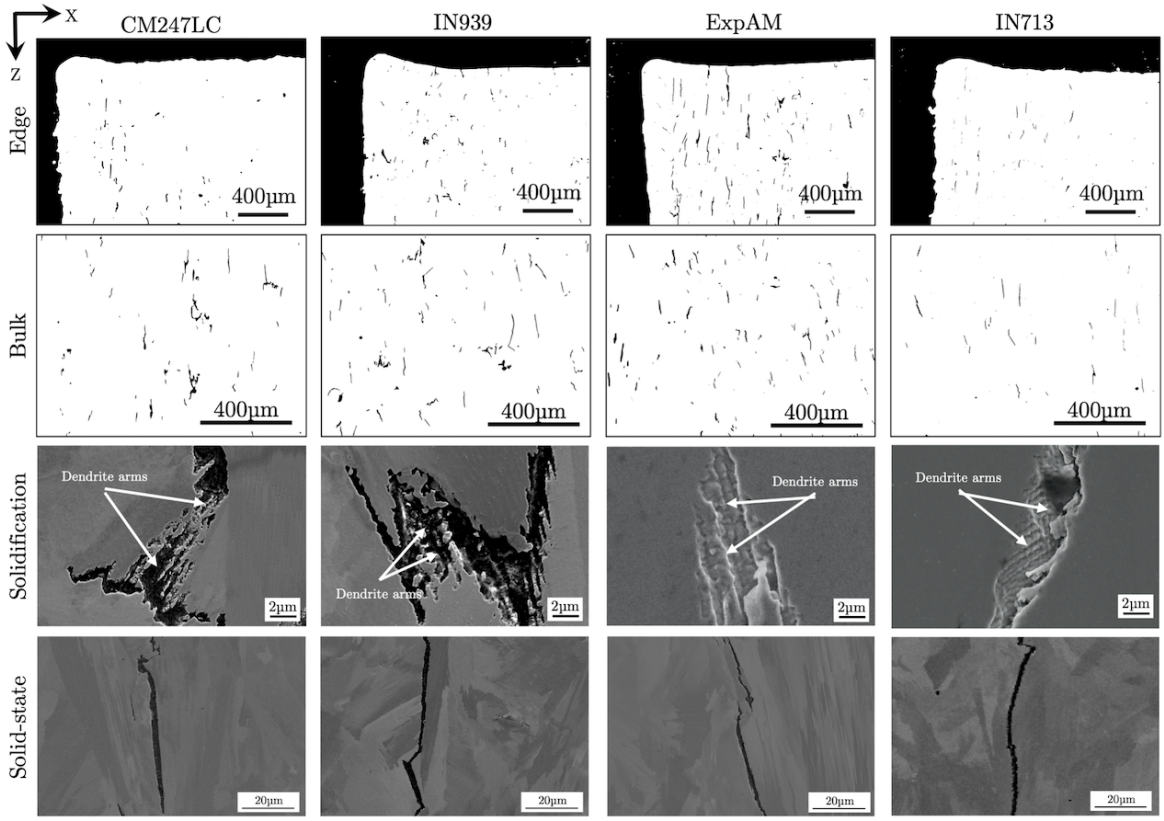

Fig. 4.7 Optical micrographs taken of the XZ plane exemplifying cracks observed at the edge and within the bulk of CM247LC, IN939, ExpAM, and IN713, as well as SEM micrographs of solidification and solid-state cracks observed in respective alloys on the XZ plane.

Finally, consider again the propensity for some alloys – IN738LC, IN939, CM247LC and ABD850AM+CB – to exhibit increased cracking at sample edges. In these alloys, cracks near edges observed on the XY plane have uniform spacing of $\approx 80\,\mu m$ - this periodicity is attributed to the preferential nucleation of cracks to minimize strain energy [207]. The slower scan speed used at the sample edge resulted in coarser microstructure less able to accommodate strain, with larger grains with increased texture component as compared to the bulk [95]. Furthermore, the sample edge was processed with greater energy density and larger melt pools, both of which have been observed in the literature to exacerbate solidification cracking in particular [208]. ExpAM and IN713 crack at the edges, though not comparatively more than in the

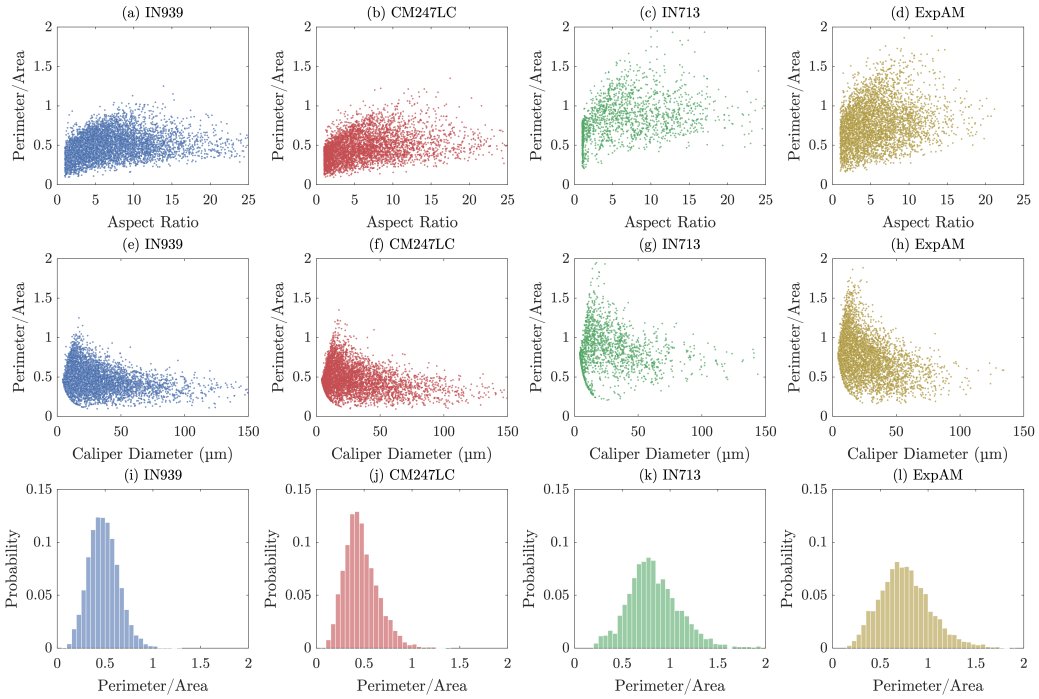

Fig. 4.8 Scatter plots quantifying the morphology of the cracks observed in IN939, CM247LC, IN713, and ExpAM in terms of perimeter/area values, aspect ratio's, and caliper diameters. The probability distribution of the perimeter to area ratio of cracks shown in (i)-(l) is most effective in identifying a composition dependence of crack morphology.

bulk. However, the 4 alloys mentioned above which are prone to more solidification cracking in the bulk exhibit more cracking at the edge (relative to their bulk) as they are more sensitive to the local microstructure and processing conditions.

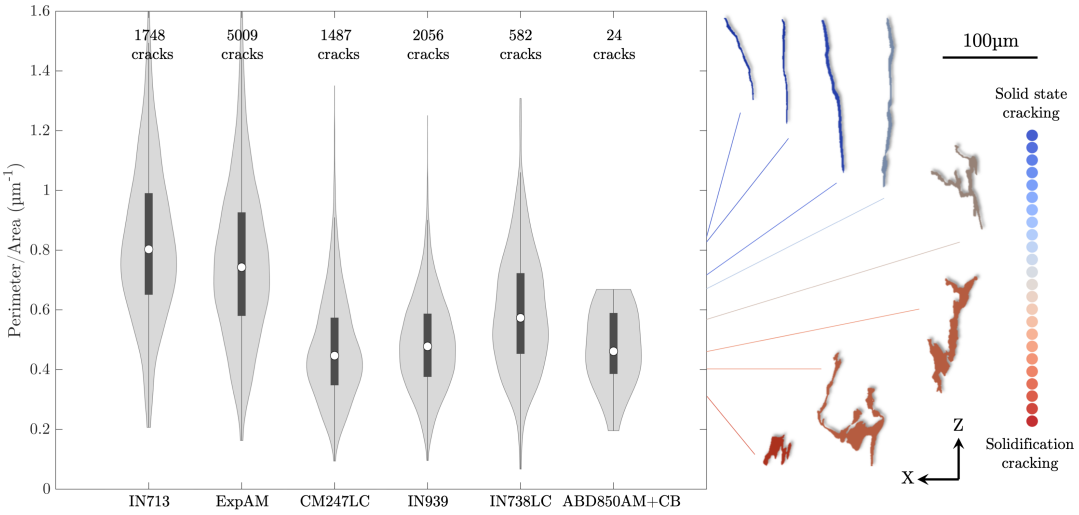

Fig. 4.9 Violin plots showing the median, interquartile range, lower/upper adjacent values, and probability distribution of the perimeter/area ratio. As well as examples of solidification and solid-state cracks and their corresponding perimeter/area values.

4.3.2 On the influence of mechanical properties on additive manufacturability

Tensile response of the alloys

The temperature-dependence of the tensile response at $10^{-2}s^{-1}$ is illustrated in Figure 4.10, for the alloys IN625, AM-Dev, and CM247LC. Note that the starting microstructure corresponds to the as-processed condition. The heritage alloys IN625 and CM247LC serve as lower and upper bounds respectively for flow stress across the full temperature range due to the appreciably smaller or larger extent of alloying. A significant degree of ductility is evident between 25 °C and 600 °C; however, a significant drop in ductility is found between 800 °C and 1000 °C.

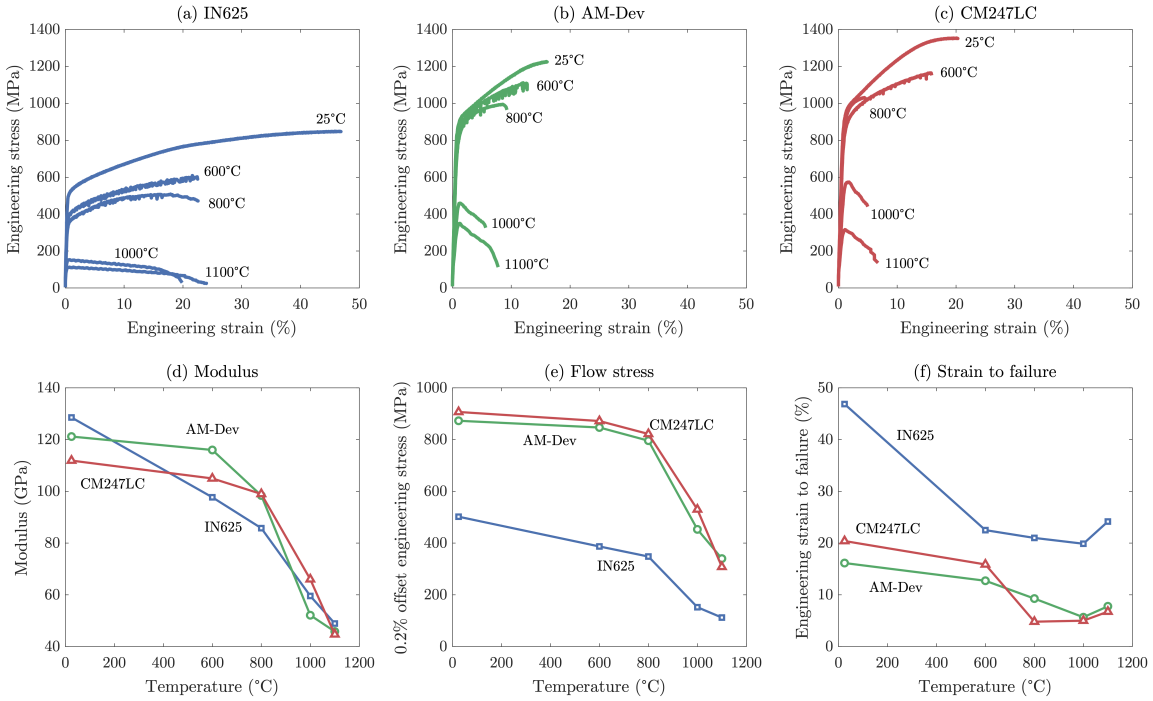

Fig. 4.10 The isothermal tensile response of (a) IN625, (b) AM-Dev, and (c) CM247LC at 25, 600, 800, 1000, and 1100 °C in the as-printed state. Summary of the temperature dependence of (d) the elastic modulus, (e) the flow stress, and (f) the strain to failure.

The above findings have justified a thorough investigation of the composition-dependence of the strain-to-failure in the ductility-dip regime. The temperature of 800 °C was chosen for this study. The ductility at 800 °C has been found to vary within the range 1% to 40% for the alloys studied, see Figure 4.11. Alloys which cracked during processing were found to exhibit significantly reduced ductility (summarized in Figure 4.12. In particular, the alloys IN713 and ExpAM – which are prone to solid-state cracking – failed by brittle fracture at a strain of $<1.5\%$ with little necking. In this case, their engineering strain to failure has been defined as the strain at which brittle fracture takes place. For the remaining alloys, the engineering strain to failure is taken as the strain at which the sample comes apart, occurring with little/no necking, and others such as IN625 and IN718 occurring after significant necking. Serrated flow

was observed in all the alloys with the exception of ExpAM, IN713, and CM247LC. This is attributed to the interaction of solute atoms and moving dislocations [209, 210].

To summarize, it is clear that the processable alloys maintain some ductility at 800 °C whereas the unprocessable alloys do not. The engineering strain to failure and 0.2% offset engineering stress (referred to as the flow stress) measured for each alloy at 800 °C are given in Figure 4.12 – one can see that alloys that developed cracks during processing each fail at engineering strain to failure less than 7% at 800 °C. Conversely, all the readily processable alloys were able to accommodate greater than 7% engineering strain. A strength/ductility trade-off is apparent. In all 12 alloys, good ductility (>15% engineering strain to failure) is observed during testing at room temperature, the results of these tests can be found in Figure A.2 of Appendix A. This confirms a negligible influence of pre-existing defects at high temperature and the relevance of a mechanism of high-temperature embrittlement.

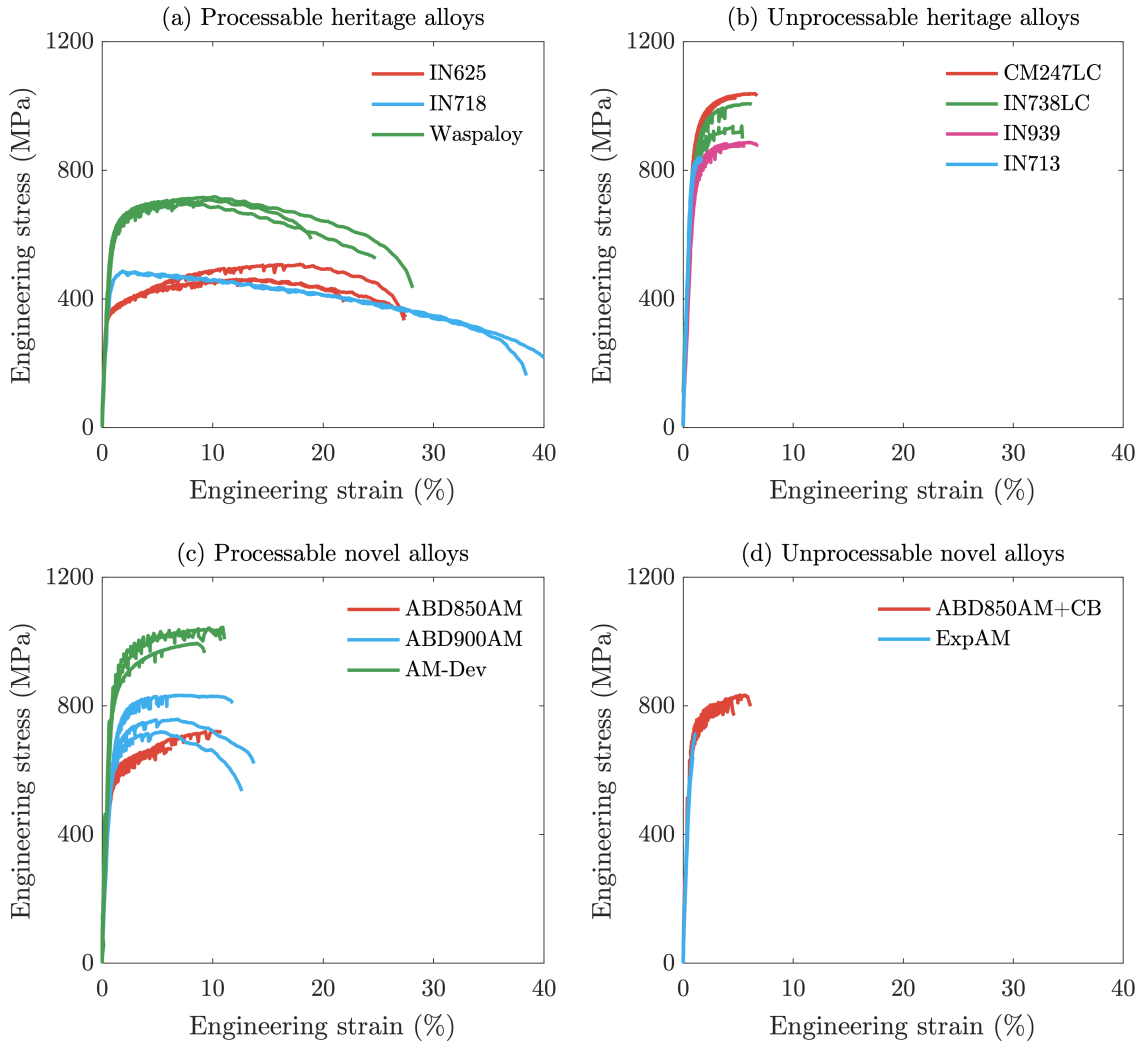

Fig. 4.11 The tensile response of (a) the processable heritage alloys (b) unprocessable heritage alloys (c) processable novel alloys (d) unprocessable novel alloys at 800 °C.

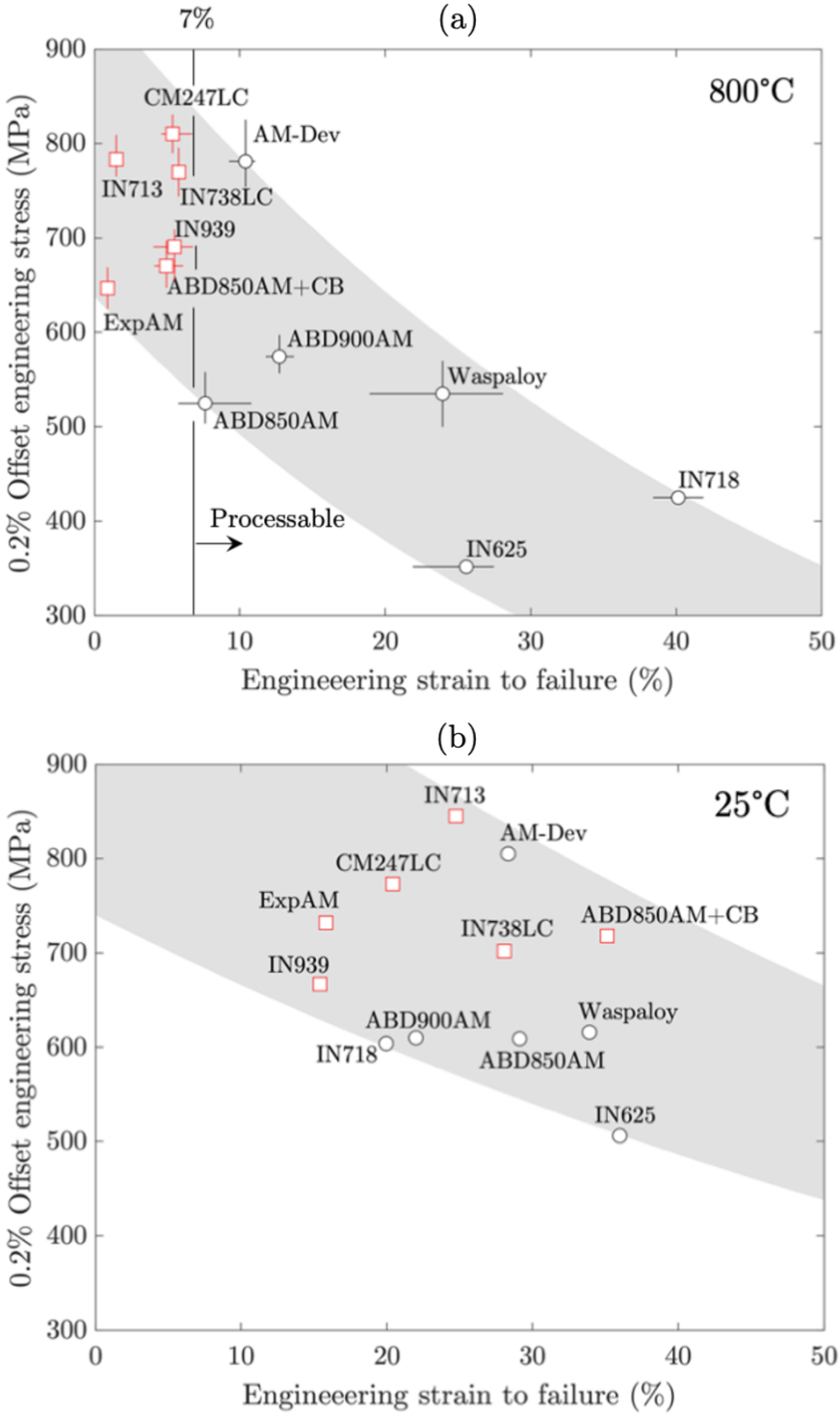

Fig. 4.12 (a) The mean flow stress vs the mean engineering strain to failure at 800 °C after 3 tests, error bars show the minimum and maximum values of the 3 repeats. (b) The flow stress vs the engineering strain to failure at 25 °C.

Stress relaxation behaviour

The isothermal stress relaxation responses of the different alloys at 1000 °C are compared in Figure 4.13, for an initially imposed stress of 100 MPa. The curves possess some common features – but also differences. A significant transient is observed within the first 10 s which is characterized by a rapidly decreasing stress, which develops into a more gradual decay at longer times.

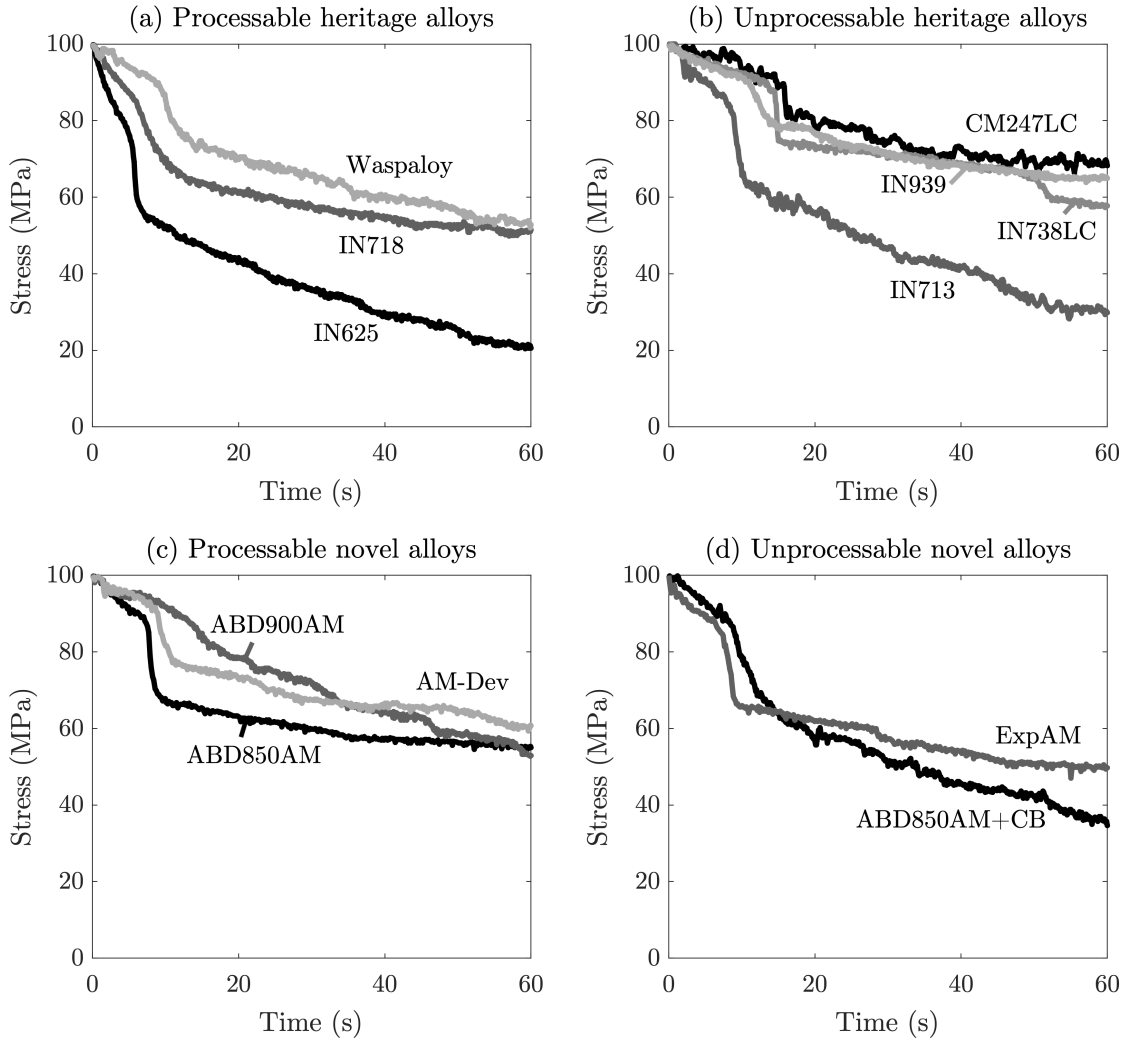

Fig. 4.13 The stress relaxation behaviour of the (a) processable heritage alloys (b) unprocessable heritage alloys (c) processable novel alloys (d) unprocessable novel alloys at 1000 °C.

The most creep resistant alloys are those of higher Al, Ti, Ta and Nb contents such as CM247LC, IN939, IN738LC and AM-Dev. However, also apparent is that some alloys such as ABD850AM, ABD900AM and AM-Dev – which print well – do not relieve stress very much more slowly than those – for example ABD850AM +CB and ExpAM – which print poorly. It follows that the capacity for stress relaxation cannot alone be responsible for conferring additive manufacturability.

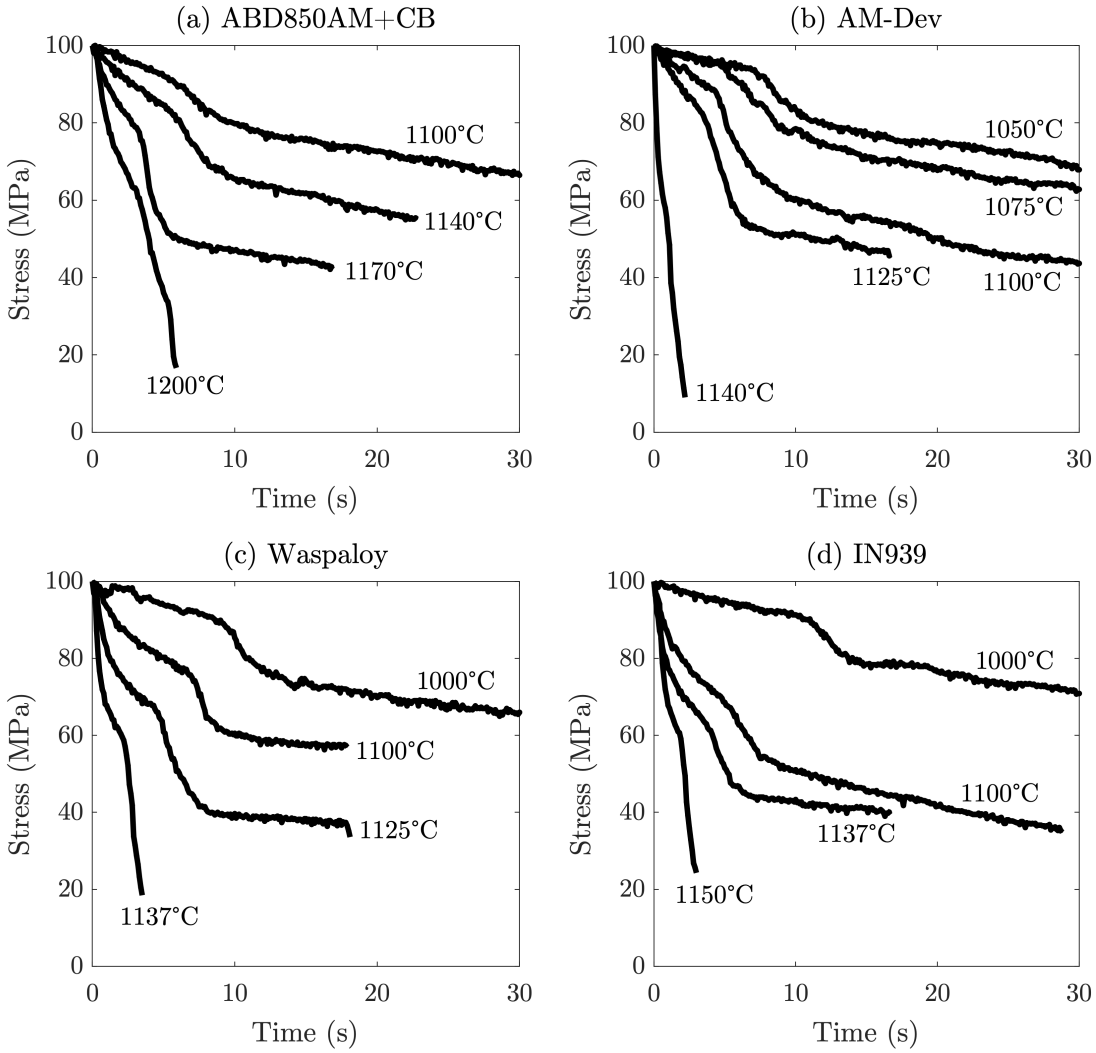

Fig. 4.14 The stress relaxation behavior of (a) ABD850AM+CB (b) AM-Dev (c) Waspaloy and (d) IN939 at various temperatures.

The above findings warrant further detailed quantitative analysis, and this is developed in Section 4. But the modelling presented there requires an estimate of the temperature-dependence of the stress relaxation phenomenon, and thus a first estimate of a constitutive law for this effect. For some of the alloys – specifically IN939, Waspaloy, AM-Dev and ABD850AM+CB – further testing has been carried out for a number of temperatures, see Figure 4.14. As expected, a strong dependence upon temperature is displayed.

Stress development during constrained cooling

The results presented thus far indicate that lack of printability may in some way be associated with the build of stress during constrained cooling coupled with a lack of ductility in the mid-temperature regime. This motivated the assessment of the non-isothermal stress build-up during constrained cooling using the fixed-grips test involving cooling from 1100 °C at 50 °C/s, see Figure 4.15.

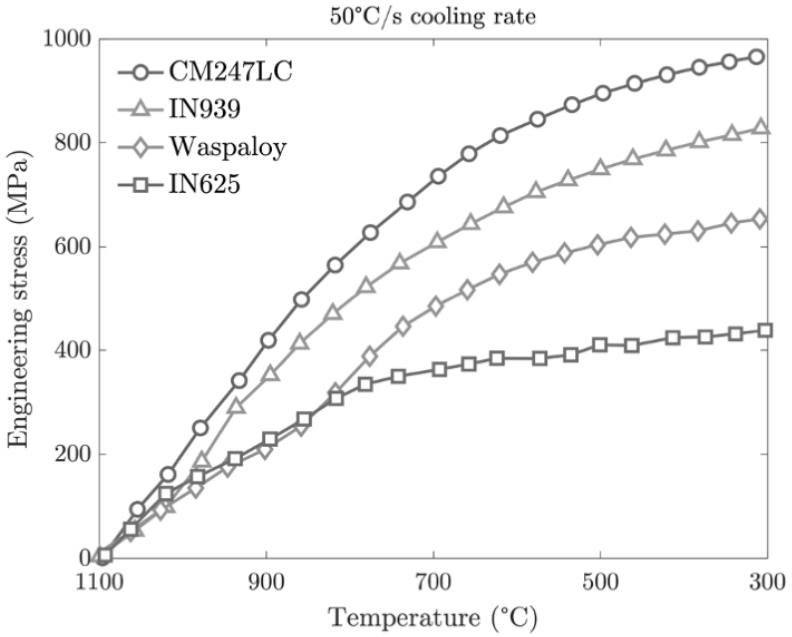

Fig. 4.15 Comparison of the stress developed during constrained bar cooling of the CM247LC, IN939, Waspaloy, and IN625 alloys at a cooling rate of 50 °C/s.

At the cooling rate of 50 °C/s – close to the fastest possible using the ETMT machine's configuration – the alloys develop stress to different extent, see Figure 4.15. Of the alloys assessed, stress develops in CM247LC and IN625 to the greatest and least extents respectively. Interestingly, cracking in this constrained-bar test has not been replicated, at least without a further imposition of a further superimposed mechanical strain. When cooling is carried out at the slower rate of 25 °C/s the stress accumulated is concomitantly less, as discussed in the later Section 4.

4.3.3 Characterisation of as-printed microstructure and influence of freezing range

As-printed microstructure

The as-printed microstructure in all cases comprises long columnar grains preferentially aligned in the build direction. There are three distinct characteristics: (i) cells of the matrix γ with very small or no secondary dendrite arms; (ii) a narrow intercellular region of differing etching characteristics and therefore likely composition, and (iii) carbides residing largely in the intercellular region. It is emphasized that no γ' precipitate phase has been detected in any of the alloys in the as-printed state or following tensile testing at 800 °C. Recent data acquired via synchrotron x-ray diffraction has provided further corroboration that superalloys processed in this manner are devoid of γ' in the as-printed state [95]. The rapid cooling rate results in very fine cellular morphologies of spacing in the range 300 nm to 1.5 μm depending on the proximity to the sample edge.

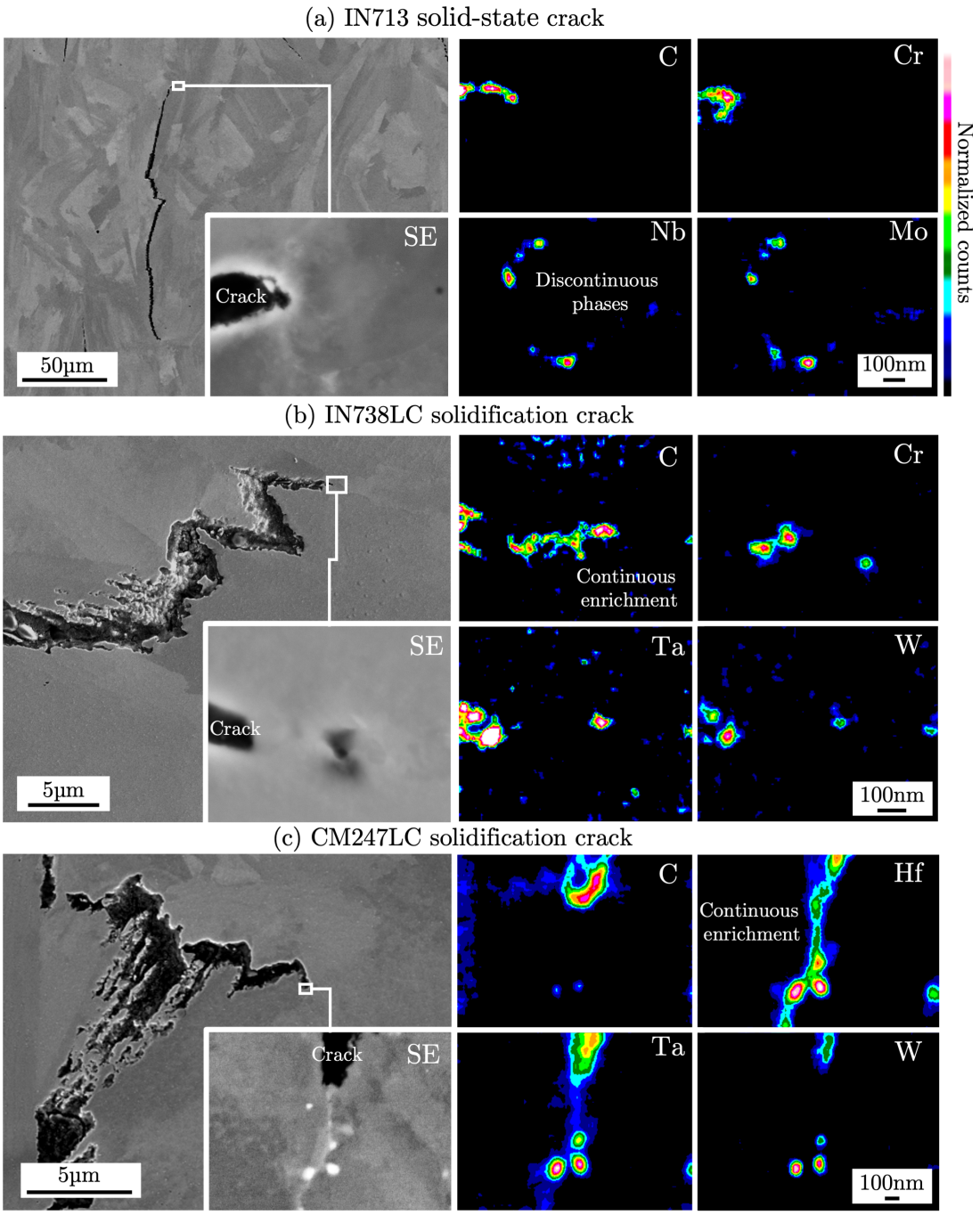

Fig. 4.16 SEM and EDX analysis at the crack tip for a typical solid-state crack in (a) IN713 and solidification cracks observed in (b) IN738LC and (c) CM247LC.

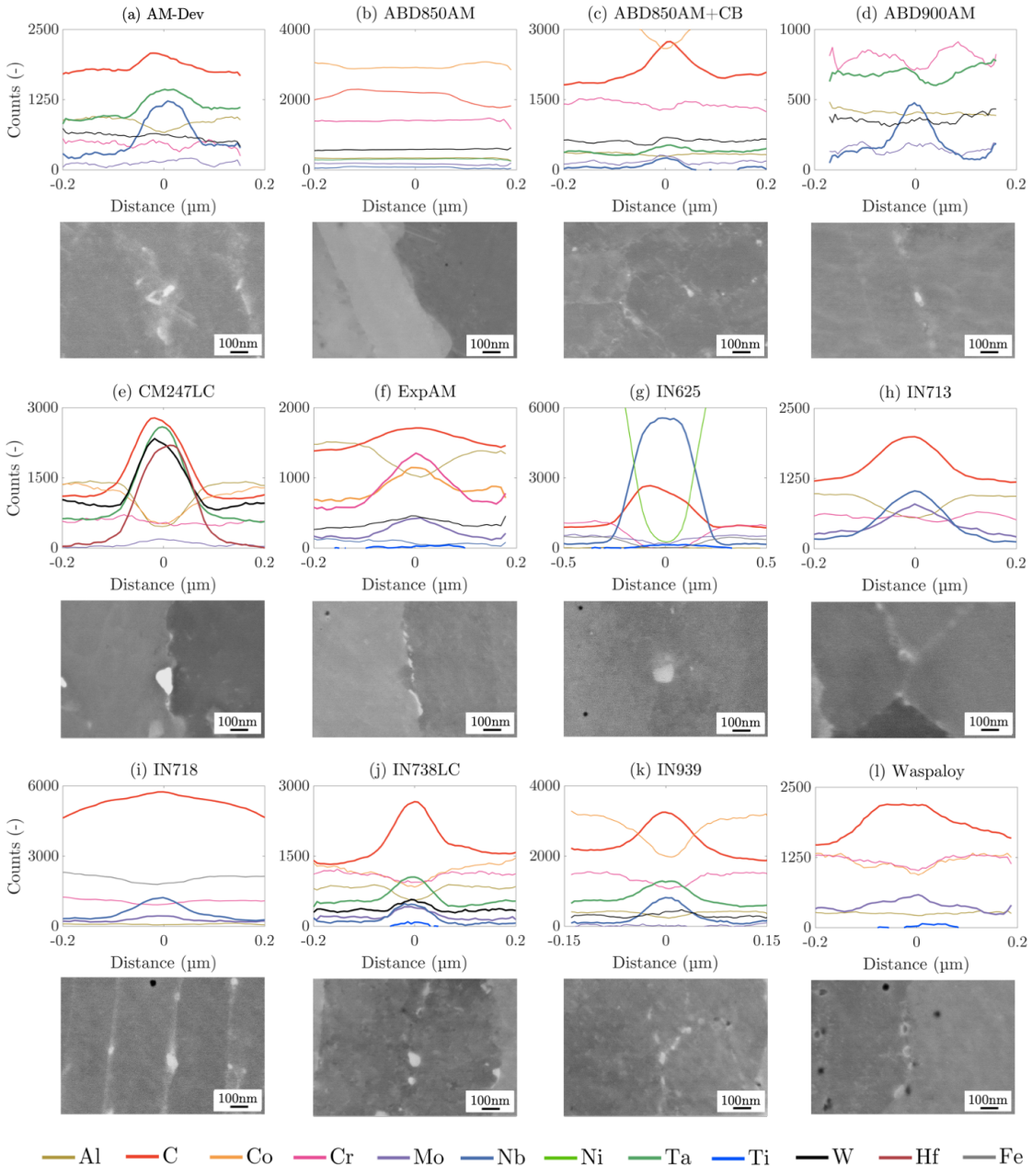

Fig. 4.17 Backscattered electron (BSE) micrographs of the as-printed microstructure after tensile testing at 800 °C showing the γ matrix and the intercellular carbides as well as EDX linescans across the carbides showing the carbide enrichment in each alloy.

Figure 4.17 shows the enrichment of the intercellular carbides in each alloy as detected by EDX linescans. A table of the enrichment observed in each alloy and confirmation from the literature is made in Table 4.2. The literature indicates that the carbides are likely of MC type of face-centered cubic structure. The presence of Cr enrichment in only ExpAM – the most severely cracked alloy – suggests a deleterious effect of chromium-rich carbides on processability.

In CM247LC, EDX analysis at high magnification reveals the presence of a continuous film of solute enrichment at the solidification crack tips. The enrichment of Ta and Hf separate from the carbide, shown in Figure 4.16, confirms the partitioning of these solutes to the final solidifying liquid. In IN713 – which cracks predominantly by the solid-state mechanism – no such continuous solute enrichment was observed, only discontinuous phases as shown in Figure 4.16. This microstructural difference between solidification and solid-state cracking confirms that CM247LC's susceptibility to solidification cracking stems from the solute enrichment of the solidifying liquid and subsequent widening of the freezing range.

Differential scanning calorimetry and thermodynamic modelling

The magnitude of the freezing range may well be a good indicator of the solidification cracking susceptibility – the alloys prone to predominately solidification type cracks freeze over wide solidification intervals. Figure 4.20 shows the magnitude of the freezing range (i) as measured by differential scanning calorimetry and (ii) and (iii) from modeling of the solidification path by thermodynamic simulation under the Scheil conditions with the TCNI8 and TTNi8 thermodynamic databases, respectively. Estimates from DSC and the TCNI8 database show the solidification cracking prone alloys ABD850AM+CB, IN738LC, and IN939 have the widest freezing range of the

12 investigated. On the other hand, TTNi8 predicts the solidification prone cracking alloys to have the 4 widest freezing ranges.

The DSC signals and labeled phase transformation temperatures of ExpAM are shown in Figure 4.18. The simulations predict significantly lower solidus temperatures than the DSC tests and the full suppression of γ' precipitation even in the alloys with highest γ' former content; this suppression is confirmed by characterization in Figure 2.5. Liquidus and solidus temperatures determined by DSC during heating and cooling are summarized in Table 4.2. One needs to bear in mind of course that it is not possible to replicate the extreme heating/cooling rates of the AM process in the DSC.

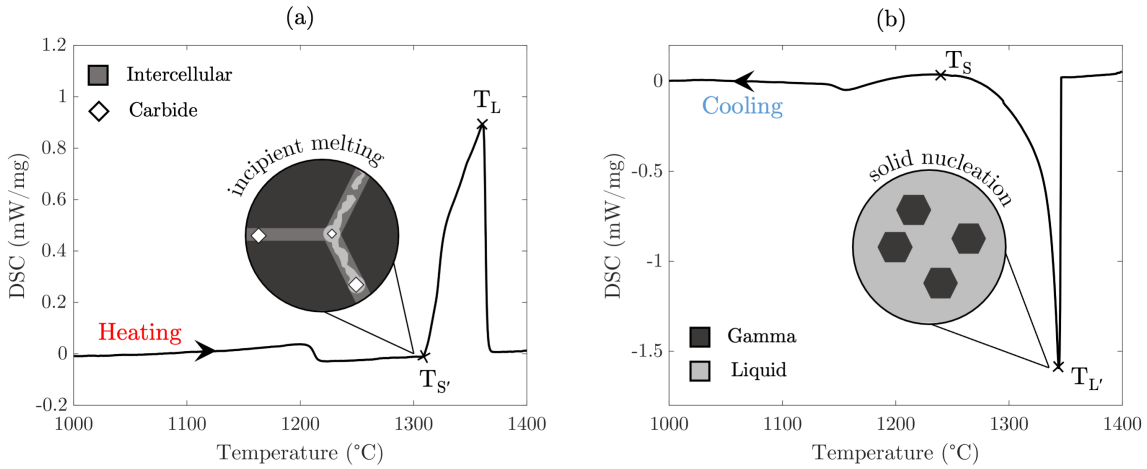

Fig. 4.18 DSC signal from ExpAM and the respective phase transformations determined by interpretation of (a) the heating cycle and (b) the cooling cycle.

Table 4.2 Experimentally determined phase transformation temperatures and carbide enrichment.

Alloy	$T_{S'}$ (°C)	T_L (°C)	$T_{L'}$ (°C)	T_S (°C)	Carbide enrichment	Corroboration of carbide enrichment
ABD850AM	1329	1384	1368	1264	-	-
ABD850AM+CB	1276	1351	1340	1209	Nb,Ta	-
ABD900AM	1270	1363	1347	1233	Nb, Ta	-
AM-Dev	1279	1366	1352	1229	Nb,Ta	-
CM247LC	1258	1375	1366	1266	Ta,Hf,W	[87, 94]
ExpAM	1309	1361	1344	1254	Cr,Co,Mo	-
IN625	1285	1357	1308	1234	Nb	[211, 212]
IN713	1240	1358	1341	1238	Nb,Mo	[213, 214]
IN718	1242	1342	1296	1182	Nb,Mo	[215]
IN738LC	1279	1351	1340	1200	Ta,W,Nb,Mo	[126, 216]
IN939	1203	1326	1319	1174	Ta,Nb	[217]
Waspaloy	1292	1371	1355	1265	Mo,Ti	[218]

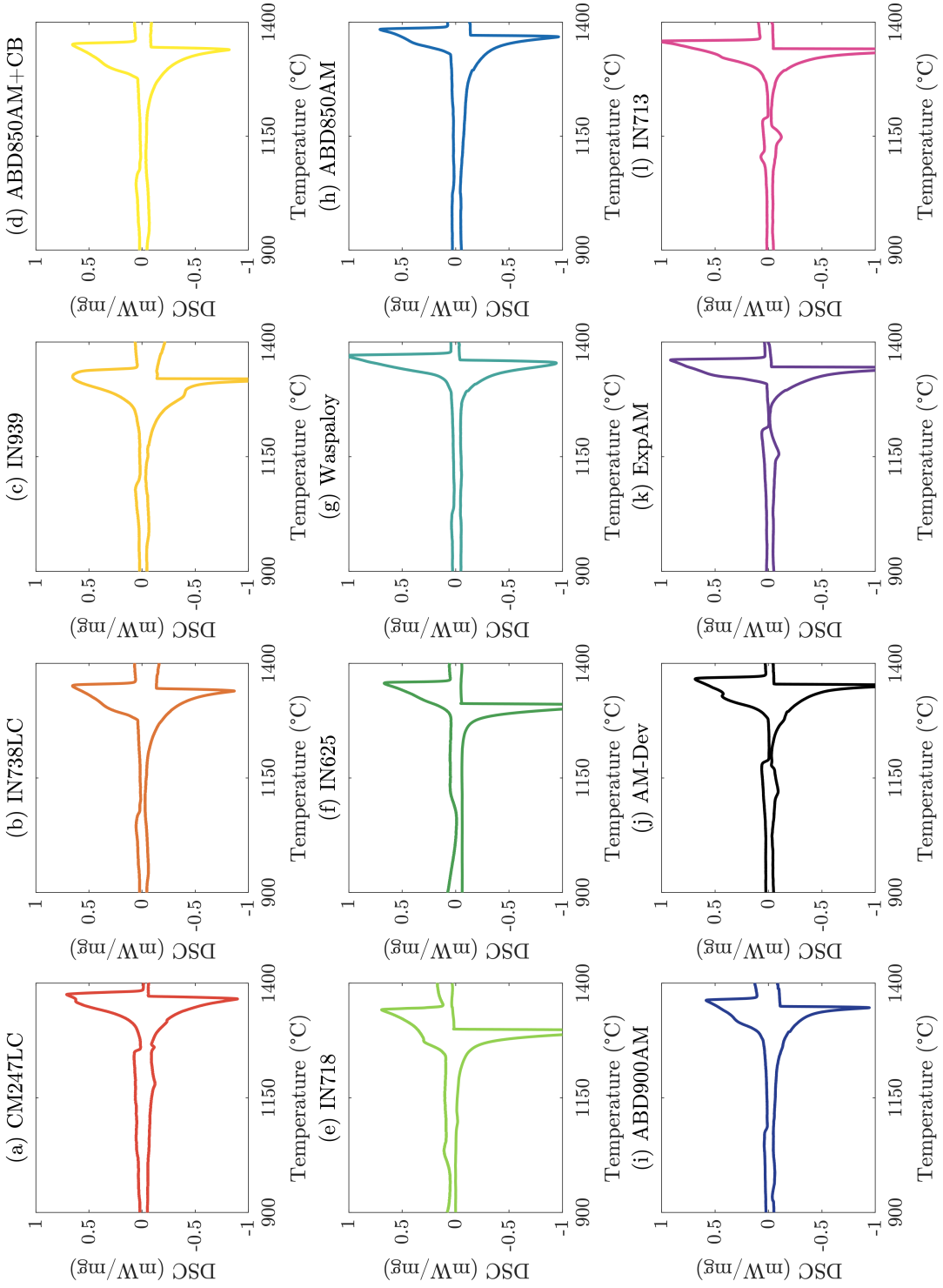

Fig. 4.19 Results of differential scanning calorimetry performed on the 12 compositions.

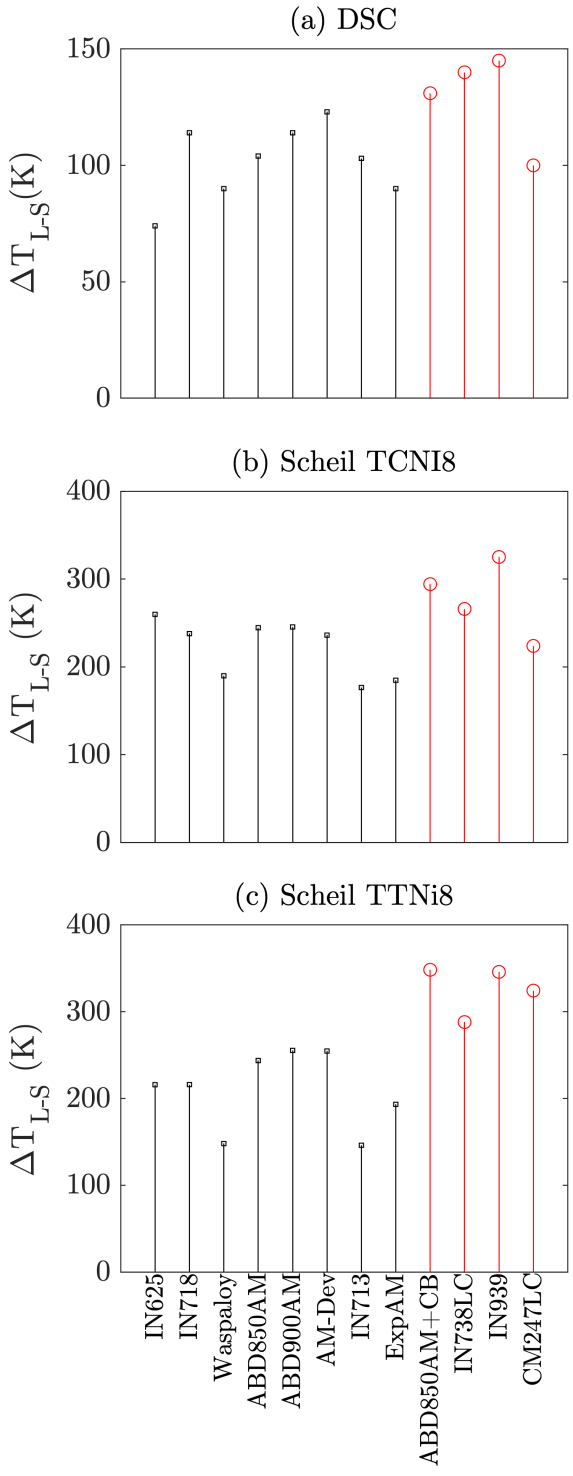

Fig. 4.20 Summary of the magnitude of the freezing range determined (a) experimentally by DSC and by scheil model using (b) the TCNI8 and (c) the TTNi8 thermodynamic databases.

4.4 Analysis and discussion

The results presented above are insightful and confirm unambiguously that a strong inter-dependence exists between processability and alloy composition. Nevertheless, further understanding can be gained via more detailed analysis. Each of the solid-state and solidification cracking phenomena is considered in turn.

4.4.1 Modelling of stress development during cooling leading to solid-state cracking

Figure 4.15 confirms that the stress experienced during cooling in the constrained-bar test depends upon alloy composition. But various factors will contribute to this to varying extents – the composition-dependence of elastic modulus and thermal expansion coefficient of Figure 4.4, but also a possible stress relaxation effect – and it is helpful to de-convolute these in order to determine which is the more important. Further experimentation has indicated that cooling rate does indeed influence somewhat the build up of stress, see Figure 4.21 which includes data for ABD850AM+CB, Waspaloy and IN939. Clearly, slower cooling provides more time for stress relaxation. Particularly for the stronger IN939 alloy, the initial rate of change of stress with temperature shows no dependence upon cooling rate, implying the need for interpretation based upon thermal-elastic-plastic behaviour with no creep relaxation playing any role in that initial regime. Figure 4.22 provides further insight into what is happening in these tests – consider the case of the least strong and most strong alloys considered here, IN625 and CM247LC respectfully. The variation of the measured stress with temperature for the two cases matches closely the product of elastic modulus, thermal expansion efficient and temperature difference $E\alpha\Delta T$ for several hundred degrees below the initial temperature of 1100 °C. Particularly for the stronger alloy CM247LC, the product

$E\alpha\Delta T$ lies below the measured uniaxial flow stress initially but surpasses it in the ductility-dip regime. For the weaker alloy IN625, the measured stress in the constrained bar test determined at low temperature matches well the measured flow stress consistent with only a weak work-hardening effect. Modelling of the constrained bar test puts the

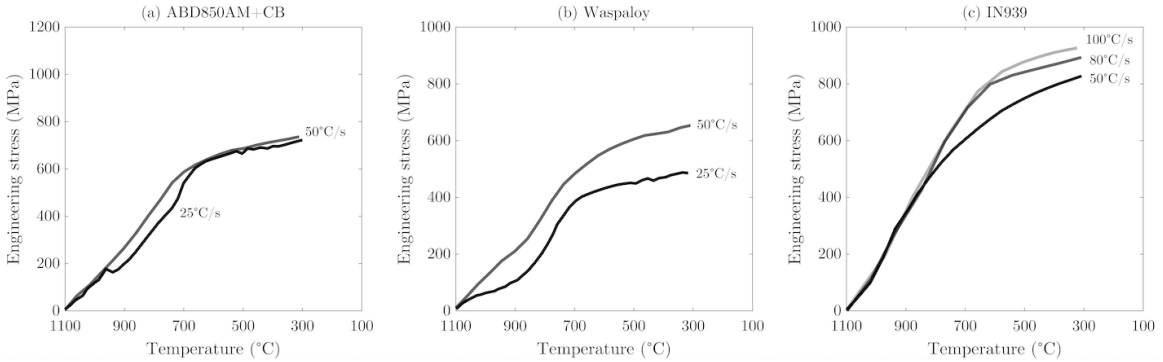

Fig. 4.21 The stress evolution during cooling at different rates in (a) ABD850AM+CB, (b) Waspaloy, and (c) IN939.

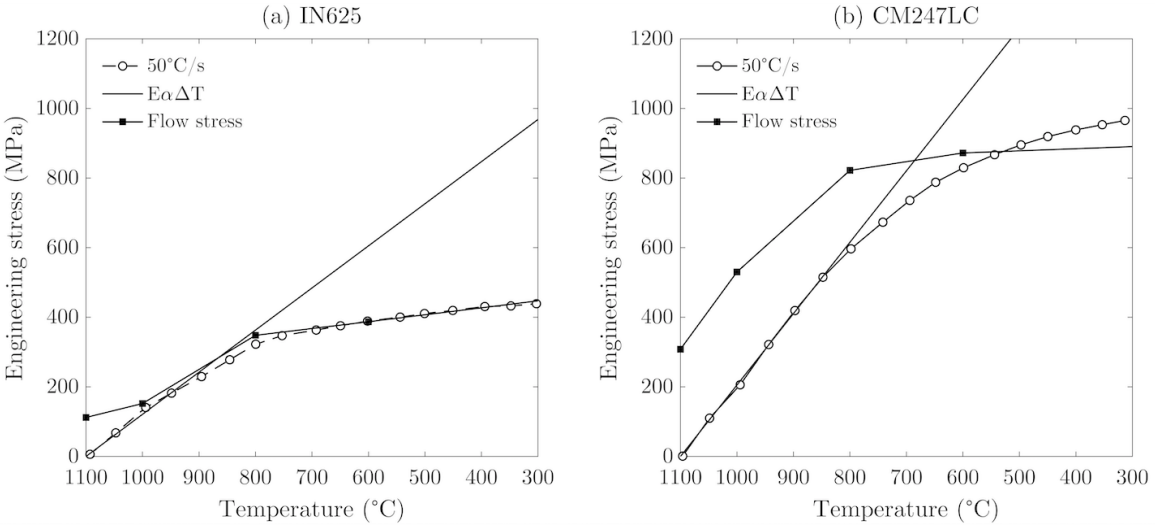

Fig. 4.22 The stress evolution during cooling at 50 °C/s superimposed with the temperature dependent flow stress and linear thermal-elastic stress development for (a) IN625 and (b) CM247LC.

thermal-mechanics of this situation on a quantitative basis. The net rate of straining is zero; therefore the rates of elastic, plastic, creep and thermal straining $\dot{\varepsilon}_{\text{elastic}}$, $\dot{\varepsilon}_{\text{plastic}}$,

$\dot{\varepsilon}_{\text{creep}}$ and $\dot{\varepsilon}_{\text{thermal}}$ must satisfy

$$\dot{\varepsilon}_{\text{elastic}} + \dot{\varepsilon}_{\text{plastic}} + \dot{\varepsilon}_{\text{creep}} + \dot{\varepsilon}_{\text{thermal}} = 0 \tag{4.2}$$

In this expression, $\dot{\varepsilon}_{\text{thermal}} = \alpha\dot{T}$ is determined by the cooling rate, it is found that as the specimen is cooled one of the mechanical strain-rates ($\dot{\varepsilon}_{\text{elastic}}$, $\dot{\varepsilon}_{\text{plastic}}$ or $\dot{\varepsilon}_{\text{creep}}$) dominates, with the range of dominance of each mechanism and therefore the detailed response depending on cooling rate and the mechanical properties of the material. Initially, the stress σ equals zero. As the sample is cooled the response is elastic and

$$\dot{\varepsilon}_{\text{elastic}} = \frac{\dot{\sigma}}{E} = -\alpha\dot{T} \tag{4.3}$$

Giving, $\sigma = \sigma_{\text{elastic}} = E\alpha\Delta T$, as shown in Figure 4.22 for IN625 and CM247LC. as the stress increases eventually creep takes over as the dominant mechanism. For a material that creeps according to Norton's Law it is expressed

$$\sigma = \sigma_{\text{creep}}\{T\} = \left(-\frac{\alpha\dot{T}}{A}\right)^{1/n} \exp\left\{\frac{Q}{nRT}\right\} \tag{4.4}$$

where R is the ideal gas constant and the parameters approximated by fitting are the creep exponent n (4.8 for both Waspaloy and CM247LC), the activation energy for creep Q (800 kJ/mol for Waspaloy and 1000 kJ/mol for CM247LC) and the pre-exponential constant in Norton's Law A ($6.1 \times 10^{-7}\,\text{MPa}^{-n}\,\text{s}^{-1}$ for both alloys). The actual stress is the smallest of those given by the elastic response and equation (4.4). The initial response is elastic, but as the sample is cooled the stress increases, creep takes over as the dominant mechanism and the stress is given by equation (4.4). For Waspaloy, which has a low creep strength at elevated temperatures, the initial elastic range is very short and creep becomes the dominant process at low stresses, as shown in

Figure 4.23a, As the temperature is decreased further the creep strength and therefore the stress given by equation (4.5) increase. In the case of Waspaloy, elastic deformation eventually dominates again. This transition occurs when

$$\dot{\sigma}_{\text{creep}} = \left(\frac{-Q}{nRT^2}\right)\left(-\frac{\alpha\dot{T}}{A}\right)^{1/n} \exp\left\{\frac{Q}{nRT}\right\} = \dot{\sigma}_{\text{elastic}} = E\alpha\dot{T} \tag{4.5}$$

Substituting (4.4) into (4.5) gives a relationship between the stress and temperature at the creep-elastic transition

$$\sigma_{\text{ce}} = \frac{E\alpha n R {T_{\text{ce}}}^2}{Q} \tag{4.6}$$

designated using the subscript ce. The actual stress and temperature a the transition is given by the intersection of equations (4.4) and (4.6) on a plot of σ against T. When $T < T_{\text{ce}}$ the response is elastic the stress is given by

$$E\alpha(T_{\text{ce}} - T) + \sigma_{\text{ce}} \tag{4.7}$$

until the onset of plastic deformation. For quantitative calculations one needs a plasticity law, taken here to be the Ramberg-Osgood relationship with σ_{y} the material's yield stress and m a material-dependent constant, fitted to be 3.4 and 3.6 for Waspaloy and CM247LC respectively, consistent with

$$\dot{\varepsilon}_{\text{plastic}} = m\frac{\dot{\sigma}}{E}\left(\frac{\sigma}{\sigma_{\text{y}}}\right)^{m-1} \tag{4.8}$$

where for simplicity it is assumed that σ_{y} does not vary with temperature. The transition to plastic deformation occurs when σ given by equation (4.4) and (4.7) equals σ_{y}. The temperature at which this occurs as is designated T_{y}. It follows that

subsequent response is given by

$$\alpha(T_{\mathrm{y}} - T) = \frac{\sigma_{\mathrm{y}}}{E}\left[\left(\frac{\sigma\{T\}}{\sigma_{\mathrm{y}}}\right)^{m} - 1\right] \tag{4.9}$$

and the stress is described as follows for $T < T_{\mathrm{y}}$

$$\sigma_{\mathrm{y}}\left(1 + \alpha\frac{E}{\sigma_{\mathrm{y}}}(T_{\mathrm{y}} - T)\right)^{1/m} \tag{4.10}$$

To summarize, the stress development during cooling can be represented by the equation set:

$$\sigma\{T\} = \begin{cases} E\alpha\Delta T & \text{if } T > T_{\mathrm{ce}} \cap \sigma_{\mathrm{elastic}} < \sigma_{\mathrm{creep}} \\ \left(-\frac{\alpha\dot{T}}{A}\right)^{1/n}\exp\left\{\frac{Q}{nRT}\right\} & \text{if } T > T_{\mathrm{ce}} \cap \sigma_{\mathrm{creep}} < \sigma_{\mathrm{elastic}} \\ E\alpha(T_{\mathrm{ce}} - T) + \sigma_{\mathrm{creep}}\{T_{\mathrm{ce}}\} & \text{if } T_{\mathrm{ce}} > T > T_{\mathrm{y}} \\ \sigma_{\mathrm{y}}\left(1 + \alpha\frac{E}{\sigma_{\mathrm{y}}}(T_{\mathrm{y}} - T)\right)^{1/m} & \text{if } T < T_{\mathrm{y}} \end{cases} \tag{4.11}$$

It has been found that the above formulation can largely rationalize the temperature-dependence of the build of stress with decreasing temperature, see Figure 4.23 for Waspaloy and CM247LC. All the above regimes of behaviour are not exhibited by all materials. In the case of Waspaloy, the initial elastic response is small and creep dominates for the slow cooling rate considered in Figure 4.23 until approximately 900 °C when the behaviour is elastic; and it becomes thermal-plastic at ∼700 °C. For CM247LC which displays much greater creep resistance, the deformation is initially linear thermal-elastic over a wide temperature regime until the onset of rate-insensitive plasticity again at ∼700 °C. In each case the temperature range over which creep occurs is small and therefore limited creep deformation occurs during cooldown. In order to compare the plastic strain accumulation to the determined composition-dependent

ductility exhaustion limit, a strain-rate independent first order approximation can be made of the plastic strain as follows

$$\varepsilon_{\text{plastic}}\{T\} \approx E\alpha\Delta T - \frac{\sigma\{T\}}{E} \tag{4.12}$$

These calculations indicate a critical minimum ductility in the range 0.5 to 1% is likely to be needed for the avoidance of ductility-dip cracking in the critical temperature range of 700 °C to 900 °C (demonstrated in Figure 4.24). These findings rationalize the poor resistance of the likes of IN713 and ExpAM to solid-state cracking.

To summarize, the analysis presented in this section allows a number of critical points to be confirmed. First, the balance of evidence suggests that solid-state cracking – in susceptible alloys – will occur in the ductility-dip regime due to the brittleness which is prevalent there. Second, since the cooling rates of the AM process are extremely rapid [18–21], the development of stress will be thermal-elastic-plastic in origin, such that for the highest strength alloys there will be little influence of stress relaxation on the composition-dependence of cracking susceptibility. Third, nonetheless the alloy composition is important: the greater the extent of alloying, the greater the stress build up to drive cracking and the greater the risk of the yield stress being exceeded in the ductility-dip regime. Thus, the cracking risk is exacerbated by greater alloy strength but for any given strength, the risk is ameliorated if the low-temperature ductility is greater. These two factors are strongly correlated via the strength/ductility relationship. Finally, the critical ductility needed to avoid solid-state cracking appears to be in the range 0.5 to 1% in the ductility dip regime. Obviously, the above applies only to solid-state cracking and ignores the solidification cracking effect which is now considered in the following section.

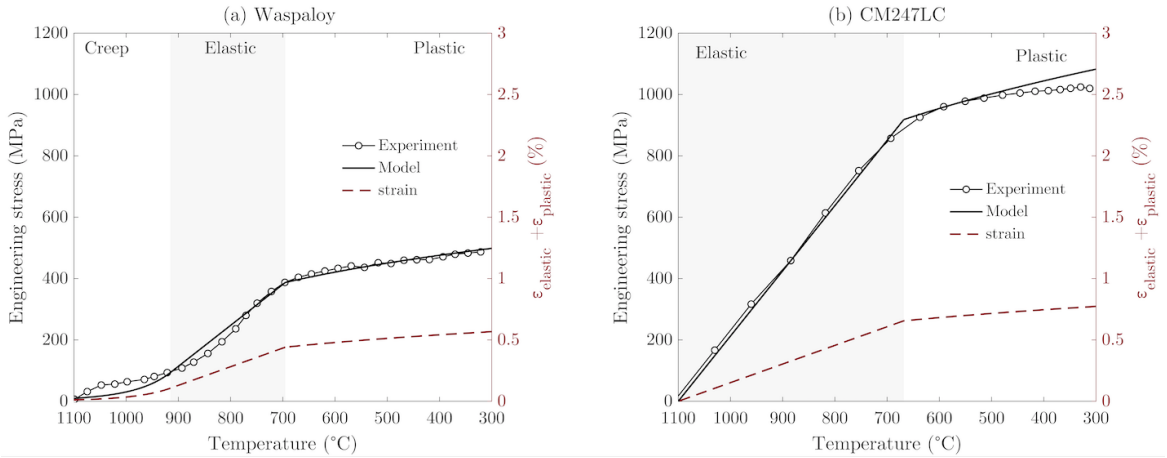

Fig. 4.23 Comparison of the experimentally measured stress during cooling and the fitted thermal-elastic-plastic-viscoplastic model for stress (left axis) and strain (right axis) development of (a) Waspaloy and (b) CM247LC.

4.4.2 Analysis of solidification cracking susceptibility

So far, the occurrence of solidification cracking has been correlated with the magnitude of the freezing range and presence of continuous films of solute enrichment at crack tips. But a number of composition-dependent solidification cracking criteria should be considered, for example those due to Clyne & Davies (CD) [116], Rappaz, Drezet, & Gremaud (RDG) [115] and Kou [219]. In each case, a parameter Φ can be identified, which is predicted to scale with cracking susceptibility. The CD approach for instance considers the dimensionless ratio of the time during solidification which the alloy is vulnerable to cracking $\Delta t_{\text{vulnerable}}$ to the time during which it can relieve the accumulated stress $\Delta t_{\text{stress relief}}$. Assuming a constant cooling rate this ratio is proportional to each respective temperature range, consistent with

$$\Phi_{\text{CD}} \propto \frac{\Delta T_{\text{vulnerable}}}{\Delta T_{\text{stress relief}}} = \frac{T_{f_s=0.99} - T_{f_s=0.9}}{T_{f_s=0.9} - T_{f_s=0.4}} \tag{4.13}$$

The CD criterion can be criticized on account of its rather arbitrary definition of the range during which the material is vulnerable; however, keeping this constant for the

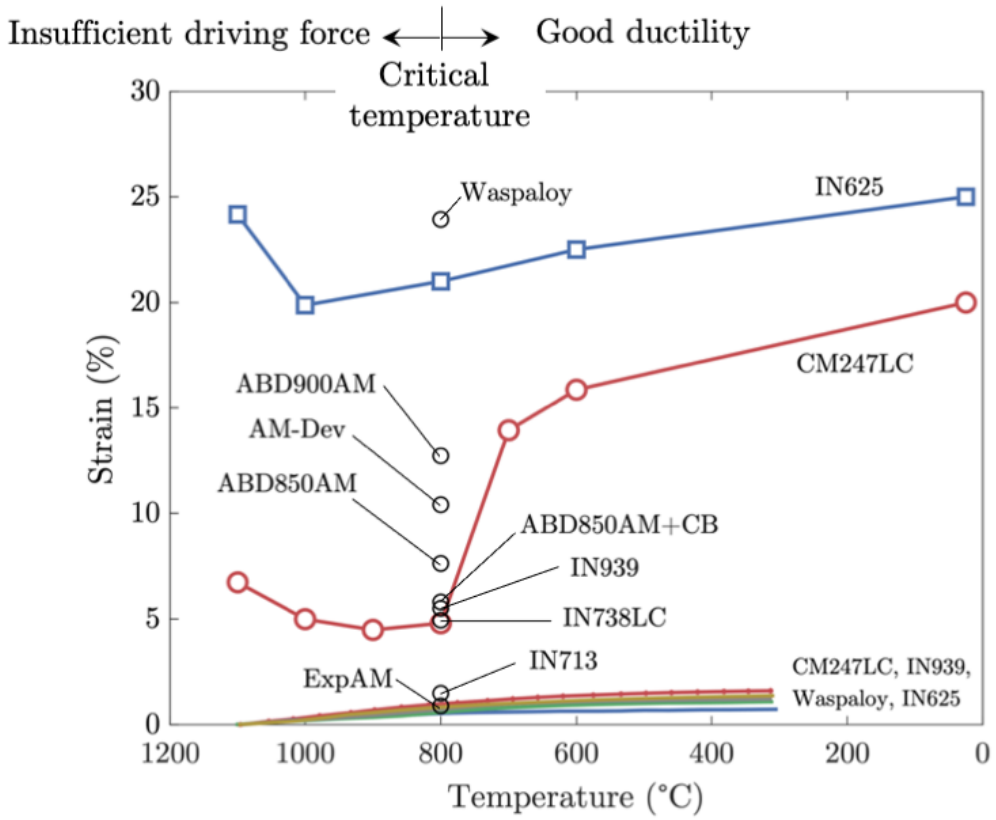

Fig. 4.24 Strain developed during constrained cooling for CM247LC, IN939, Waspaloy, and IN625 compared to the ductility limit of the 12 alloys at 800 °C and the ductility limit of CM247LC and IN625 across the full temperature range.

12 alloys allows for comparison. The alternative RDG criterion is based on a balance of pressure, such that the formation of hot tears depends upon the maximum strain rate $\dot{\varepsilon}_{\max}$ before a cavitation pressure Δp_c results in the formation of a void. Both the mechanical contribution and the ability for liquid to back fill are dictated by integrals of the solid fraction vs temperature $f_s(T)$, A, B, and C [115] consistent with

$$\Phi_{\mathrm{RDG}} \propto \frac{1}{\dot{\varepsilon}_{\max}} = \frac{(1+\beta)B}{G}\left[\frac{\Delta p_c G \lambda_2^2}{180\mu} - v_T \beta A\right]^{-1} \tag{4.14}$$

where

$$A = \int_{T_{cg}}^{T_L} \frac{f_s\{T\}^2}{(1-f_s\{T\})^2} \mathrm{d}T \tag{4.15}$$

and

$$B = \int_{T_{\mathrm{cg}}}^{T_{\mathrm{L}}} \frac{C}{(1 - f_{\mathrm{s}}\{T\})^3} \mathrm{d}T \tag{4.16}$$

where

$$C = f_{\mathrm{s}}\{T\}^2 \int_{T_{\mathrm{cg}}}^{T_{\mathrm{L}}} f_{\mathrm{s}}\{T\} \mathrm{d}T \tag{4.17}$$

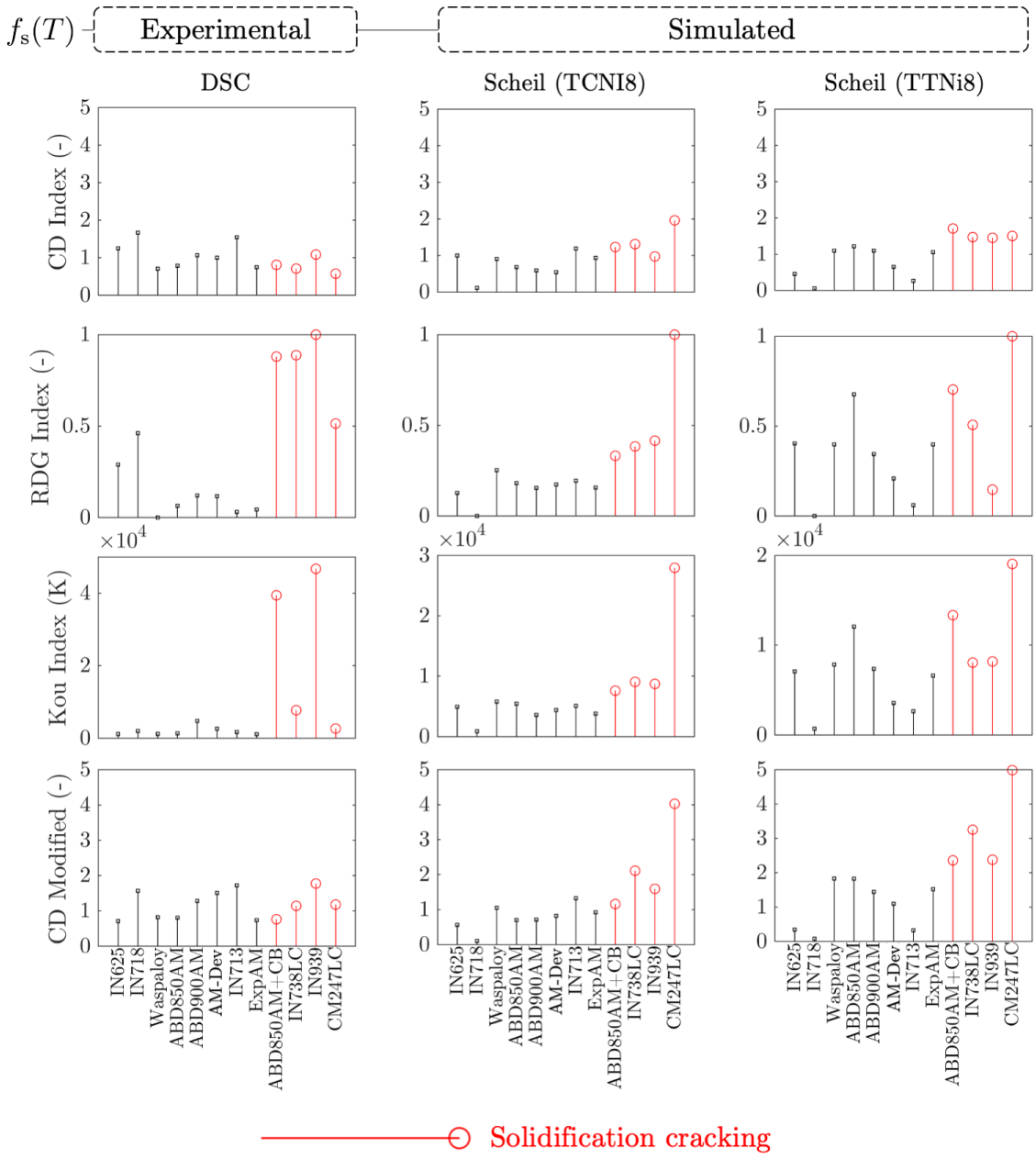

Fig. 4.25 Solidification cracking susceptibility as predicted by the Clyne-Davies criterion, the Rappaz-Drezet-Gremaud criterion, the Kou criterion, and a modified Clyne-Davies criterion, each determined as a function of the solidification path determined experimentally and via scheil with the TCNI8 and TTNi8 databases.

For the calculations carried out here, the viscosity μ, the thermal gradient G, the velocity of the isotherms v_T, and the shrinkage factor β have been taken from [115],

the secondary arm spacing λ_2 from [9]. The grain coalescence temperature T_{cg} is taken to correspond to $T_{f_s=0.99}$. The hot cracking susceptibility is proportional to $\dot{\varepsilon}_{\mathrm{max}}^{-1}$ and values are normalized between zero and unity. The RDG criterion suffers from a similar criticism to the CD criterion, as the grain coalescence temperature – critical to evaluating the integrals A, B and C – is not well understood. Furthermore, approximating liquid filling by the flow of fluid through a packed bed may not be the most appropriate for the cellular AM microstructures. Finally, the Kou solidification cracking index is formulated around the balance of increasing spatial dimensions associated with solid formation and volumetric liquid flow within a differential control volume between two growing grains [219]. Here, the cracking susceptibility is taken to be proportional to the maximal value of the ratio of change in temperature $\mathrm{d}T$ relative to the change in square root in the solid fraction $\mathrm{d}(\sqrt{f_{\mathrm{s}}})$ near the final stages of solidification, consistent with

$$\Phi_{\mathrm{Kou}} \propto \left| \frac{\mathrm{d}T}{\mathrm{d}(\sqrt{f_{\mathrm{s}}})} \right|_{f_{\mathrm{s}} \to 1} \tag{4.18}$$

Figure 4.25 summarizes the predictions of the different criteria considered. One can see that, with the exception of the CD index evaluated with the experimentally-evaluated DSC traces (which probably gives an underestimate of the solidification range) – the indices are in line with the findings of the experimentally-determined solidification cracking susceptibility. However, no single index predicts correctly the composition-dependence of solidification cracking for all methods of determining $f_{\mathrm{s}}\{T\}$. Moreover, no one method of estimating $f_{\mathrm{s}}\{T\}$ correctly predicts solidification cracking across all the indices. The strength of applying these legacy criteria to multi-component Ni-superalloys is their sensitivity to the final stages of solidification whereby the final liquid is solute enriched and stable at lower temperatures. This in turn presents a problem, as $f_{\mathrm{s}}\{T\}$ is discontinuous when a new phase becomes stable, making the

exact numerical procedure by which the Kou criterion is evaluated highly sensitive to these discontinuities.

One can argue that a modified criterion is needed to take account of contributions of mechanical and stress relaxation properties. A very detailed analysis is beyond the scope of this paper, but approximate calculations can be made as follows. Assume the contribution of stress relaxation is more pronounced at near solidus temperatures as is suggested by the strong temperature dependence of stress relaxation of Figure 4.14. A modified criterion could consider the solidification cracking susceptibility to be proportional to the ratio of strain accumulated during the vulnerable regime $\alpha\Delta T_{\text{vulnerable}}$ to the strain relieved in the stress relief regime. This is applied as shown in Equation 4.19 using experimentally determined values of E, and α, and the $\mathrm{d}\sigma/\mathrm{d}t$ derived from the secant line of the stress relaxation behaviour from 0 to 30 s at 1000 °C, according to:

$$\Phi_{\text{CD modified}} \propto \frac{\varepsilon_{\text{vulnerable}}}{\varepsilon_{\text{stress relief}}} = \frac{\alpha\Delta T_{\text{vulnerable}}}{\left(\frac{\dot{\sigma}}{E}\right)\frac{\Delta T_{\text{stress relief}}}{\partial T/\partial t}} \tag{4.19}$$

This is in essence a mechanically-weighted CD index. The modified index increases the relative predicted susceptibility of the solidification cracking alloys IN738LC, IN939, and CM247LC appreciably, see Figure 4.25, by accounting for thermal expansion, stiffness and the capacity of the material to stress relax.

4.5 Final considerations

An intriguing aspect of the as-processed microstructures produced in the present work is the absence of the γ' phase due to the suppression of the $\gamma \rightarrow \gamma + \gamma'$ reaction caused by the rapid cooling rates achieved. It follows that the varying strength levels measured arise from different degrees of solid-solution hardening, since the same processing parameters yield similar in-plane grain size distributions and thus approximately

similar degrees of sub-structure hardening via the Hall-Petch effect. Thus one has a very supersaturated solution of hardening elements present in significant concentrations in the matrix γ phase. For this situation, there is a complete paucity of information in the literature for the relative contributions of the elements to the strengthening levels achieved in this situation. Although measurements have been made on just 12 different alloys in this work, it has proven possible to come to interesting findings in the following way. Assume that the contributions to the strengthening of each element i via a coefficient k_i can be summed according to a simple model consistent with [220]

$$\sigma_{\text{solid solution}} = \left(\sum_i k_i^{\frac{1}{n}} x_i \right)^n \tag{4.20}$$

where x_i the concentration of solute i, k_i is the respective strengthening constant and the value of n is taken as 2/3 [220]. A multi-regression fitting procedure then allows an estimate of the values of k_i, see Table 4.3. The values obtained are compared with those determined by Roth et al [26] on much more dilute alloys, via a trawling of the literature. Similar trends are observed, which lends confidence to the strength measurements. When the coefficients k_i are plotted as a function of the location of element i in the d-block of transition metals, one sees that the elements from the far-west of the d-block confer a greater degree of hardening, on an atomic percent basis. Moreover, it would appear that the extent of hardening for each column in the d-block is consistent with 5d > 4d > 3d, see Figure 4.26. The data is sparse, but these findings are worthy of future investigations along these lines.

Despite previous work having suggested that improving the solid solution strengthening can improve processability [176], the research presented here indicates that it is the exhaustion of ductility – not strength – which must be conferred for crack-free printing if the best strength levels are to be approached. This is summarized succinctly in Figure 4.28. Plotting the alloys' ductility vs cracking severity indicates alloys be-

Table 4.3 Strengthening coefficients for solution strengthening in Ni for AM at 800 °C in comparison to [26] (MPa at. Fraction$^{1/2}$).

Alloying Element	k_i^{AM}	k_i [26]
Al	1787	225
Co	43	39
Cr	285	337
Fe	-	153
Mo	795	1015
Nb	1155	1183
Ta	3736	1191
Ti	1438	775
W	1813	977
C	5355	1061
Hf	-	1401

come unprocessable when their ductility is less than 7%, though it should be noted that it would appear to be possible to achieve strength levels comparable to those of CM247LC without embrittlement. In general, a strength/ductility trade-off is apparent as the macroscopic elongation in the ductility-loss regime (∼800 °C) is governed by the balance of plasticity of grain interiors and the cohesion of grain boundaries. For very strong alloys – such as CM247LC and ExpAM – the failure mechanism is purely intergranular – see Figure 4.27 – implying grain boundaries are the ductility-limiting feature of the unprocessable alloys. Whereas for alloys such as IN718 and IN625, the fracture surfaces show only transgranular features such as those due to micro-void coalescence – suggesting grain boundaries are sufficiently cohesive, making the grain interior the ductility-limiting feature. The fracture surfaces of the moderate ductility ABD alloys such as ABD850AM and 1005AM are somewhere in between: they exhibit features characteristic of both intergranular and transgranular fracture, see Figure 4.27, further examples can be found in Figure A.3 of Appendix A. Further experimental evidence supporting this is given in Figure A.4 of Appendix A, where the side profiles

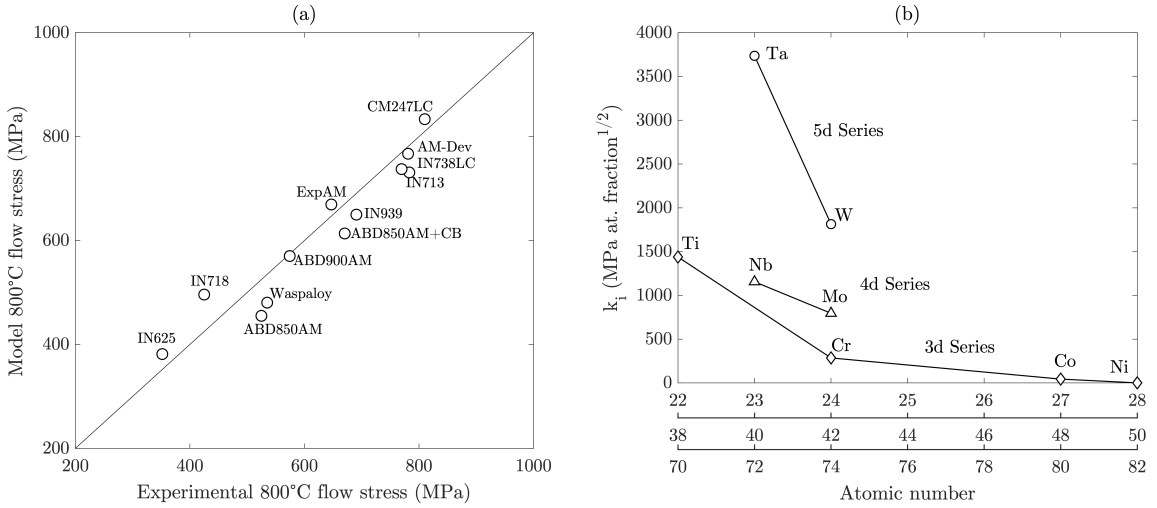

Fig. 4.26 (a) Comparison of the experimentally determined flow stress and the solid solution strengthening model at 800 °C and (b) strengthening coefficients as a function of atomic number for solutes in the 3d, 4d, and 5d groups.

of the 800 °C tensile specimens give an indication of the extent to which cavitation took place and if strain was accommodated within the grain or at the grain boundary.

This work finds that despite the presence of such carbides in the processable and ductile Nb/Mo-rich carbide forming alloys IN625, IN718 and the ABD alloys, their occurrence in the un-processable IN713 alloy suggests that carbide enrichment alone does not guarantee grain boundary properties. An analysis of the influence of composition on the 800 °C ductility by multiple linear regressions can be found in Figure A.5 of Appendix A. It seems likely that the ratio of grain boundary strength to grain strength – in this case controlled by the contribution of elements in solid solution – dictates the extent to which fracture is inter- or intragranular. These need to be balanced to maximize performance whilst maintaining processability. Clearly, further advances in the field of grain boundary engineering are needed if further improvements in property levels are to be achieved.

Fig. 4.27 Fracture surfaces of CM247C, AM-Dev, and IN625 after tensile tests at 800 °C illustrating the transition from intra/transgranular to intergranular fracture.

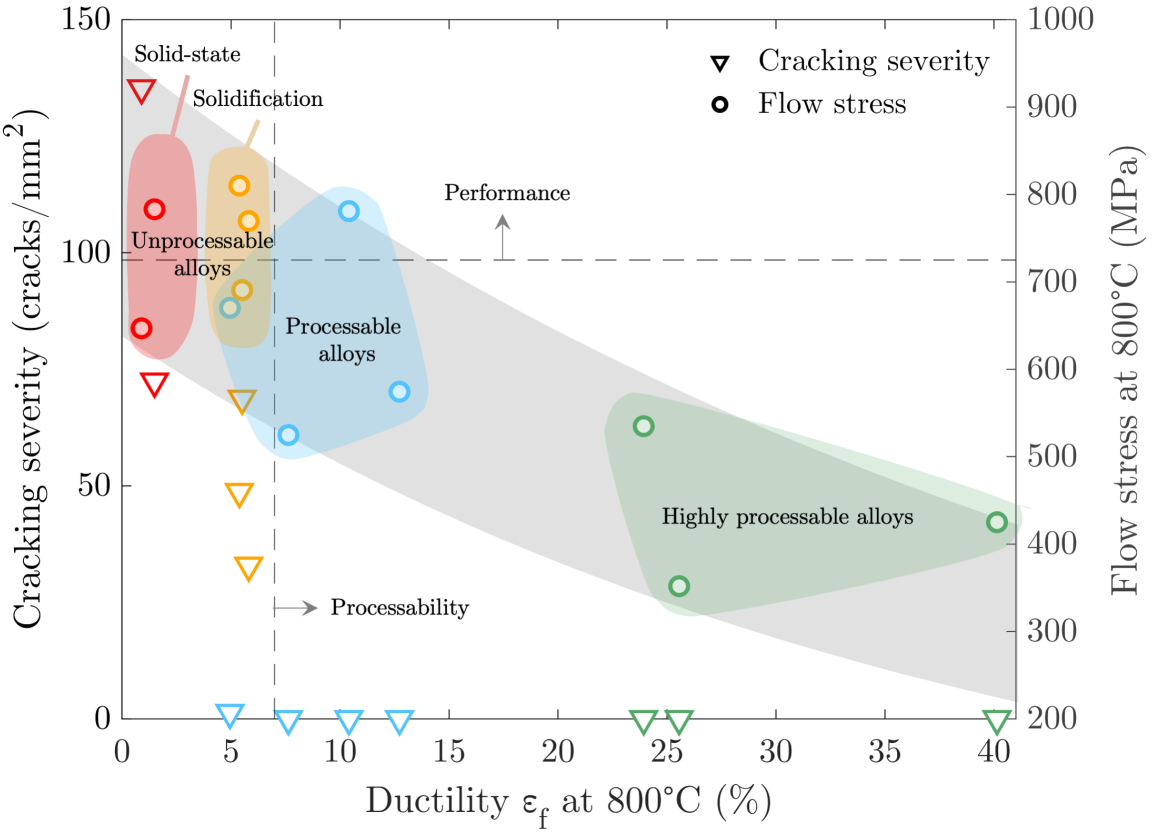

Fig. 4.28 Processing map demonstrating four classes of alloys based upon measurements of their cracking severity (left axis) and flow stress at 800 °C (right axis) as a function of their the ductility at 800 °C.

4.6 Summary and conclusions

In this paper, the additively manufacturability of nickel-based superalloys has been considered in detail. The laser powder bed fusion technique is used. Twelve different alloys have been studied, some of the heritage type but also some new ones designed specifically for this process. Emphasis has been placed on the influence of composition on cracking susceptibility. The following specific conclusions can be drawn from this work:

On the influence of alloy composition on the additive manufacturability of Ni-based superalloys

1. A dependence of alloy composition on processability has been proven. Of the twelve alloys studied, quantitative stereology confirmed that half are susceptible to processing-induced crack defect formation under the experimental conditions employed. In particular, IN713 and ExpAM compositions were shown to be prone to solid-state cracking, whilst CM247LC, IN738LC, ABD850AM+CB and IN939 exhibited a tendency towards solidification cracking.

2. Solid-state cracking arises from a significant loss of tensile ductility at 800 °C (<7%) which was prevalent in all unprocessable alloys – as exemplified in particular by the IN713 and ExpAM alloys for which it was <1%. Stereological analysis indicates that this brittleness is intergranular in form implying grain boundary weakness and exacerbated by increased γ' former content.

3. A thermal-elastic-plastic-viscoplastic analysis of a 1D constrained bar has shed light on the factors exacerbating solid-state cracking. It seems likely that this effect is not strongly affected by creep-driven stress-relaxation, under the cooling rates experienced. Instead, processing is compromised by brittleness in the ductility-dip regime. Nevertheless, at any given strength level it appears to be possible to find alloys which are processable, and others which are not.

4. When solidification cracking occurs, it is in alloys that freeze over a wide temperature interval and relieve stress (by creep processes) at a slower rate. Increased C content and the presence of of Hf/Ta enriched crack tips is characteristic of the alloys which cracked by the solidification mechanism.

5. Solidification cracking criteria following Clyne-Davies, Rappaz, and Kou have been considered as a means of rationalizing these findings concerning solidification cracking; these are shown to have predictive power. However, they do not account for the composition-dependent near-solidus mechanical properties which may be

important for the stress relaxation processes needed for crack-free processing. A modified Clyne-Davies model is proposed to account for this.

6. The processing/performance relationships of existing and newly designed alloys have been compared. It has been shown that the strength levels of the former can be approached whilst engendering the AM processability which is apparently lacking.

7. These results suggest pathways by which the new alloys may be further improved. Since creep relaxation does not seem to play a role in the solid-state cracking phenomena, it might prove possible to design alloys of creep resistance equivalent to the very best conventionally-cast grades which are amenable to AM processing, provided that they resist solidification cracking.

Chapter 5

On the influence of composition on the performance of additively manufactured Ni-based superalloys

5.1 Introduction

As discussed in previous chapters, the Achilles' heel of 3D printing superalloys is the propensity for processing-related defects to occur [86]. Defects include porosity [150], solidification cracking [105] and solid-state (ductility-dip) cracking [221]. Such susceptibility is a disadvantage because conventional processing – involving investment casting for example – has evolved over many years to be a low and defect-free route with which 3D printing must compete [222]. Its inherent advantages such as a strong coupling to computer-aided design technology help in this regard [223].

What are the factors which might accelerate the insertion of 3D printing into a modern manufacturing economy? One approach involves tailoring the process through better understanding of the heat transfer and thermal-mechanical effects arising. The use of pre-heating [224] or multiple heat sources [225] are good examples of this first

strategy. Alternatively, one can improve the input material employed as feedstock, arguing that a new process such as 3D printing will require new grades of alloy to be designed and proven – as emphasized in Chapters 3 and 4. There is evidence that this second approach has merit [180, 226]. Alloy design approaches are emerging for this purpose [14, 9]. Nevertheless, work of the type reported here is needed to assess the effectiveness of the modelling strategies. Are the compositions designed by the computer modelling truly superior? The only way to confirm this is via vigorous fair-minded programmes of experimentation.

In this chapter, we examine the processing and performance of a new grade of superalloy for high temperature applications. Three distinct attributes are considered: processability, heat treatment response and finally mechanical behaviour. In this way, a holistic picture of the processing/property relationship is built up. We make use of a benchmark, CM247LC, which is a widely available heritage alloy usually processed using conventional investment casting. The performances of three variants of the new alloy are compared with that of CM247LC. Consistent with the intended applications of these materials, the high temperature properties are emphasised particularly in creep and oxidation; the low temperature strength in the athermal regime is also considered.

5.2 Experimental methods

5.2.1 Alloy compositions and feedstock materials

A new Ni-based superalloy designed for AM has been studied. The alloy was designed using the Alloys-by-Design (ABD) method [189, 227], allowing for a multi-objective optimization of various property trade-offs. In this case, the alloy processability as well as the creep resistance, oxidation resistance, predicted maximal theoretical strength, and density have been considered, several examples of these design trade-offs are shown

in Figure A.6 of Appendix A. Three variants of the alloy named Alloy 1, Alloy 2, and Alloy 3 were selected on the basis of these criteria. These three compositions have equal equilibrium γ' volume fraction at 900 °C, but possess varying (Nb+Ta)/Al ratios. This allowed for a novel experimental study of how the enrichment of γ' with either Al or Nb+Ta altered the microstructure-properties relationships. The equilibrium γ' volume fraction as a function of temperature for each composition was predicted by Thermo-Calc employing the TTNi8 database [205]. Alloy 3 had the greatest Nb and Ta content with reduced Al content, Alloy 1 had greatest Al content with reduced Nb and Ta, and Alloy 2 had a middling (Nb+Ta)/Al ratio. These are bench marked against the popular CM247LC alloy.

Table 5.1 Compositions of the alloy powders (at.%).

Alloy	Ni	Al	Co	Cr	Mo	Nb	Ta	Ti	W	C	B	Hf	(Nb+Ta)/Al
Alloy 1	bal.	9.5	33.4	8.4	0.62	1.1	0.89	0.12	1.8	0.15	0.02	-	0.21
Alloy 2	bal.	8.6	33.5	8.5	0.62	1.5	1.24	0.13	1.9	0.15	0.02	-	0.32
Alloy 3/AM-Dev	bal.	7.8	34.2	8.4	0.64	1.9	1.53	0.13	1.9	0.13	0.02	-	0.43
CM247LC	bal.	10.9	17.8	8.5	0.31	-	0.95	0.82	2.8	0.31	0.10	0.42	

The pre-alloyed argon gas atomised feedstock powders were prepared by Aubert & Duval with median particle diameter (D50) between 32.3 and 33.0 µm. The D10 and D50 values were ∼19 and 55 µm respectively. The measured alloy powder compositions, as determined by inductively coupled plasma-optical emission spectroscopy (ICP-OES) and ICP-combustion analysis, are given in Table 5.1. The powder particles were spherical, with a small number of satellites and other morphological irregularities present.

5.2.2 Processing by additive manufacturing

Laser-powder bed fusion (L-PBF) was carried out in a Renishaw AM 400 pulsed fibre laser system of wavelength 1075 nm under an argon atmosphere with a build plate

size of $80\times80\times64\,\mathrm{mm}^3$. The processing parameters employed were: laser power 200 W, laser focal spot diameter 70 µm, powder layer thickness 30 µm, and pulse exposure time 60 µs. A 'meander' laser scan path pattern was used with hatch spacing of 70 µm and laser scan speed of 0.875 m/s, the path frame of reference was rotated by 67 ° with each layer. In order to produce a high quality surface finish, the laser traced the border of the sample after each layer, the laser speed on the borders was reduced to 0.5 m/s. Each powder was processed with identical parameters as these had previously been investigated and determined to be suitable for minimizing cracking in this Ni-based alloy system [178]. Operation of the apparatus was performed by William Dick-Cleland.

For each alloy, the same build plate configuration was employed comprising several geometries. Cubes of dimensions $10\times10\times10\,\mathrm{mm}^3$ were printed for microstructural characterization and for the preparation of oxidation test coupons. Vertical bars of dimensions $10\times10\times52\,\mathrm{mm}^3$ were printed and were used for the machining of mechanical test pieces. These bars were manufactured with 16 inverted pyramid legs in order to allow for easy removal from the baseplate. Discs of diameter 3 mm and height 1 mm were produced differential scanning calorimetry (DSC). The turbine blade shaped-parts were printed to simulate the manufacture of an engineering component; in this case representative of those used in a helicopter engine, these had a height of 30 mm.

5.2.3 Materials characterization

Optical and scanning electron microscopy (SEM)

Optical microscopy was used to assess the cracking susceptibility. The cube samples were sectioned on planes parallel (termed XZ) and perpendicular (termed XY plane) to the build direction. For the XY plane, a section was taken at the mid-height. The severity of cracking was determined by imaging the XY plane; 5 images were considered per alloy. The ImageJ software [228] was used to compare the alloys by determining

the crack count density (cracks/mm^2) and crack length density (mm/mm^2) – note that the crack length was defined as the caliper diameter corresponding to the largest line length across each crack. The microstructure was investigated in the as-printed, heat treated, and oxidized condition using backscattered electron (BSE) imaging and energy dispersive X-ray spectroscopy (EDX) in a Zeiss Merlin Gemini 2 field emission gun scanning electron microscope (FEG-SEM) equipped with an Oxford Instruments XMax 150mm/mm^2 energy-dispersive detector and a electron backscattered diffraction (EBSD) system. EDX maps were acquired using accelerating voltage of 10 kV and probe current 500 pA. Samples were electrolytically etched to remove the γ matrix using 10% phosphoric acid at 3 V direct current in order to observe the γ' size, distribution, and morphology.

Atom probe tomography (APT)

The Alloy 3 cube was cut into rectangular prism matchsticks of dimensions $10\times1\times1$ mm^3 using a Struers Accutom-50 and alumina saw. These were prepared for atom probe analysis through electrochemical polishing in a solution of 25 % perchloric acid and 90 % acetic acid with voltage of 25 V. A second stage of polishing to finalize the tip was done in a solution of 2 % perchloric acid and 98 % butoxyethanol with voltage of 20 V. Specimens were analysed using a Cameca LEAP 5000XR system with detection rate of 52 % and laser wavelength 355 nm. Samples were cryogenically cooled to 50 K inside an ultra high vacuum chamber at $< 4\times10^{-11}$ Torr. Laser mode was employed at a pulse frequency of 200 Hz and energy 50 pJ. The datasets were reconstructed using Integrated Visualization and Analysis Software (IVAS). Due to the laser mode, the crystallographic poles could not be used for more accurate spatial calibration; the parameters used were geometric field-factor of 3.5, image compression factor (ICF) of

1.55, and an initial cap radius of 25 nm. Sample preparation and operation of the atom probe was performed by Dr. Przemysław Klupś.

X-ray computed tomography (XCT)

X-ray computed tomography of the turbine blade-shaped samples was carried out by Dr. Katy Rankin with a custom Nikon XTEK XTH 225 kVp micro-focus CT system fitted with a 2000×2000 pixel Perkin Elmer XRD 1621 CN14 HS Detector (PerkinElmer Optoelectronics, Germany). In order to detect the micron length scale defects characteristic of L-PBF a slice of the top 1 mm of the miniature turbine blade was machined by wire electrical discharge machining (EDM) for analysis. Three separate XCT scans were performed on each sample which were concatenated together to maximise the voxel (volume element or cubic pixel) resolution achievable for the entire length.

Scans were performed at 210 kVp peak voltage and 42 µA current, with a source to object distance of 17 mm and an source to detector distance of 797 mm. Using an analogue gain of 24 dB, 3142 projection images were acquired throughout 360 degrees rotation, averaging 8 frames per projection with 1 s exposure time per frame. Projection images were reconstructed into 32 bit float volumes using filtered back-projection algorithms implemented within CTPro3D and CTAgent software v2.2 (Nikon Metrology, UK). These were converted to 8 bit and had a threshold applied manually, and the defects were quantified in terms of size distribution – where size is defined by defect volume using the 3D objects counter in ImageJ. A further analysis of a $\sim$500×500×500 µm^3 sub-volume in the bulk of the CM247LC was carried out to understand the crack morphology in 3D.

Table 5.2 Summary of phase transformation temperatures determined experimentally.

Alloy	Solidus (°C)	Liquidus (°C)	γ' dissolution temperature (°C)	Carbide dissolution temperature (°C)
Alloy 1	1304	1379	1172	1344
Alloy 2	1292	1371	1179	1335
Alloy 3/AM-Dev	1278	1366	1182	1331
CM247LC	1265	1375	1249	1365

Table 5.3 Heat treatment process's applied to Alloy 2.

Process	Stage 1	Stage 2	Stage 3
HT 1 (super-solvus)	1220 °C 2 h AC	1100 °C 4 h AC	850 °C 20 h AC
HT 2 (sub-solvus)	1100 °C 4 h AC	850 °C 20 h AC	-
HT 3 (sub-solvus)	1080 °C 4 h AC	-	-

5.2.4 Differential scanning calorimetry and heat treatment

In order to design suitable heat treatments, differential scanning calorimetry (DSC) was first used to determine the heat treatment window. A NETZSCH 404 F1 Pegasus instrument with a nitrogen cover gas flowing at 50 ml/min was employed. Samples were heated to 700 °C at 20 °K/min, then from 700 °C to 1450 °C at 10 °K/min. The thermophysical characteristics derived from the DSC signal during heating were the γ' dissolution temperature, solidus, liquidus, and the carbide dissolution temperature. The γ' and carbide dissolution temperatures were determined by their respective inflexions apparent in the DSC signal. The solidus and liquidus on heating were estimated following Chapman and Quested [192, 193]. Figure 5.1 shows the DSC trace and the simulated equilibrium γ' fraction as a function of temperature. The phase transformation temperatures of interest upon which the heat treatments were developed are summarized in Table 5.2.

Super-solvus and sub-solvus heat treatments (HT) designated HT 1 and HT 2 respectively were performed on Alloy 2 on the basis of the measured γ' solvus temperature. These are summarized in Table 5.3, each heat treatment step was followed by air

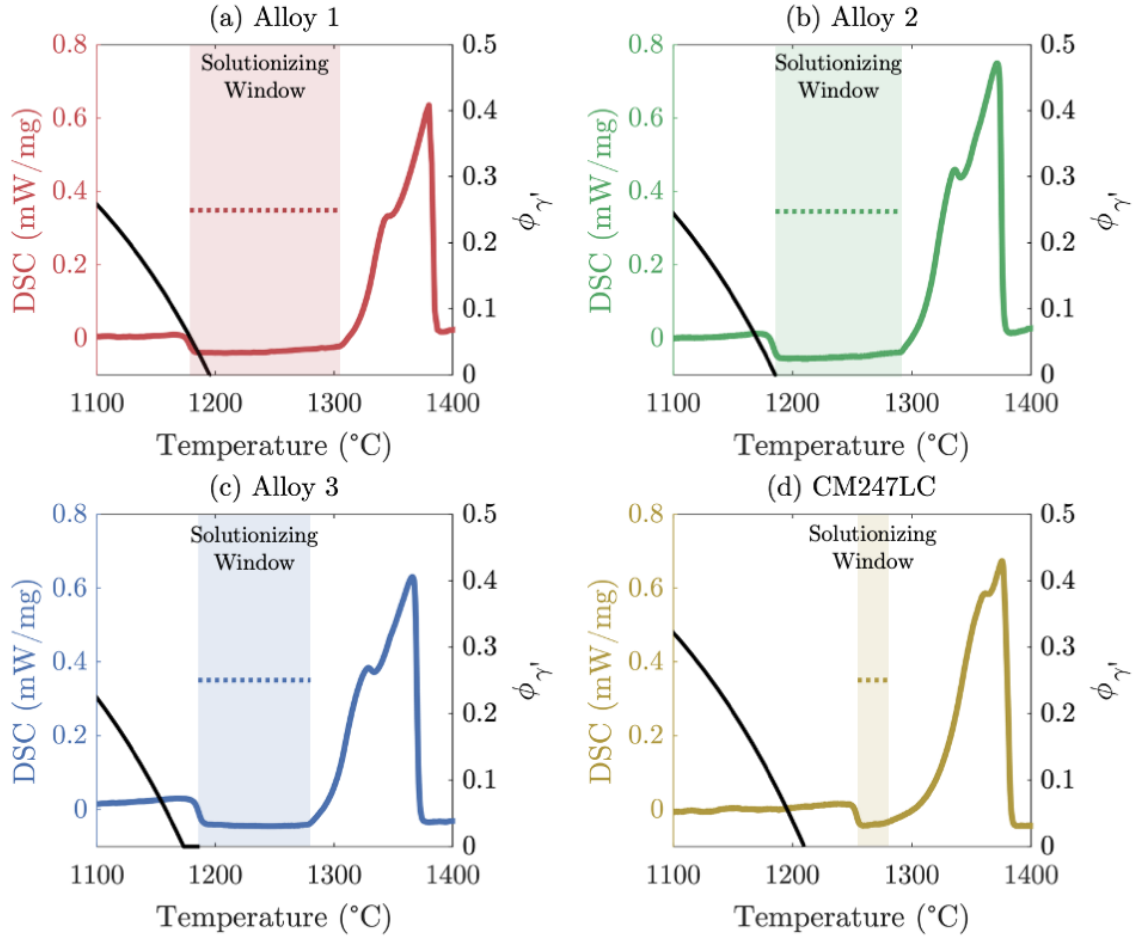

Fig. 5.1 Results of differential scanning calorimetry upon heating of (a) Alloy 1 (b) Alloy 2 (c) Alloy 3 (d) CM247LC with superimposed equilibrium γ' volume fraction ($\phi_{\gamma'}$) predicted by Thermo-Calc.

cooling (AC). Following microstructural analysis – shown in Figure 5.5 – a further sub-solvus heat treatment (HT 3) was applied to Alloy 2 in an attempt to generate a more bi-modal distribution of γ' precipitates. This was done by choosing a heat treatment temperature of 1080 °C, which was ∼100 °C below the solvus temperatures of the novel compositions.

5.2.5 Oxidation study

Thermo-gravimetric analysis (TGA) was used to assess the oxidation resistance of the alloy, using a NETZSCH STA 449 F1 Jupiter. Specimens of dimensions 10 mm×10 mm×1 mm were cut perpendicular to the build direction and polished to a mirror finish with 4000 grit SiC paper. The tests were carried out in 5 steps, initially a the protective Ar gas flow is run for 1 h to ensure equilibrium of the system. This was following by a increase of temperature by 20 K/min to the test temperature of 1000 °C followed by another hold for 30 min under protective Ar and then the onset of the oxidizing laboratory air flow at 50 ml/min for 24 h, after this period the sample is cooled to room temperature at 20 K/min. The evolution of mass gain was analysed starting at the onset of oxidizing air.

5.2.6 Thermo-mechanical testing

Tensile properties

Isothermal uniaxial tensile tests were performed using a 5 kN Instron electro-thermal mechanical testing (ETMT) machine. Specimens of full length 40 mm, gauge length 14 mm, and 1 mm^2 cross sectional area were machined with axis along the build direction from the additively manufactured bars by wire electrical discharge machining (EDM), and polished to mirror finish 4000 grit SiC paper to negate the influence of EDM induced surface defects. The strain was measured via a non-contact iMetrum digital

image correlation system. Joule heating under free expansion conditions was employed to reach the test temperatures using a heating rate of 200 K/s. The temperature was measured by spot-welding a K-type thermocouple to the center of specimen gauge.

The 4 compositions were tested at room temperature and in the range of 600-1100 °C in increments of 100 °C. Specimens were strained rapidly at a rate of $10^{-2}\,s^{-1}$ to reduce the influence of dynamic precipitation during testing and facilitate high-throughput experimental work. At all temperatures the flow stress respectively were taken as the 0.2% proof stress. The sub-solvus and super-solvus properties of Alloy 2 were additionally compared across the temperature range by testing at a strain rate of $10^{-3}\,s^{-1}$.

Creep testing

For each alloy, bars of dimensions $10\times10\times52\,mm^3$ were heat treated and machined into specimens for creep testing. Bars were heat treated at 1080 °C for 4 h and air cooled. The selection of this sub-solvus heat treatment is elucidated in the results section. Bars were machined and tested externally by the accredited laboratory Westmoreland Mechanical Testing & Research Ltd. in accordance to ASTM E139. Samples were machined with gauge length of 20 mm and full length of 52 mm. Creep tests were performed at temperatures ranging between 800 °C and 1050 °C at various stress levels between 180 MPa and 500 MPa

Resistance to oxidation-assisted cracking (OAC)

In order to assess the capability of the alloys to withstand oxidation-assisted cracking (OAC), specimens were tensile tested by ETMT at strain rates of $10^{-2}\,s^{-1}$, $10^{-3}\,s^{-1}$, and $10^{-5}\,s^{-1}$ in laboratory air at 800 °C. This methodology, developed by Németh et al

[129], allows for the assessment of the compound influence of oxidation resistance and the mechanical properties, and is critical for high temperature component design [229].

5.3 Results

5.3.1 Resistance to processing induced defects

With regard to processability, the situation has been found to be very complicated so in this first introductory paragraph – in order to inprove readability – an overview is first provided; further confirmatory evidence is provided in the following two paragraphs. Consider Figure 5.2 which contains optical micrographs taken within the bulk of XZ plane cross-sections – containing the build direction – obtained from printed cubes. These micrographs illustrate that the new compositions print with no evidence of defects, at least within the bulk; no cracks were detected across an area of 100 mm^2 at a magnification of 100×. On the other hand, alloy CM247LC was found to contain crack-like defects due to processing: measured were a crack length density of ∼49 $\mathrm{cracks/mm}^2$ and crack count density of 2.6 $\mathrm{mm/mm}^2$. This disparity in behaviour is further evidence for the strong composition dependence of cracking in L-PBF processing consistent with observations reported elsewhere [93]. Interestingly, nevertheless for all compositions examined here – both CM247LC and the novel compositions – the edges of the built structures contained gas-related porosity which had survived the harsh thermal-fluid flow induced by the laser/material interaction and indeed the higher energy density processing which was carried out at these locations. This suggests that the formation of such gas porosity is not strongly related to alloy composition but rather to processing conditions. In what follows below, further evidence is provided for purposes of corroboration.

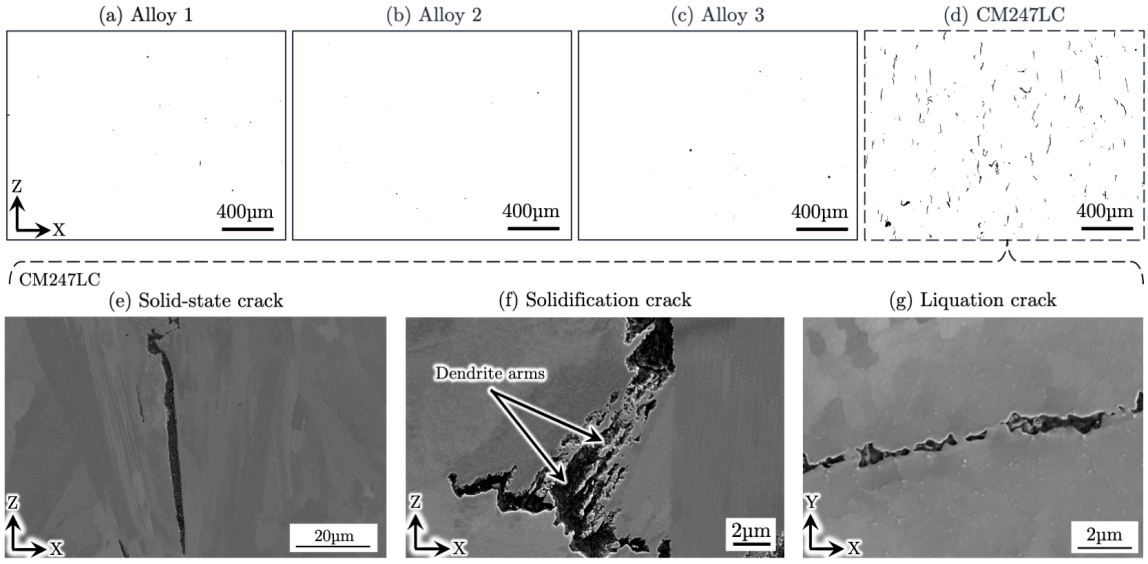

Fig. 5.2 (a-d) Optical micrographs with black and white threshold applied showing the cracking in CM247LC vs lack thereof in Alloys 1-3. SEM micrographs showing examples of (e) solid-state cracking (f) solidification and (g) liquation cracking observed in CM247LC.

With regard to the crack-like defects in CM247LC, optical microscopy on the 2D sections XZ confirm a strong directionality, with the cracks appearing largely straight and aligned in the Z build direction. Further characterisation by SEM indicates that cracks formed by three mechanisms: solid-state, solidification, and liquation cracking. Examples of these cracks are shown in Figure 5.2. The presence of solid-state cracks is strongly evidenced by their length being greater than the dimensions of a single melt pool – the use of the pulsed laser system employed here results in discretized melting events. These melt pools were determined to have radii of $\sim$>70 µm; on the basis of this it was concluded that cracks of length greater than >70 µm propagated at least in part in the solid-state. The occurrence of solidification cracks is supported by the presence of intact dendrite arms, which confirm that the crack edges had never fully fused. Lastly, the manifestation of liquation cracking is suggested by µm length scale cracks with smoothed edges indicative of a solidified liquid film [9]. Higher resolution characterisation using XCT on the miniature turbine blades has helped to elucidate

the situation further, by revealing the 3D nature of cracking in CM247LC. No cracks were detected by XCT for any grades of the alloy, but for CM247LC cracking was detected by XCT throughout the entirety of top 1mm of the blade profile characterised, as shown in Figure 5.3. Analysis of the sub-volume in the CM247LC blade revealed the 3D shape of the cracks; when observed on the XY plane they appear skeleton-like, whereas when observed on the XZ or YZ plane they appear plate-like. This mirrors observations made by optical microscopy and arises because cracking occurs on high angle grain boundaries (HAGB) [105, 106] and the microstructure produced by AM is highly textured with grains elongated in the build direction (Z-axis).

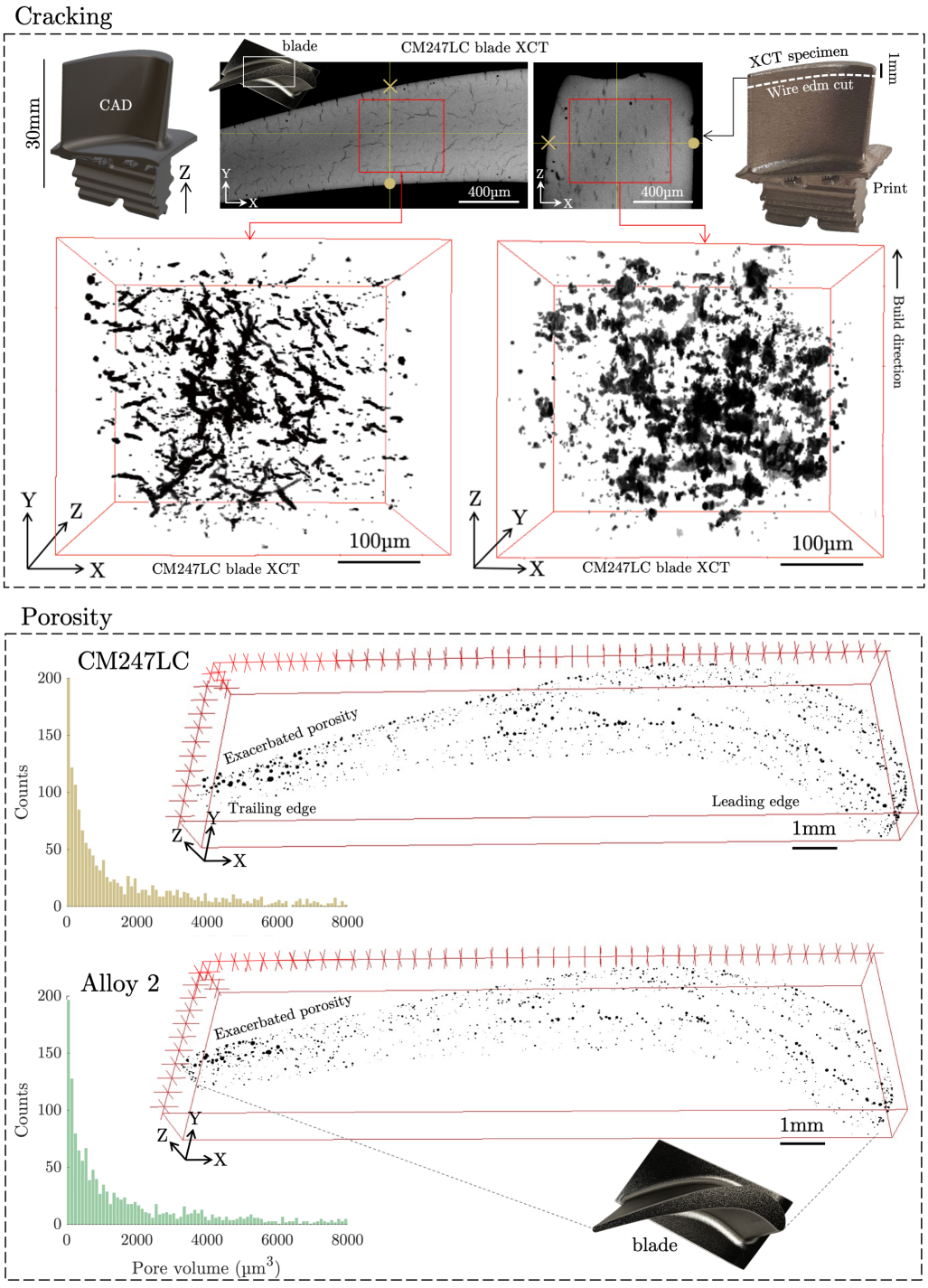

Fig. 5.3 Slices of the CM247LC blade sample XY and XZ planes as observed by XCT and 3D reconstruction of cracks as observed on each plane. Quantification of porosity and 3D reconstruction showing where porosity occurred in CM247LC and Alloy 2. XCT was performed by Dr. Kathryn E. Rankin at the µ-VIS X-ray Imaging Centre of the University of Southampton.

We now turn to the gas-related porosity. Quantification of the XCT data has confirmed porosity occurred to the same extent and in both new alloys and CM247LC. The total number of pores, mean, median, and max pores size were 1561, 3690 μm^3, 1090 μm^3, and 15590 μm^3 for Alloy 2 and 1860, 4350 μm^3, 885 μm^3, and 18920 μm^3 for CM247LC. Porosity occurred largely at the sample edges, hence it provides a delineation of the outline of the blade when visualized in 3D. In all cases here, porosity was exacerbated at the trailing edge and leading edge. The influence of processing conditions on porosity has been widely reported [150, 68, 230] where increased energy density in particular can cause keyholing and entrainment of the chamber cover gas [67]. The reduced laser velocity used at the sample edges – selected to improve the sample surface finish – is one cause of the porosity observed. Furthermore, the thin sections at the trailing edge have incurred even greater gas porosity due to the beam turning corners frequently and increasing further the energy density [62, 231]. The spatial dependence of defects in the blades confirm geometric changes – even in a small miniatured blade – have profound influence of the local formation of defects. Hence, the influence of changing geometry suggests that forgiving compositions that are processable across a wide range of heat transfer conditions are required to account for geometric effects in actual engineering components.

5.3.2 On the influence of heat treatment and microstructure

The Ni-based superalloy microstructure following printing consisted of cellular dendrites with small or no secondary dendrite arms. The intercellular enrichment of γ' formers and intercellular precipitation of Ta and Nb-rich MC carbides was observed; in CM247LC, Hf-rich carbides also precipitated at the cell boundaries, consistent with Ref. [87, 94]. Despite their substantial equilibrium γ' volume fractions, the novel alloy variants and CM247LC printed to γ, as observed on the lengthscale detectable by SEM. While it is

possible that nm length scale γ' – not observable by SEM – precipitated by reheating from subsequent passes, these findings emphasize that heat treatment is needed in order to develop desirable mechanical properties.

The changes in (Nb+Ta)/Al ratio in the new alloy variants resulted in slightly altered phase transition temperatures. As the Nb and Ta content was increased, the heat treatment window is narrowed – the γ' solvus increased and solidus temperature decreased; the inverse occurred when Al was maximized. Figure 5.1 shows the thermodynamic predictions of the γ' solvus correlated well with the novel alloys, but it under-predicted the solvus of CM247LC. The freezing range of CM247LC measured experimentally was appreciably wider than that of the new alloy variants, which is primarily attributed to the increased C, B, and Hf contents. The γ' solvus of CM247LC was $\sim$ 70 °C greater than that of the new alloys, consistent with its equilibrium γ' volume fraction being $\sim$10 % greater.

When tensile tested at a strain rate of $10^{-3}\,s^{-1}$ Alloy 2 exhibited greater high temperature ductility and similar flow stress following the sub-solvus HT 2 – as compared to the super-solvus HT 1. When Alloy 2 was heat treated in the super-solvus condition the material exhibited brittleness, accommodating only $\sim$1 % ductility when tested between 700 °C-1000 °C, see Figure 5.4. The root cause of the embrittlement following HT 1 is discussed in Section 4. But here, it is sufficient to note for now that the flow stress of Alloy 2 at 800 °C was 30 MPa greater when processed by HT 3 in contrast to HT 2. In light of this, as well as (i) the desirable bi-modal distribution of precipitates developed and (ii) the 20 h reduction in processing time, HT 3 was used to process the alloys for comparison of their properties in all work that follows.

The SEM micrographs in Figure 5.5 show the microstructure developed following HT 3 for each of the 4 compositions considered in this work. In the case of CM247LC, the primary γ' was larger than in the new compositions. APT analysis performed on

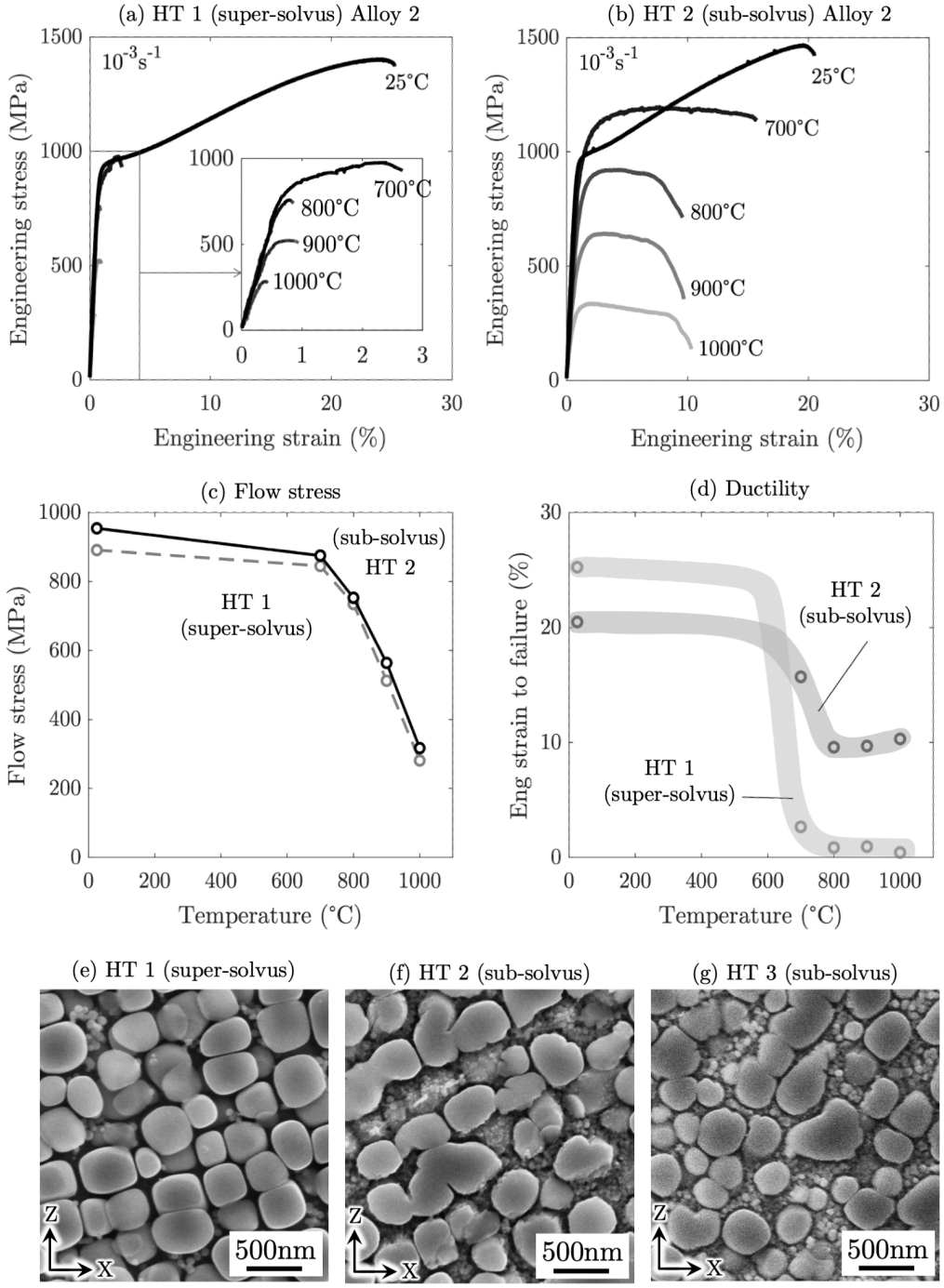

Fig. 5.4 Tensile response of Alloy 2 at various temperatures following (a) HT 1 (super-solvus) and (b) HT 2 (sub-solvus), as well as their summarized (c) flow stress and (d) ductility across the temperature range. SE micrographs of the Alloy 2 microstructure following (e) HT 1 (f) HT 2 (g) HT 3 showing the γ' inside the grain on the XZ plane.

Alloy 3 was performed by assessing γ' precipitates of 3 different sizes with the cuboid regions of interest that have an axes normal to the interface. These volumes were divided into bins of width of 0.5 nm and the composition of each bin was calculated using AtomprobeLab software and the error of the composition of each element was calculated as established in [232]. APT confirmed the segregation of Ta, Nb, Al, and Ni, segregated to γ' in the primary and secondary precipitates. Conversely, Co, Cr, and Mo segregated to γ, while no clear partitioning was observed for W. Tertiary γ' of diameter $\sim$8 nm was observed, in these precipitates Ta did not reach its equilibrium concentration of $\sim$2 at.% observed in the primary and secondary precipitates. The influence of the Nb and Ta content observed in the γ' of Alloy 3 is elucidated in what follows.

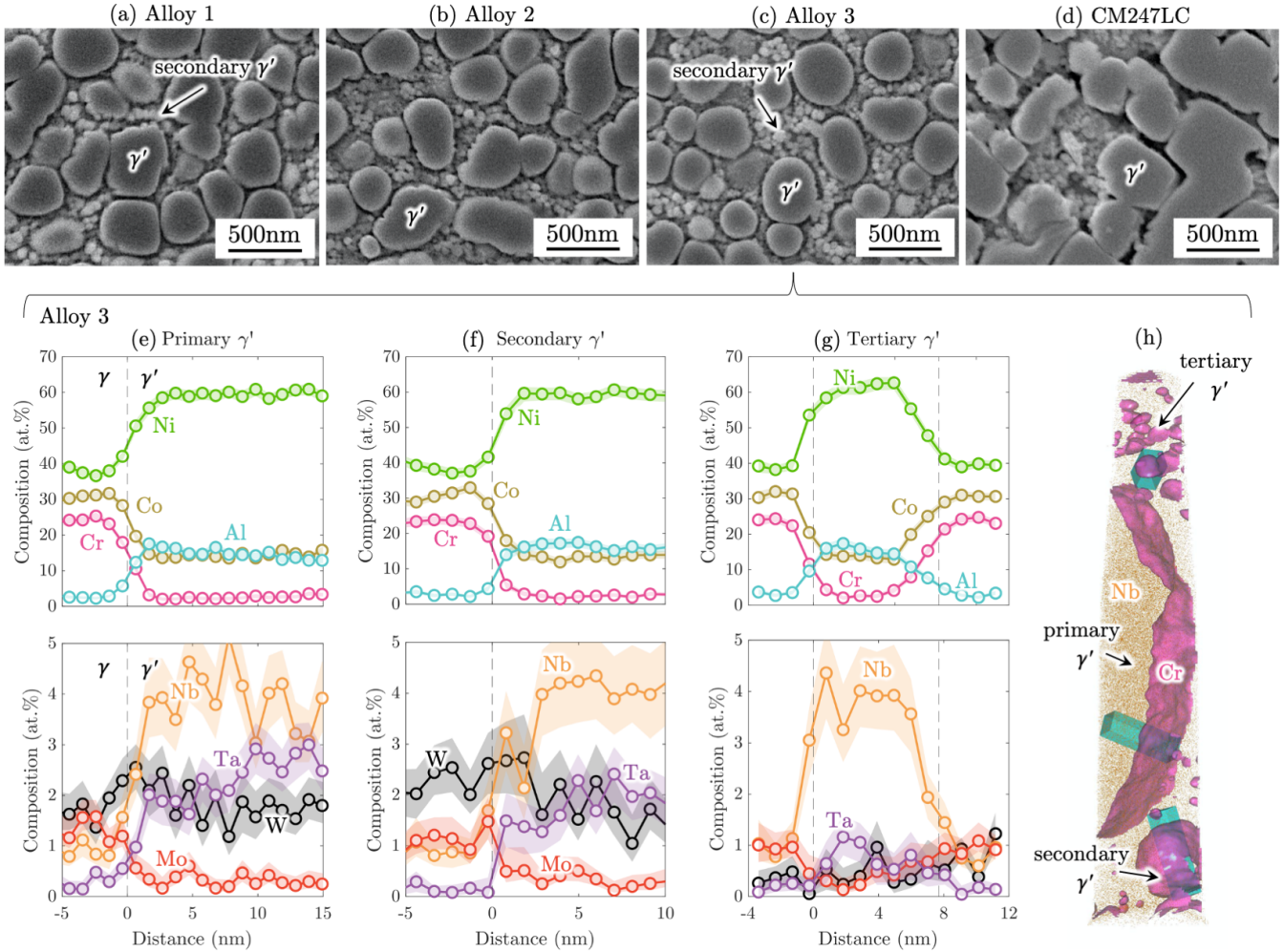

Fig. 5.5 SE micrographs showing the bi-modal distributions of γ' produced after HT 3 in (a) Alloy 1 (b) Alloy 2 (c) Alloy 3 (d) CM247LC. Concentration profiles across the γ-γ' interface for (e) primary (f) secondary and (g) tertiary γ' observed in Alloy 3 by APT. (h) 3D reconstruction of the atom probe tip of the Alloy 3 microstructure showing the γ' precipitates and cuboid regions of interest used to extract the concentration profiles. Atom probe tomography was carried out by Przemysław Klupś at the University of Oxford APT research group.

5.3.3 On the alloy properties developed

Flow behaviour

Figure 5.6 contains the data confirming the variation of flow stress and ductility as a function of temperature for the 4 compositions. Consistent with the observed Nb and Ta-rich γ' observed by APT, Alloy 3 exhibited the greatest flow stress of the 4 compositions up to 900 °C. Across the three novel alloy compositions, the flow stress increased with greater (Nb+Ta)/Al ratio. This occurred because Nb and Ta increases the energies of planar faults such as the anti-phase boundary (APB) and intrinsic/extrinsic stacking faults, which in turn inhibited γ' shearing [37]. Alloys 1 and 2 – with reduced Nb and Ta content – displayed a corresponding reduction in strength across the temperature range tested.. The increased strength of Alloy 3 came with a corresponding reduction in ductility in the 700 °C-1100 °C temperature regime. A ductility dip was observed in the 4 compositions at 1000 °C, which is also observed down to 800 °C in Alloy 3 and CM247LC. At the higher temperatures of 1000 °C and 1100 °C, CM247LC exhibited greater flow stress by ∼50 MPa. Testing at such a rapid strain rate reduces the influence of any oxidation-assisted cracking [129]. Further investigation of the alloy properties taking into account the influence of oxidation-assisted cracking is carried out in the discussion section.

Creep resistance

Figure 5.7 shows that the creep performance of CM247LC exceeded that of the novel alloy variants across the range of temperatures and stresses tested by plotting the stress level vs the Larson-Miller parameter (LMP). The factors conferring CM247LC with increased creep life relative to the novel alloy variants are likely (i) the greater γ' volume fraction [233, 234] as well as (ii) the substantially higher C and B contents [40, 50, 114]. Good agreement was observed between the creep performance of L-PBF produced

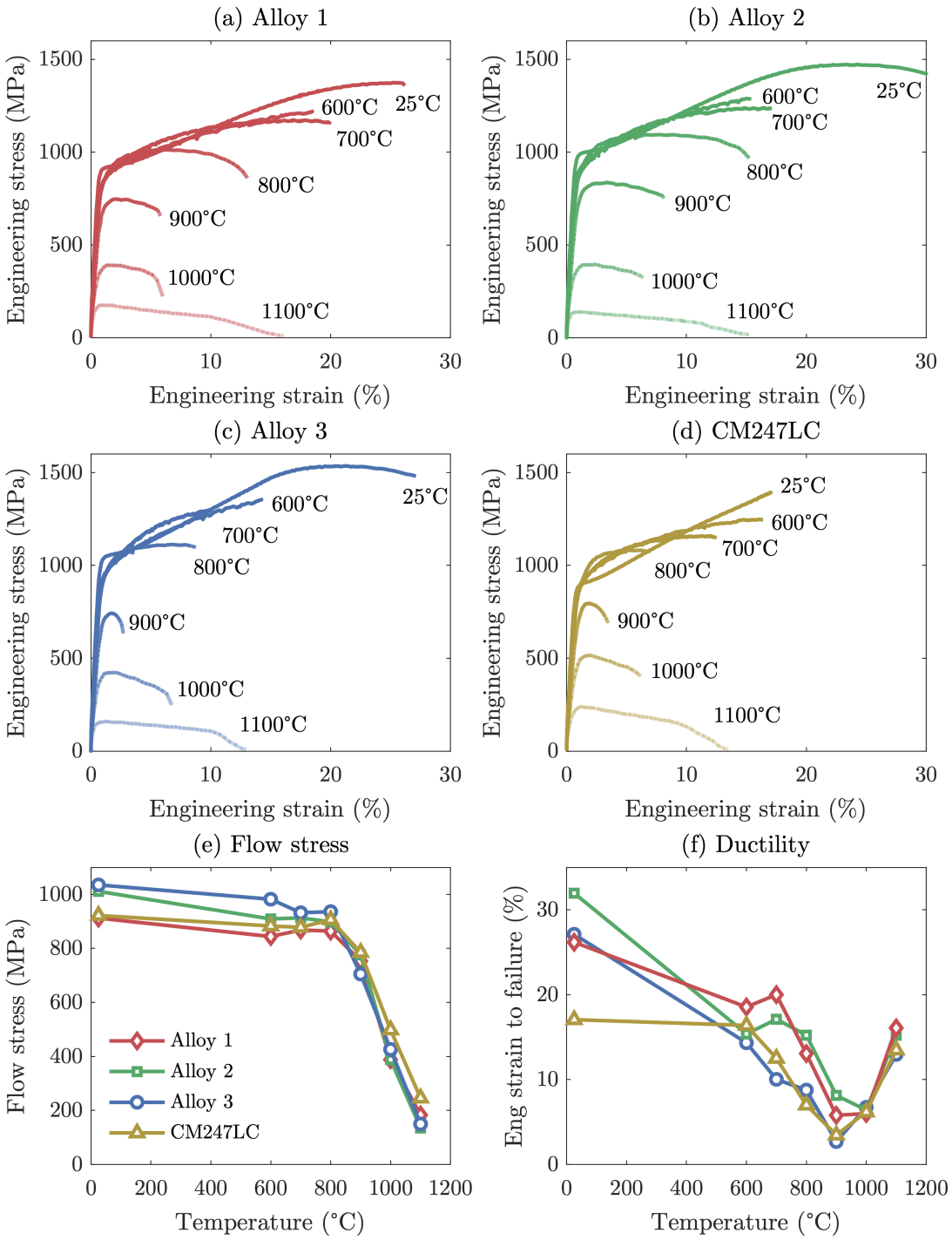

Fig. 5.6 Tensile response of (a) Alloy 1 (b) Alloy 2 (c) Alloy 3 (d) CM247LC when strained at $10^{-2}\,s^{-1}$ and summary of their (e) flow stress vs temperature and (f) engineering strain to failure vs temperature.

CM247LC – tested parallel to the build direction – reported here and in the literature [9, 15, 14]. The superiority of CM247LC was reduced under conditions of higher stress and lower temperatures where APB shearing is the dominant deformation mechanism, as opposed to the low stress and high temperature conditions where dislocation climb bypass dominates [45, 7].

The creep resistance of CM247LC was fair despite the extensive cracking incurred during processing. This performance was maintained as a result of the directionality of the cracks, which were planar in form and parallel to the build direction as shown in Figure 5.3. This meant the load state on the process induced cracks during the testing performed in this study was a combination of Mode II and Mode III, in-plane shear and out-of-plane shear respectively. If the tensile axis of the mechanical testing performed had instead been perpendicular to the build direction, the load state on the internal cracks of CM247LC would be Mode I – tensile stress normal to the crack plane – which would likely increase the detrimental impact of the processing induced defects [235].

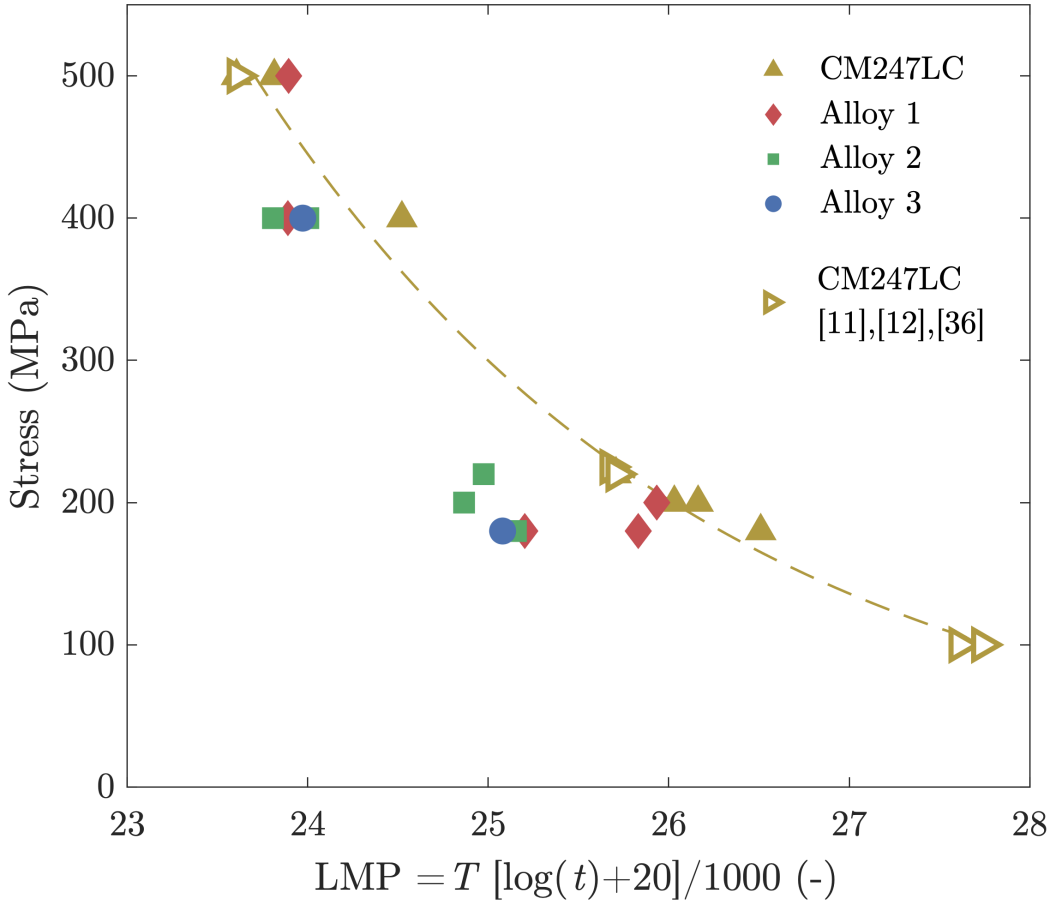

Fig. 5.7 Plot of the stress level vs Larson-Miller parameter for the compositions creep tested with the build directon as the tensile axis with data from the literature superimposed on the results of this study [14, 9, 15].

5.3.4 Oxidation behaviour

A combination of TGA and post mortem characterization shown in Figure 5.8 demonstrates that the (Nb+Ta)/Al ratio had a substantial influence on the oxidation behaviour. Alloy 1 had greatest oxidation resistance on account of the stable continuous alumina layer formed. The total mass gain of the Alloy 1 specimen after 24 h was $\sim 60\,\%$ less than that of CM247LC and Alloy 3. This is consistent with its having the highest Al content of the 3 novel alloy variants and thus most preferential thermodynamics for the formation of a stable and continuous Al_2O_3 layer. This is evidenced by TGA and in the BSE micrographs which show increasing mass gain and increasing discontinuity of the Al_2O_3 layers with decreasing Al content. In Alloy 3 discontinuities are observed every $\sim$5µm.

Characterization by EDX shed light on the nature of the scale formed in the novel alloy variants. The new compositions exhibited a thin outer Ni, Co, O rich oxide layer hypothesized to be $(Ni_{1-x}Co_x)O$, with a thicker Cr and O-rich Cr_2O_3 layer beneath, followed by a thin Nb, Ta-rich layer, Al_2O_3, and AlN precipitates in the Al-depleted zone. While the overall combined oxide layer thicknesses of the 3 novel compositions were not statistically distinguishable, the Nb, Ta-rich layer was qualitatively observed to be thinner in Alloy 1 – the low Nb+Ta variant. The aluminium nitrides formed below the oxide layer in the new alloy variants are hypothesized to be as a result of penetration of N through the oxide layer, as (i) compositional analysis of the Alloy 1, 2, and 3 powders determined the N content to be $< 0.005\,\text{wt}\%$ and (ii) composition independent N uptake specific to the printing configuration would have also affected the CM247LC alloy.

Discontinuous NiO oxide formed on the outer surface of CM247LC, followed by spinel, Cr_2O_3, Ti/W-rich oxides, and lastly HfO_2 which was found throughout the oxide layers, having large concentration in the Al_2O_3 oxide layer in particular. The

average sizes of the Al depletion zone in Alloy 1 and CM247LC (2.9 µm and 3.3 µm) were approximately half those of Alloy 3 and Alloy 2 (5.9 µm and 6.2 µm), while the standard deviations ranged from 0.4 µm to 0.6 µm. Despite its greater Al content, CM247LC is outperformed by Alloys 1-3 within this relatively rapid test period. This is likely due to its greater Ti content, which has been shown to have a deleterious effect on the oxidation resistance [236, 237].

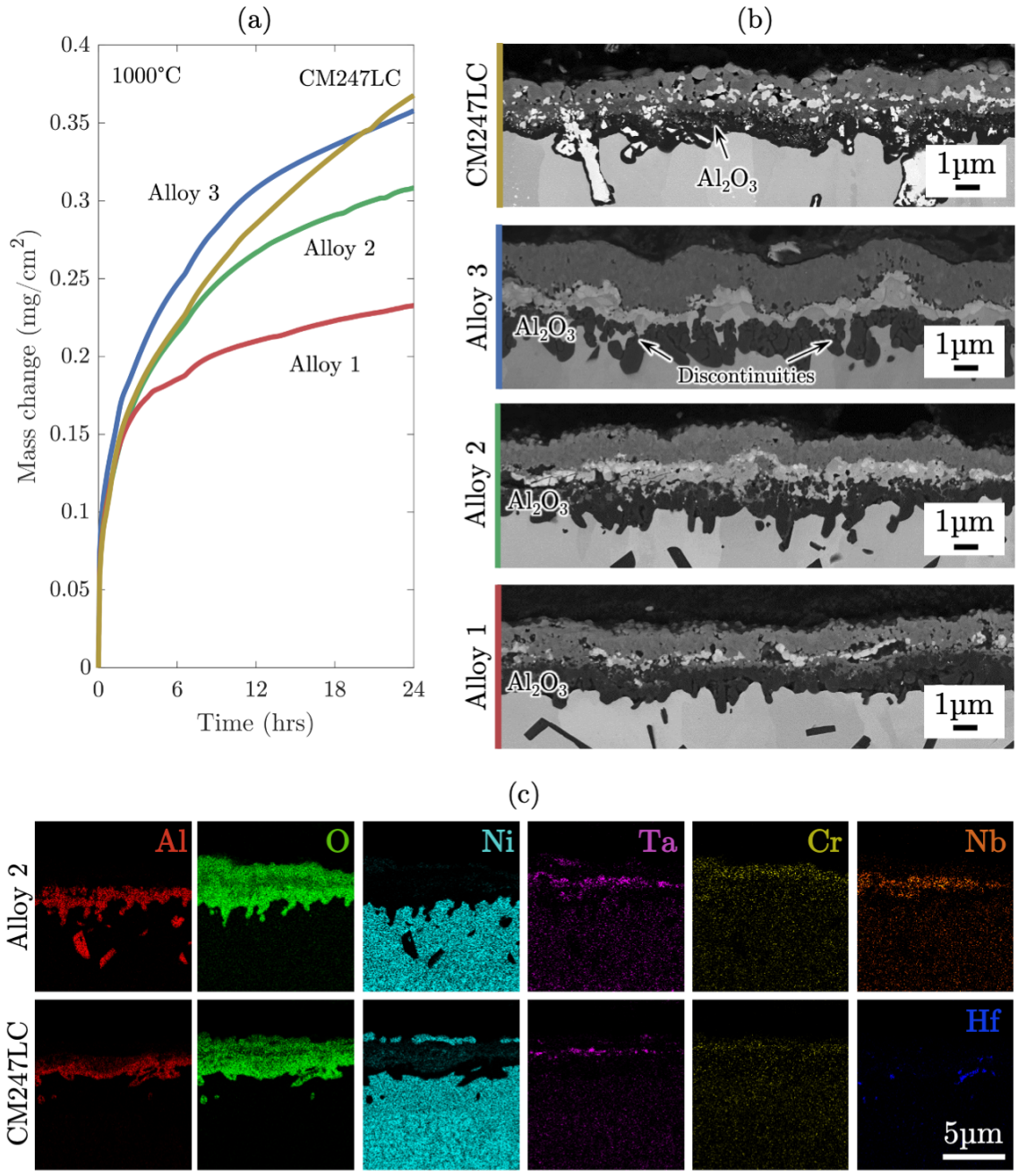

Fig. 5.8 (a) mass change vs time during isothermal thermo-gravimetric testing. (b) BSE micrographs of the oxide developed on each composition following testing. (c) EDX maps showing the distributions of elements in the oxide layers formed on Alloy 2 and CM247LC.

5.4 Discussion

The above results indicate that the new alloy and its variants show substantially improved processability and comparable performance in comparison with CM247LC. However, key elements of these results warrant further analysis and are considered in what follows, namely, (i) the mechanism of super-solvus embrittlement, (ii) the resistance to oxidation-assisted cracking which is assuming greater and greater importance, and (iii) the implications of the influence of the (Nb+Ta)/Al ratio on alloy design.

5.4.1 On the mechanism of super-solvus ductility loss

Characterization of the microstructure sheds light on the mechanism by which the embrittlement of Alloy 2 following super-solvus heat treatment took place. The microstructures developed differ in terms of grain structure, carbide distributions, and local grain boundary microstructure. When heat treated above the γ' solvus, γ' is fully dissolved and recrystallization occurs; the growth of large equiaxed grains – exemplified by EBSD and BSE in Figure 5.9 – gives rise to long straight grain boundaries perpendicular to the tensile axis. In contrast, the sub-solvus microstructure remains serrated with the small grains consistent with the as-printed microstructure. Carbide coarsening occurred during both heat treatments, but takes place to a greater extent under super-solvus conditions after which large $\sim$1µm diameter carbides were observed only on grain boundaries and often at grain boundary triple points. These grain boundary carbides have been shown to have a deleterious effect on ductility due to their pinning effect and ultimately decohesion of the carbide-matrix interface [238, 239]. After sub-solvus heat treatment the grain boundaries were decorated with some large and many fine γ' precipitates. This arises since γ' formers segregate to grain and cell boundaries during printing process [95], and promote the initial γ' precipitation when heated to 1080 °C which then coarsens during the air cooling, during this cooling

the fine γ' nucleates on the grain boundary. The precipitation of fine γ' at the grain boundary during sub-solvus heat treatment of and its subsequent preservation of ductility has been previously reported [240].

The distribution of γ' in the grain interior following super and sub-solvus heat treatments are quantitatively indistinguishable. As such, it is concluded that (i) the texture and (ii) local grain boundary microstructure are the key factors causing the embrittlement incurred by Alloy 2 following super-solvus heat treatment.

5.4.2 On the resistance to oxidation-assisted cracking

Alloy 3 exhibits the superior strength and Alloy 1 demonstrates the superior oxidation resistance, but the question is now asked; which is more optimal given the intersection of both tensile deformation and environmental attack? After all, it has been shown in the literature that superalloys strained at slow rates for longer periods of time exhibit oxidation at crack tips [129]; this accelerates crack propagation and substantially deteriorates the material properties and is of particular interest under dwell fatigue crack propagation conditions [241]. When deformed at a rate of $10^{-5}\,\mathrm{s}^{-1}$ the alloys fracture after $\sim$2 h. Each alloy exhibits a loss of approximately half their strength and ductility when deformed at this slower rate, see Figure 5.10. This is consistent with the effects of oxidation as reported in the literature [242, 243].

Alloy 2 displayed the most resistance to oxidation-assisted cracking, having the greatest flow stress $\sim$705 MPa and ductility $\sim$8 % under uniaxial tension at a strain rate of $10^{-5}\,\mathrm{s}^{-1}$. Neither the most oxidation resistant high Al variant or the strongest – high Nb+Ta variant – performed best under these conditions, as such it appears the moderate ratio (Nb+Ta)/Al was most effective, with sufficient Nb and Ta to increase the γ' APB energy for strength as well as the Al to have oxidation resistance. The measured flow stress of CM247LC under a strain rate of $10^{-2}\,\mathrm{s}^{-1}$ was $\sim$900 MPa,

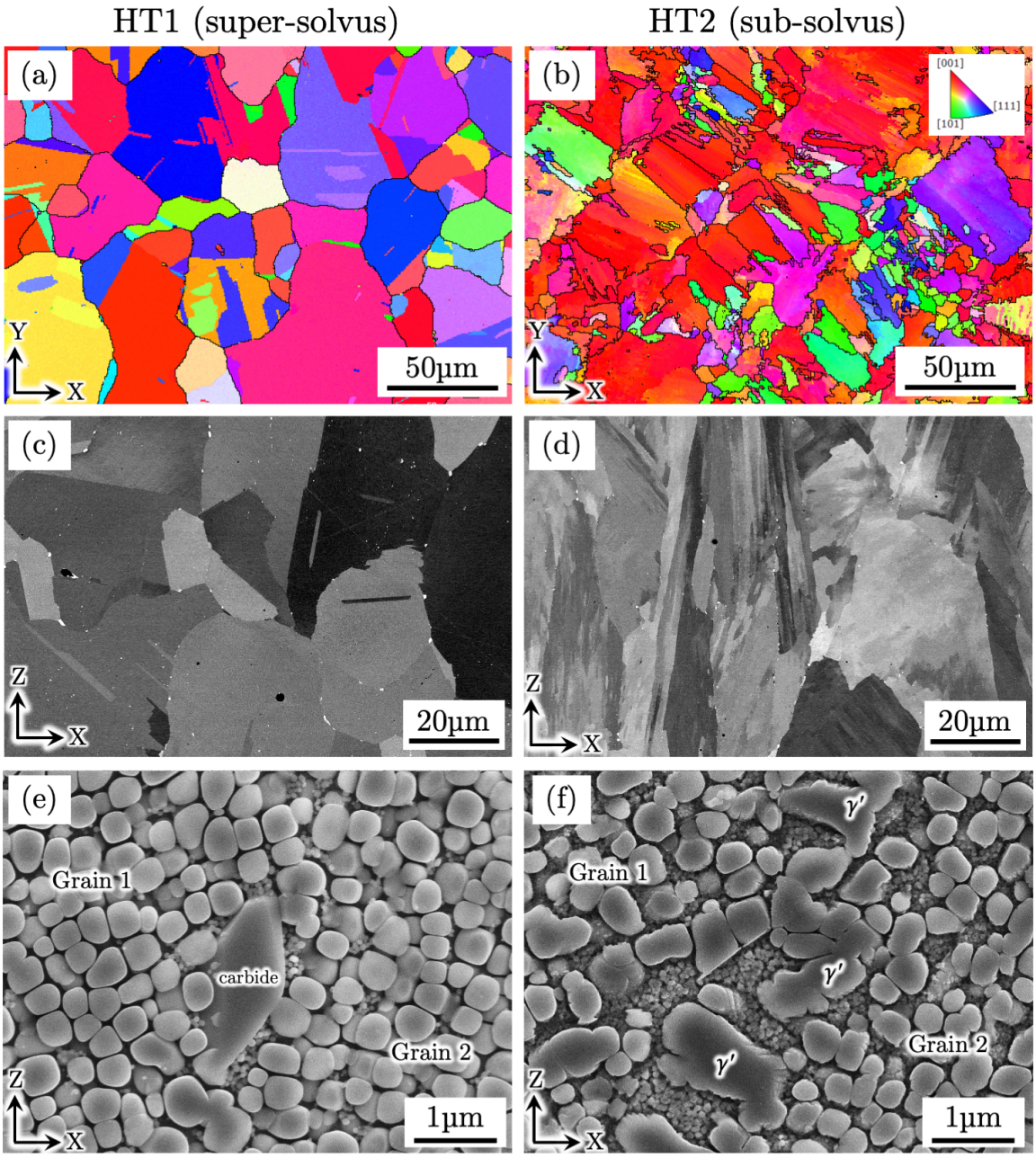

Fig. 5.9 Microstructural analysis of the super-solvus embrittlement showing for super and sub-solvus respectively (a-b) EBSD inverse pole figure along the z-axis on the XY plane (c-d) BSE micrographs on the XZ plane (e-f) SE micrographs of the grain boundary microstructures on the XZ plane (where γ matrix has been etched away). EBSD was carried out by Dr. Yuanbo T. Tang of the University of Oxford high temperature materials research group.

which dropped to ∼610 MPa given the contribution of oxidation. It is noted that the processing induced defects in CM247LC may have contributed to the decrease in properties at slower strain rate.

These findings highlight that despite initial tensile tests reflecting favourably on the strategy of designing stronger alloys by substituting Al in γ' for Nb and Ta, a more holistic perspective affirms that maintaining sufficient Al content is vital. Overall a balance of (Nb+Ta)/Al ratio must be struck to mitigate oxidation-assisted cracking and likely the ensuing dwell fatigue crack propagation.

5.4.3 Composition-processing-performance trade-offs

Here, five metrics are considered to summarize the performance trade-offs when the (Nb+Ta)/Al ratio is varied: strength, creep resistance, oxidation resistance, OAC resistance, and affordability. Maximizing each metric is ideal, the metrics are defined as follows; strength: the flow stress at 800 °C (MPa), affordability: the reciprocal of cost (kg/$), creep resistance: the LMP at 180 MPa, oxidation resistance: reciprocal of mass gain during isothermal oxidation, OAC resistance: the flow stress at 800 °C when strained at $10^{-5}\,s^{-1}$. The metric values for the 3 alloy variants are summarized in Table 5.4. Figure 5.11 summarizes the trade-offs of these metrics in spider plots, the scaling of relative metrics is linear. Contrasting Alloy 1 and Alloy 3 shows that achieving the same γ' fraction through additions of either Al or Nb+Ta yields oxidation resistance or strength respectively. Given the Al is more readily available than Nb or Ta, the strength of Alloy 3 also comes with greater cost. Alloy 2 maintains a balance of strength and oxidation resistance and in doing so achieves good resistance to oxidation-assisted cracking relative to Alloys 1, 3.

Direct comparison of CM247LC with the new compositions must be done with prudence, taking into account the material application. The superior creep performance

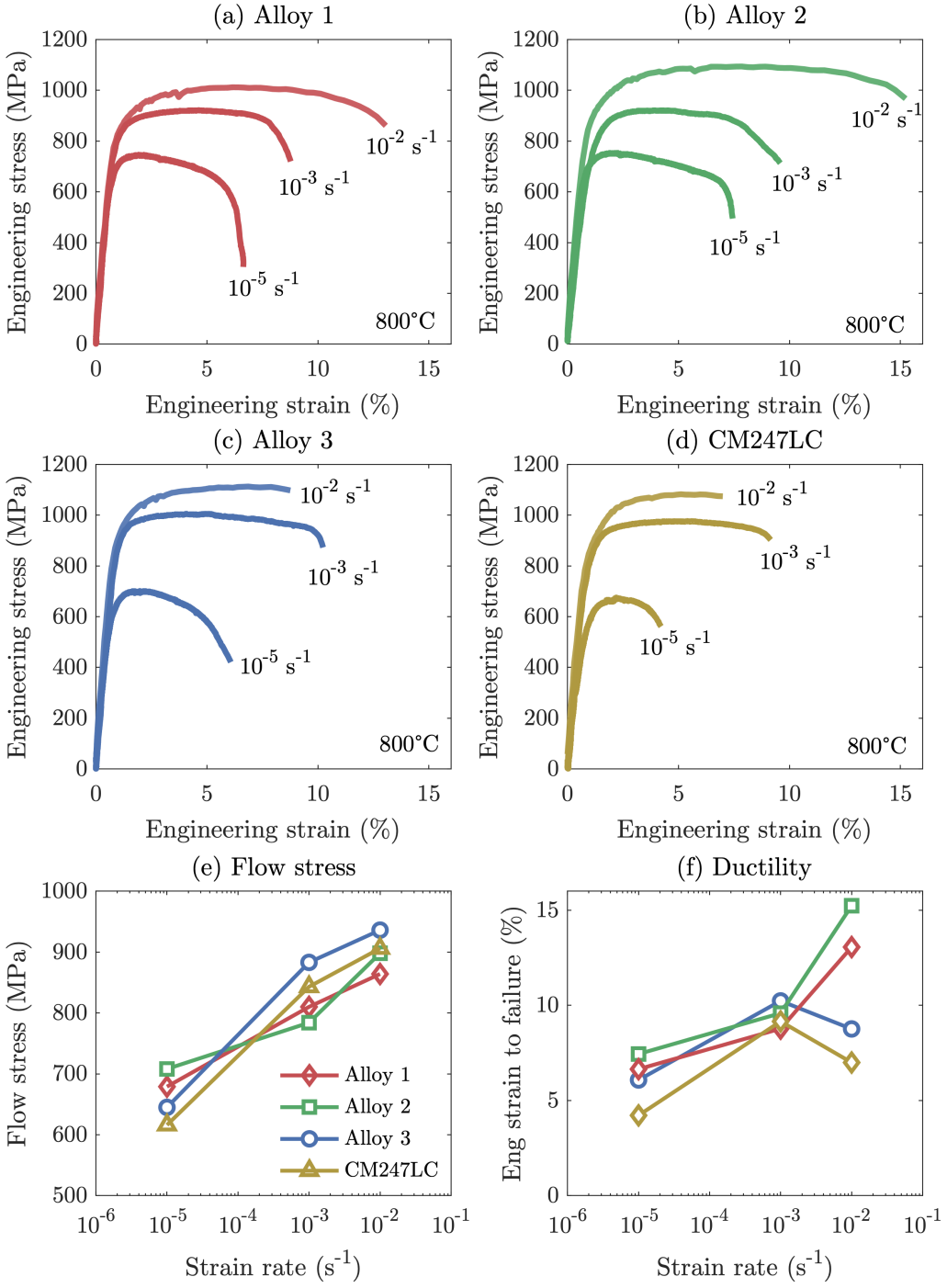

Fig. 5.10 Strain rate dependence of the tensile response of (a) Alloy 1 (b) Alloy 2 (c) Alloy 3 and (d) CM247LC illustrating the their susceptibility to oxidation-assisted cracking. Summary of the strain rate sensitivity of (e) the flow stress and (f) the ductility.

Table 5.4 Spider plot performance values.

Alloy	Strength (MPa)	Creep Resistance (LMP)	Oxidation Resistance ($24\,h/cm^2/mg$)	Affordability (kg/$)	OAC Resistance (MPa)
Alloy 1	864	25.20	4.3	3.37	679
Alloy 2	898	25.15	3.3	3.17	708
Alloy 3/AM-Dev	936	25.08	2.9	3.00	645

of CM247LC, which attributed to its more elevated solid solution and interstitial content inhibiting diffusion through the γ channels comes at the price of processability, as the C and B content makes it susceptible to cracking [114]. While it does retain superior creep properties despite the cracking it incurred during processing, these cracks make it unsuitable on account of their deleterious implications for fatigue life. Therefore, CM247LC is unemployable in an engineering component absent costly post-processing such as hot isostatic pressing (HIP). In the mid-termperature regime – where the shearing of γ' is the dominant deformation mechanism – the novel compositions marginally exceed the performance of CM247LC. However, it is noted the heat treatment conditions applied in this work were selected on the basis of the γ' solvus temperatures of the new alloy variants and not CM247LC, and that there may be scope to optimize the heat treatment of CM247LC processed by AM [91].

The strength and oxidation resistance as well as the processability and creep trade-offs highlighted here offer valuable insights into alloy design. Esoteric amplification of any given material property at the expense of others may have unforeseen ramifications. Hence, design must be undertaken with all the failure and damage mechanisms in mind, going past isothermal creep testing to assess alloy performance under conditions such as thermal-mechanical fatigue and dwell fatigue where oxidation-assisted cracking plays a role.

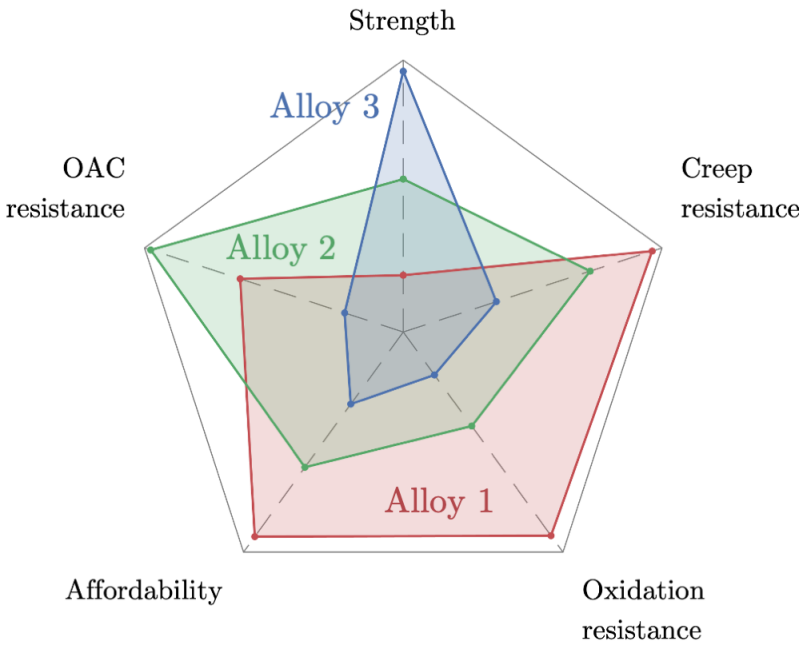

Fig. 5.11 Spider plots summarizing the alloy design trade-offs with varying (Nb+Ta)/Al ratio.

5.5 Summary and conclusions

In this body of work, the processability and performance of 3 variants of a novel Ni-based superalloy have been assessed and contrasted with the heritage alloy CM247LC. The following specific conclusions have been drawn:

1. The new grade of superalloy is shown to be processable; processing-related cracking has not been detected by either optical microscopy coupled with stereology or else high resolution x-ray computed tomography. Conversely, the benchmark CM247LC alloy exhibited extensive cracking of various types, including both solidification cracking and solid-state cracking.

2. The response of the as-processed material to heat treatment is critically important. Heat treatment conditions absent solutionizing need to be chosen carefully – super-solvus heat treatment causes embrittlement due to the texture of the recrystallized grain structure and the local microstructure of the grain boundaries which then

consist of γ and coarse blocky carbides. In contrast, sub-solvus heat treatment is effective for the maintenance of ductility and strength, due to a fine decoration of γ' at the grain boundaries.

3. Increasing the (Nb+Ta)/Al ratio at a fixed γ' fraction increases the yield stress of the alloy consistent with enhanced energies of planar faults. However, this comes at the expense of the alloy cost, oxidation – and lastly – the oxidation-assisted cracking resistance – which is of increasing importance for the intended applications. It is highlighted that this ratio can be tailored to match the application of the alloy.

4. This work demonstrates that it is possible to identify compositions of superior yield stress, oxidation resistance, and oxidation-assisted cracking resistance which are nonetheless processable.

Chapter 6

On the influence of alloy composition on oxidation behaviour

6.1 Introduction

The severe impact of oxidation assisted cracking highlighted in Chapter 5 suggests further investigation of the high temperature oxidation behaviour of these alloys is necessary. In light of this, the influence of composition on the oxidation behaviour and resistance of Ni-based superalloys produced by AM is investigated here to design alloys with improved resistance to environmental degradation. Several approaches to this can be taken such as thermodynamic and kinetic modelling [38] and exhaustive experimental trials [244]. The potential for cost savings and rapid analysis has made modelling increasingly popular and in recent years important models in have been produced [245, 246]. However, any such models still require experimental validation. This along with the need to experimentally test unexplored compositional spaces has motivated the assessment of the oxidation behaviour of a wide variety of alloys performed here.

6.2 Experimental methods

6.2.1 Alloy compositions and feedstock material

Here a total of 15 different alloy compositions were tested: 13 compositions discussed through chapters 3, 4, and 5 whose compositions are given in Tables 4.1 and 5.1 as well as 2 additional compositions – Alloy 1+Hf and AM-Dev-Low Gamma Prime (LGP). All 15 compositions used in this study are given in at% in Table 6.1.

Table 6.1 Measured alloy powder compositions (at.%).

Alloy	Ni	Al	Co	Cr	Fe	Mo	Nb	Ta	Ti	W	C	B	Hf
ABD850AM	bal.	2.4	31.5	18.8	-	1.03	0.34	0.13	2.30	1.29	0.041	0.014	-
ABD900AM	bal.	3.7	34.5	15.7	-	1.04	0.95	0.32	2.38	0.79	0.186	0.013	-
Alloy 1	bal.	9.5	33.4	8.4	-	0.62	1.13	0.89	0.12	1.84	0.150	0.024	-
Alloy 1+Hf	bal.	9.4	33.1	8.3	-	0.60	1.14	0.91	0.12	1.84	0.183	0.017	0.13
Alloy 2	bal.	8.6	33.5	8.5	-	0.62	1.50	1.24	0.13	1.87	0.152	0.023	-
Alloy 3/AM-Dev	bal.	7.8	34.2	8.4	-	0.64	1.93	1.53	0.13	1.93	0.129	0.022	-
AM-Dev-LGP	bal.	9.7	18.8	10.0	-	0.83	1.11	0.21	0.13	1.55	0.156	0.023	-
CM247LC	bal.	11.0	18.0	8.6	-	0.31	-	0.96	0.83	2.85	0.316	0.100	0.42
ExpAM	bal.	10.8	14.1	11.7	-	1.08	0.61	-	2.17	1.04	0.017	-	-
IN625	bal.	-	-	22.9	4.1	5.49	2.35	-	0.21	-	0.244	-	-
IN713	bal.	12.2	-	12.7	0.2	2.47	1.24	-	0.81	-	0.275	0.051	-
IN718	bal.	1.3	2.2	21.1	17.6	1.91	3.01	-	0.96	-	0.381	0.003	-
IN738LC	bal.	6.4	15.8	15.8	-	0.94	0.49	0.49	3.59	0.77	0.478	0.053	-
IN939	bal.	3.1	31.6	20.4	-	-	0.51	0.34	3.54	0.41	0.627	0.048	-
Waspaloy	bal.	2.4	21.6	19.4	-	2.30	-	-	3.16	-	0.210	0.037	-

Table 6.2 Measured alloy powder compositions (wt.%).

Alloy	Ni	Al	Co	Cr	Mo	Nb	Ta	Ti	W	C	B	Hf
Alloy 1 + Hf	bal.	5.2	18.9	8.8	1.17	2.16	3.34	0.11	6.89	0.0447	0.004	0.49
AM-Dev-LGP	bal.	5.1	10.2	10.0	1.53	1.98	0.72	0.12	5.47	0.0360	0.005	-

As was done in previous chapters these powders were produced by argon gas atomisation (prepared by Aubert & Duval) with median particle diameter (D50) of 32.1 and 32.7 µm. The alloy powder compositions, measured by ICP-OES and ICP-combustion analysis, are given in Table 6.2. While these 15 compositions do not serve as a targeted design of experiments to reveal the nature of specific compositional interactions, they are sufficiently varied as to give insight into key overarching questions such as the critical thresholds of Al, Cr, and Ti content which change the nature of oxide scales formed at elevated temperatures. The sliding scale of these compositions is perhaps best illustrated by their varied equilibrium γ' volume fraction; this is reflected in their microstructures (after 24 h at 1000 °C) shown in Figure 6.1. Clearly illustrated here is the increase in γ' precipitate volume fraction in the alloys of greater Al, Ti, Ta, and Nb cotent such as ExpAM and CM247LC in contrast to alloys of more moderate γ' content such as ABD850AM and Waspaloy. In order to test and characterise these compositions, additively manufactured cubes were produced using the same processing conditions outlined in Chapter 4. Specimens of dimensions 10 mm×10 mm×1 mm were cut perpendicular to the build direction and polished to a mirror finish with 4000 grit SiC paper.

6.2.2 Thermo-gravimetric analysis

Thermo-gravimetric analysis was performed as outlined in Chapter 5 albeit on 11 more alloys. The tests were carried out in 5 steps; a protective Ar gas flow is run for 1 h to ensure equilibrium of the system. This was followed by a increase of temperature by

20 K/min to the test temperature of 1000 °C followed by another hold for 30 mins under protective Ar and then the onset of the oxidizing laboratory air flow at 50 ml/min for 24 hrs. After this period the sample is cooled to room temperature at 20 K/min. The evolution of mass gain was analysed starting at the onset of oxidizing air. While these 24 h tests are short in contrast to typically reported analysis of oxidation behaviour, the strong composition dependence of oxidation has nonetheless become apparent.

6.2.3 Microstructural characterisation

The spatial distribution of elements and chemical composition of phases in each alloys oxide layers following testing was quantified with a Zeiss Merlin Gemini 2 field emission gun scanning electron microscope (FEG-SEM). This was equipped with an Oxford Instruments XMax 150mm/mm^2 energy-dispersive X-ray spectroscopy (EDX) detector. Maps were acquired with an accelerating voltage of 15 kV and probe current 500 pA. Oxford Instruments Aztec software was employed to perform phase mapping; the stoichiometric coefficients of each phase was confirmed by analysis of the respective atomic % of each element. This enabled high throughput analysis of the oxide scales for relative comparison at the cost of accuracy afforded by the more conventional x-ray diffraction (XRD) methodologies. The γ' precipitated in the bulk of the samples was characterised by SEM following an electrolytic etching with 10% phosphoric acid at 3 V. The oxide layers of each alloy were characterized by mounting the TGA samples in conductive resin followed by polishing. A set of 10 BSE images were taken of the oxide layer and depletion zone in each alloy to quantify their thickness using a macro in ImageJ.

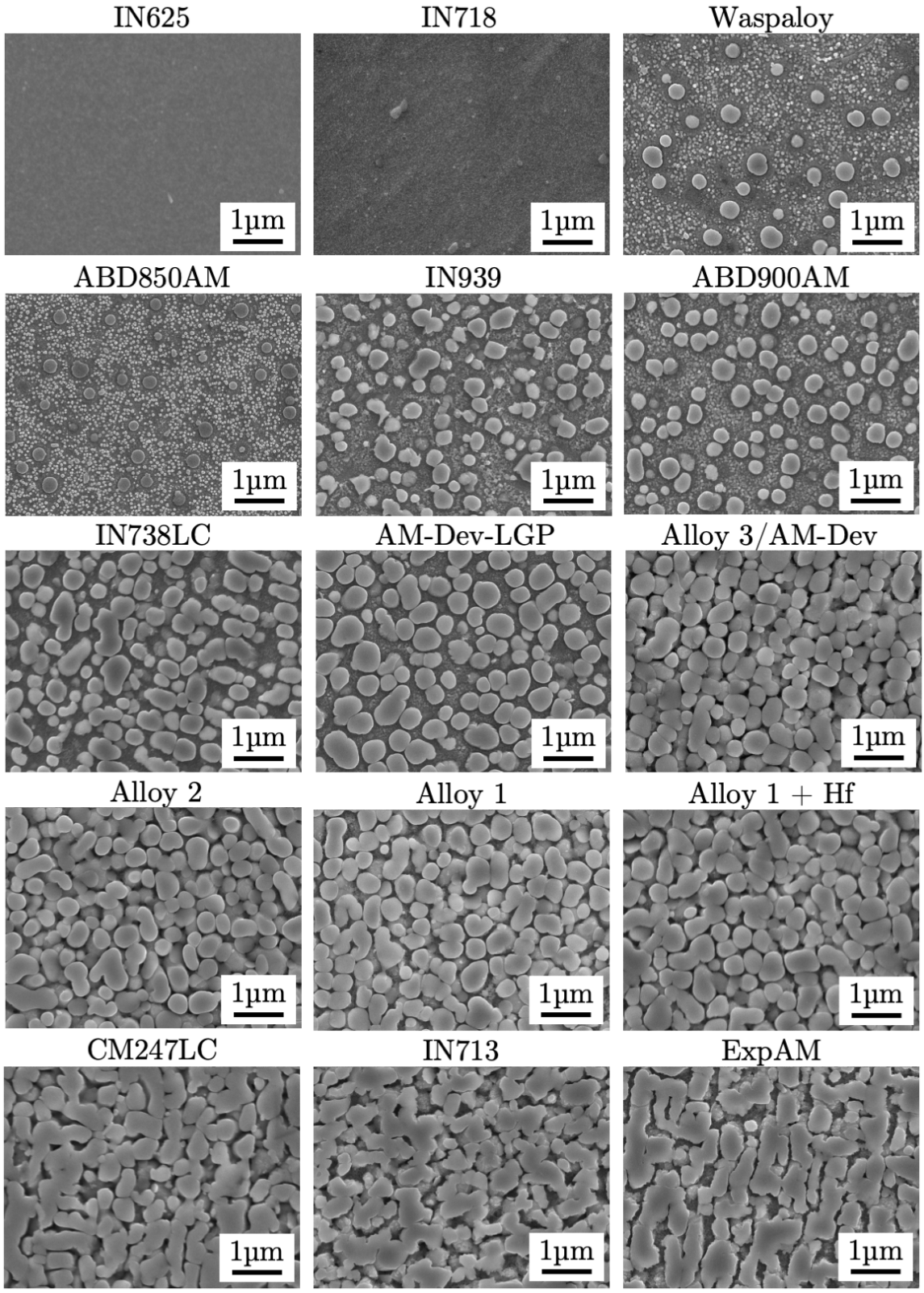

Fig. 6.1 SEM micrographs showing the precipitation of γ' in the bulk of each alloy after 24 h at 1000 °C.

6.3 Results and analysis

6.3.1 Mass gain

Figure 6.2 summarizes the results of thermo-gravimetric analysis. In order to view all 15 mass gain 15 curves the alloys are divided by classification into novel and heritage alloys. In all alloys an initial transient behaviour was apparent in the first 1-6 h. IN625 and IN718 demonstrated a second transient behaviour between 2-4 h where the oxidation rate increased rather than decreased – as it did consistently in the other 13 compositions. Of all the alloys, ExpAM exhibited the least mass gain under the test conditions employed here. ABD900AM and ABD850AM show very similar mass gain for the first 4 h after which ABD900AM tapered off and the rate of mass gain decreased comparatively. Of the heritage alloys, IN625 and IN718 gained the most mass in this time frame, which was anticipated given they were not designed for use at the elevated temperature of 1000 °C. IN713 and CM247LC gained the least mass of the heritage alloys and did so at a similar rate, whereas IN738LC – which oxidized to a slightly larger degree – gained mass more slowly initially but surpassed them after ∼10 h. The mass gain over 24 h of each alloy is summarized in Figure 6.3. Further analysis of the composition dependent mass gain is performed in subsequent sections.

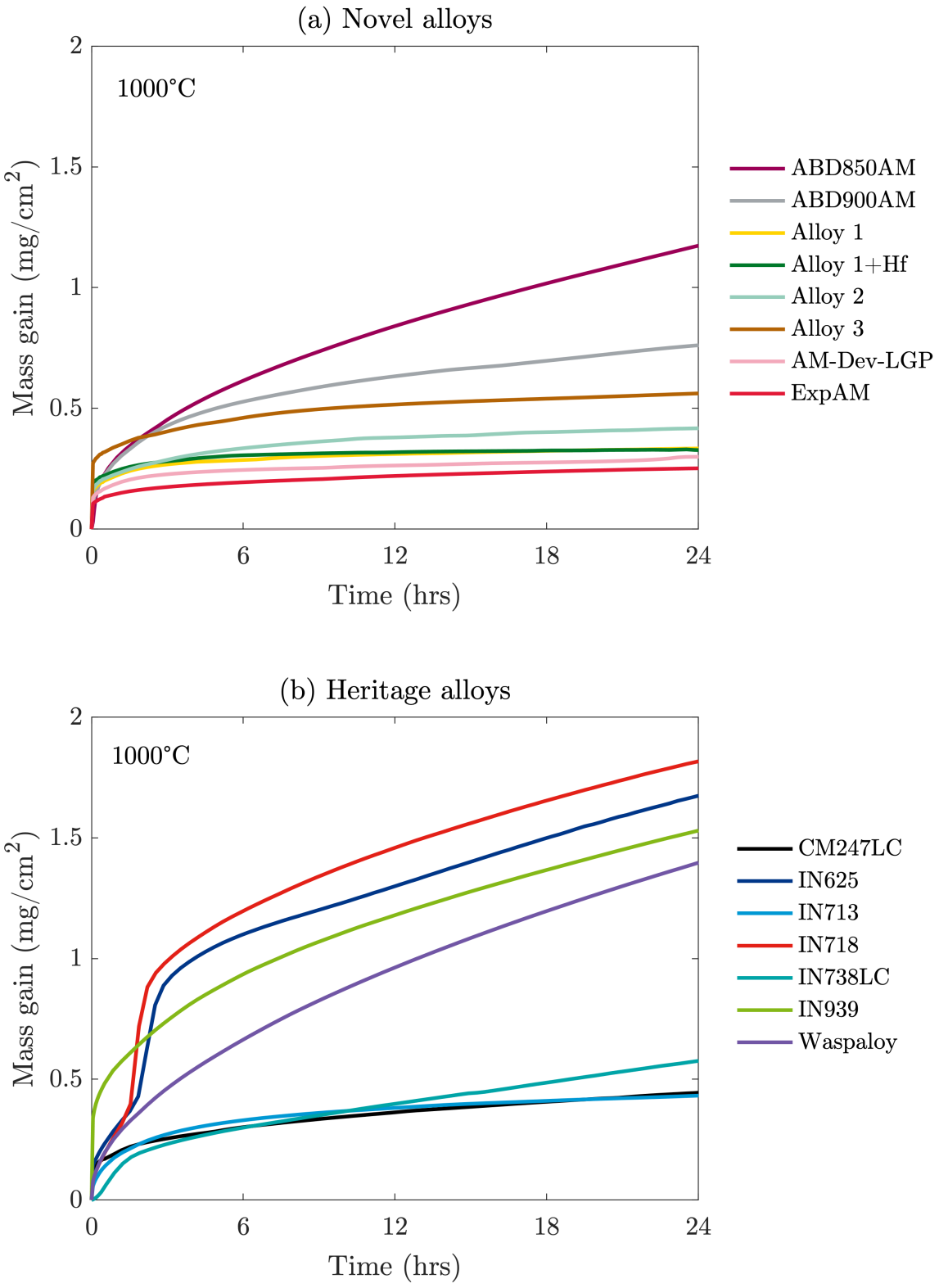

Fig. 6.2 Results thermo-gravimetric analysis at 1000 °C for 24 h for (a) the novel alloys and (b) the heritage alloys.

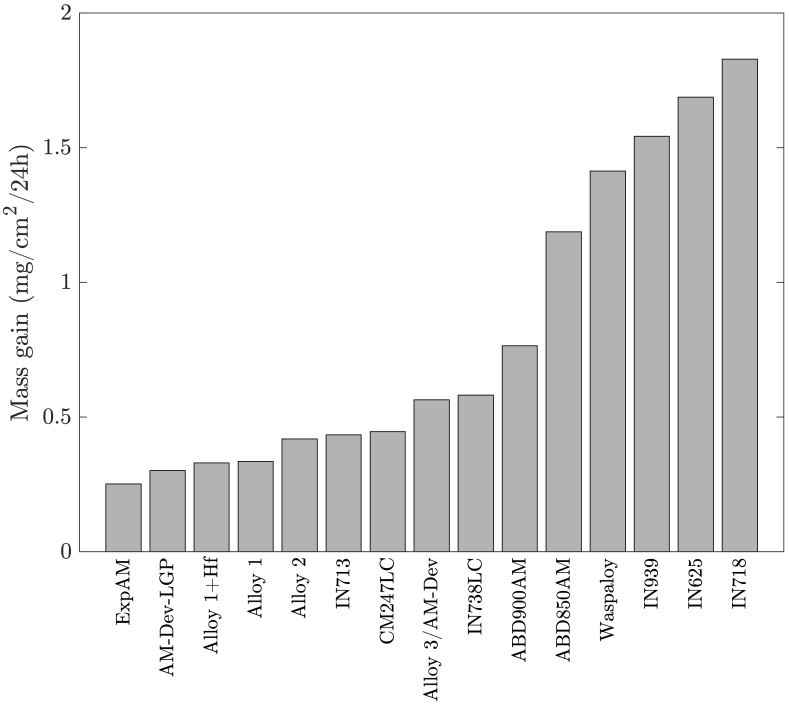

Fig. 6.3 Summary of the mass gain in 24 h for each alloy.

6.3.2 Growth kinetics and parabolic rate coefficient

The kinetics of oxide growth are assessed here. Figure 6.4 shows the parabolic rate coefficient determined for each composition. The parabolic rate coefficient k_p was measured by the standard method [247] as well as in accordance to Monceau et al [16]. The standard k_p was determined as follows

$$\left(\frac{\Delta m}{A}\right)^2 = k_\mathrm{p} t \tag{6.1}$$

where Δm is the mass change, A is the surface area, and t is time. The methodology outlined by Monceau et al emphasizes the assessment of k_p over a sliding interval [16]. Employing both methods allows for an interrogation of the assumptions needed for the classic parabolic growth rate law: pure diffusion control and no transient regime.

Applying Monceau's methodology results in large scatter. This occurs due to the short nature of these accelerated tests and the short sliding intervals of 100 data points over which the rate is measured.

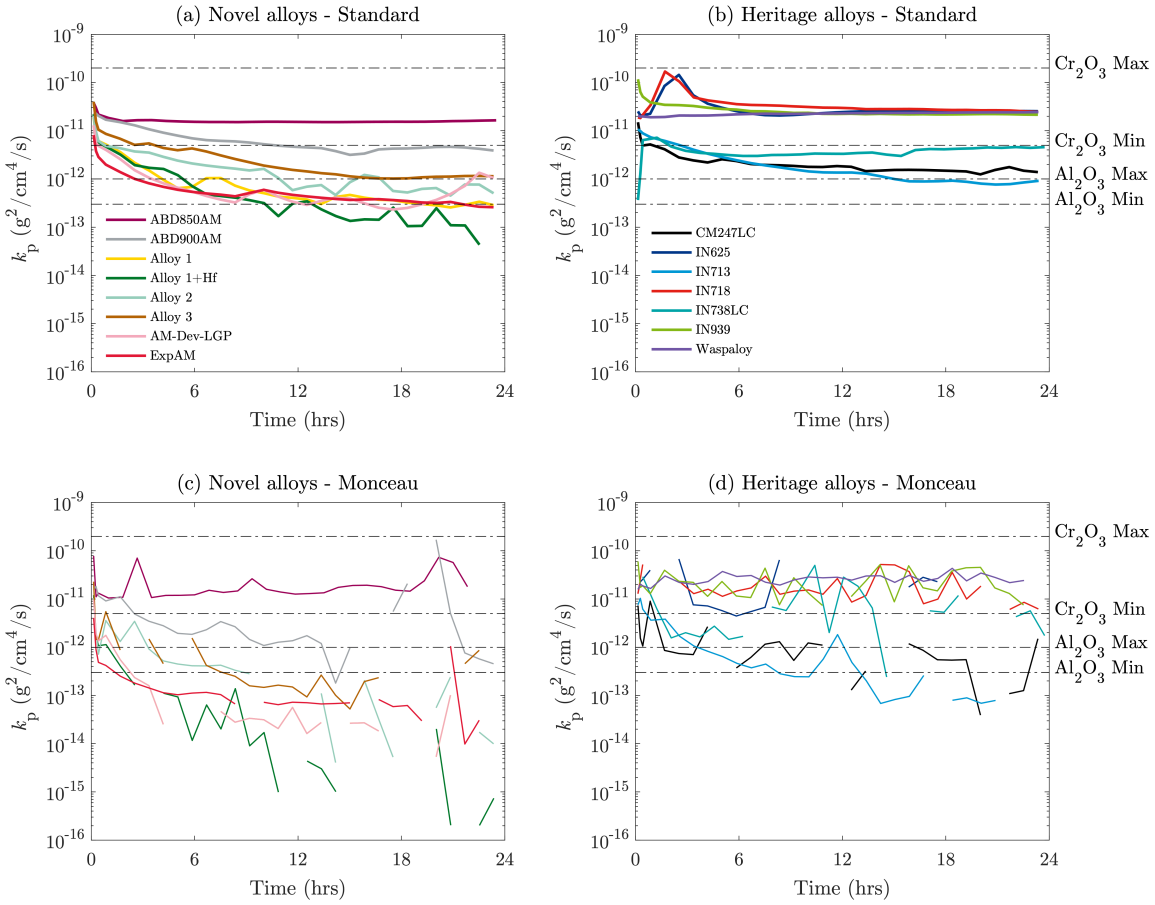

Fig. 6.4 The evolution of the parabolic rate coefficient measured by the standard method for (a) the novel alloys and (b) the heritage alloys and the method outlined by Monceau et al [16] for (c) the novel alloys and (d) the heritage alloys.

Estimates of the expected minimum and maximum values of the parabolic growth rate for Al_2O_3 and Cr_2O_3 found in the literature for pure Cr and Al [248] are superimposed on Figure 6.4. Of the heritage alloys, IN625, IN718, IN939, and Waspaloy all fall well within the range of Cr_2O_3 growth, whereas CM247LC and IN713 appear to be in the Al_2O_3 growth regime. from the novel alloys, only ABD850AM and ABD900AM grew oxides that grew at Cr_2O_3-like rates. The remaining alloys trended towards

the growth rates of Al_2O_3. The initial transient behaviour observed in the mass gain curves of IN625 and IN718 manifests as an increasing slope of $k_p - t$ until the oxide layer reaches a stable condition. The initial growth rate of of IN738LC follows the same trend as the IN625 and IN718 alloys but rapidly reverts to a more traditional behaviour. This cause of this initial transient is unknown but is postulated to be due to heterogeneity induced by the AM process. However, it is noted that this was not observed in the other alloys.

6.3.3 γ' depletion zones

The depletion of γ' near the sample edges was observed. The magnitude of this depletion zone was highly alloy dependent. The formation of the Al_2O_3 oxide scale at the edge was made possible by the transport of Al and hence the depletion of γ'. In the IN625 and IN718 alloys – which did not precipitate γ' and did not form an Al_2O_3 oxide scale – no depletion zone was observed. The depletion zones of the remaining alloys are exemplified in Figure A.7 of Appendix A, note the SEM micrograph scale bars are not equal. The measured magnitude of the γ' depletion zone sizes are shown in Figure 6.8 and are discussed in what follows.

6.3.4 Oxide layers

Understanding the nature of the oxidation layers formed in each composition is key to mapping the composition, microstructure, property relationships of these alloys. BSE micrographs shown in Figure 6.5 illustrate the variety of scales formed. The two alloys which underwent the greatest mass gain – IN625 and IN718 – exhibited thicker oxide scales. These two alloys as well as Waspaloy, ABD850AM and IN939 – the compositions most prone to mass gain in the 24 h test. The ABD900AM and IN738LC alloys underwent moderate mass gain during testing – both had discontinuous Al_2O_3

dispersed below their oxide scales, indicating insufficient Al content and thermodynamic driving force for the formation of a stable Al_2O_3 layer. Blocky AlN is apparent below the oxide layers of Alloy 1, 2, 3, 1+Hf, and AM-Dev-LGP. As was briefly highlighted in Chapter 5, compositional analysis of their feedstock powders determined the N content to be < 0.005 wt%, therefore the N uptake and resulting presence of AlN is concluded to have occurred during testing. This is discussed further in subsequent sections. Very fine TiN is visible in Waspaloy, ABD850AM, and IN939; a mixture of TiN and AlN precipitated in ABD900AM and IN738LC. The formation of these nitrides is well explained by Krupp et al [17] and Han et al [249] who highlight the inability of the Cr_2O_3 to prevent N transport and the need for discontinuous Al_2O_3 to permit N transport through Al_2O_3. This is shown schematically in Figure 6.7. Hf is present in the oxide scales of CM247LC and Alloy 1+Hf, appearing as a bright white phase since Hf's atomic number – 72 – is high relative to that of Cr – 24 – and Al – 13.

EDX map analysis of the oxide layers shown in Figure 6.6 reveals which oxides formed in each alloy. In IN625 an outer NiO oxide layer was detected followed by $NiCr_2O_4$, a thick Cr_2O_3 layer then what is presumed $NbCrO_4$ and/or Nb_2O_5. These findings are largely consistent with those of Vesel et al [250] and Kumar et al [251] which highlight IN625's tendency towards formation of Nb_2O_5 and $NiCr_2O_4$. IN718 formed an outer layer of FeO, followed by Cr_2O_3 with Nb oxide below, $NiAl_2O_4$ was detected in discontinuous form subsurface. Characterisation of oxide scales in the literature find TiO_2 and $MnCr_2O_4$ [252, 253] but no Ti and Mn-rich phases were detected in this body of work. Waspaloy, ABD850AM, and IN939 formed similar oxide scales consisting a of Cr_2O_3 layer with Ti-oxides on the inner and outer scale and Al-rich particles and branches subscale. Waspaloy and IN939 formed discontinuous TiO_2 on the outmost layer with Cr_2TiO_5 below, below the Cr_2O_3 and inter Cr_2TiO_5 layer a thin $NiCr_2O_4$ was observed. The Al-rich subsurface particles were Al_2O_3 with

a $NiAl_2O_4$ coot/transition layer. The phases in Waspaloy and IN939 detected here were in agreement with the findings of [254, 255] which differed only in that they reported the presence of Ta and Nb oxides in IN939 which were not observed in the present study. IN738LC and ABD900AM both developed TiO_2 on their outer scale but no Cr_2TiO_5, each developed a continuous Cr_2O_3 layer though IN738LC's layer was highly porous. Large Al_2O_3 precipitated subscale in IN738LC with a transient layer of $NiAl_2O_4$, furthermore, TaO_2 particles were dispersed in the $Al_2O_3/NiAl_2O_4$ layer underneath the Cr_2O_3. Litz et al reported similar findings but additionally reported the presence of NiO, NbO_2, and TiO_2 [255].

Alloys 1-3, Alloy 1+Hf, and AM-Dev-LGP have similar microstructures but with minor tweaks; this resulted in minor changes to their oxide layers. Each exhibited a Cr_2O_3 layer and a stable Al_2O_3 layer of approximately similar size beneath. For Alloy 1, 2, and AM-Dev-LGP an $NiAl_2O_4$ layer was found between the two main Cr and Al layers. In Alloy 3/AM-Dev – with increased Nb and Ta content – Ta and Nb-rich oxides were found in place of the $NiAl_2O_4$ layer. Of these 5 alloys AM-Dev-LGP was the sole composition to exhibit some NiO on the outer scale. Naturally Alloy 1+Hf was the only alloy to have Hf oxides in its layer. Some porosity was observed in the oxide scales of these 5 alloys, though no trend in severity across compositions was observed.

CM247LC, IN713, and ExpAM did not form Cr_2O_3 layers. In ExpAM on a stable Al_2O_3 layer was observed. CM247LC had a discontinuous NiO outermost layer followed by an $NiAl_2O_4$ layer with Nb, Ni, and Hf-oxide particles inside then a continuous Al_2O_3 inner layer. These findings are consistent with the literature though the tendency of CM247LC to form TiO_2 and Ta_2O_5 has also been highlighted in other works [256, 257]. In IN713 Al_2O_3 with $NiAl_2O_4$ on either side was found, congruous with the findings of the literature [258, 259]. The oxide scales observed in each alloy are summarized in Table 6.3.

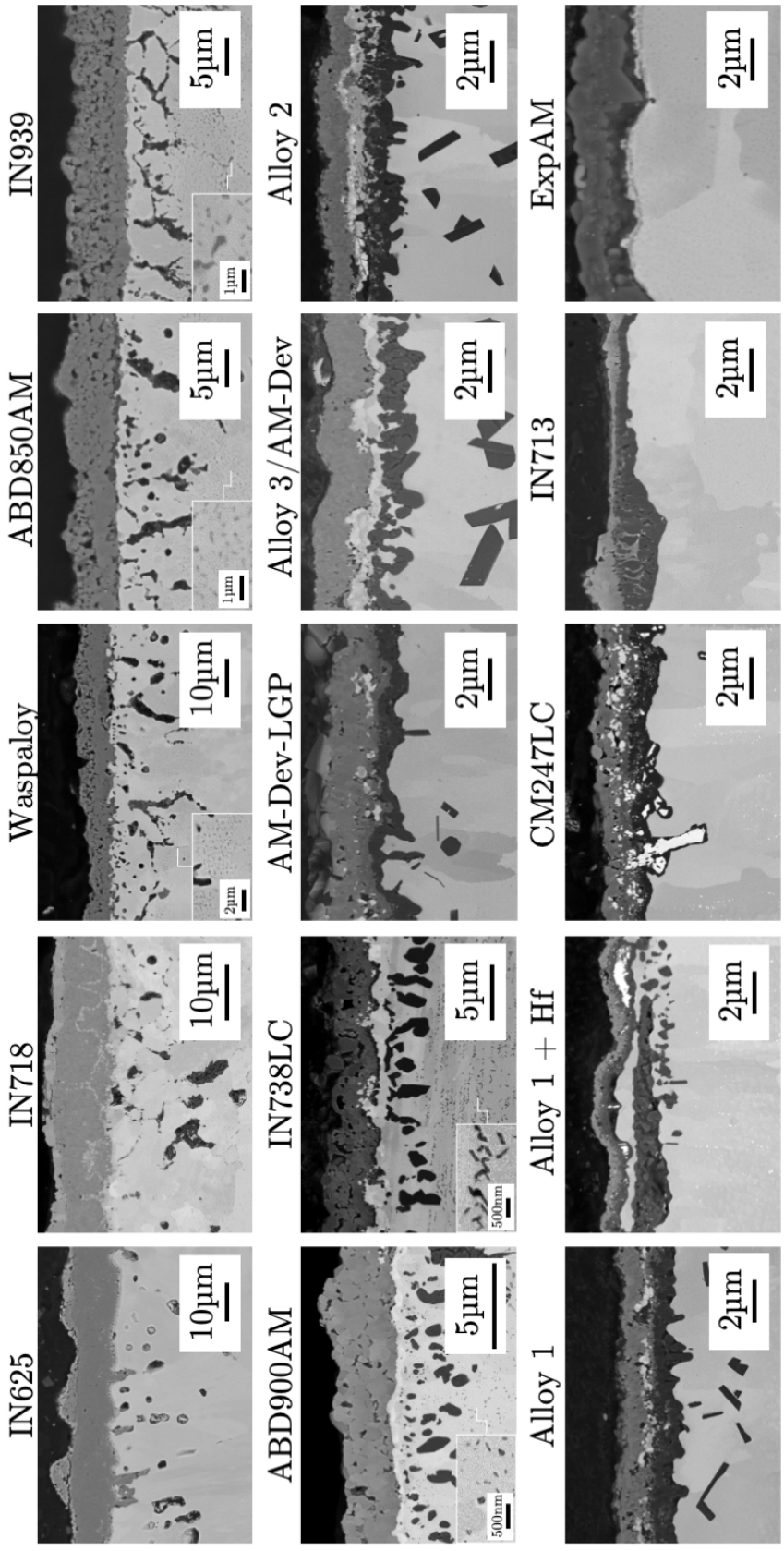

Fig. 6.5 BSE micrographs showing the oxide layers formed at the surface of each alloy after 24 h at 1000 °C.

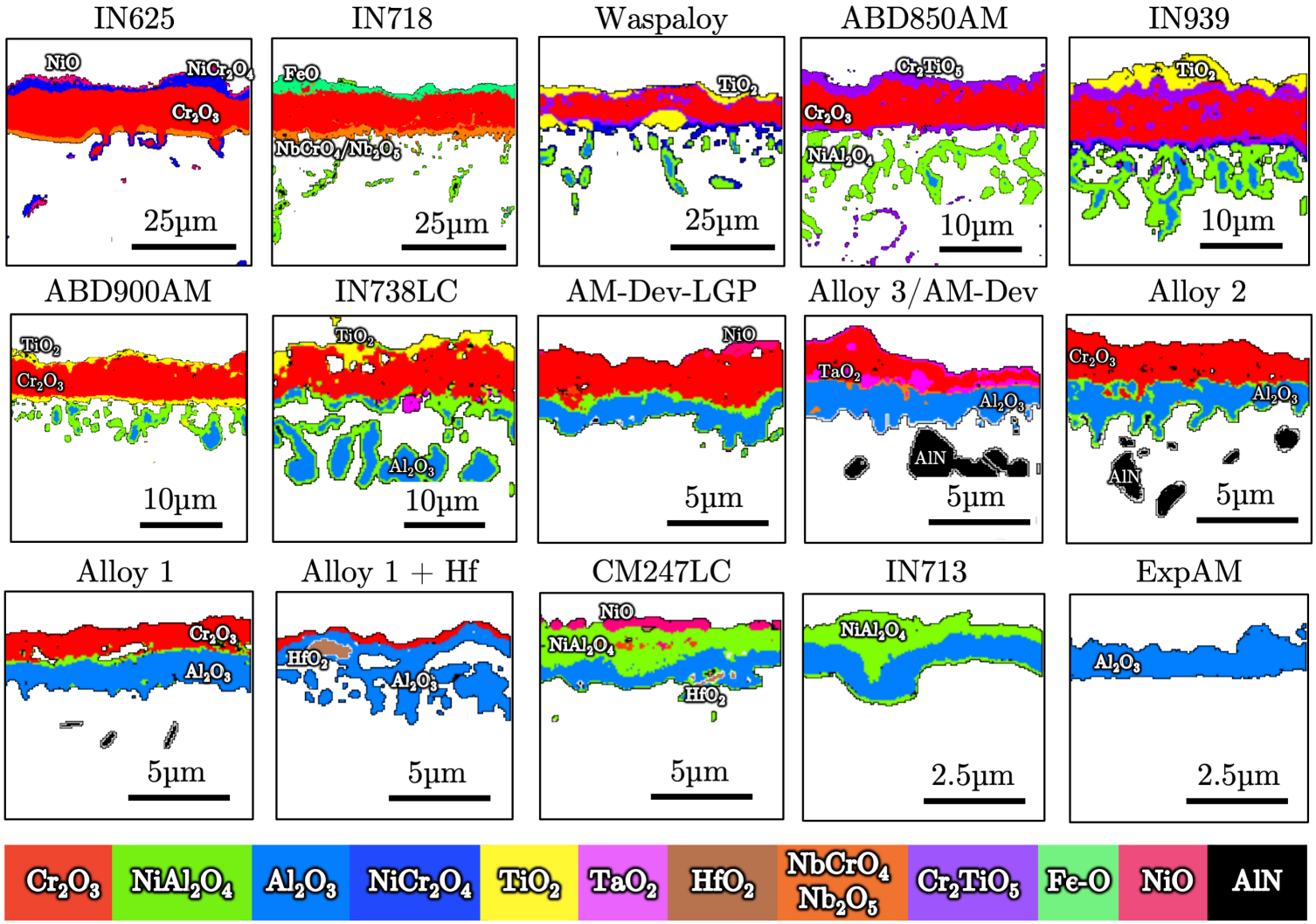

Fig. 6.6 Phases in each alloy identified by high resolution SEM-EDX after 24 h at 1000 °C.

Table 6.3 Summary of oxide scales formed after 24 h at 1000 °C.

Alloy	Outer scale	Scale	Chromia	Scale	Scale	Spinel	Alumina	Scale	Nitride
IN625	NiO	$NiCr_2O_4$	Cr_2O_3		$NbCrO_4/Nb_2O_5$				
IN718	FeO		Cr_2O_3		$NbCrO_4/Nb_2O_5$	$NiAl_2O_4$			
ABD850AM		Cr_2TiO_5	Cr_2O_3	Cr_2TiO_5		$NiAl_2O_4$	Al_2O_3		
Waspaloy	TiO_2	Cr_2TiO_5	Cr_2O_3	Cr_2TiO_5	$NiCr_2O_4$	$NiAl_2O_4$	Al_2O_3		
IN939	TiO_2	Cr_2TiO_5	Cr_2O_3	Cr_2TiO_5	$NiCr_2O_4$	$NiAl_2O_4$	Al_2O_3		
ABD900AM	TiO_2		Cr_2O_3		TiO_2	$NiAl_2O_4$	Al_2O_3		
IN738LC	TiO_2		Cr_2O_3			$NiAl_2O_4$	Al_2O_3		
Alloy 3/AM-Dev	TaO_2		Cr_2O_3	TaO_2	$NbCrO_4/Nb_2O_5$		Al_2O_3		AlN
AM-Dev-LGP	NiO		Cr_2O_3			$NiAl_2O_4$	Al_2O_3	$NiAl_2O_4$	AlN
CM247LC	NiO	$NiAl_2O_4$		TaO_2		$NiAl_2O_4$	Al_2O_3	HfO_2	
Alloy 2			Cr_2O_3			$NiAl_2O_4$	Al_2O_3	$NiAl_2O_4$	AlN
Alloy 1			Cr_2O_3			$NiAl_2O_4$	Al_2O_3		AlN
Alloy 1 + Hf			Cr_2O_3				Al_2O_3	HfO_2	AlN
IN713						$NiAl_2O_4$	Al_2O_3	$NiAl_2O_4$	
ExpAM							Al_2O_3		

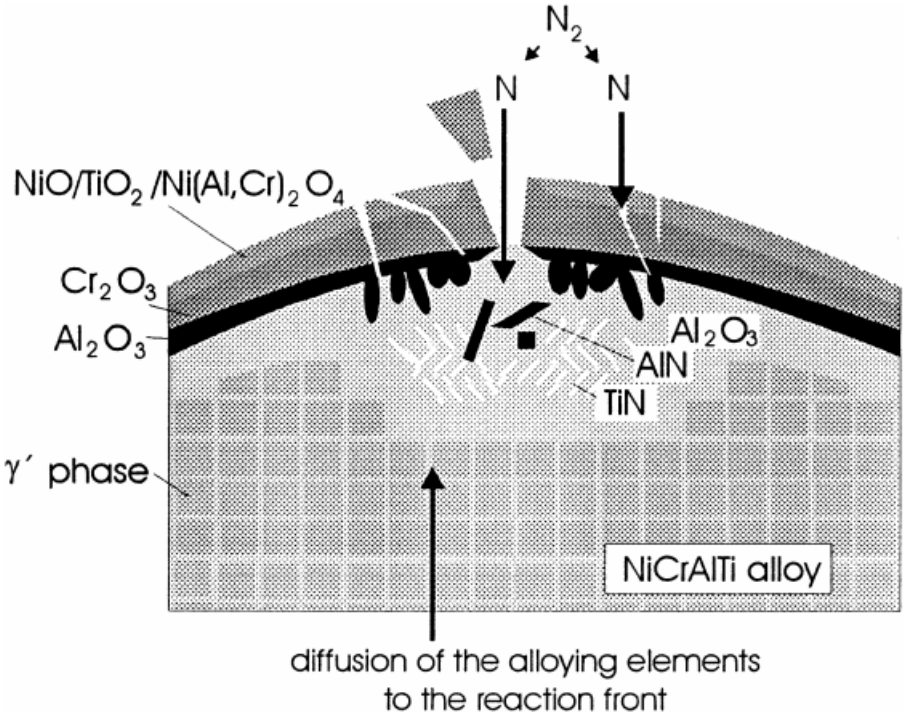

Fig. 6.7 Schematic representation of the mechanism of internal nitridation caused by cracks and pores in the oxide scale from Ref. [17].

The γ' depletion zone size and oxide layer thickness were measured in each alloy. These are summarized in Figures 6.8 and 6.9 respectively. IN625 and IN718 were excluded from the γ' depletion zone size analysis as no γ' was observed. The observed depletion zone was largest in Waspaloy followed by ABD850AM. The transition between Al_2O_3 and Cr_2O_3 formers is apparent in Figure 6.8 between the bars of AM-Dev-LGP ($\sim$10 µm) and IN738LC ($\sim$20 µm). The difference in oxide phases has unambiguously changed the oxidation resistance even in these short tests. Analysis of the oxide layer thickness shows IN625 and IN718 developed the thickest oxide layers. ExpAM and IN713 developed the smallest layers but the scale of IN713 had a less uniform thickness as illustrated by the wide measured standard deviation. The oxide layer of IN713 in Figure 6.6 exemplifies how this variability manifests itself: a pocket of $NiAl_2O_4$ sitting atop Al_2O_3 that has depressed into the bulk of material. IN738LC was the only other alloy to have an observably more variable oxide layer thickness.

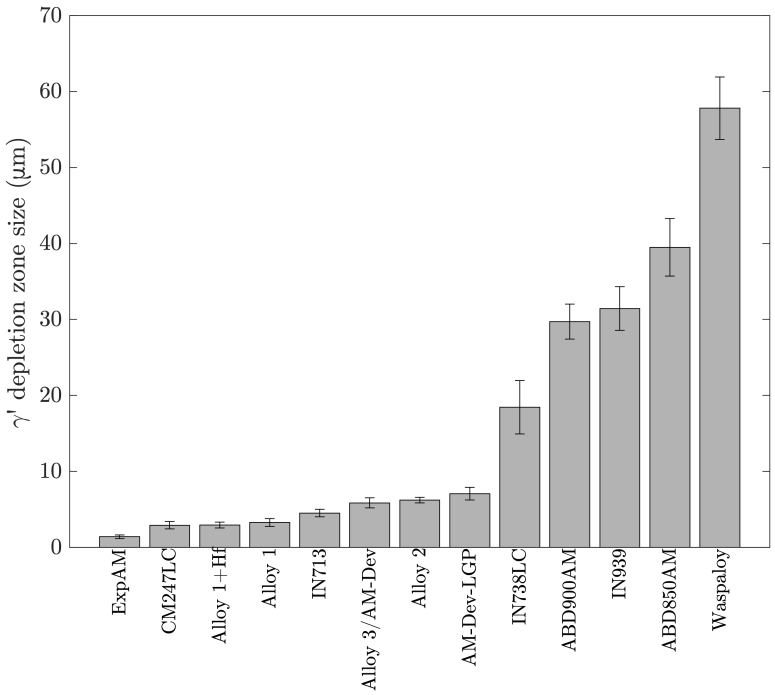

Fig. 6.8 Summary of the measured γ' depletion zone size for each alloy. Error bars represent 1 standard deviation.

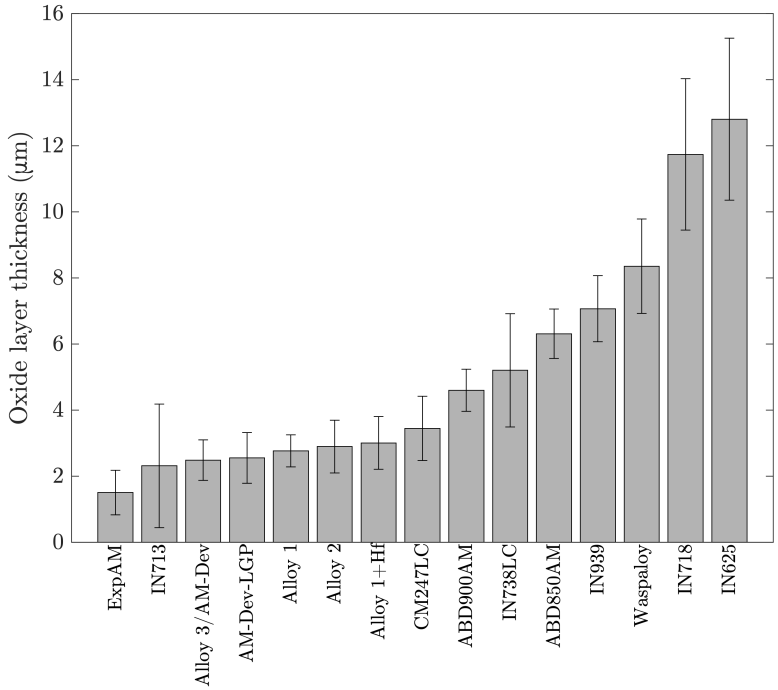

Fig. 6.9 Summary of the measured oxide layer thickness for each alloy. Error bars represent 1 standard deviation.

6.3.5 Analysis of quantitative microscopy

Figure 6.10 summarizes the influence of Al content on the measured mass gain, depletion zone size, and oxide thickness. This illustrates a clear transition in oxidation behaviour between 6.4 and 7.8 at% Al. None of the 7 alloys with Al content <6.4at% developed a continuous Al_2O_3 oxide layer; instead they formed Cr_2O_3 scales. The thickness of the oxide layers of the Cr_2O_3 forming alloys ranged between 4 and 14 µm. These were substantially thicker than those of the Al_2O_3 formers. The alloys with greater oxide layer thickness had greater γ' depletion zone sizes; this was due to dissolution of γ' and subsequent diffusion of Ti to the TiO_2 and Cr_2TiO_5 oxide scales. The Al_2O_3 forming alloys had smaller depletion zones as the stable Al_2O_3 layers substantially reduced the oxidation rate. Mass gain and oxide layer thickness correlated well since the diffusion of elements in the bulk and their bonding with O^{2-} resulted in the growth of oxide at the surface. The depletion zone sizes and oxide layer thicknesses of most of the Al_2O_3 forming alloys were not statistically distinguishable; the exception was ExpAM whose oxide layer was thinner and more uniform .

6.3.6 Design for oxidation resistance

Figure 6.11 shows the alloys mapped on the basis of their Al and Cr content. The alloys are categorised into groups that share major oxide phases and nitrides. The map illustrates how the Al and Ti content trades-off in γ' forming alloys. This in turn influences the formation of oxides; in alloys of moderate to elevated Ti content such as ABD900AM, IN738LC, and IN939 the Ti the formation of TiN, TiO_2, and Cr_2TiO_5 took place. In high Al alloys such as Alloys 1-3 the phases that formed were Al_2O_3 and AlN. Thus from an oxidation perspective increasing the γ' content by increasing Al is more favourable from than by increasing the Ti content. The same is observed in the case of Nb and Ta, as illustrated by the oxidation behaviour and phase formation

in Alloy 3, which gained greater mass and had Nb_2O_5 and $NiCr_2O_4$ mixed in its Cr_2O_3 and Al_2O_3 layers. Alloys 1-3 formed Cr_2O_3 while IN713 and ExpAM did not despite the latter having greater Cr content. This illustrates empirically that approximately >10 at% Al is required in for Al_2O_3 to be stable and prevent Cr_2O_3 formation given Cr_2O_3 levels of 8-14 at%.

The precipitation of AlN by the Alloys 1-3, Alloys 1+Hf, and AM-Dev-LGP was due to N permeation into the material. When observed after 24 h these 5 alloys all exhibited relatively continuous Al_2O_3 layers, suggesting that the N uptake of the material occurred early on before the Al_2O_3 layers was established. In light of this it is concluded empirically that Al content in excess of approximately 10 at% is required in order for rapid formation of Al_2O_3 to take place and to avoid the formation of aluminum nitrides.

6.4 Summary and conclusions

High throughput thermo-gravimetric testing was performed at 1000 °C on a set of 15 different Ni-based superalloy compositions in an effort to (i) establish a consistent dataset for oxidation of AM materials and (ii) identify composition-microstructure-property relationships to assist in alloy design for oxidation and specifically oxidation assisted cracking resistance.

1. A consistent experimental dataset has been developed comparing the oxidation resistance of 7 novel and 8 heritage Ni-based superalloys. Correlation between their Al content, mass gained during testing, depletion zone size, and oxide layer thickness formed was found. This was coupled with phase identification to develop processing maps useful for alloy design.

2. The compositions of Al at% greater than 7.8 at% were found to rapidly form Al_2O_3 at 1000 °C. A threshold for stable Al_2O_3 formation was identified between 6.4 and 7.8 at% Al.

3. Al content greater than 10 at% is empirically concluded to be the threshold to form a stable Al_2O_3 fast enough to avoid the early uptake of nitrogen and ensuing formation of AlN. This is also the threshold above which only Al_2O_3 is stable and Cr_2O_3 is not developed.

4. Alloys with Ti content 2.3 at% and greater formed TiO_2 and Cr_2TiO_5 phases in their oxide scales as well as TiN subscale. It is unclear if these played a deleterious role or if the substitution of Al for Ti in these alloys resulted in an increase in mass gain.

5. Nb oxides were observed in IN625, IN718, and Alloy 3/AM-Dev, the 3 compositions with Nb content in excess of ∼1.9 at%. Ta oxides were observed only in Alloy 3/AM-Dev which had Ta content of 1.5 at% – the largest of the 15 alloys.

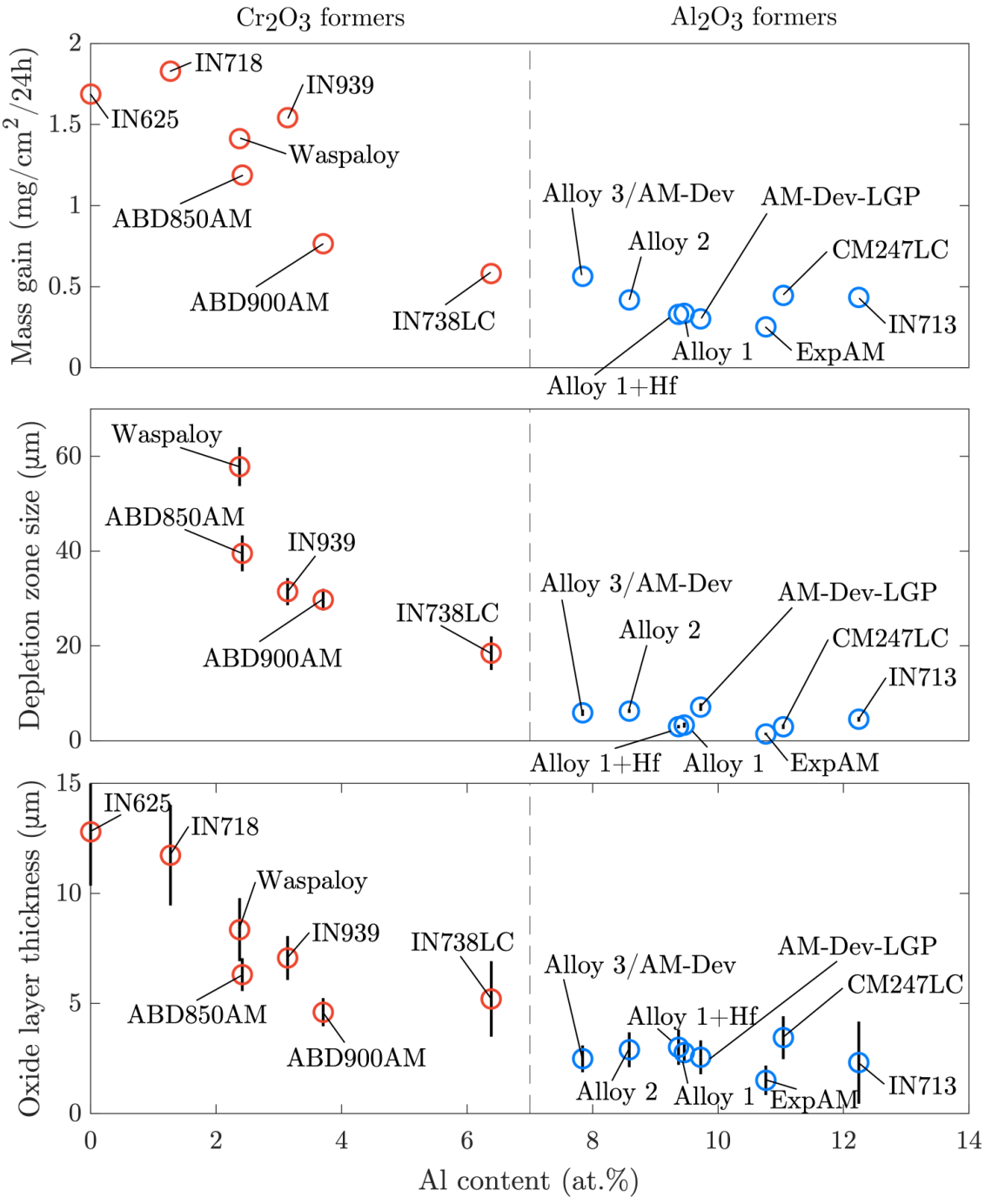

Fig. 6.10 Summary of the measured mass gain, oxide layer thickness, and γ' depletion zone size as a function of Al content (at%.).

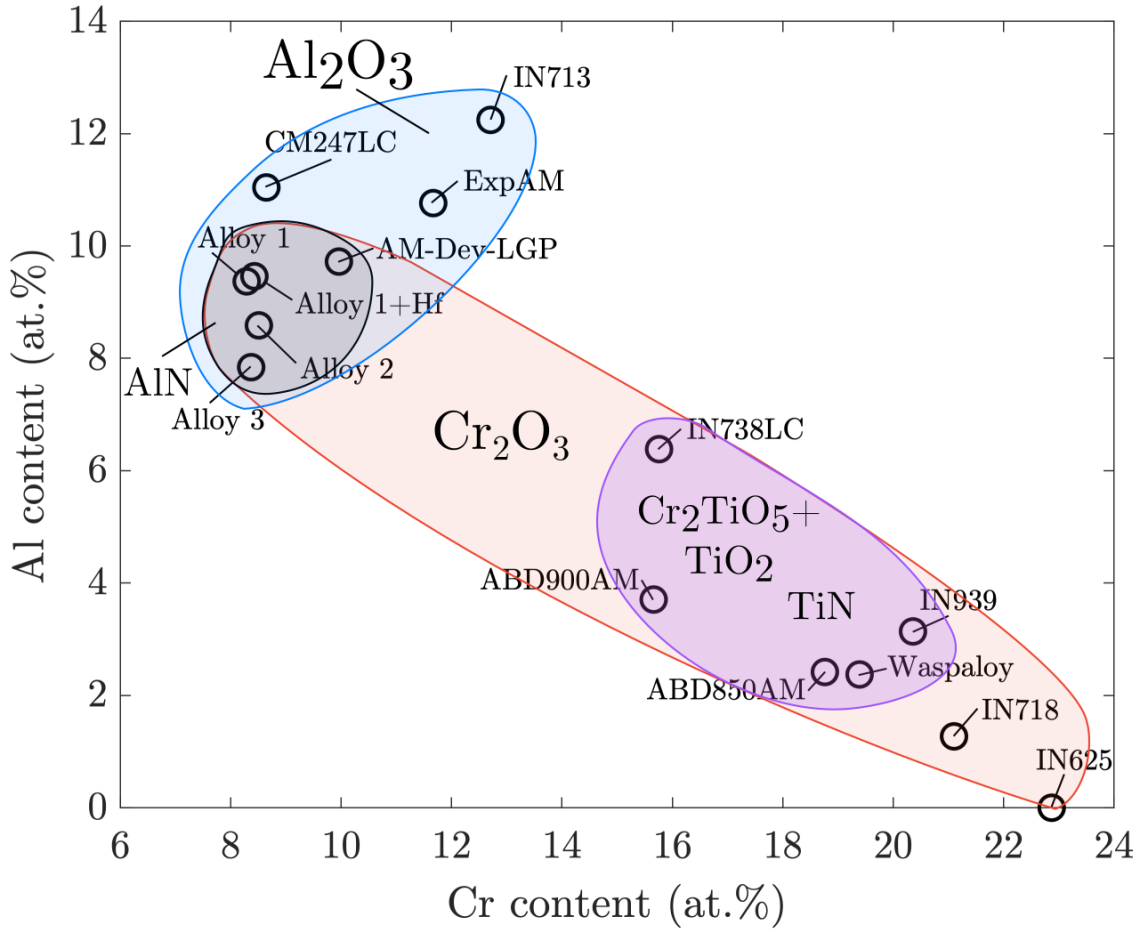

Fig. 6.11 Plot of Al vs Cr content (at%.) for the 15 alloy compositions with regions of different oxide phases highlighted in groups.

Chapter 7

Conclusions and future work

7.1 Conclusions

The aim of this research was to investigate the influence of composition on the processability and performance of Ni-based superalloys. A combination of experimental work and modelling performed on a wide range alloy compositions resulted in key insights that allow further development of new alloys tailored for AM.

Printing trials of IN939 and CM247LC which varied the spatial distribution and density of laser pulses were unable to eliminate cracking entirely. However, it was demonstrated that reduction of cracking in heritage alloys designed for investment casting is possible, albeit at the cost of incurring significant material anisotropy. The propensity for CM247LC to crack as a function of the hatch distance and velocity within the processing regime investigated here correlates strongly with the nature of the resulting microstructure: namely, the grain size, texture, and proportion of high angle grain boundaries. From this it is concluded that new novel grades of alloys are required in order to achieve crack free material with microstructure tailored for mechanical properties, and not crack reduction.

The dependence of alloy composition on processability was proven through an analysis of 12 different alloy compositions. High resolution microscopy revealed the presence of solid-state and solidification cracks in all the cracked alloys. Quantitative stereology confirmed the IN713 and ExpAM alloys were prone to solid-state cracking, whilst CM247LC, IN738LC, ABD850AM+CB and IN939 exhibited a tendency towards solidification cracking. The heritage alloys IN625, IN718, and Waspaloy as well as the novel compositions ABD850AM, ABD900AM, Alloy 1, Alloy 2, Alloy 3/AM-Dev, AM-Dev-LGP exhibit increased additive manufacturability with respect to their reduced susceptibility to solid-state and solidification cracks.

Solidification cracking occurred in the alloys that freeze over a wide temperature interval. Increased C content and the presence of Hf and Ta enriched crack tips is characteristic of alloys which cracked by the solidification mechanism. Solidification cracking criteria following Clyne-Davies, Rappaz, and Kou have been considered and are shown to have predictive power. However, they do not account for the composition-dependent near-solidus mechanical properties, which may be important for crack-free processing. A modified Clyne-Davies model is proposed to account for this.

Solid-state cracking arises from a significant loss of tensile ductility at 800 °C (<7%). This was observed in all the unprocessable alloys, and was particularly pronounced in IN713 and ExpAM alloys which exhibited ductility of <1%. This brittleness was intergranular in form, implying grain boundary weakness, and was exacerbated by increased solid solution strengtheners such as W, Ta, Al, and Ti. Mapping the high temperature tensile properties of all the as-printed alloys showed a typical strength-ductility trade-off. Crucially, a property space was identified along the pareto front where the ductility is greater than 7% and the strength as elevated as the most high performance alloys designed for investment casting. This confirms the ability to design alloys for AM of equivalent tensile performance as heritage such as IN738LC, IN939, and

CM247LC. A novel constrained bar test was developed to establish the extent of stress relaxation by creep during processing. Thermal-elastic-plastic-viscoplastic analysis of the test showed that stress relaxation was negligible at cooling rates of 50-100 °C/s. Thus, the effects of stress relaxation are concluded to be inconsequential during AM where cooling rates range between 10^4-10^6 °C/s. This means there is potential for printing alloys of creep resistance equivalent to the very best conventionally-cast grades, provided they also resist solidification cracking.

Testing and characterisation of the novel Alloys 1, 2, and 3 gave valuable insights into the influence of composition on performance and the design of heat treatments for AM. Investigation of influence of the (Nb+Ta)/Al ratio on performance showed that alloys of equal γ' volume fraction can be tailored for different purposes. Increasing the (Nb+Ta)/Al ratio increases the yield stress of the alloy, consistent with enhanced energies of planar faults. However, this comes at the expense of the alloy cost, oxidation resistance, and the oxidation-assisted cracking resistance, which is of increasing importance for the intended applications. The response of the as-processed material to heat treatment was found to be critically important. Heat treatment conditions absent solutionizing need to be chosen carefully; super-solvus heat treatment caused embrittlement due to the texture of the recrystallized grain structure and the local microstructure of the grain boundaries which then consist of γ and coarse blocky carbides. In contrast, sub-solvus heat treatment was effective for the maintenance of ductility and strength, due to a fine decoration of γ' at the grain boundaries. The performance of these 3 alloy variants was contrasted with the heritage alloy CM247LC. The new alloys outperformed CM247LC in all but creep life and tensile strength at temperatures greater than 900 °C. The new grade of superalloy was shown to be processable when producing simple cube geometries but also for a more complex miniaturized turbine blade geometry. This was confirmed by optical microscopy, scanning electron

microscopy, and high resolution micro x-ray computed tomography. Conversely, the benchmark CM247LC alloy exhibited extensive cracking which was exacerbated by the complex geometry. This further demonstrated the urgent need to develop a better understanding of the composition dependence of processability and performance.

An experimental dataset has been developed comparing the oxidation resistance of 7 novel and 8 heritage Ni-based superalloys processed by AM. Correlation between their Al content, mass gained during testing, depletion zone size, and oxide layer thickness was found. This was coupled with phase identification to develop compositional processing maps to inform for alloy design. The compositions of Al content greater than 7.8 at% were found to rapidly form Al_2O_3 at 1000 °C. A threshold for stable alumina formation was identified between 6.4 and 7.8 at% Al, though only alloys with Al content greater than 10 at% were concluded to have formed a stable Al_2O_3 layer fast enough to avoid the early uptake of nitrogen and ensuing formation of AlN. The database and set of empirical guidelines developed in this study can be used moving forward to inform models and alloy design decisions.

This work confirms that some Ni-based superalloys are indeed more processable than others and elucidates the factors that govern this so-called 'processability'. Furthermore, it shows there is scope for designing new grades of Ni-based superalloy of high performance which are more amenable to AM than the heritage alloys which were designed for conventional processing routes.

7.2 Recommendations for future work

This body of research gives rise to several branches of further questions. The primary recommendations for further work include: (1) improving understanding of the factors influencing the ductility limit; (2) developing methodologies for assessing the liquation

and strain-age cracking susceptibility of the alloys; and (3) the performance of critical tests needed to fully assess the performance of alloys produced for AM.

7.2.1 Factors influencing the ductility limit

The work presented in Chapter 4 considered the root cause of solid-state cracking and how this varied across the alloys. An empirical model for predicting the as-printed strength of the alloys as a function of composition was established. However, no model for predicting the ductility as a function of alloy composition has been produced. The factors influencing this ductility are numerous. Carbide size, volume fraction, morphology, and composition have all been discussed in literature as having a potential impact. The morphology of the grain boundaries themselves has also been shown to influence how strain is accommodated at the local microstructure level and the resulting macroscopic ductility [49, 48]. This understanding that the trade-off between the strength of the grain boundary and grain interior dictates the strain localisation which in turn influences the macroscopic strain limit is generally accepted, but not unambiguously confirmed. It is suggested that moderate temperature tensile tests be performed in an SEM in order to observe the strain localisation around microscopic features such as grain boundaries and carbides. This in turn could be related to the macroscopic strain and carried for various compositions; examples of similar work include papers by Kontis et al. [50] and Summers et al. [260].

Figure 7.1 demonstrates the target as-printed properties for superalloys designed for AM. As of yet, the flow stress on the y-axis can be estimated on the basis of alloy composition (see Figure 4.26) but not ductility on the x-axis. The development of this type of predictive power would be invaluable for alloy design, given that a predictor for solid-state cracking has been established here as 7 % ductility in the ductility dip temperature regime.

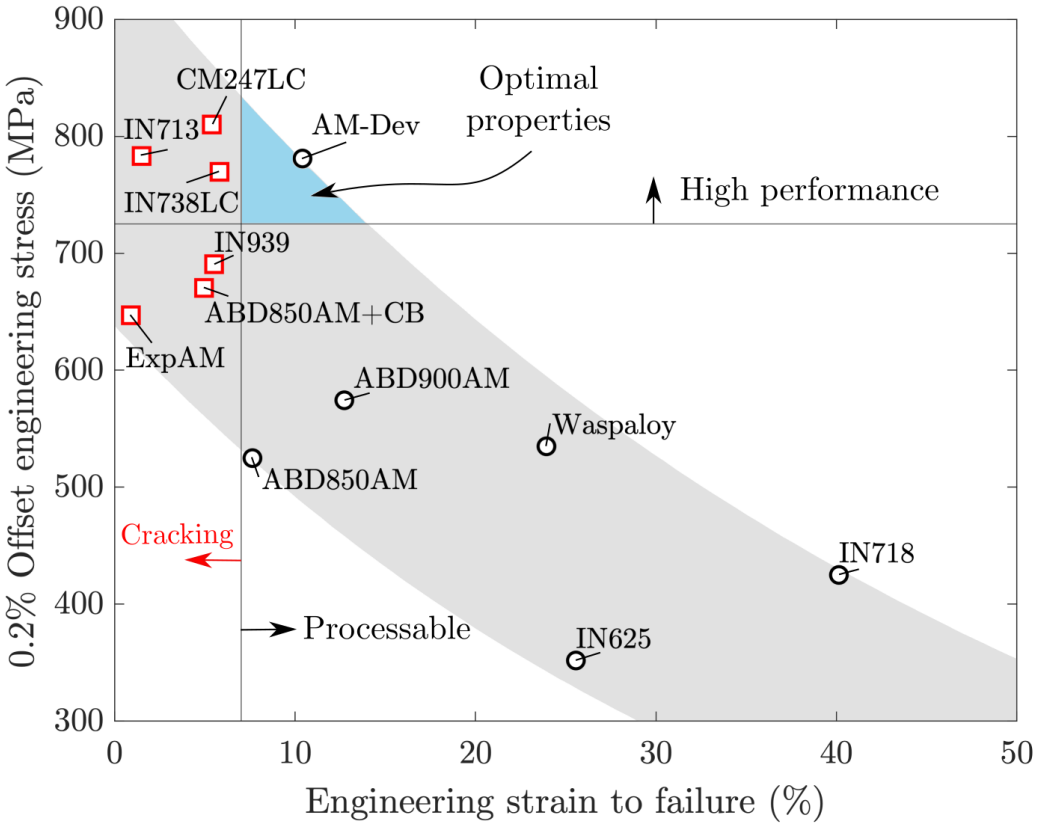

Fig. 7.1 The as-printed flow stress vs ductility for the 12 alloys discussed in Chapter 4. The ductility threshold below which alloys crack during processing is highlighted as well as a flow stress – arbitrarily chosen – representing a performance threshold. These thresholds superimposed on the empirically determined strength/ductility trade-off are used to identify the optimal property space that needs to be targeted when designing superalloys for AM.

7.2.2 Assessment of liquation and strain-age cracking susceptibility

The solid-state and solidification cracking mechanisms have been studied here in-depth. The methods used to assess an alloy's susceptibility to these defects can be adapted for the liquation and strain-age mechanisms. The propensity of liquation to take place can be ranked through use of electro thermal mechanical testing. Heating an ETMT sample under a consistent load of 20-100 MPa while slowly heating the sample from room temperature to its liquidus would cause any non-equilibrium second phase particle to undergo constitutional liquation, when severe enough the sample would fail. Establishing the temperature at failure, temperature at failure relative to the solidus, the time to failure (given constant heating rate), and the composition of liquated films observed on the fracture surface would all shed light on the liquation cracking susceptibility. This requires experimental consistency and precision and its success is limited by the accuracy of the thermo-couple and welding procedure. In order to assess the strain-age cracking susceptibility, ETMT samples could be held under strain control just below the γ' solvus and the stress developed during precipitation could be assessed similar to the constrained bar test presented in Chapter 4. The test has a major caveat, since it would capture the stress accumulation during precipitation but also instantaneously relax that stress depending on the γ' precipitation kinetics. Assessment of resistivity in-situ may offer a solution to de-coupling these competing factors.

7.2.3 Thermo-mechanical fatigue

The need for thermo-mechanical fatigue testing on superalloys alloys designed for AM is pressing. The currently published alloys summarized in Table 2.3 have all been characterised to an extent in terms of tensile and creep performance but it is

recommended that thermo-mechanical fatigue and dwell fatigue tests in particular are performed. Creep resistance is emphasised as the critical to maximize [261–264], but a balance of moderate temperature strength, oxidation assisted cracking resistance, creep resistance, must be struck for practical engineering purposes.

References

[1] Roger C Reed. *The superalloys: fundamentals and applications*. Cambridge university press, 2008.

[2] GE Aviation. GE9X Commercial Aircraft Engine, 2018.

[3] Siemens. Hyflexpower: The world's first integrated power-to-X-to-power hydrogen gas turbine demonstrator, 2020.

[4] CFMAeroengines. The LEAP Engine, 2019.

[5] Iain Waugh, Ed Moore, Greig Blandin, and William Dick-Cleland. Additive manufacture of rocket engine combustion chambers using the ABD-900AM nickel superalloys.

[6] EOS. Additive Manufacturing, 2019.

[7] D Barba, E Alabort, Stella Pedrazzini, DM Collins, AJ Wilkinson, PAJ Bagot, MP Moody, C Atkinson, A Jérusalem, and RC Reed. On the microtwinning mechanism in a single crystal superalloy. *Acta Materialia*, 135:314–329, 2017.

[8] Chinnapat Panwisawas, Yuanbo T Tang, and Roger C Reed. Metal 3D printing as a disruptive technology for superalloys. *Nature Communications*, 11(1):1–4, 2020.

[9] Yuanbo T Tang, Chinnapat Panwisawas, Joseph N Ghoussoub, Yilun Gong, John W-G Clark, André A-N Németh, D Graham McCartney, and Roger C Reed. Alloys-by-design: Application to new superalloys for additive manufacturing. *Acta Materialia*, 202:417–436, 2021.

[10] Michael Cloots, Peter J Uggowitzer, and Konrad Wegener. Investigations on the microstructure and crack formation of IN738LC samples processed by selective laser melting using Gaussian and doughnut profiles. *Materials & Design*, 89:770–784, 2016.

[11] Jinghao Xu, Hans Gruber, Ru Lin Peng, and Johan Moverare. A Novel γ'-Strengthened Nickel-Based Superalloy for Laser Powder Bed Fusion. *Materials*, 13(21):4930, 2020.

[12] Jinghao Xu. *Alloy Design and Characterization of γ' Strengthened Nickel-based Superalloys for Additive Manufacturing*. PhD thesis, Linköping University Electronic Press, 2021.

[13] Ali Gökhan Demir, Paolo Colombo, and Barbara Previtali. From pulsed to continuous wave emission in SLM with contemporary fiber laser sources: effect of temporal and spatial pulse overlap in part quality. *The International Journal of Advanced Manufacturing*, 91(5-8):2701–2714, 2017.

[14] Ning Zhou, Austin D Dicus, Stephane AJ Forsik, Tao Wang, Gian A Colombo, and Mario E Epler. Development of a New Alumina-Forming Crack-Resistant High-γ' Fraction Ni-Base Superalloy for Additive Manufacturing. In *Superalloys 2020*, pages 1046–1054. Springer, 2020.

[15] Luke Nelson Carter. *Selective laser melting of nickel superalloys for high temperature applications*. PhD thesis, University of Birmingham, 2013.

[16] Daniel Monceau and Bernard Pieraggi. Determination of parabolic rate constants from a local analysis of mass-gain curves. *Oxidation of metals*, 50(5):477–493, 1998.

[17] U Krupp and H-J Christ. Selective oxidation and internal nitridation during high-temperature exposure of single-crystalline nickel-base superalloys. *Metallurgical and Materials Transactions A*, 31(1):47–56, 2000.

[18] C Li, J-F Liu, X-Y Fang, and Y-B Guo. Efficient predictive model of part distortion and residual stress in selective laser melting. *Additive Manufacturing*, 17:157–168, 2017.

[19] Mohammad Masoomi, Scott M Thompson, and Nima Shamsaei. Laser powder bed fusion of Ti-6Al-4V parts: Thermal modeling and mechanical implications. *International Journal of Machine Tools and Manufacture*, 118:73–90, 2017.

[20] Chinnapat Panwisawas, Yuanbo Tony Tang, Joseph Ghoussoub, and Roger C Reed. Additive manufacturability of nickel-based superalloys: Composition-process induced vapourization. In Sammy Tin, Mark Hardy, Justin Clews, Jonathan Cormier, Qiang Feng, John Marcin, Chris O'Brien, and Akane Suzuki, editors, *Superalloys 2020*, pages 1055–1065. Springer, 2020.

[21] Patcharapit Promoppatum, Shi-Chune Yao, P Chris Pistorius, and Anthony D Rollett. A comprehensive comparison of the analytical and numerical prediction of the thermal history and solidification microstructure of Inconel 718 products made by laser powder-bed fusion. *Engineering*, 3(5):685–694, 2017.

[22] YP Yang, M Jamshidinia, P Boulware, and SM Kelly. Prediction of microstructure, residual stress, and deformation in laser powder bed fusion process. *Computational Mechanics*, 61(5):599–615, 2018.

[23] Paraskevas Kontis. *A study on the effect of grain boundary elements on polycrystalline superalloys*. PhD thesis, University of Oxford, 2016.

[24] Michael Schmidt and Hod Lipson. Distilling free-form natural laws from experimental data. *science*, 324(5923):81–85, 2009.

[25] Tarasankar DebRoy, HL Wei, JS Zuback, T Mukherjee, JW Elmer, JO Milewski, Allison Michelle Beese, A Wilson-Heid, A De, and W Zhang. Additive manufacturing of metallic components–process, structure and properties. *Progress in Materials Science*, 92:112–224, 2018.

[26] H-A. Roth, C-L. Davis, and R-C. Thomson. Modeling solid solution strengthening in nickel alloys. *Metallurgical and Materials Transactions A*, 28(6):1329–1335, 1997.

[27] Tresa M Pollock and Sammy Tin. Nickel-based superalloys for advanced turbine engines: chemistry, microstructure and properties. *Journal of propulsion and power*, 22(2):361–374, 2006.

[28] Metal-AM. GE Aviation reaches milestone with 100,000 fuel nozzle tips, 2021.

[29] GE Reports. Disruptive Additive Technology, 2018.

[30] Terry Wohlers and Tim Gornet. History of additive manufacturing. *Wohlers report*, 24(2014):118, 2014.

[31] Edouard Chauvet, Catherine Tassin, Jean-Jacques Blandin, Rémy Dendievel, and Guilhem Martin. Producing Ni-base superalloys single crystal by selective electron beam melting. *Scripta Materialia*, 152:15–19, 2018.

[32] Lei Wang, Nan Wang, and Nikolas Provatas. Liquid channel segregation and morphology and their relation with hot cracking susceptibility during columnar growth in binary alloys. *Acta Materialia*, 126:302–312, 2017.

[33] Catherine MF Rae and Roger C Reed. The precipitation of topologically close-packed phases in rhenium-containing superalloys. *Acta materialia*, 49(19):4113–4125, 2001.

[34] RC Reed and CMF Rae. Physical metallurgy of the nickel-based superalloys. In *Physical metallurgy*, pages 2215–2290. Elsevier, 2014.

[35] C Hammond and J Nutting. The physical metallurgy of superalloys and titanium alloys. *Metal science*, 11(10):474–490, 1977.

[36] CMF Rae and RC Reed. Primary creep in single crystal superalloys: origins, mechanisms and effects. *Acta Materialia*, 55(3):1067–1081, 2007.

[37] DJ Crudden, A Mottura, N Warnken, B Raeisinia, and RC Reed. Modelling of the influence of alloy composition on flow stress in high-strength nickel-based superalloys. *Acta Materialia*, 75:356–370, 2014.

[38] Atsushi Sato, Y-L Chiu, and RC Reed. Oxidation of nickel-based single-crystal superalloys for industrial gas turbine applications. *Acta Materialia*, 59(1):225–240, 2011.

[39] Carelyn E Campbell, William J Boettinger, and Ursula R Kattner. Development of a diffusion mobility database for Ni-base superalloys. *Acta Materialia*, 50(4):775–792, 2002.

[40] P Kontis, HA Mohd Yusof, S Pedrazzini, M Danaie, KL Moore, PAJ Bagot, MP Moody, CRM Grovenor, and RC Reed. On the effect of boron on grain boundary character in a new polycrystalline superalloy. *Acta Materialia*, 103:688–699, 2016.

[41] Markus Kolb, Lisa Patricia Freund, Fabian Fischer, Ivan Povstugar, Surendra Kumar Makineni, Baptiste Gault, Dierk Raabe, Julian Müller, Erdmann Spiecker, Steffen Neumeier, et al. On the grain boundary strengthening effect of boron in γ-γ' Cobalt-base superalloys. *Acta Materialia*, 145:247–254, 2018.

[42] Mahesh Chandran and SK Sondhi. First-principle calculation of APB energy in Ni-based binary and ternary alloys. *Modelling and Simulation in Materials Science and Engineering*, 19(2):025008, 2011.

[43] Sabin Sulzer and Roger Reed. Critical assessment 31: on the modelling of tertiary creep in single-crystal superalloys. *Materials Science and Technology*, 34(18):2174–2201, 2018.

[44] TM Smith, BD Esser, N Antolin, GB Viswanathan, T Hanlon, A Wessman, D Mourer, W Windl, DW McComb, and MJ Mills. Segregation and η phase formation along stacking faults during creep at intermediate temperatures in a Ni-based superalloy. *Acta Materialia*, 100:19–31, 2015.

[45] Timothy M Smith, Raymond R Unocic, Hallee Deutchman, and Michael J Mills. Creep deformation mechanism mapping in nickel base disk superalloys. *Materials at High Temperatures*, 33(4-5):372–383, 2016.

[46] TM Smith, Y Rao, Y Wang, M Ghazisaeidi, and MJ Mills. Diffusion processes during creep at intermediate temperatures in a Ni-based superalloy. *Acta Materialia*, 141:261–272, 2017.

[47] R Raj and MF Ashby. On grain boundary sliding and diffusional creep. *Metallurgical transactions*, 2(4):1113–1127, 1971.

[48] Yuanbo T Tang, Phani Karamched, Junliang Liu, Jack C Haley, Roger C Reed, and Angus J Wilkinson. Grain boundary serration in nickel alloy Inconel 600: Quantification and mechanisms. *Acta Materialia*, 181:352–366, 2019.

[49] E Alabort, D Barba, S Sulzer, M Lißner, N Petrinic, and RC Reed. Grain boundary properties of a nickel-based superalloy: characterisation and modelling. *Acta Materialia*, 151:377–394, 2018.

[50] Paraskevas Kontis, Enrique Alabort, Daniel Barba, David M Collins, Angus J Wilkinson, and Roger C Reed. On the role of boron on improving ductility in a new polycrystalline superalloy. *Acta Materialia*, 124:489–500, 2017.

[51] Paraskevas Kontis, Aleksander Kostka, Dierk Raabe, and Baptiste Gault. Influence of composition and precipitation evolution on damage at grain boundaries in a crept polycrystalline Ni-based superalloy. *Acta Materialia*, 166:158–167, 2019.

[52] HY Bor, CG Chao, CY Ma, et al. The influence of magnesium on carbide characteristics and creep behavior of the Mar-M247 superalloy. *Scripta materialia*, 38(2):329–335, 1997.

[53] Carolin Körner, Markus Ramsperger, Carla Meid, Daniel Bürger, Philipp Wollgramm, Marion Bartsch, and Gunther Eggeler. Microstructure and mechanical properties of CMSX-4 single crystals prepared by additive manufacturing. *Metallurgical and Materials Transactions A*, 49(9):3781–3792, 2018.

[54] Iver E Anderson, Emma MH White, and Ryan Dehoff. Feedstock powder processing research needs for additive manufacturing development. *Current Opinion in Solid State and Materials Science*, 22(1):8–15, 2018.

[55] Zackary Snow, Richard Martukanitz, and Sanjay Joshi. On the development of powder spreadability metrics and feedstock requirements for powder bed fusion additive manufacturing. *Additive Manufacturing*, 28:78–86, 2019.

[56] Sebastian Berumen, Florian Bechmann, Stefan Lindner, Jean-Pierre Kruth, and Tom Craeghs. Quality control of laser-and powder bed-based Additive Manufacturing (AM) technologies. *Physics procedia*, 5:617–622, 2010.

[57] G Chen, SY Zhao, P Tan, J Wang, CS Xiang, and HP Tang. A comparative study of Ti-6Al-4V powders for additive manufacturing by gas atomization, plasma rotating electrode process and plasma atomization. *Powder technology*, 333:38–46, 2018.

[58] Alan Lawley. Atomization of specialty alloy powders. *JOM*, 33(1):13–18, 1981.

[59] Iver E Anderson and Robert L Terpstra. Progress toward gas atomization processing with increased uniformity and control. *Materials Science and Engineering: A*, 326(1):101–109, 2002.

[60] Stanislav Lagutkin, Lydia Achelis, Sheikhali Sheikhaliev, Volker Uhlenwinkel, and Vikas Srivastava. Atomization process for metal powder. *Materials Science and Engineering: A*, 383(1):1–6, 2004.

[61] Chu Lun Alex Leung, Sebastian Marussi, Michael Towrie, Robert C Atwood, Philip J Withers, and Peter D Lee. The effect of powder oxidation on defect formation in laser additive manufacturing. *Acta Materialia*, 166:294–305, 2019.

[62] S Catchpole-Smith, N Aboulkhair, L Parry, C Tuck, IA Ashcroft, and AJAM Clare. Fractal scan strategies for selective laser melting of unweldable nickel superalloys. *Additive Manufacturing*, 15:113–122, 2017.

[63] Marc Dimter, Ralph Mayer, Ludger Hümmeler, Rainer Salzberger, Juha Kotila, and Tatu Syvänen. Method and device for manufacturing a three-dimensional object, October 11 2011. US Patent 8,034,279.

[64] William J Sames, F-A List, Sreekanth Pannala, Ryan R Dehoff, and Sudarsanam Suresh Babu. The metallurgy and processing science of metal additive manufacturing. *International Materials Reviews*, 61(5):315–360, 2016.

[65] Sudarsanam Suresh Babu, Narendran Raghavan, Jacob Raplee, Sarah J Foster, Curtis Frederick, Michael Haines, R Dinwiddie, MK Kirka, A Plotkowski, Yousub Lee, et al. Additive manufacturing of nickel superalloys: opportunities for innovation and challenges related to qualification. *Metallurgical and Materials Transactions A*, 49(9):3764–3780, 2018.

[66] D Dye, O Hunziker, and RC Reed. Numerical analysis of the weldability of superalloys. *Acta Materialia*, 49(4):683–697, 2001.

[67] Chinnapat Panwisawas, Bama Perumal, R Mark Ward, Nathanael Turner, Richard P Turner, Jeffery W Brooks, and Hector C Basoalto. Keyhole formation and thermal fluid flow-induced porosity during laser fusion welding in titanium alloys: Experimental and modelling. *Acta Materialia*, 126:251–263, 2017.

[68] Saad A Khairallah, Andrew T Anderson, Alexander Rubenchik, and Wayne E King. Laser powder-bed fusion additive manufacturing: Physics of complex melt flow and formation mechanisms of pores, spatter, and denudation zones. *Acta Materialia*, 108:36–45, 2016.

[69] Zhengtao Gan, Hao Liu, Shaoxia Li, Xiuli He, and Gang Yu. Modeling of thermal behavior and mass transport in multi-layer laser additive manufacturing of Ni-based alloy on cast iron. *International Journal of Heat and Mass Transfer*, 111:709–722, 2017.

[70] HC Basoalto, C Panwisawas, Y Sovani, MJ Anderson, RP Turner, B Saunders, and JW Brooks. A computational study on the three-dimensional printability

of precipitate-strengthened nickel-based superalloys. *Proceedings of the Royal Society A*, 474(2220):20180295, 2018.

[71] Magnus J Anderson, Chinnapat Panwisawas, Yogesh Sovani, Richard P Turner, Jeffery W Brooks, and Hector C Basoalto. Mean-field modelling of the intermetallic precipitate phases during heat treatment and additive manufacture of Inconel 718. *Acta Materialia*, 156:432–445, 2018.

[72] G Vastola, G Zhang, QX Pei, and Y-W Zhang. Modeling and control of remelting in high-energy beam additive manufacturing. *Additive Manufacturing*, 7:57–63, 2015.

[73] Mohammad S Alsoufi and AE Elsayed. Warping deformation of desktop 3D printed parts manufactured by open source fused deposition modeling (FDM) system. *International Journal of Mechanical and Mechatronics Engineering*, 17:7–16, 2017.

[74] Moataz M Attallah, Rachel Jennings, Xiqian Wang, and Luke N Carter. Additive manufacturing of Ni-based superalloys: The outstanding issues. *MRS Bulletin*, 41(10):758–764, 2016.

[75] Panagiotis Michaleris, Andrew DeBiccari, et al. Prediction of welding distortion. *Welding Journal-Including Welding Research Supplement*, 76(4):172s, 1997.

[76] CL Tsai, SC Park, WT Cheng, et al. Welding distortion of a thin-plate panel structure. *Welding Jorunal New York*, 78:156–s, 1999.

[77] T Schenk, IM Richardson, Martin Kraska, and S Ohnimus. A study on the influence of clamping on welding distortion. *Computational Materials Science*, 45(4):999–1005, 2009.

[78] H Farhangi, S Norouzi, and M Nili-Ahmadabadi. Effects of casting process variables on the residual stress in Ni-base superalloys. *Journal of Materials Processing Technology*, 153:209–212, 2004.

[79] Chinnapat Panwisawas, Neil D'Souza, David M Collins, and Ayan Bhowmik. The contrasting roles of creep and stress relaxation in the time-dependent deformation during in-situ cooling of a nickel-base single crystal superalloy. *Scientific reports*, 7(1):1–14, 2017.

[80] Erik R Denlinger, Jeff Irwin, and Pan Michaleris. Thermomechanical modeling of additive manufacturing large parts. *Journal of Manufacturing Science and Engineering*, 136(6), 2014.

[81] Erik R Denlinger and Pan Michaleris. Effect of stress relaxation on distortion in additive manufacturing process modeling. *Additive Manufacturing*, 12:51–59, 2016.

[82] G Vastola, G Zhang, QX Pei, and Y-W Zhang. Controlling of residual stress in additive manufacturing of Ti6Al4V by finite element modeling. *Additive Manufacturing*, 12:231–239, 2016.

[83] T Mukherjee, W Zhang, and Tarasankar DebRoy. An improved prediction of residual stresses and distortion in additive manufacturing. *Computational Materials Science*, 126:360–372, 2017.

[84] Jack Francis and Linkan Bian. Deep learning for distortion prediction in laser-based additive manufacturing using big data. *Manufacturing Letters*, 20:10–14, 2019.

[85] Noha Peter, Zachary Pitts, Spencer Thompson, and Ankit Saharan. Benchmarking build simulation software for laser powder bed fusion of metals. *Additive Manufacturing*, 36:101531, 2020.

[86] Dirk Herzog, Vanessa Seyda, Eric Wycisk, and Claus Emmelmann. Additive manufacturing of metals. *Acta Materialia*, 117:371–392, 2016.

[87] V-D Divya, R Muñoz-Moreno, O-M-D-M Messé, J-S Barnard, S Baker, T Illston, and H-J Stone. Microstructure of selective laser melted CM247LC nickel-based superalloy and its evolution through heat treatment. *Materials Characterization*, 114:62–74, 2016.

[88] Umberto Scipioni Bertoli, Gabe Guss, Sheldon Wu, Manyalibo J Matthews, and Julie M Schoenung. In-situ characterization of laser-powder interaction and cooling rates through high-speed imaging of powder bed fusion additive manufacturing. *Materials & Design*, 135:385–396, 2017.

[89] Vivek Thampy, Anthony Y Fong, Nicholas P Calta, Jenny Wang, Aiden A Martin, Philip J Depond, Andrew M Kiss, Gabe Guss, Qingfeng Xing, Ryan T Ott, et al. Subsurface cooling rates and microstructural response during laser based metal additive manufacturing. *Scientific reports*, 10(1):1–9, 2020.

[90] Naresh Nadammal, Sandra Cabeza, Tatiana Mishurova, Tobias Thiede, Arne Kromm, Christoph Seyfert, Lena Farahbod, Christoph Haberland, Judith Ann Schneider, Pedro Dolabella Portella, et al. Effect of hatch length on the development of microstructure, texture and residual stresses in selective laser melted superalloy Inconel 718. *Materials & Design*, 134:139–150, 2017.

[91] R Muñoz-Moreno, VD Divya, SL Driver, OMDM Messé, T Illston, S Baker, MA Carpenter, and HJ Stone. Effect of heat treatment on the microstructure, texture and elastic anisotropy of the nickel-based superalloy CM247LC processed by selective laser melting. *Materials Science and Engineering: A*, 674:529–539, 2016.

[92] Andrew T Polonsky, McLean P Echlin, William C Lenthe, Ryan R Dehoff, Michael M Kirka, and Tresa M Pollock. Defects and 3D structural inhomogeneity in electron beam additively manufactured Inconel 718. *Materials Characterization*, 143:171–181, 2018.

[93] Ghoussoub Joseph N, Yuanbo Tang, and Roger C Reed. On the influence of alloy composition on the additive manufacturability of Ni-based superalloys. *Under Review*, 2021.

[94] Xiqian Wang, Luke N Carter, Bo Pang, Moataz M Attallah, and Michael H Loretto. Microstructure and yield strength of SLM-fabricated CM247LC Ni-superalloy. *Acta Materialia*, 128:87–95, 2017.

[95] Yuanbo T Tang, Joseph N Ghoussoub, Chinnapat Panwisawas, David M Collins, Sajjad Amirkhanlou, John W-G Clark, André A-N Németh, D Graham McCartney, and Roger C Reed. The effect of heat treatment on tensile yielding response of the new superalloy ABD-900AM for additive manufacturing. In Sammy Tin, Mark Hardy, Justin Clews, Jonathan Cormier, Qiang Feng, John Marcin, Chris O'Brien, and Akane Suzuki, editors, *Superalloys 2020*, pages 1055–1065. Springer, 2020.

[96] S Griffiths, H Ghasemi Tabasi, T Ivas, X Maeder, A De Luca, K Zweiacker, R Wróbel, J Jhabvala, RE Logé, and C Leinenbach. Combining alloy and process modification for micro-crack mitigation in an additively manufactured Ni-base superalloy. *Additive Manufacturing*, 36:101443, 2020.

[97] JC Lippold, WAIII Baeslack, and I Varol. Heat-affected zone liquation cracking in austenitic and duplex stainless steels. *Welding Journal (USA)*, 71(1):1, 1988.

[98] John C Lippold and Damian J Kotecki. Welding metallurgy and weldability of stainless steels, 2005.

[99] John C Lippold, Samuel D Kiser, and John N DuPont. *Welding metallurgy and weldability of nickel-base alloys*. John Wiley & Sons, 2011.

[100] John C Lippold et al. *Welding metallurgy and weldability*. Wiley Online Library, 2015.

[101] HL Wei, HKDH Bhadeshia, SA David, and T DebRoy. Harnessing the scientific synergy of welding and additive manufacturing. *Science and Technology of Welding and Joining*, pages 1–6, 2019.

[102] Luke N Carter, Moataz M Attallah, and Roger C Reed. Laser powder bed fabrication of nickel-base superalloys: influence of parameters; characterisation, quantification and mitigation of cracking. *Superalloys*, 2012:577–586, 2012.

[103] Luke N Carter, Christopher Martin, Philip J Withers, and Moataz M Attallah. The influence of the laser scan strategy on grain structure and cracking behaviour in SLM powder-bed fabricated nickel superalloy. *Journal of Alloys and Compounds*, 615:338–347, 2014.

[104] Luke N Carter, Xiqian Wang, Noriko Read, Raja Khan, M Aristizabal, Khamis Essa, and Moataz M Attallah. Process optimisation of selective laser melting using energy density model for nickel based superalloys. *Materials Science and Technology*, 32(7):657–661, 2016.

[105] Edouard Chauvet, Paraskevas Kontis, Eric A Jägle, Baptiste Gault, Dierk Raabe, Catherine Tassin, Jean-Jacques Blandin, Rémy Dendievel, Benjamin Vayre, Stéphane Abed, et al. Hot cracking mechanism affecting a non-weldable Ni-based superalloy produced by selective Electron Beam Melting. *Acta Materialia*, 142:82–94, 2018.

[106] Avinash Hariharan, Lin Lu, Jeroen Risse, Aleksander Kostka, Baptiste Gault, Eric A Jägle, and Dierk Raabe. Misorientation-dependent solute enrichment at interfaces and its contribution to defect formation mechanisms during laser additive manufacturing of superalloys. *Physical Review Materials*, 3(12):123602, 2019.

[107] M Rappaz, A Jacot, and William J Boettinger. Last-stage solidification of alloys: theoretical model of dendrite-arm and grain coalescence. *Metallurgical and Materials Transactions A*, 34(3):467–479, 2003.

[108] Zhiyuan Liu, Dandan Zhao, Pei Wang, Ming Yan, Can Yang, Zhangwei Chen, Jian Lu, and Zhaoping Lu. Additive manufacturing of metals: Microstructure evolution and multistage control. *Journal of Materials Science & Technology*, 2021.

[109] Chunlei Qiu, Haoxiu Chen, Qi Liu, Sheng Yue, and Huaming Wang. On the solidification behaviour and cracking origin of a nickel-based superalloy during selective laser melting. *Materials Characterization*, 148:330–344, 2019.

[110] Zhengrong Yu, Chuan Guo, Shuang Han, Xiaogang Hu, Lijie Cao, Zhen Xu, Hui Ding, and Qiang Zhu. The effect of Hf on solidification cracking inhibition of IN738LC processed by Selective Laser Melting. *Materials Science and Engineering: A*, 804:140733, 2021.

[111] Trevor Keller, Greta Lindwall, Supriyo Ghosh, Li Ma, Brandon M Lane, Fan Zhang, Ursula R Kattner, Eric A Lass, Jarred C Heigel, Yaakov Idell, et al. Application of finite element, phase-field, and CALPHAD-based methods to additive manufacturing of Ni-based superalloys. *Acta materialia*, 139:244–253, 2017.

[112] Jiayu Xu, Yutian Ding, Yubi Gao, Hao Wang, Yong Hu, and Dong Zhang. Grain refinement and crack inhibition of hard-to-weld Inconel 738 alloy by altering the scanning strategy during selective laser melting. *Materials & Design*, 209:109940, 2021.

[113] Dacian Tomus, Paul A Rometsch, Martin Heilmaier, and Xinhua Wu. Effect of minor alloying elements on crack-formation characteristics of Hastelloy-X manufactured by selective laser melting. *Additive Manufacting*, 16:65–72, 2017.

[114] Arthur Després, Stoichko Antonov, Charlotte Mayer, Catherine Tassin, Muriel Veron, Jean-Jacques Blandin, Paraskevas Kontis, and Guilhem Martin. On the role of boron, carbon and zirconium on hot cracking and creep resistance of an additively manufactured polycrystalline superalloy. *Materialia*, page 101193, 2021.

[115] M Rappaz, J-M Drezet, and Met Gremaud. A new hot-tearing criterion. *Metallurgical and Materials Transactions A*, 30(2):449–455, 1999.

[116] T-W Clyne and G-J Davies. Influence of composition on solidification cracking susceptibility in binary alloy systems. *British Foundryman*, 74:65–73, 1981.

[117] TW Clyne and W Kurz. Solute redistribution during solidification with rapid solid state diffusion. *Metallurgical and Materials Transactions A*, 12(6):965–971, 1981.

[118] TW Clyne, M Wolf, and W Kurz. The effect of melt composition on solidification cracking of steel, with particular reference to continuous casting. *Metallurgical and Materials Transactions B*, 13(2):259–266, 1982.

[119] Sindo Kou. Solidification and liquation cracking issues in welding. *JOM*, 55(6):37–42, 2003.

[120] OA Ojo, NL Richards, and MC Chaturvedi. Contribution of constitutional liquation of gamma prime precipitate to weld HAZ cracking of cast Inconel 738 superalloy. *Scripta Materialia*, 50(5):641–646, 2004.

[121] RG Thompson, DE Mayo, and B Radhakrishnan. The relationship between carbon content, microstructure, and intergranular liquation cracking in cast nickel alloy 718. *Metallurgical Transactions A*, 22(2):557–567, 1991.

[122] B Radhakrishnan and RG Thompson. The effect of weld heat-affected zone (HAZ) liquation kinetics on the hot cracking susceptibility of alloy 718. *Metallurgical and Materials Transactions A*, 24(6):1409–1422, 1993.

[123] André Seidel, Thomas Finaske, Ariane Straubel, Horst Wendrock, Tim Maiwald, Mirko Riede, Elena Lopez, Frank Brueckner, and Christoph Leyens. Additive Manufacturing of Powdery Ni-Based Superalloys Mar-M-247 and CM 247 LC

in Hybrid Laser Metal Deposition. *Metallurgical and Materials Transactions A*, 49(9):3812–3830, 2018.

[124] Jianjun Xu, Xin Lin, Yufan Zhao, Pengfei Guo, Xiaoli Wen, Qiuge Li, Haiou Yang, Hongbiao Dong, Lei Xue, and Weidong Huang. HAZ Liquation Cracking Mechanism of IN-738LC Superalloy Prepared by Laser Solid Forming. *Metallurgical and Materials Transactions A*, 49(10):5118–5136, 2018.

[125] Yao Li, Kai Chen, and Nobumichi Tamura. Mechanism of heat affected zone cracking in Ni-based superalloy DZ125L fabricated by laser 3D printing technique. *Materials & Design*, 150:171–181, 2018.

[126] Jianjun Xu, Xin Lin, Pengfei Guo, Hongbiao Dong, Xiaoli Wen, Qiuge Li, Lei Xue, and Weidong Huang. The initiation and propagation mechanism of the overlapping zone cracking during laser solid forming of IN-738LC superalloy. *Journal of Alloys and Compounds*, 749:859–870, 2018.

[127] B Radhakrishnan and RG Thompson. A model for the formation and solidification of grain boundary liquid in the heat-affected zone (HAZ) of welds. *Metallurgical Transactions A*, 23(6):1783–1799, 1992.

[128] NE Nissley and JC Lippold. Ductility-dip cracking susceptibility of nickel-based weld metals part 1: strain-to-fracture testing. *Welding journal*, 87(10):257s–264s, 2008.

[129] AAN Németh, DJ Crudden, DEJ Armstrong, DM Collins, K Li, AJ Wilkinson, CRM Grovenor, and RC Reed. Environmentally-assisted grain boundary attack as a mechanism of embrittlement in a nickel-based superalloy. *Acta Materialia*, 126:361–371, 2017.

[130] A-J Ramirez and J-C Lippold. High temperature behavior of Ni-base weld metal: Part I. Ductility and microstructural characterization. *Materials Science and Engineering: A*, 380(1-2):259–271, 2004.

[131] G-A Young, T-E Capobianco, M-A Penik, B-W Morris, and J-J McGee. The mechanism of ductility dip cracking in nickel-chromium alloys. *Welding Journal*, 87(2):31, 2008.

[132] FF Noecker and JN DuPont. Metallurgical investigation into ductility dip cracking in Ni-based alloys: Part II. *Welding Journal*, 88(3):62s–77s, 2009.

[133] AW Dix and WF Savage. Factors influencing strain-age cracking in Inconel X-750. *Welding Journal*, 50(6):247, 1971.

[134] Ramazan Kayacan, Remzi Varol, and Olcay Kimilli. The effects of pre-and post-weld heat treatment variables on the strain-age cracking in welded Rene 41 components. *Materials Research Bulletin*, 39(14-15):2171–2186, 2004.

[135] MD Rowe. Ranking the resistance of wrought superalloys to strain-age cracking. *Welding journal*, 85(2):27s–33s, 2006.

[136] Seksak Asavavisithchai, Weerasak Homkrajai, and Panyawat Wangyao. Strain-age cracking after postweld heat treatments in Inconel 738 superalloy. *High Temperature Materials and Processes*, 29(1-2):61–68, 2010.

[137] DA Metzler. A Gleeble-based method for ranking the strain-age cracking susceptibility of Ni-based superalloys. *Welding Journal*, 87(10):249s–256s, 2008.

[138] David A Metzler. Strain-age cracking susceptibility of Ni-based superalloys as a function of strain rate, temperature, and alloy composition. *Welding Journal*, 91(6):64, 2012.

[139] Kamran Aamir Mumtaz, Poonjolai Erasenthiran, and Neil Hopkinson. High density selective laser melting of Waspaloy. *Journal of materials processing technology*, 195(1-3):77–87, 2008.

[140] Tuhin Mukherjee, JS Zuback, A De, and Tarasankar DebRoy. Printability of alloys for additive manufacturing. *Scientific reports*, 6(1):1–8, 2016.

[141] Ming Tang, P Chris Pistorius, and Jack L Beuth. Prediction of lack-of-fusion porosity for powder bed fusion. *Additive Manufacturing*, 14:39–48, 2017.

[142] T Mukherjee and T DebRoy. Mitigation of lack of fusion defects in powder bed fusion additive manufacturing. *Journal of Manufacturing Processes*, 36:442–449, 2018.

[143] T Mukherjee, HL Wei, A De, and T DebRoy. Heat and fluid flow in additive manufacturing–Part II: Powder bed fusion of stainless steel, and titanium, nickel and aluminum base alloys. *Computational Materials Science*, 150:369–380, 2018.

[144] Jinqiang Ning, Wenjia Wang, Bruno Zamorano, and Steven Y Liang. Analytical modeling of lack-of-fusion porosity in metal additive manufacturing. *Applied Physics A*, 125(11):1–11, 2019.

[145] Chunlei Qiu, Chinnapat Panwisawas, Mark Ward, Hector C Basoalto, Jeffery W Brooks, and Moataz M Attallah. On the role of melt flow into the surface structure and porosity development during selective laser melting. *Acta Materialia*, 96:72–79, 2015.

[146] Junji Shinjo and Chinnapat Panwisawas. Digital materials design by thermal-fluid science for multi-metal additive manufacturing. *Acta Materialia*, 210:116825, 2021.

[147] Wayne E King, Andrew T Anderson, Robert M Ferencz, Neil E Hodge, Chandrika Kamath, Saad A Khairallah, and Alexander M Rubenchik. Laser powder bed

fusion additive manufacturing of metals; physics, computational, and materials challenges. *Applied Physics Reviews*, 2(4):041304, 2015.

[148] Wayne King, Andrew T Anderson, Robert M Ferencz, Neil E Hodge, Chandrika Kamath, and Saad A Khairallah. Overview of modelling and simulation of metal powder bed fusion process at Lawrence Livermore National Laboratory. *Materials Science and Technology*, 31(8):957–968, 2015.

[149] Manyalibo J Matthews, Gabe Guss, Saad A Khairallah, Alexander M Rubenchik, Philip J Depond, and Wayne E King. Denudation of metal powder layers in laser powder-bed fusion processes. In *Additive Manufacturing Handbook*, pages 677–692. CRC Press, 2017.

[150] Aiden A Martin, Nicholas P Calta, Saad A Khairallah, Jenny Wang, Phillip J Depond, Anthony Y Fong, Vivek Thampy, Gabe M Guss, Andrew M Kiss, Kevin H Stone, et al. Dynamics of pore formation during laser powder bed fusion additive manufacturing. *Nature Communications*, 10(1):1–10, 2019.

[151] Nima Shamsaei, Aref Yadollahi, Linkan Bian, and Scott M Thompson. An overview of Direct Laser Deposition for additive manufacturing; Part ii: Mechanical behavior, process parameter optimization and control. *Additive Manufacturing*, 8:12–35, 2015.

[152] JP Oliveira, TG Santos, and RM Miranda. Revisiting fundamental welding concepts to improve additive manufacturing: from theory to practice. *Progress in Materials Science*, 107:100590, 2020.

[153] João Pedro Oliveira, AD LaLonde, and J Ma. Processing parameters in laser powder bed fusion metal additive manufacturing. *Materials & Design*, 193:108762, 2020.

[154] Jinghao Xu, Hans Gruber, Dunyong Deng, Ru Lin Peng, and Johan J Moverare. Short-term creep behavior of an additive manufactured non-weldable Nickel-base superalloy evaluated by slow strain rate testing. *Acta Materialia*, 179:142–157, 2019.

[155] Hossein Eskandari Sabzi, Suhyun Maeng, Xingzhong Liang, Marco Simonelli, Nesma T Aboulkhair, and Pedro EJ Rivera-Díaz-del Castillo. Controlling crack formation and porosity in laser powder bed fusion: Alloy design and process optimisation. *Additive Manufacturing*, 34:101360, 2020.

[156] Syed Z Uddin, Lawrence E Murr, Cesar A Terrazas, Philip Morton, David A Roberson, and Ryan B Wicker. Processing and characterization of crack-free aluminum 6061 using high-temperature heating in laser powder bed fusion additive manufacturing. *Additive Manufacturing*, 22:405–415, 2018.

[157] Ali Gökhan Demir, Luca Mazzoleni, Leonardo Caprio, Matteo Pacher, and Barbara Previtali. Complementary use of pulsed and continuous wave emission modes to stabilize melt pool geometry in laser powder bed fusion. *Optics & Laser Technology*, 113:15–26, 2019.

[158] Daniel Rosenthal. Mathematical theory of heat distribution during welding and cutting. *Welding journal*, 20:220–234, 1941.

[159] V Pavelic. Experimental and computed temperature histories in gas tungsten arc welding of thin plates. *Welding Journal Research Supplement*, 48:296–305, 1969.

[160] John Goldak, Aditya Chakravarti, and Malcolm Bibby. A new finite element model for welding heat sources. *Metallurgical transactions B*, 15(2):299–305, 1984.

[161] Babis Schoinochoritis, Dimitrios Chantzis, and Konstantinos Salonitis. Simulation of metallic powder bed additive manufacturing processes with the finite element method: A critical review. *Proceedings of the Institution of Mechanical Engineers, Part B: Journal of Engineering Manufacture*, 231(1):96–117, 2017.

[162] Henk Kaarle Versteeg and Weeratunge Malalasekera. *An introduction to computational fluid dynamics: the finite volume method*. Pearson education, 2007.

[163] T Mukherjee, HL Wei, A De, and T DebRoy. Heat and fluid flow in additive manufacturing–Part II: powder bed fusion of stainless steel, and titanium, nickel and aluminum base alloys. *Computational Materials Science*, 150:369–380, 2018.

[164] M Haines, A Plotkowski, CL Frederick, EJ Schwalbach, and Sudarsanam Suresh Babu. A sensitivity analysis of the columnar-to-equiaxed transition for Ni-based superalloys in electron beam additive manufacturing. *Computational Materials Science*, 155:340–349, 2018.

[165] YS Lee and Wei Zhang. Modeling of heat transfer, fluid flow and solidification microstructure of nickel-base superalloy fabricated by laser powder bed fusion. *Additive Manufacturing*, 12:178–188, 2016.

[166] YS Lee, Michael M Kirka, Ralph Barton Dinwiddie, Narendran Raghavan, J Turner, Ryan R Dehoff, and Sudarsanam Suresh Babu. Role of scan strategies on thermal gradient and solidification rate in electron beam powder bed fusion. *Additive Manufacturing*, 22:516–527, 2018.

[167] Ryan R Dehoff, MM Kirka, WJ Sames, H Bilheux, AS Tremsin, LE Lowe, and SS Babu. Site specific control of crystallographic grain orientation through electron beam additive manufacturing. *Materials Science and Technology*, 31(8):931–938, 2015.

[168] Thomas F Flint, Chinnapat Panwisawas, Yogesh Sovani, Mike C Smith, and HC Basoalto. Prediction of grain structure evolution during rapid solidification of high energy density beam induced re-melting. *Materials & Design*, 147:200–210, 2018.

[169] Sarah K Everton, Matthias Hirsch, Petros Stravroulakis, Richard K Leach, and Adam T Clare. Review of in-situ process monitoring and in-situ metrology for metal additive manufacturing. *Materials & Design*, 95:431–445, 2016.

[170] Emmanuel Rodriguez, Jorge Mireles, Cesar A Terrazas, David Espalin, Mireya A Perez, and Ryan B Wicker. Approximation of absolute surface temperature measurements of powder bed fusion additive manufacturing technology using in situ infrared thermography. *Additive Manufacturing*, 5:31–39, 2015.

[171] RP Turner, C Panwisawas, Y Lu, I Dhiman, HC Basoalto, and JW Brooks. Neutron tomography methods applied to a nickel-based superalloy additive manufacture build. *Materials Letters*, 230:109–112, 2018.

[172] Yan Ma, Dominic Cuiuri, Nicholas Hoye, Huijun Li, and Zengxi Pan. The effect of location on the microstructure and mechanical properties of titanium aluminides produced by additive layer manufacturing using in-situ alloying and gas tungsten arc welding. *Materials Science and Engineering: A*, 631:230–240, 2015.

[173] Chi Zhang, Fei Chen, Zhifeng Huang, Mingyong Jia, Guiyi Chen, Yongqiang Ye, Yaojun Lin, Wei Liu, Bingqing Chen, Qiang Shen, et al. Additive manufacturing of functionally graded materials: A review. *Materials Science and Engineering: A*, 764:138209, 2019.

[174] Ashley Reichardt, Andrew A Shapiro, Richard Otis, R Peter Dillon, John Paul Borgonia, Bryan W McEnerney, Peter Hosemann, and Allison M Beese. Advances in additive manufacturing of metal-based functionally graded materials. *International Materials Reviews*, 66(1):1–29, 2021.

[175] K Harris, GL Erickson, and RE Schwer. MAR-M247 derivations—CM247 LC DS alloy, CMSX single crystal alloys, properties and performance. *Superalloys*, 1984:221–230, 1984.

[176] Neil J Harrison, Iain Todd, and Kamran Mumtaz. Reduction of micro-cracking in nickel superalloys processed by Selective Laser Melting: A fundamental approach. *Acta Materialia*, 94:59–68, 2015.

[177] Maria L Montero-Sistiaga, Raya Mertens, Bey Vrancken, Xiebin Wang, Brecht Van Hooreweder, Jean-Pierre Kruth, and Jan Van Humbeeck. Changing the alloy composition of Al7075 for better processability by selective laser melting. *Journal of Materials Processing Technology*, 238:437–445, 2016.

[178] Joseph N Ghoussoub, Yuanbo T Tang, Chinnapat Panwisawas, André Németh, and Roger C Reed. On the influence of alloy chemistry and processing conditions on additive manufacturability of Ni-based superalloys. *Superalloys 2020 Proceedings*, pages 153–162, 2020.

[179] Y. T. Tang, J. N. Ghoussoub, C. Panwisawas, D.M Collins, S. Amirkhanlou, J.W.G. Clark, A. N. Németh, D.G. McCartney, and R. C. Reed. The effect of heat treatment on tensile yielding response of the new superalloy ABD-900AM for additive manufacturing. *Superalloys 2020*, 2020.

[180] Sean P Murray, Kira M Pusch, Andrew T Polonsky, Chris J Torbet, Gareth GE Seward, Ning Zhou, Stéphane AJ Forsik, Peeyush Nandwana, Michael M Kirka, Ryan R Dehoff, et al. A defect-resistant Co–Ni superalloy for 3D printing. *Nature Communications*, 11(1):1–11, 2020.

[181] Ashutosh Jena, Sila Ece Atabay, Alexandre B Gontcharov, Paul Lowden, and Mathieu Brochu. Laser Powder Bed Fusion of a New High gamma prime Ni-based Superalloy with Improved Weldability. *Materials & Design*, page 109895, 2021.

[182] Praveen Sreeramagiri, Ajay Bhagavatam, Abhishek Ramakrishnan, Husam Alrehaili, and Guru Prasad Dinda. Design and development of a high-performance Ni-based superalloy WSU 150 for additive manufacturing. *Journal of Materials Science & Technology*, 47:20–28, 2020.

[183] Qun Yu, Cunshan Wang, Zisong Zhao, Chuang Dong, and Yu Zhang. New Ni-based superalloys designed for laser additive manufacturing. *Journal of Alloys and Compounds*, 861:157979, 2021.

[184] Paraskevas Kontis, Edouard Chauvet, Zirong Peng, Junyang He, Alisson Kwiatkowski da Silva, Dierk Raabe, Catherine Tassin, Jean-Jacques Blandin, Stéphane Abed, Rémy Dendievel, et al. Atomic-scale grain boundary engineering to overcome hot-cracking in additively-manufactured superalloys. *Acta Materialia*, 177:209–221, 2019.

[185] MB Henderson, D Arrell, R Larsson, M Heobel, and G Marchant. Nickel based superalloy welding practices for industrial gas turbine applications. *Science and Technology of Welding and Joining*, 9(1):13–21, 2004.

[186] Matthew J Donachie and Stephen J Donachie. *Superalloys: a technical guide*. ASM international, 2002.

[187] D.J. Crudden and A.A.N. Németh. A nickel-based alloy, 2018. International Patent Application WO2019021015A1.

[188] RC Reed, Z Zhu, A Sato, and DJ Crudden. Isolation and testing of new single crystal superalloys using alloys-by-design method. *Materials Science and Engineering: A*, 667:261–278, 2016.

[189] Roger C Reed, Alessandro Mottura, and David J Crudden. Alloys-by-design: Towards Optimization of Compositions of Nickel-Based Superalloys. In *Superalloys 2016: Proceedings of the 13th Intenational Symposium of Superalloys*, pages 13–23. Wiley Online Library, 2016.

[190] Roger Reed, ZHU Zailing, and David Crudden. Method for designing alloys, March 22 2018. US Patent App. 15/563,100.

[191] KN Amato, SM Gaytan, LE Murr, E Martinez, PW Shindo, J Hernandez, S Collins, and F Medina. Microstructures and mechanical behavior of Inconel 718 fabricated by selective laser melting. *Acta Materialia*, 60(5):2229–2239, 2012.

[192] LA Chapman. Application of high temperature DSC technique to nickel based superalloys. *Journal of Materials Science*, 39(24):7229–7236, 2004.

[193] PN Quested, RF Brooks, L Chapman, R Morrell, Y Youssef, and KC Mills. Measurement and estimation of thermophysical properties of nickel based superalloys. *Materials Science and Technology*, 25(2):154–162, 2009.

[194] N Wang, S Mokadem, M Rappaz, and W Kurz. Solidification cracking of superalloy single-and bi-crystals. *Acta Materialia*, 52(11):3173–3182, 2004.

[195] JN DuPont, CV Robino, and AR Marder. Solidification and weldability superalloys. *Welding Journal*, 1998.

[196] H Guo, MC Chaturvedi, and NL Richards. Effect of boron concentration and grain size on weld heat affected zone microfissuring in Inconel 718 base superalloys. *Science and Technology of Welding and Joining*, 4(4):257–264, 1999.

[197] NL Richards and MC Chaturvedi. Effect of minor elements on weldability of nickel base superalloys. *International Materials Reviews*, 45(3):109–129, 2000.

[198] Xiao Huang, NL Richards, and MC Chaturvedi. Effect of grain size on the weldability of cast alloy 718. *Materials and Manufacturing Processes*, 19(2):285–311, 2004.

[199] Narendran Raghavan, Ryan Dehoff, Sreekanth Pannala, Srdjan Simunovic, Michael Kirka, John Turner, Neil Carlson, and Sudarsanam S Babu. Numerical modeling of heat-transfer and the influence of process parameters on tailoring the grain morphology of IN718 in electron beam additive manufacturing. *Acta Materialia*, 112:303–314, 2016.

[200] Narendran Raghavan, Srdjan Simunovic, Ryan Dehoff, Alex Plotkowski, John Turner, Michael Kirka, and Suresh Babu. Localized melt-scan strategy for site specific control of grain size and primary dendrite arm spacing in electron beam additive manufacturing. *Acta Materialia*, 140:375–387, 2017.

[201] Thomas Boellinghaus, John C Lippold, and Carl Edward Cross. *Cracking phenomena in welds IV*. Springer, Cham, first edition, 2016.

[202] Hugh Morrow, D-L Sponseller, and M Semchyshen. The effects of molybdenum and aluminum on the thermal expansion coefficients of nickel-base alloys. *Metallurgical and Materials Transactions A*, 6(3):477, 1975.

[203] Do Lee and E-W Hart. Stress relaxation and mechanical behavior of metals. *Metallurgical Transactions*, 2(4):1245–1248, 1971.

[204] William J Boettinger and Ursula R Kattner. On differential thermal analyzer curves for the melting and freezing of alloys. *Metallurgical and Materials Transactions A*, 33(6):1779–1794, 2002.

[205] Jan-Olof Andersson, Thomas Helander, Lars Höglund, Pingfang Shi, and Bo Sundman. Thermo-Calc & DICTRA, computational tools for materials science. *Calphad*, 26(2):273–312, 2002.

[206] Wilfried Kurz and David J Fisher. *Fundamentals of solidification*. Trans Tech Publ, 1989.

[207] S-B Tang, H Zhang, C-A Tang, and H-Y Liu. Numerical model for the cracking behavior of heterogeneous brittle solids subjected to thermal shock. *International Journal of Solids and Structures*, 80:520–531, 2016.

[208] D Grange, J-D Bartout, B Macquaire, and C Colin. Processing a non-weldable nickel-base superalloy by Selective Laser Melting: role of the shape and size of the melt pools on solidification cracking. *Materialia*, 12:100686, 2020.

[209] Reza Sharghi-Moshtaghin and Sirous Asgari. The characteristics of serrated flow in superalloy IN738LC. *Materials Science and Engineering: A*, 486(1-2):376–380, 2008.

[210] YC Lin, Hui Yang, Yunchang Xin, and Chang-Zheng Li. Effects of initial microstructures on serrated flow features and fracture mechanisms of a nickel-based superalloy. *Materials Characterization*, 144:9–21, 2018.

[211] Alena Kreitcberg, Vladimir Brailovski, and Sylvain Turenne. Elevated temperature mechanical behavior of IN625 alloy processed by laser powder-bed fusion. *Materials Science and Engineering: A*, 700:540–553, 2017.

[212] Eric A Lass, Mark R Stoudt, Maureen E Williams, Michael B Katz, Lyle E Levine, Thien Q Phan, Thomas H Gnaeupel-Herold, and Daniel S Ng. Formation of the Ni_3 Nb δ-phase in stress-relieved Inconel 625 produced via laser powder-bed fusion additive manufacturing. *Metallurgical and Materials Transactions A*, 48(11):5547–5558, 2017.

[213] M Lachowicz, W Dudziński, K Haimann, and M Podrez-Radziszewska. Microstructure transformations and cracking in the matrix of γ–γ' superalloy Inconel 713C melted with electron beam. *Materials Science and Engineering: A*, 479(1-2):269–276, 2008.

[214] A Chamanfar, M Jahazi, A Bonakdar, E Morin, and A Firoozrai. Cracking in fusion zone and heat affected zone of electron beam welded Inconel-713LC gas turbine blades. *Materials Science and Engineering: A*, 642:230–240, 2015.

[215] Michael D Sangid, Todd A Book, Diwakar Naragani, John Rotella, Priya Ravi, Peter Kenesei, Jun-Sang Park, Hemant Sharma, Jonathan Almer, and Xianghui Xiao. Role of heat treatment and build orientation in the microstructure sensitive deformation characteristics of IN718 produced via SLM additive manufacturing. *Additive Manufacturing*, 22:479–496, 2018.

[216] Xiaoqiang Zhang, Huabin Chen, Luming Xu, Jijin Xu, Xukai Ren, and Xiaoqi Chen. Cracking mechanism and susceptibility of laser melting deposited Inconel 738 superalloy. *Material and Design*, 183:108105, 2019.

[217] MA González, DI Martínez, A Pérez, H Guajardo, and A Garza. Microstructural response to heat affected zone cracking of prewelding heat-treated Inconel 939 superalloy. *Materials Characterization*, 62(12):1116–1123, 2011.

[218] Philipp Hoier, Amir Malakizadi, Pietro Stuppa, Stefan Cedergren, and Uta Klement. Microstructural characteristics of Alloy 718 and Waspaloy and their influence on flank wear during turning. *Wear*, 400:184–193, 2018.

[219] Sindo Kou. A criterion for cracking during solidification. *Acta Materialia*, 88:366–374, 2015.

[220] LA Gypen and AJJoMS Deruyttere. Multi-component solid solution hardening. *Journal of materials science*, 12(5):1028–1033, 1977.

[221] Dan Qian, Jiawei Xue, Anfeng Zhang, Yao Li, Nobumichi Tamura, Zhongxiao Song, and Kai Chen. Statistical study of ductility-dip cracking induced plastic deformation in polycrystalline laser 3D printed Ni-based superalloy. *Scientific reports*, 7(1):1–9, 2017.

[222] Sarojrani Pattnaik, D Benny Karunakar, and PK Jha. Developments in investment casting process—a review. *Journal of Materials Processing Technology*, 212(11):2332–2348, 2012.

[223] Melissa E Orme, Michael Gschweitl, Michael Ferrari, Ivan Madera, and Franck Mouriaux. Designing for additive manufacturing: lightweighting through topology optimization enables lunar spacecraft. *Journal of Mechanical Design*, 139(10):100905, 2017.

[224] DA Ramirez, LE Murr, E Martinez, DH Hernandez, JL Martinez, Brenda I Machado, F Medina, Pedro Frigola, and RB Wicker. Novel precipitate–microstructural architecture developed in the fabrication of solid copper components by additive manufacturing using electron beam melting. *Acta Materialia*, 59(10):4088–4099, 2011.

[225] Salomé Sanchez, CJ Hyde, IA Ashcroft, GA Ravi, and AT Clare. Multi-laser scan strategies for enhancing creep performance in LPBF. *Additive Manufacturing*, 41:101948, 2021.

[226] TM Pollock, AJ Clarke, and SS Babu. Design and tailoring of alloys for additive manufacturing. *Metallurgical and Materials Transactions A*, 51(12):6000–6019, 2020.

[227] David Crudden and Andre Németh. A nickel-based alloy, 2020. US Patent App. 16/634,406, Jun, 2020.

[228] Michael D Abràmoff, Paulo J Magalhães, and Sunanda J Ram. Image processing with ImageJ. *Biophotonics International*, 11(7):36–42, 2004.

[229] HY Li, JF Sun, MC Hardy, HE Evans, SJ Williams, TJA Doel, and P Bowen. Effects of microstructure on high temperature dwell fatigue crack growth in a coarse grain PM nickel based superalloy. *Acta Materialia*, 90:355–369, 2015.

[230] K Moussaoui, Walter Rubio, Michel Mousseigne, T Sultan, and F Rezai. Effects of Selective Laser Melting additive manufacturing parameters of Inconel 718 on porosity, microstructure and mechanical properties. *Materials Science and Engineering: A*, 735:182–190, 2018.

[231] Raphael Comminal, Marcin P Serdeczny, David B Pedersen, and Jon Spangenberg. Motion planning and numerical simulation of material deposition at corners in extrusion additive manufacturing. *Additive Manufacturing*, 29:100753, 2019.

[232] Andrew J London. Quantifying uncertainty from mass-peak overlaps in atom probe microscopy. *Microscopy and Microanalysis*, 25(2):378–388, 2019.

[233] Takao Murakumo, Toshiharu Kobayashi, Yutaka Koizumi, and Hiroshi Harada. Creep behaviour of Ni-base single-crystal superalloys with various γ' volume fraction. *Acta Materialia*, 52(12):3737–3744, 2004.

[234] Zailing Zhu, Hector Basoalto, Nils Warnken, and RC Reed. A model for the creep deformation behaviour of nickel-based single crystal superalloys. *Acta Materialia*, 60(12):4888–4900, 2012.

[235] Quanquan Han, Yuchen Gu, Shwe Soe, Franck Lacan, and Rossitza Setchi. Effect of hot cracking on the mechanical properties of Hastelloy X superalloy fabricated by laser powder bed fusion additive manufacturing. *Optics & Laser Technology*, 124:105984, 2020.

[236] André AN Németh, David J Crudden, David M Collins, V Kuksenko, CH Liebscher, David EJ Armstrong, Angus J Wilkinson, and Roger C Reed. On the influence of Nb/Ti ratio on environmentally-assisted crack growth in high-strength nickel-based superalloys. *Metallurgical and Materials Transactions A*, 49(9):3923–3937, 2018.

[237] Hee-Soo Kim, Si-Jun Park, Seong-Moon Seo, Young-Soo Yoo, Hi-Won Jeong, and HeeJin Jang. Regression analysis of high-temperature oxidation of Ni-based superalloys using artificial neural network. *Corrosion Science*, 180:109207, 2021.

[238] LZ He, Q Zheng, XF Sun, HR Guan, ZQ Hu, AK Tieu, C Lu, and HT Zhu. Effect of carbides on the creep properties of a Ni-base superalloy M963. *Materials Science and Engineering: A*, 397(1-2):297–304, 2005.

[239] Gong-xian Yang, Yong-feng Xu, Lei Jiang, and Shu-hua Liang. High temperature tensile properties and fracture behavior of cast nickel-base K445 superalloy. *Progress in Natural Science*, 21(5):418–425, 2011.

[240] Ceena Joseph, Christer Persson, and Magnus Hörnqvist Colliander. Influence of heat treatment on the microstructure and tensile properties of Ni-base superalloy Haynes 282. *Materials Science and Engineering: A*, 679:520–530, 2017.

[241] Leif Viskari, Magnus Hörnqvist, KL Moore, Yu Cao, and Krystyna Stiller. Intergranular crack tip oxidation in a Ni-base superalloy. *Acta Materialia*, 61(10):3630–3639, 2013.

[242] AG Evans, MY He, A Suzuki, M Gigliotti, B Hazel, and TM Pollock. A mechanism governing oxidation-assisted low-cycle fatigue of superalloys. *Acta Materialia*, 57(10):2969–2983, 2009.

[243] MA Lafata, LH Rettberg, MY He, and TM Pollock. Oxidation-assisted crack growth in single-crystal superalloys during fatigue with compressive holds. *Metallurgical and Materials Transactions A*, 49(1):105–116, 2018.

[244] Si-Jun Park, Seong-Moon Seo, Young-Soo Yoo, Hi-Won Jeong, and HeeJin Jang. Effects of Al and Ta on the high temperature oxidation of Ni-based superalloys. *Corrosion Science*, 90:305–312, 2015.

[245] Y Gong, DJ Young, P Kontis, Yu-Lung Chiu, H Larsson, A Shin, JM Pearson, MP Moody, and RC Reed. On the breakaway oxidation of Fe9Cr1Mo steel in high pressure CO2. *Acta Materialia*, 130:361–374, 2017.

[246] Y Gong, DJ Young, C Atkinson, T Olszewski, WJ Quadakkers, and RC Reed. Modelling of the degradation of martensitic stainless steels by the Boudouard reaction. *Corrosion Science*, 173:108699, 2020.

[247] Carl Wagner. Beitrag zur theorie des anlaufvorgangs. *Zeitschrift für physikalische Chemie*, 21(1):25–41, 1933.

[248] Brian Gleeson. High-temperature corrosion of metallic alloys and coatings. *Corrosion and environmental degradation*, 2:173, 2000.

[249] S Han and DJ Young. Simultaneous internal oxidation and nitridation of Ni–Cr–Al alloys. *Oxidation of metals*, 55(3):223–242, 2001.

[250] Alenka Vesel, Aleksander Drenik, Kristina Elersic, Miran Mozetic, Janez Kovac, Tomaz Gyergyek, Jan Stockel, Jozef Varju, Radomir Panek, and Marianne Balat-Pichelin. Oxidation of Inconel 625 superalloy upon treatment with oxygen or hydrogen plasma at high temperature. *Applied surface science*, 305:674–682, 2014.

[251] Lalit Kumar, R Venkataramani, M Sundararaman, P Mukhopadhyay, and SP Garg. Studies on the oxidation behavior of Inconel 625 between 873 and 1523 K. *Oxidation of Metals*, 45(1):221–244, 1996.

[252] Kh A Al-Hatab, MA Al-Bukhaiti, U Krupp, and M Kantehm. Cyclic oxidation behavior of IN718 superalloy in air at high temperatures. *Oxidation of metals*, 75(3):209–228, 2011.

[253] C Juillet, A Oudriss, J Balmain, X Feaugas, and F Pedraza. Characterization and oxidation resistance of additive manufactured and forged IN718 Ni-based superalloys. *Corrosion Science*, 142:266–276, 2018.

[254] JH Chen, PM Rogers, and JA Little. Oxidation behavior of several chromia-forming commercial nickel-base superalloys. *Oxidation of Metals*, 47(5):381–410, 1997.

[255] J Litz, A Rahmel, M Schorr, and J Weiss. Scale formation on the Ni-base superalloys IN 939 and IN 738 LC. *Oxidation of metals*, 32(3):167–184, 1989.

[256] DK Das, Vakil Singh, and Shrikant V Joshi. High temperature oxidation behaviour of directionally solidified nickel base superalloy CM–247LC. *Materials science and technology*, 19(6):695–708, 2003.

[257] Te-Kang Tsao, An-Chou Yeh, Chen-Ming Kuo, and Hideyuki Murakami. High temperature oxidation and corrosion properties of high entropy superalloys. *Entropy*, 18(2):62, 2016.

[258] M Yoshihara and Y-W Kim. Oxidation behavior of gamma alloys designed for high temperature applications. *Intermetallics*, 13(9):952–958, 2005.

[259] AA Vicente, JRS Moreno, Jas Tenório, ABB Junior, TFA Santos, and DCR Espinosa. Comparison of Behaviour to Oxidation at High Temperature of Two superalloys: Inconel 713C and IC-50. *Oxidation Communications*, 41:195–204, 2018.

[260] WD Summers, E Alabort, P Kontis, F Hofmann, and RC Reed. In-situ high-temperature tensile testing of a polycrystalline nickel-based superalloy. *Materials at High Temperatures*, 33(4-5):338–345, 2016.

[261] Santhosh Banoth, Thaviti Naidu Palleda, Sota Shimazu, and Koji Kakehi. Yttrium's Effect on the Hot Cracking and Creep Properties of a Ni-Based Superalloy Built Up by Additive Manufacturing. *Materials*, 14(5):1143, 2021.

[262] Yuantao Zhao, Rui Wang, Yanle Sun, Lianbo Wang, Xinfeng Wu, and Wenge Li. Roles definition of TiN particles in enhancing the creep properties of IN718C high temperature alloys. *Journal of Alloys and Compounds*, 887:161441, 2021.

[263] S Sanchez, G Gaspard, CJ Hyde, IA Ashcroft, GA Ravi, and AT Clare. The creep behaviour of nickel alloy 718 manufactured by laser powder bed fusion. *Materials & Design*, 204:109647, 2021.

[264] JJ Shi, SA Zhou, HH Chen, GH Cao, AM Russell, ZJ Zhou, XB Qi, CP Li, and GF Chen. Microstructure and creep anisotropy of Inconel 718 alloy processed by selective laser melting. *Materials Science and Engineering: A*, 805:140583, 2021.

Appendix A

Supplemental Data

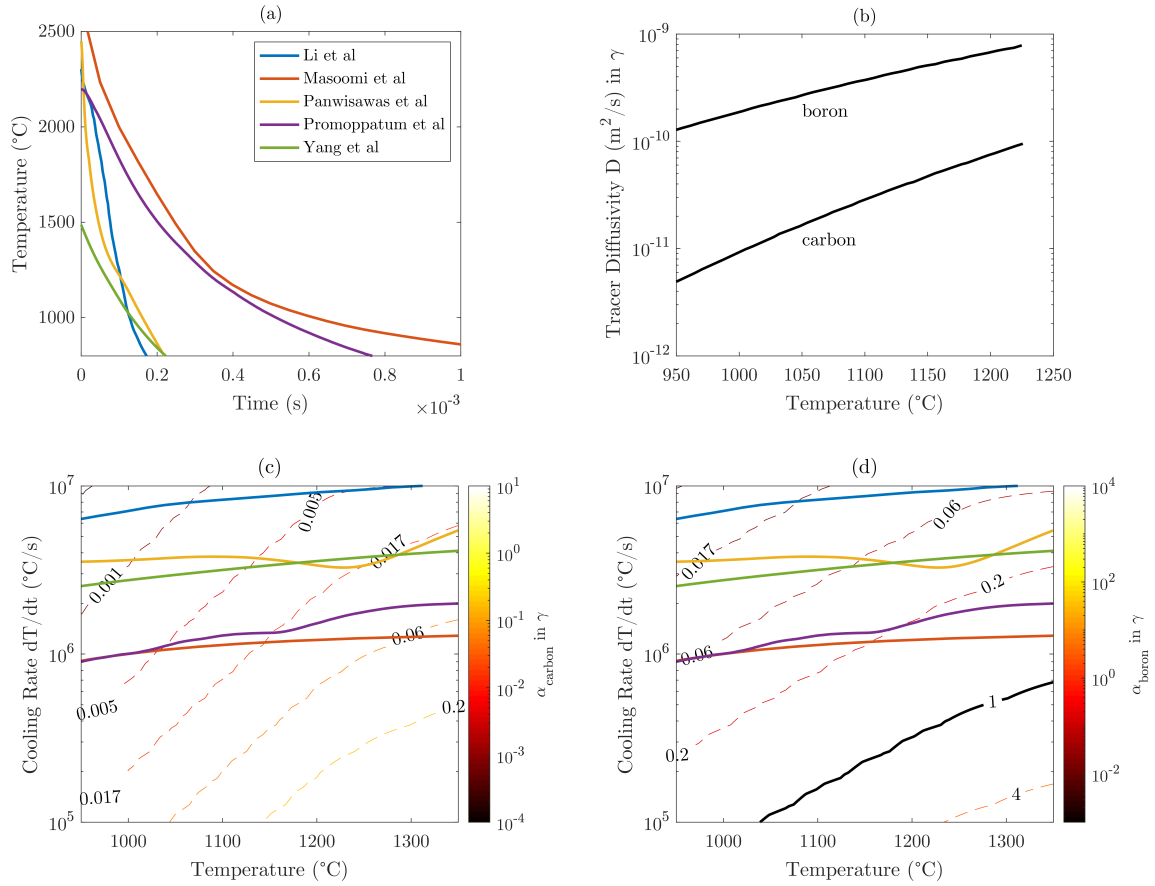

Fig. A.1 (a) Temperature histories predicted numerically for L-PBF processing conditions from the literature [18–22] (b) the tracer diffusivity of carbon and boron in γ as a function of temperature as determined through the MOBNI3 thermodynamic database, reproduced from [23]. Contour plots showing the magnitude of the backdiffusion coefficient α as a function of the cooling rate and the temperature of (c) carbon and (d) boron in γ. With the cooling rate extracted from the temperature histories in (a) overlaid. As the cooling rates do not intersect $\alpha = 1$ backdiffusion is deemed negligible in this analysis and simulation of AM solidification is performed under scheil assumptions.

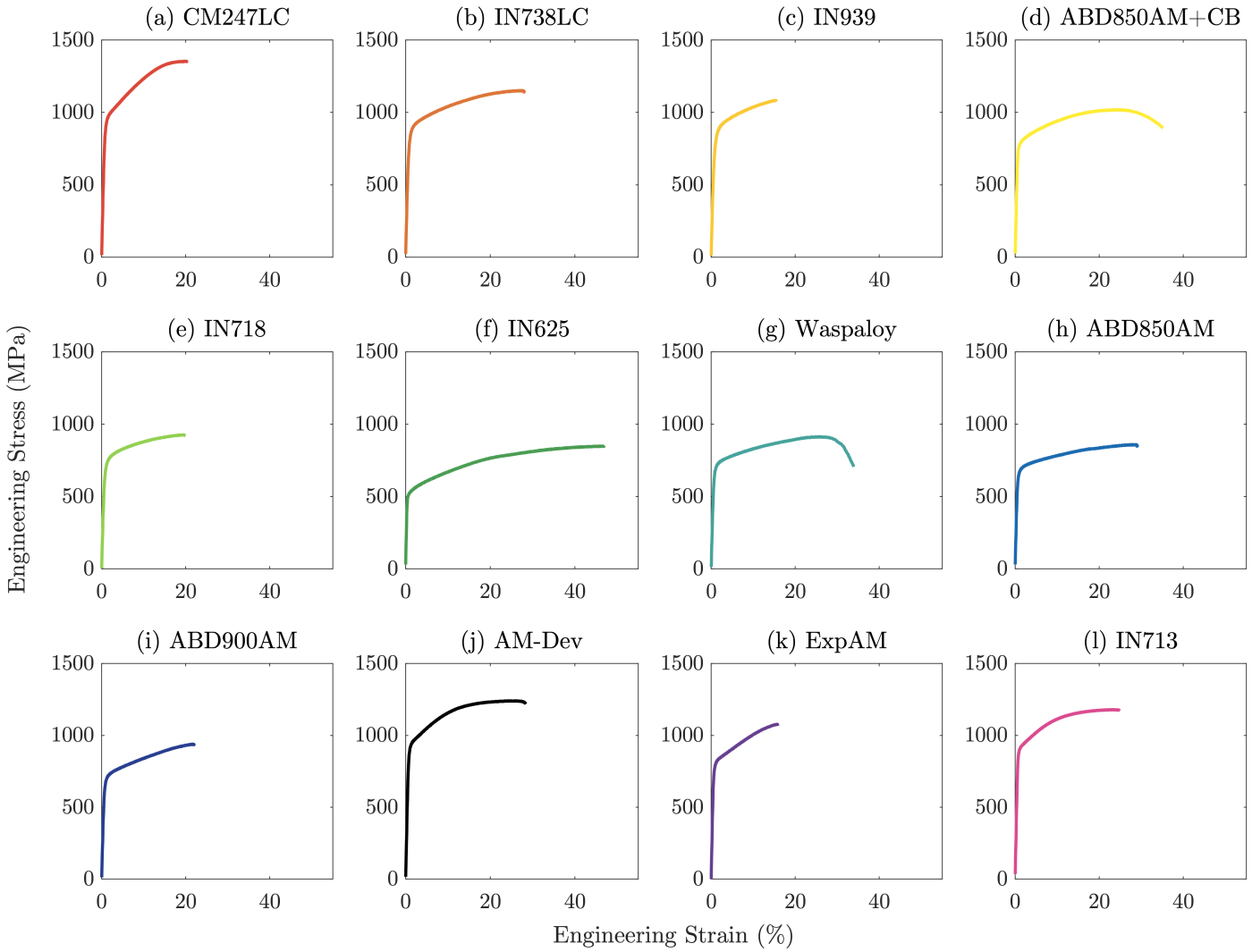

Fig. A.2 Room temperature tensile response of the 12 alloys discussed in Chapter 4, tests performed with strain rate of $10^{-2}\,\mathrm{s}^{-1}$.

Fig. A.3 Fracture surfaces of ExpAM, CM247LC, AM-Dev, ABD850AM, Waspaloy, and IN625 after tensile tests at 800 °C illustrating the transition from intra/transgranular to intergranular fracture as the amount of solid solution strengtheners is increased.

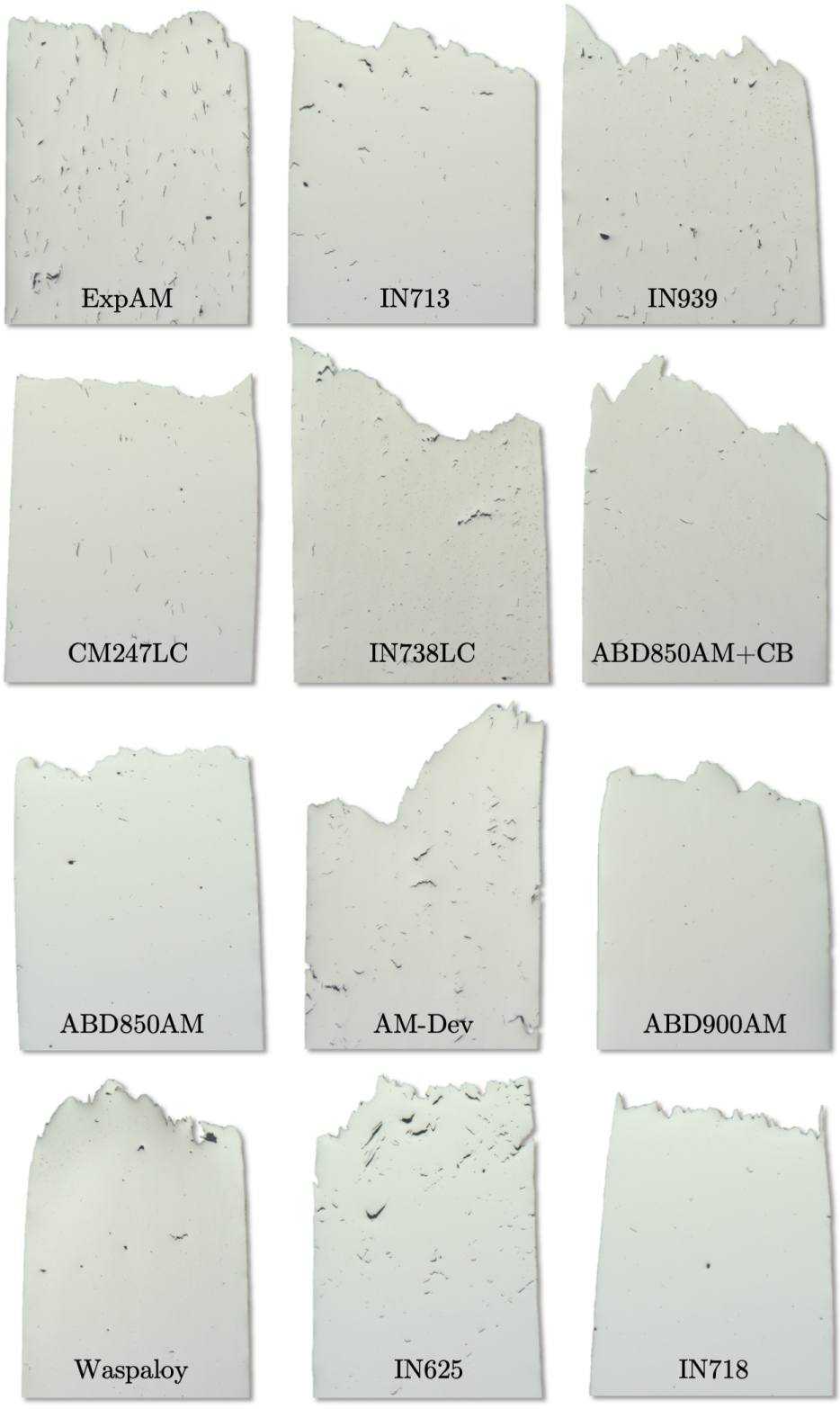

Fig. A.4 Optical micrographs of the side profile from the 800 °C tensile specimens after testing. The side profiles show pre-existing defects pointing along the tensile axis as well as cavitation incurred during tensile testing oriented perpendicular to the tensile axis.

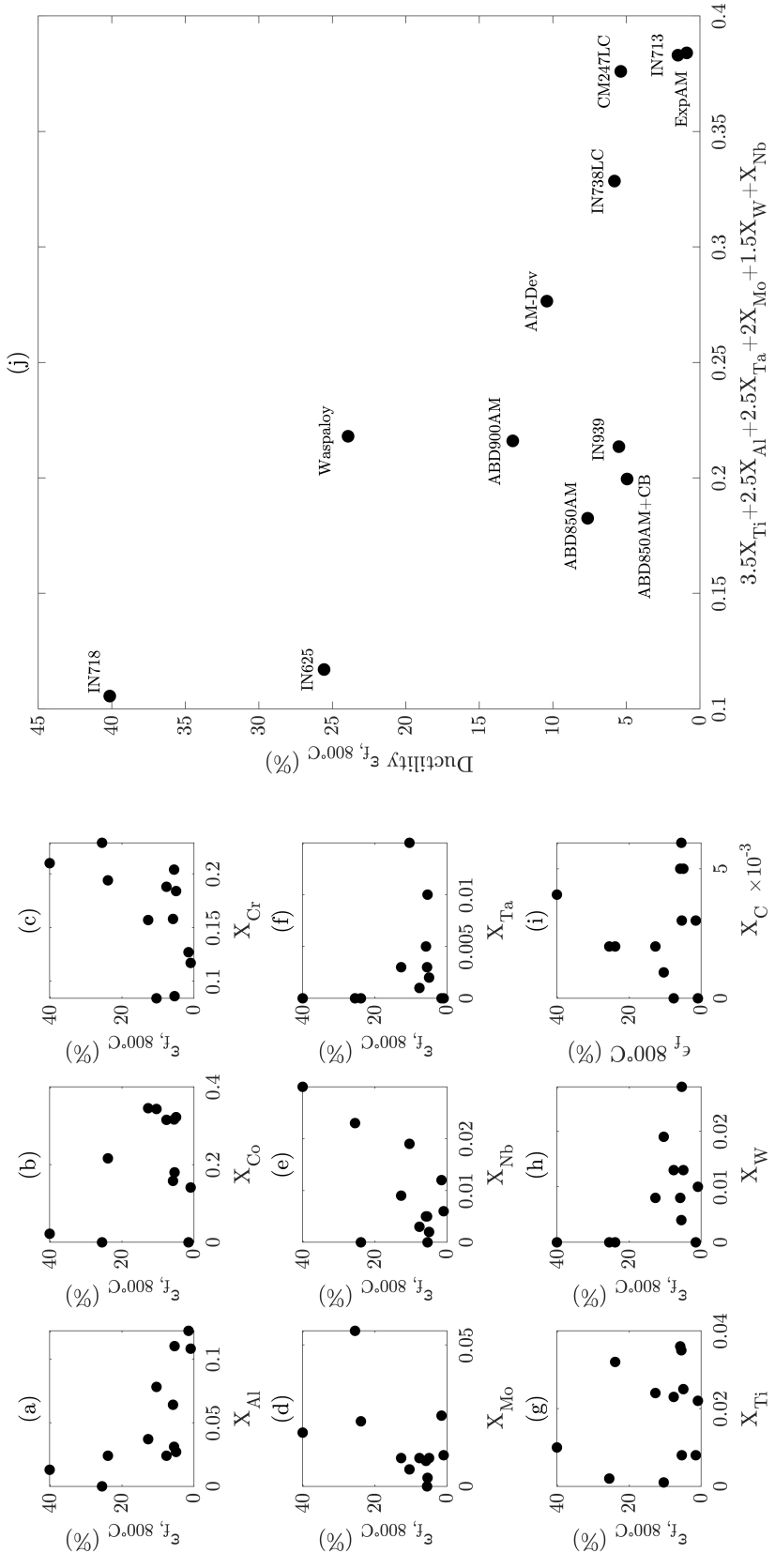

Fig. A.5 (a-i) Analysis of the influence of different elements (at.%) on the 800 °C ductility (j) best fit expression for ductility as a function of the composition solved by multiple linear regressions with Eureqa [24].

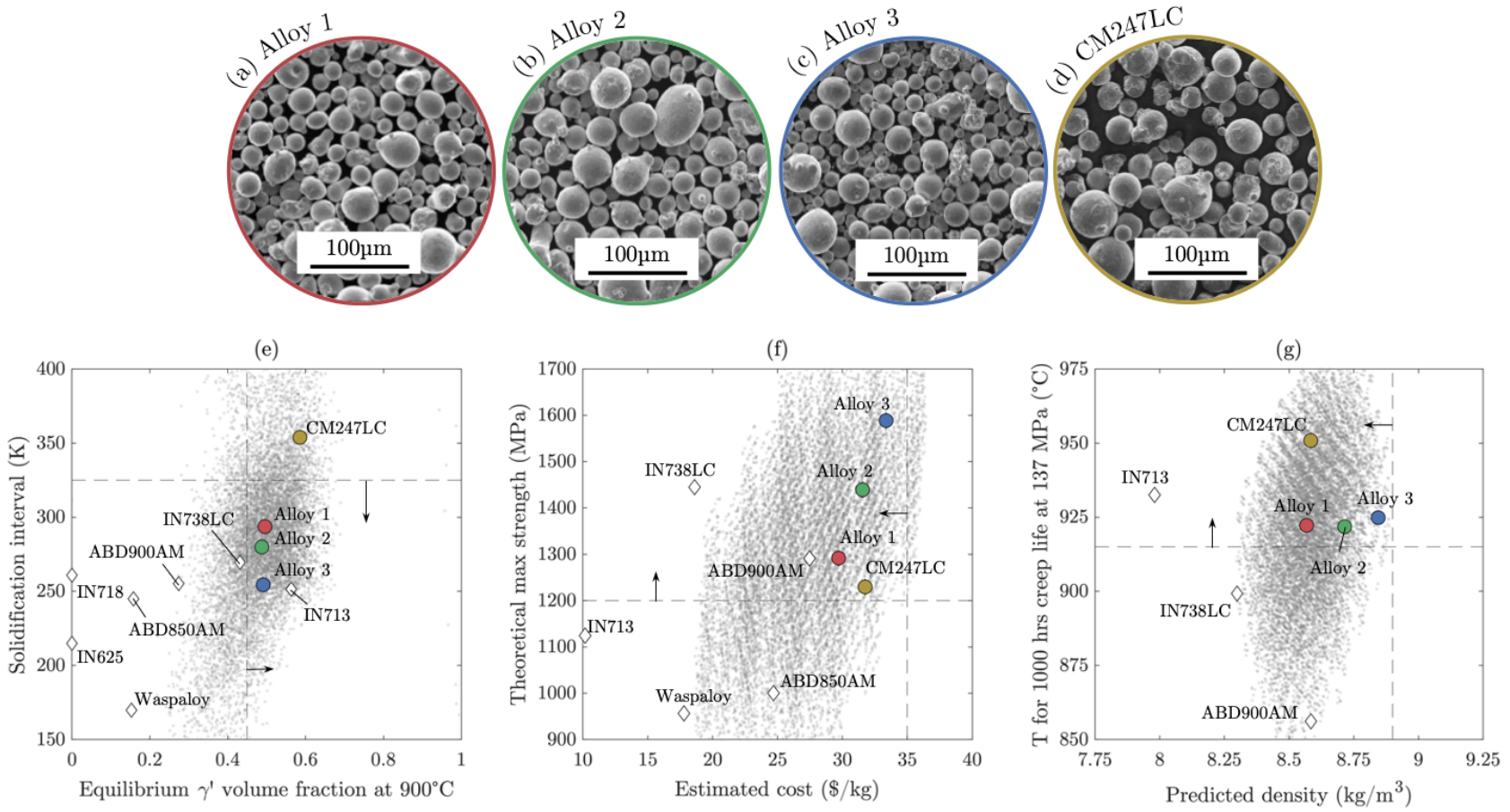

Fig. A.6 (a-d) SEM micrographs of the Alloy 1-3 feedstock powders (e) the equilibrium γ' volume fraction at 900 °C vs the magnitude of the freezing range predicted by Thermo-Calc under scheil assumptions, (f) predicted alloy density vs predicted temperature at which the creep life is 1000 hrs given 137 MPa applied stress, (g) the estimated alloy cost vs predicted maximum theoretical strength.

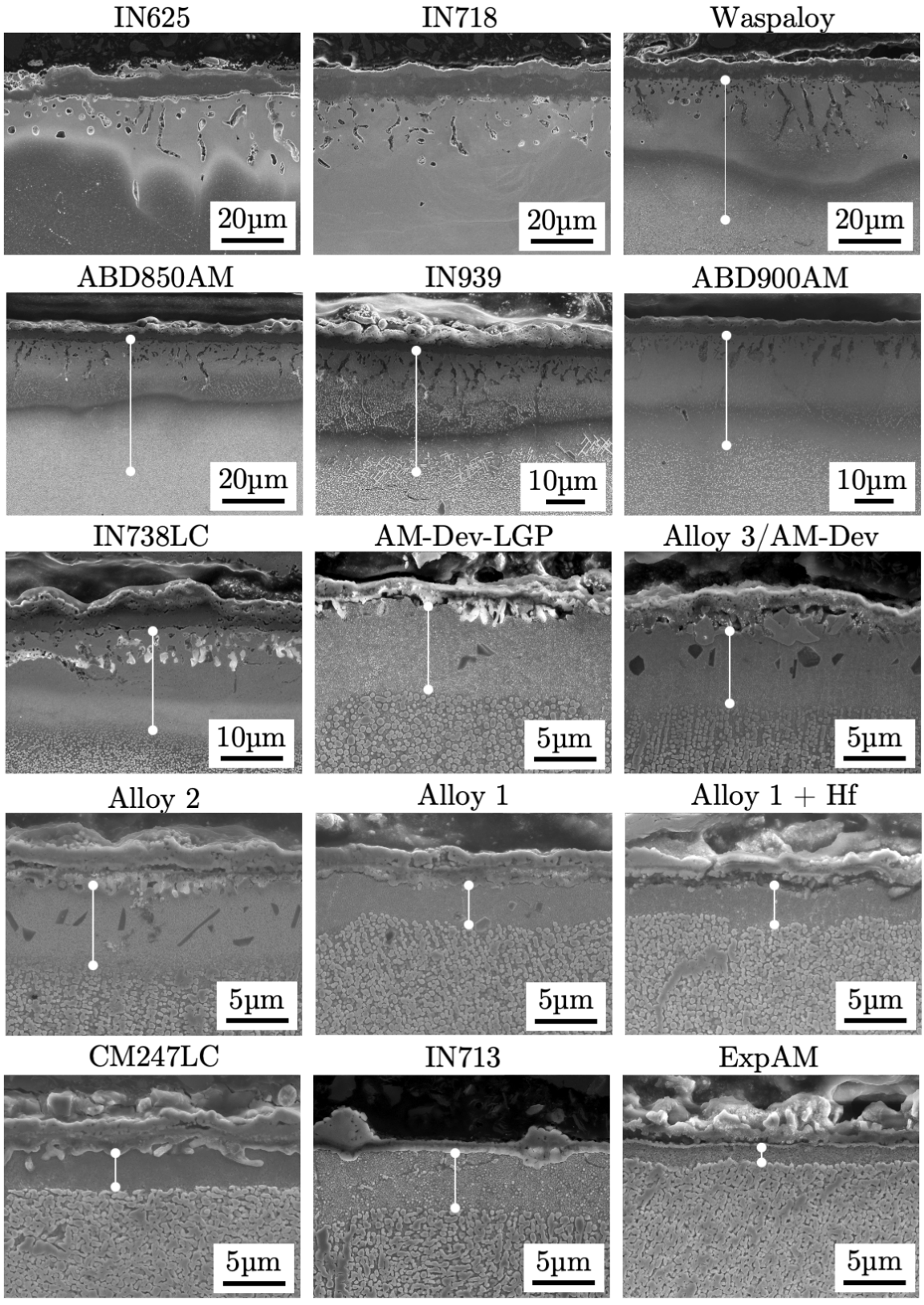

Fig. A.7 SEM micrographs showing the γ' and Al depletion zones each alloy following thermo-gravimetric analysis.